# Very Fast Losses of the Circulating LHC Beam, their Mitigation and Machine Protection

## Dissertation

zur Erlangung des Doktorgrades
des Fachbereichs Physik
der Universität Hamburg

vorgelegt von
**Tobias Bär**
aus Hamburg

Hamburg
2013

| | |
|---|---|
| Gutachter der Dissertation: | Prof. Dr. Eckhard Elsen<br>Dr. Jörg Wenninger |
| Gutachter der Disputation: | Prof. Dr. Eckhard Elsen<br>Prof. Dr. Jörg Rossbach |
| Datum der Disputation: | 25.11.2013 |
| Vorsitzender des Prüfungsausschusses: | Dr. Georg Steinbrück |
| Vorsitzender des Promotionsausschusses: | Prof. Dr. Peter Hauschildt |
| Dekan der MIN Fakultät: | Prof. Dr. Heinrich Graener |
| Leiterin des Fachbereichs Physik: | Prof. Dr. Daniela Pfannkuche |


This work has been carried out through the Wolfgang-Gentner-Program
at the European Organization for Nuclear Research (CERN),
Geneva, Switzerland.

# Abstract

The Large Hadron Collider (LHC) has a nominal energy of 362 MJ stored in each of its two counter-rotating beams - over two orders of magnitude more than any previous accelerator and enough to melt 880 kg of copper. Therefore, in case of abnormal conditions comprehensive machine protection systems extract the beams safely from the LHC within not more than three turns ($\approx 270\,\mu$s). The first years of LHC operation demonstrated a remarkable reliability of the major machine protection systems. However, they also showed that the LHC is vulnerable to losses of the circulating beams on very fast timescales, which are too fast to ensure an active protection.

Very fast equipment failures, in particular of normal-conducting dipole magnets and the transverse damper can lead to such beam losses. Whereas these failures were already studied in the past, other unexpected beam loss mechanisms were observed after the LHC start-up: so-called (un)identified falling objects (UFOs), which are believed to be micrometer-sized macro particles, lead to beam losses with a duration of a few LHC turns when interacting with the beams. UFOs have significantly affected the LHC availability and may become a major performance limitation for future LHC operation. Another unconsidered beam loss mechanism is the sudden absence of the long-range beam-beam interactions after the extraction of a single beam. This leads to significant losses of the counter-rotating beam within a single turn. In the long-term future, crab cavities will be installed in the LHC with the High-Luminosity LHC (HL-LHC) upgrade in 2022/23. However, in a failure case, they can lead to large beam trajectory perturbations and related beam losses within the reaction time of the machine protection systems.

The focus of this thesis is on very fast losses of the circulating LHC beams, their mitigation and the related protection of the LHC. The operational experience from the first LHC run, dedicated studies and the state of knowledge are summarized. Extrapolations for mid-term and long-term future are presented and mitigation strategies and optimizations of the machine protection systems are discussed.

# Zusammenfassung

Der Large Hadron Collider (LHC) hat in jedem seiner zwei gegenläufig zirkulierenden Strahlen eine nominelle Energie von 362 MJ gespeichert - über zwei Größenordnungen mehr als jeder bisherige Teilchenbeschleuniger und ausreichend, um 880 kg Kupfer zu schmelzen. Im Falle von anomalen Bedingungen gewährleisten umfangreiche Maschinensicherheitssysteme, dass die Strahlen in bis zu drei Umläufen ($\approx 270\,\mu$s) sicher aus der Maschine extrahiert werden. Die ersten Jahre LHC Betrieb haben eine beeindruckende Verlässlichkeit der wichtigsten Maschinensicherheitssysteme demonstriert. Es zeigte sich aber auch, dass der LHC anfällig ist für Verluste der zirkulierenden Strahlen auf sehr schnellen Zeitskalen, die zu schnell sind, um aktive Schutzmaßnahmen gewährleisten zu können.

Sehr schnelle Betriebsfehler, insbesondere der normalleitenden Dipolmagnete und des transversalen Dämpfers, können derartige Verluste verursachen. Während diese Fehler bereits in der Vergangenheit untersucht wurden, sind nach der Inbetriebnahme des LHCs auch andere unerwartete Strahlverlustmechanismen beobachtet worden: Sogenannte (un)identifizierte fallende Objekte (UFOs), die höchstwahrscheinlich Mikrometer große Staubteilchen sind, verursachen, wenn sie mit dem Strahl interagieren, Strahlverluste mit einer Dauer von wenigen LHC Umläufen. UFOs haben die Effizienz des LHCs beeinträchtigt und stellen eine möglicherweise wesentliche Einschränkung für den zukünftigen Strahlbetrieb des LHCs dar. Ein weiterer unberücksichtigter Strahlverlustmechanismus basiert auf der plötzlichen Abwesenheit der Strahl-Strahl Wechselwirkungen nach der Extraktion eines einzelnen Strahls. Dies führt innerhalb von einem Umlauf zu signifikanten Verlusten des gegenläufigen Strahls. Langfristig werden mit dem High-Luminosity LHC (HL-LHC) Upgradeprogramm 2022/23 sogenannte Crab Kavitäten im LHC installiert. Diese können im Fehlerfall zu großen Strahloszillationen und daraus resultierenden Strahlverlusten innerhalb der Reaktionszeit der Maschinensicherheitssysteme führen.

Der Fokus dieser Arbeit liegt auf sehr schnellen Verlusten der zirkulierenden LHC Strahlen, entsprechenden Gegenmaßnahmen und den damit verbundenen Aspekten der Maschinensicherheit. Die Betriebserfahrungen des ersten LHC Betriebslaufs, spezifische Studien und der aktuelle Wissensstand sind zusammengefasst. Mittel- und langfristige Extrapolationen werden präsentiert und zusammen mit Gegenmaßnahmen und Verbesserungen der Maschinensicherheitssysteme diskutiert.

# Acknowledgments

The results achieved in the three years of work on this doctoral thesis were only possible thanks to the collaboration of many great colleagues. I am particularly grateful for the enormous helpfulness which I continuously experienced throughout the past years.

First and foremost, I wish to express my most sincere gratitude to my supervisor at CERN, Jörg Wenninger. He supported me in carrying out own ideas and helped with his incredible competence in accelerator physics and accelerator operation. His guidance and supervision were outstanding.

I extend my gratitude to my supervisor from the University of Hamburg, Eckhard Elsen. His comprehensive and thorough view resulted in many very valuable discussions, suggestions and feedback. I am particularly glad that we had such frequent contact throughout the whole Ph.D. period. I cannot imagine a better constellation of supervision.

Special thanks are dedicated to my colleagues from the BE-OP-LHC and BE-OP-SPS sections at CERN for their exceptional helpfulness and friendliness: Verena Kain, Matteo Solfaroli Camillocci, Mirko Pojer, Giulia Papotti and the other EiCs, Fabio Follin, Markus Albert, Delphine Jacquet and the other operators, Lene Norderhaug Drøsdal and the other students in the group, Mike Lamont and Sylvia Dubourg. I am very glad that I had the opportunity to be a part of this great operations team throughout the amazing LHC commissioning time.

In extension to that, I want to thank in particular my former office mate and good friend Kajetan Fuchsberger, among others for the many excellent advices on good software development and the uncountable discussions we had about work-related and off-work topics. Most grateful thanks go also to Rüdiger Schmidt for his continuous support in many different aspects. In the same context, I want to thank Markus Zerlauth, who always replied instantly and with precise answers to my machine protection related questions.

I am particularly glad about the very fruitful collaboration with the many colleagues who contributed to the UFO Studies. In particular, I want to thank Jan Uythoven, Mike Barnes, Brennan Goddard, Volker Mertens, Frank Zimmermann, Anton Lechner for the excellent FLUKA simulations and Maria Hempel for the MAD-X simulations of MKI UFOs and her help with the commissioning of the dia-

mond BLMs. In this context, I am also very thankful for the help and support from the BLM team and the controls group, especially from Christos Zamantzas, Stephen Jackson, Marek Misiowiec, Bernd Dehning, Ewald Effinger, Annika Nordt, Eduardo Nebot del Busto, Mariusz Sapinski, Barbara Holzer and Erich Griesmayer.

In addition, I want to thank the transverse damper experts Wolfgang Höfle and Daniel Valuch for spending sleepless nights in the control room to help with various experiments.

Most sincere thanks go also to Rama Calaga and Joachim Tückmantel for giving advice and support to my crab cavity studies and to Riccardo de Maria and Stéphane Fartoukh for helping with the HL-LHC optics for MAD-X.

I also want to thank Ralph Steinhagen and Daniel Wollmann for many fruitful discussions and my colleagues from the organizing team of the LHC Beam Operation Committee, Gianluigi Arduini and Chiara Bracco.

Last but not least, special thanks go to my family. I am most grateful for their love and support under all circumstances and for proof-reading this thesis over and over again. Likewise, I am most thankful for the personal and emotional support from Mareike throughout the past two years.

# Contents

# 1. Introduction

The Large Hadron Collider (LHC) is the particle collider with the highest center-of-mass energy, worldwide. It is therefore one of the most promising facilities for fundamental discoveries on the high-energy frontier. On 4 July 2012, the discovery of a new elementary particle was announced by the LHC experiments ATLAS and CMS, which was later confirmed to be consistent with a Higgs boson, the until then only undiscovered particle in the Standard Model of particle physics [1, 2]. Thereupon, the 2013 Nobel prize in physics was awarded to François Englert and Peter W. Higgs for the "theoretical discovery of a mechanism that contributes to our understanding of the origin of mass of subatomic particles, and which recently was confirmed through the discovery of the predicted fundamental particle, by the ATLAS and CMS experiments at CERN's Large Hadron Collider" [3].

The LHC is a 27 km long circular machine, located up to 175 m underground on the French/Swiss border close to Geneva, Switzerland. It consists of over 8000 superconducting magnets, operating mainly at 1.9 K, which guide and focus two high-energy proton and/or lead-ion beams. The two counter-rotating beams collide at four interaction points, surrounded by the main experiments ATLAS, CMS, ALICE and LHCb.

On 10 September 2008, the first proton beams were circulating in the LHC. However, only nine days later a major incident occurred, which caused severe damage to the LHC. The repairs took over 14 month and beam operation was resumed on 20 November 2009. In the following years, the accelerator routinely collided beams of up to $2.2 \cdot 10^{14}$ protons per beam at a center-of-mass energy of up to 8 TeV. This first LHC run ended on 16 February 2013. At present, the LHC is in a biennial shutdown (LS1) during which the collider is prepared for even higher center-of-mass energies of up to $\approx 13$ TeV from 2015 onwards.

In 2012, the LHC was routinely operated with an energy of up to about 140 MJ stored in each circulating beam - enough to melt 340 kg of copper. This stored beam energy will increase up to about 330 MJ per beam after LS1 and up to about 700 MJ per beam with the High-Luminosity LHC (HL-LHC) upgrade program in 2022/23.

Thus, comprehensive machine protection systems constantly monitor several ten thousand measurement channels. In case of abnormal conditions the machine is brought into a fail-safe state and the beams are automatically extracted from the LHC. One of the most important of these systems is the beam loss monitoring (BLM) system, which consists of almost 4000 beam loss detectors (mainly ionization chambers), distributed all around the LHC. If the beam losses at a single detector exceed the corresponding thresholds, the beams are safely extracted from the LHC within not more than 3 LHC revolution periods ($\approx 270\,\mu$s). The experience after the LHC start-up showed a remarkable reliability of the BLM system, including a multiple redundancy for the detection of critical beam losses. Nevertheless, failure scenarios, which may lead to critical beam losses within the reaction time of the machine protection systems imply a severe damage potential.

The focus of this thesis is on such very fast losses of the circulating LHC beams, for LHC operation during run 1, after LS1 and in the HL-LHC era. The protection against known failure scenarios is reviewed with the experience gained during run 1. Unexpected fast beam loss mechanisms, which were not considered before the LHC start-up and failure scenarios which are specific to the HL-LHC upgrade are discussed. Failure detection and mitigation strategies are presented together with related improvements of the LHC efficiency.

Single-turn failures of the beam injection or extraction systems are not covered by this document. These failure scenarios were extensively studied in the past [4–7] and are under careful surveillance [8, 9].

## Outline

The LHC and the relevant systems are described in Chap. 2. A basic introduction to accelerator physics is given in Chap. 3. Both chapters are introductory chapters and are addressed to readers which have a basic accelerator physics knowledge, but are no experts of the LHC and/or the discussed topics.

The focus of Chap. 4 is on very fast beam losses due to equipment failures, in particular of normal-conducting dipole circuits and the transverse damper. The operational experience gained during run 1 is summarized and the protection systems are reviewed against this background. Increases of protection system thresholds to avoid unnecessary beam aborts while ensuring safe operation are discussed and extrapolations for LHC operation in the mid-term and long-term future are presented.

Chapter 5 is focused on one of the most relevant surprises after the LHC start-up: so-called (un)identified falling objects (UFOs) are believed to be micrometer-sized

macro particles, which can lead to significant beam losses when interacting with the beam. Such events caused 58 protection beam aborts in run 1 and are a potential major limitation for the LHC performance after LS1. The state of knowledge, mid-term extrapolations and mitigation strategies are presented.

In July 2012 an unforeseen single-turn beam loss mechanism was observed in the LHC: after the extraction of a single beam, the electrodynamic beam-beam interactions with the counter-rotating beam are suddenly missing. This leads to a trajectory perturbation of the counter-rotating beam and subsequent beam losses within a single turn. The details of this beam loss mechanism are explained in Chap. 6. The results from experimental studies and simulations are compared and extrapolations for LHC operation in the mid-term and long-term future are discussed.

With the HL-LHC upgrade program so-called crab cavities will be installed in the LHC. These can increase the collision rate without the need for even higher stored beam energies. However, in a failure case, crab cavities can lead to significant beam position perturbations within the reaction time of the LHC machine protection systems. The results of dedicated failure studies are presented in Chap. 7. Failure detection and mitigation strategies to limit the impact of crab cavity failures to an acceptable level are proposed.

A final discussion, including a reflection of the main results of this thesis, is given in Chap. 8.

# 2. The Large Hadron Collider

The Large Hadron Collider (LHC) is the world's largest particle accelerator. It is hosted by the European Organization for Nuclear Research (CERN[1]) which is located near Geneva, Switzerland on the French/Swiss border. An introduction to the LHC and its relevant systems is given in this chapter.

## 2.1. Motivation and Specifications

The LHC was proposed already in the early 1980s as discovery facility for fundamental particle physics at the high-energy frontier [10]. Its design was in particular motivated by the requirements for the discovery of the Standard Model Higgs boson [11, p. 21], which was after the discovery of the top-quark in 1995 the only undiscovered elementary particle in the Standard Model of particle physics. This determines the two main design goals for the LHC:

- **High energy:** the nominal center-of-mass energy of the LHC is with 14 TeV about 7 times larger compared to its predecessor Tevatron. This allows fundamental discoveries in an unprecedented energy-regime. The upper energy limitation is mainly given by the circumference of the LHC tunnel and the reasonably achievable field strength in the superconducting dipole magnets (see Sec. 2.3.1).
- **High collision rate:** even at such high energies the production of e.g. a Standard Model Higgs boson is extremely rare - below one event in one billion proton-proton collisions [12]. Thus, in order to achieve the required statistical significance, an extremely high collision rate of nominally up to 700 million inelastic proton-proton collisions per second in each high-luminosity[2] experiment is required. The corresponding nominal peak luminosity is $1 \cdot 10^{34} \frac{1}{\mathrm{cm}^2 \cdot \mathrm{s}}$. This implies that a very good understanding of the experimental background is needed in order to be sensitive to the extremely rare events of interest.

[1] From French: Conseil Européen pour la Recherche Nucléaire.

[2] Luminosity denotes the number of collisions per time and unit area of the interaction cross section. The concept is explained in more detail in Sec. 3.2.

To reach this collision rate, high-intensity beams with nominally up to $3.2 \cdot 10^{14}$ protons per beam are needed, which are divided into 2808 bunches with a spacing of 25 ns. The two counter-rotating beams collide at four interaction points (see Sec. 2.3), which are surrounded by the four main experiments ATLAS, CMS, LHCb and ALICE. The first two are multi-purpose high-luminosity experiments, LHCb is focused on b-physics, in particular on CP violation measurements, and ALICE is designed for quark-gluon plasma studies in heavy-ion collisions. Thus, besides the proton physics program, the LHC is also accelerating lead ions ($Pb^{82+}$) for lead-lead, lead-proton or proton-lead collisions. The nominal LHC parameters are summarized in Tab. 2.1 together with the typical values at the end of the 2012 proton physics run and possible parameters for operation in mid-term and long-term future (see also Sec. 2.5).

## 2.2. CERN Accelerator Complex

The LHC is at the top of the CERN accelerator complex, which is illustrated in Fig. 2.1. In the LHC pre-accelerators, protons and lead-ions are accelerated up to 450 GeV beam energy (per charge[4]) until they are injected into the LHC and are further accelerated up to a nominal energy of 7 TeV per charge per beam. The proton injector chain starts with the linear accelerator LINAC 2 that accelerates particles up to 50 MeV. In a next step, the Booster accelerates the protons up to 1.4 GeV. In the Proton Synchrotron (PS) protons from the Booster and ions from the Low Energy Ion Ring (Leir) are accelerated up to 26 GeV per charge. At this energy the particles are injected into the almost 7 km long normal-conducting Super Proton Synchrotron (SPS) which has a top energy of 450 GeV per charge. Via the two transfer lines TI 2 and TI 8, with a total length of about 6 km, the particles are injected into the LHC.

## 2.3. LHC Layout

The LHC is built in the circular tunnel of the former Large Electron-Positron Collider (LEP), between 50 m and 175 m underground [11]. The 26658.9 m long LHC has an eightfold symmetry with eight long straight sections or insertion regions (IRs) intercepted by eight arcs, as illustrated in Fig. 2.2. The center of each IR is named

[4] Ions are accelerated up to $450\,\text{GeV} \cdot Z$, where $Z$ is the atomic number of the nucleus.

| **Parameter** | **unit** | **Nominal** | **2012** | **Post LS1** | **HL-LHC** |
|---|---|---|---|---|---|
| Beam energy (per charge) | [TeV] | 7.0 | 4.0 | 6.5 | 7.0 |
| Protons per bunch | $[10^{11}]$ | 1.15 | 1.6 | 1.15 | 2.20 |
| Bunch-spacing | [ns] | 25 | 50 | 25 | 25 |
| Number of bunches | | 2808 | 1374 | up to 2760 | 2808 |
| Protons per beam | $[10^{14}]$ | 3.2 | 2.2 | up to 3.2 | 6.2 |
| Stored beam energy | [MJ] | 362 | 141 | up to 330 | 693 |
| Normalized transverse emittance | $[\mu\text{m} \cdot \text{rad}]$ | 3.5[3] | 2.5 | down to 1.9 | 2.5 |
| $\beta^*$ (IP1,5) | [cm] | 55 | 60 | $\approx 40$ | 15 |
| Half crossing angle (IP1,5) | $[\mu\text{rad}]$ | 142.5 | 145 | $\approx 150$ | 295 |
| RMS bunch length | [cm] | 7.55 | 9 - 10 | 8 - 10 | 7.55 |
| (Virtual) peak luminosity | $[10^{34}\,\text{cm}^{-2}\text{s}^{-1}]$ | 1.0 | 0.7 | $\approx 1.6$ | 24 |

Table 2.1.: Design parameters for the nominal LHC [11], typical parameters used at the end of the 2012 proton physics run [13], possible parameters for LHC operation after the first long shutdown (LS1, 25 ns option) [14] and design parameters for the High-Luminosity LHC (HL-LHC, 25 ns option) [15]. The values refer to the beginning of stable beams (see Sec. 2.4.1).

[3] In the LHC design report [11] a normalized transverse emittance of $3.75\,\mu\text{m} \cdot \text{rad}$ is specified during collisions. Nevertheless, for the collimation system a normalized transverse emittance of $3.5\,\mu\text{m} \cdot \text{rad}$ is assumed throughout the whole LHC cycle. In the following the nominal (normalized) transverse emittance refers to the latter value.

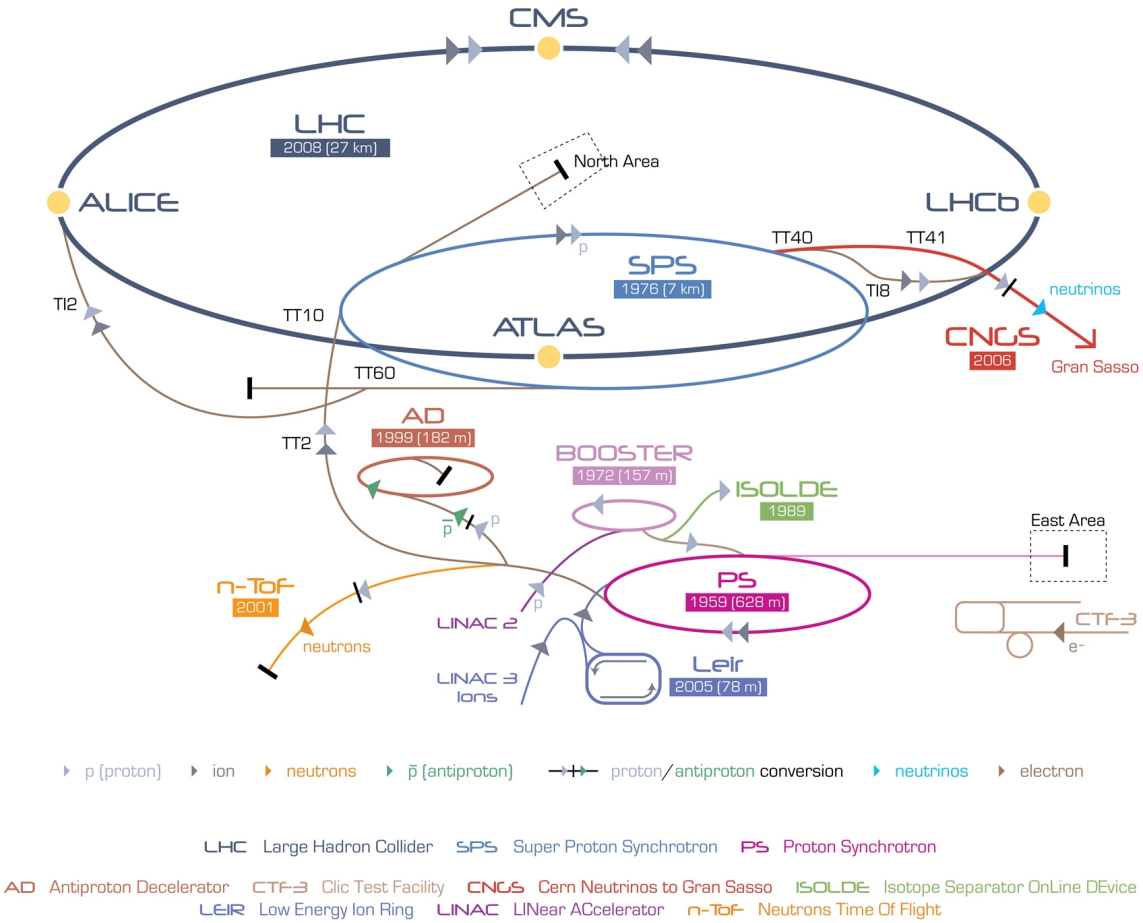


Figure 2.1.: Overview of the CERN accelerator complex (courtesy of C. Lefèvre [16]).

interaction point (IP)[5], the regions between the IPs are called sections and are numbered as illustrated in Fig. 2.2. Beam 1 and beam 2 are injected in IR2 and IR8, respectively and collide in IP1 (ATLAS), IP2 (ALICE), IP5 (CMS) and IP8 (LHCb). IR3 and IR7 host the collimation system (see Sec. 2.3.2). The accelerating RF and specific beam instrumentation are installed in IR4. IR6 hosts the beam dump system, which is explained in Sec. 2.3.4. A comprehensive description of the LHC and its sub-systems is given in [11]. The most relevant systems for this document are explained in the following.

### 2.3.1. Magnet System

The LHC consists of 1232 superconducting main dipole magnets, operating at 1.9 K. Each of which has a length of 14.3 m and deflects the beam with a magnetic field of up to 8.3 T by $\frac{2\pi\,\mathrm{rad}}{1232} = 5.1\,\mathrm{mrad}$. Figure 2.3 shows the schematic layout of an

[5]Except for IP8, which denotes the collision point of the two beams. It is shifted by 11.22 m w.r.t. the center of the long straight section [11, p. 9].

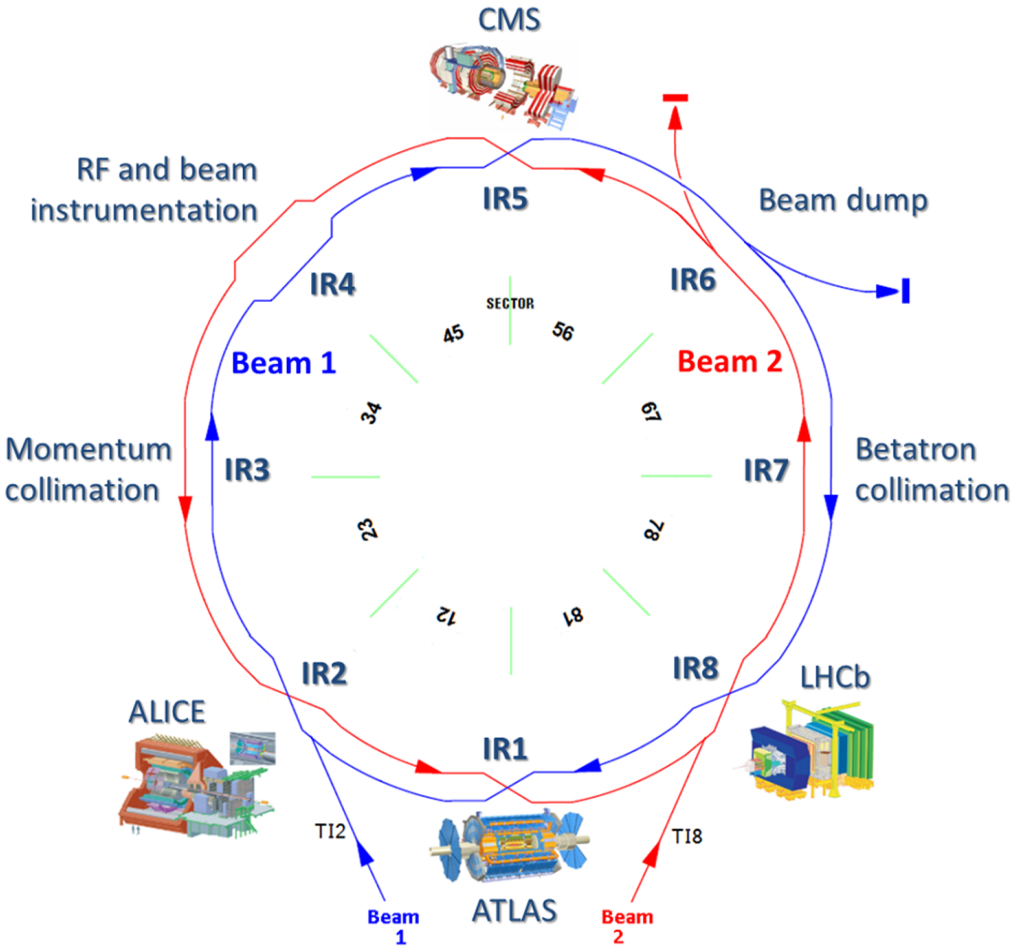


Figure 2.2.: Illustration of the LHC layout as seen from the top (courtesy of maalpu.org [17]).

LHC main dipole magnet. In the arcs, these magnets are arranged in a so-called FODO lattice consisting of groups of three dipole magnets, which are alternately separated by a focusing or a defocusing quadrupole magnet. Each half FODO cell is numbered according to its location. For example half-cell 24L3 refers to the $24^{\text{th}}$ half-cell in the sector left of IP3 (as seen from the center of the LHC). The magnetic layout in the IRs is more complex (see [11]). Of particular importance are the superconducting final focus triplet quadrupole magnets which focus the beams at the collision point down to a nominal transverse RMS beam size of about 16 $\mu$m to increase the collision rate. Additional 1060 orbit corrector dipole magnets and about 6500 higher order magnets (up to dodecapole) are distributed around the LHC. The two beams are (apart from the interaction regions) circulating in separate vacuum chambers, as illustrated in Fig. 2.3. At each collision point, the beams change between inner and outer vacuum chamber such that the circumferences are exactly equal for both beams, as shown in Fig. 2.2. The innermost aperture limitation in the arcs is a copper-coated stainless steel beam-screen, which shields the cold mass

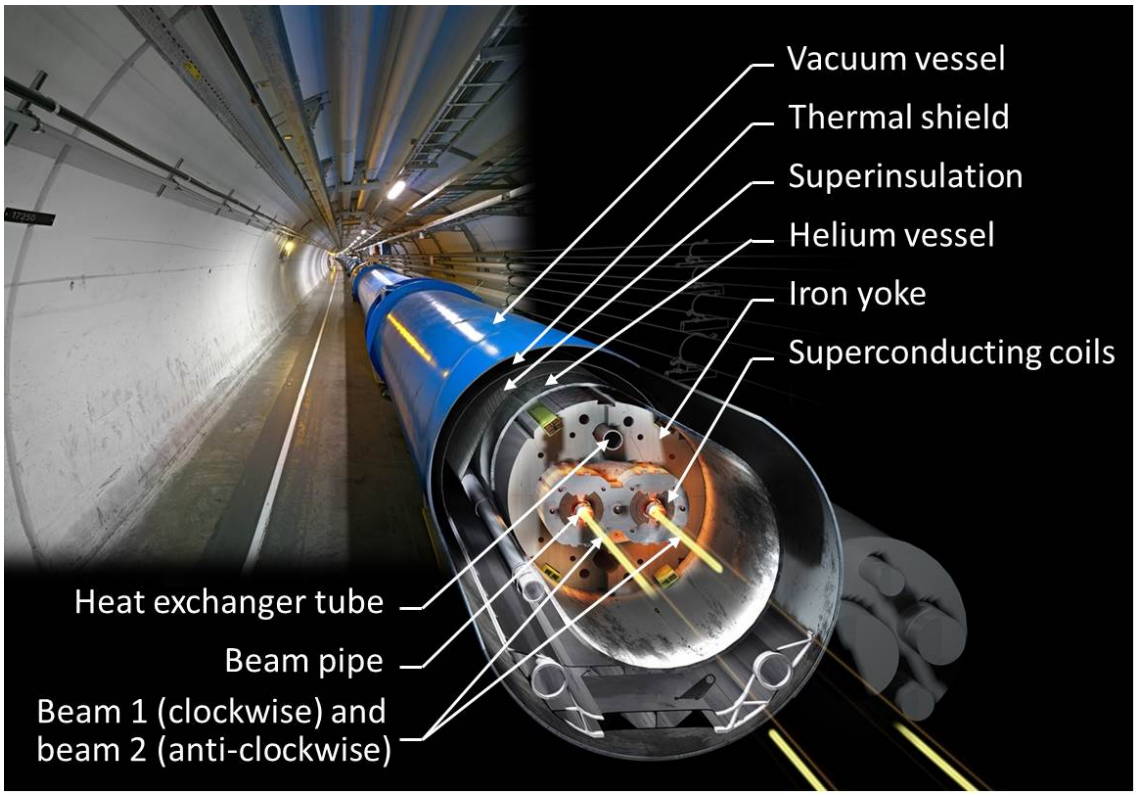


Figure 2.3.: Illustration of an LHC main dipole magnet in the LHC tunnel (courtesy of M. Brice [18]). See [11, pp. 162] for a detailed explanation.

from synchrotron radiation and ensures good electrical conductivity for the image currents of the beam. It has a radius of 22 mm in the plane of larger beam size.

Since all the arc magnets are superconducting, small energy depositions (e.g. by beam losses) are sufficient to quench the magnets and inhibit beam operation. The quench limit of the superconducting dipole and quadrupole magnets for operation at top energy is of the order of a few $\mathrm{mJ/cm^3}$ [19]. This has to be compared to several hundred MJ stored in each circulating beam (see Tab. 2.1). Magnet quenches due to beam losses corresponding to a few per mil of a single nominal bunch were observed (see Sec. 5.4.3).

The superconducting magnets are protected (among others) by a quench protection system (QPS) [11, p. 265]. The QPS measures the voltage drop over different parts of the superconducting circuits. If the corresponding thresholds are exceeded, a beam abort is triggered (see also Sec. 2.3.4) and the energy stored in the superconducting circuit is extracted into dump resistors. For the main circuits, so-called quench heaters warm up the complete magnet above the quench limit, electrical conductivity is ensured by a normal-conducting bypass. The QPS for the main circuits has a reaction time of up to $\approx 15\,\mathrm{ms}$ ($\approx 170$ LHC turns) for the detection of a quench [20].

### Normal-Conducting Separation Dipole Magnets

Downstream of each collision point, the beams are separated horizontally into the two vacuum chambers by separation dipole magnets, called D1. Due to the high dose rate from collision products around IP1 and IP5, superconducting magnets are impractical and six normal-conducting separation dipole magnets are installed on either side of each IP [11, p. 230]. Figure 2.4 illustrates the magnetic layout around IP1. The 12 separation dipole magnets in each IR are powered in series by one single electrical circuit named RD1.LR1 and RD1.LR5 in IR1 and IR5, respectively.

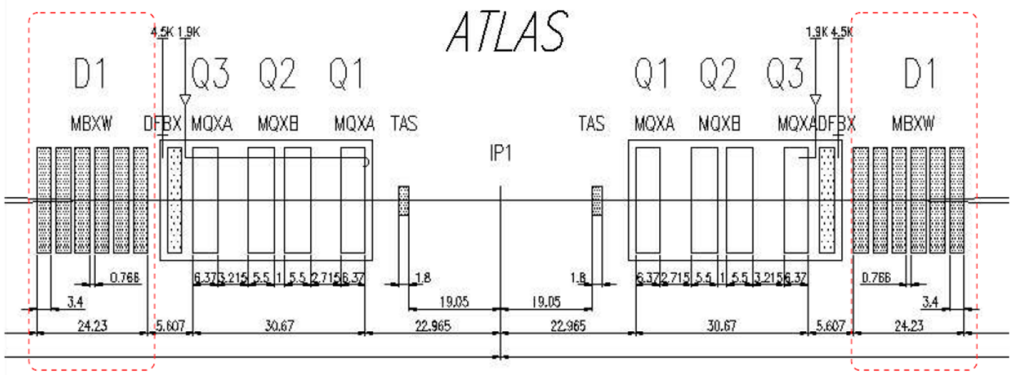


Figure 2.4.: Magnet layout around IP1. The D1 separation dipole magnets (highlighted with red boxes) are directly downstream of the final focus triplet quadrupoles Q1 - Q3 (courtesy of V. Kain et al. [21]).

The field decay time constant $\tau = \frac{L}{R}$ of these circuits is particularly short as their resistance $R = 850\,\mathrm{m\Omega}$ [22] is much larger than for superconducting circuits. With an inductance of $L = 1740\,\mathrm{mH}$ [22], their time constant is $\tau \approx 2\,\mathrm{s}$. The impact on the beam trajectory is amplified by the very large $\beta$-function[6] at the separation dipole magnets in IR1 and IR5 (see also Sec. 3.1.3). Thus, in a failure case, the beam can be perturbed on a very fast timescale. A failure of these circuits is therefore one of the most critical equipment failure scenarios in the LHC. Related simulations indicate that critical beam losses above the damage level of the equipment can be reached in only a few 10 LHC revolution periods [23].

Hence, these circuits are equipped with dedicated failure detection devices: fast magnet current change monitors (FMCMs) can detect a fast change of the magnet current by monitoring voltage changes over the magnet circuit [24]. Fast reaction times ($< 50\,\mu\mathrm{s} \approx \frac{1}{2}$ LHC turn) are combined with a high relative sensitivity ($\approx 10^{-4}$) [25]. In total 12 FMCMs are installed in normal-conducting LHC circuits [26].

[6] The concept of $\beta$-function is explained in Sec. 3.1.1.

### Injection Kicker Magnets

The beams are injected into the LHC via the TI 2 and TI 8 transfer lines in multiple bunch trains of up to 288 bunches each. Four injection kicker magnets (MKIs) per beam, in IR2 and IR8, deflect the beam to be injected, which arrives from below, vertically by 850 $\mu$rad onto the trajectory of the circulating beam. In order to minimize the required spacing between consecutive bunch trains, the MKIs have a particularly fast field rise-time of $\approx$ 900 ns [11, p. 422]. The MKIs nominally operate at ambient temperature, however beam induced heating can increase the yoke temperature significantly (see Sec. 2.4.2). Figure 2.5 illustrates the machine layout of the region around the MKIs for beam 2.

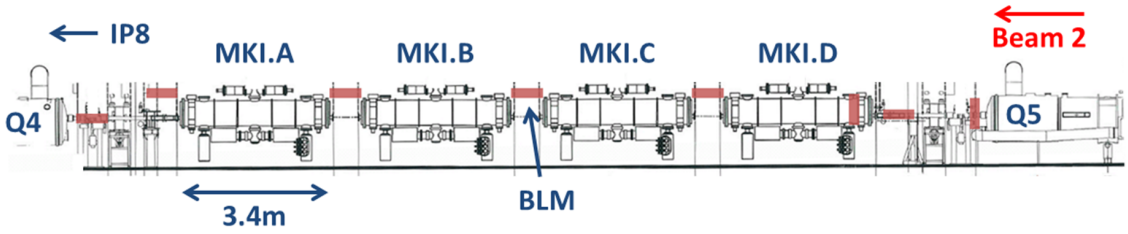


Figure 2.5.: Layout around the injection kicker magnets for beam 2. The red boxes indicate the locations of beam loss monitors (see also Sec. 2.3.3).

In order to achieve this fast field rise-time, the use of metallic vacuum chambers in the magnet is excluded. However, an electrical continuity for beam image currents is required. Thus, up to 24 metal wires surround the beam, supported by a ceramic tube. Figure 2.6a shows a schematic MKI cross section. The counter-rotating, circulating beam bypasses the MKI in a copper tube in a practically field-free region. The beam to be injected passes through the ceramic tube in the center of the MKI, shown in Fig. 2.6b. To avoid undue impact on the field rise-time from a DC coupling, the metal wires are not directly connected to the subsequent vacuum chamber on one side. For the high frequency currents, electrical conductivity is ensured by a capacitive coupling through the ceramic tube to a metallic layer on its outside. Due to electrical breakdown problems only 15 out of the 24 metal wires were installed during LHC run 1. This is further discussed in Sec. 5.5.1.

Similarly, 15 beam dump kicker magnets (MKDs) per beam in IR6 are used for the extraction of the beams from the LHC. Their field rise-time of 3 $\mu$s is synchronized with a beam free region in the machine, the so-called abort gap, to minimize beam losses on the aperture. The layout of the MKDs is similar to the MKIs, but they have a metalized ceramic tube, due to the less stringent rise-time requirements. The beam dump system is explained in Sec. 2.3.4.

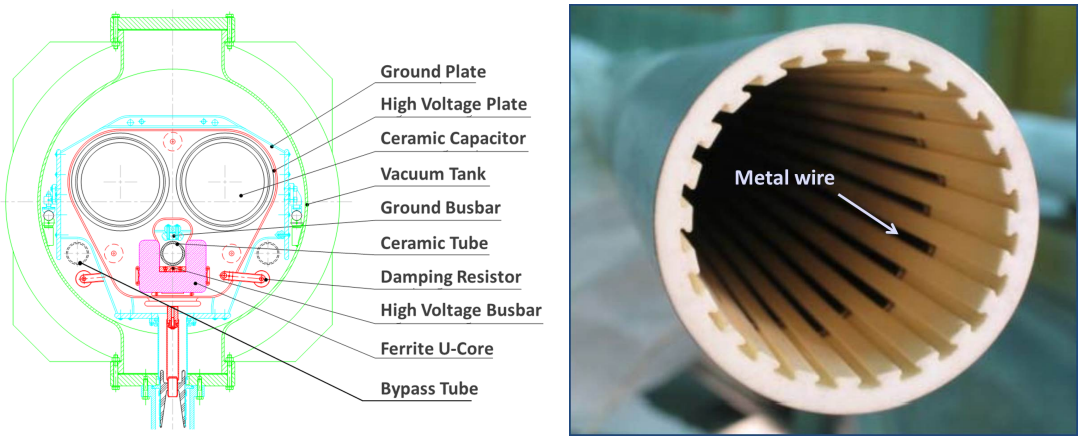


(a) MKI cross section. See [11, p. 424] for a detailed explanation.

(b) Ceramic tube.

Figure 2.6.: Schematic cross section of an MKI magnet (a) and a picture of the ceramic tube with 24 metal wires (b). During LHC run 1, the 9 metal wires on the bottom of the ceramic tube were deliberately removed to reduce electrical breakdown (courtesy of M. J. Barnes).

### 2.3.2. Collimation System

Even during routine operation, beam losses cannot be completely avoided, as discussed in Sec. 3.4. Therefore, a comprehensive collimation system which consists of over 100 collimators is installed in the LHC, mainly to minimize losses at superconducting elements, to reduce the background for the experiments and to protect the machine aperture against accidental beam losses [11, p. 467]. Most collimators have two movable jaws which define a gap for the circulating beam.

The collimators in IR7 are dedicated to absorb particles that have too large (betatron[7]) oscillation amplitudes. These particles typically impact on the robust primary collimators (TCPs), which define the global aperture limitation. Most impacting primary protons are subject to elastic scattering processes and are deflected by the collimator. Some also undergo an inelastic nuclear interaction resulting in secondary particle showers. This secondary particle halo is (partially) absorbed by secondary collimators (TCS). The remaining tertiary showers are absorbed by dedicated absorbers (TCLA) in IR7 or tertiary collimators (TCTs). The TCTs are installed around the experimental IRs to protect the final focus quadrupole magnets, which define the aperture limitation of the machine in physics conditions. Figure 2.7 illustrates this multi-stage betatron collimation system and the collimator jaw retractions from the beam center (half-gap) for different operational conditions. It has to be

[7]The concept of betatron oscillations is explained in Sec. 3.1.2.

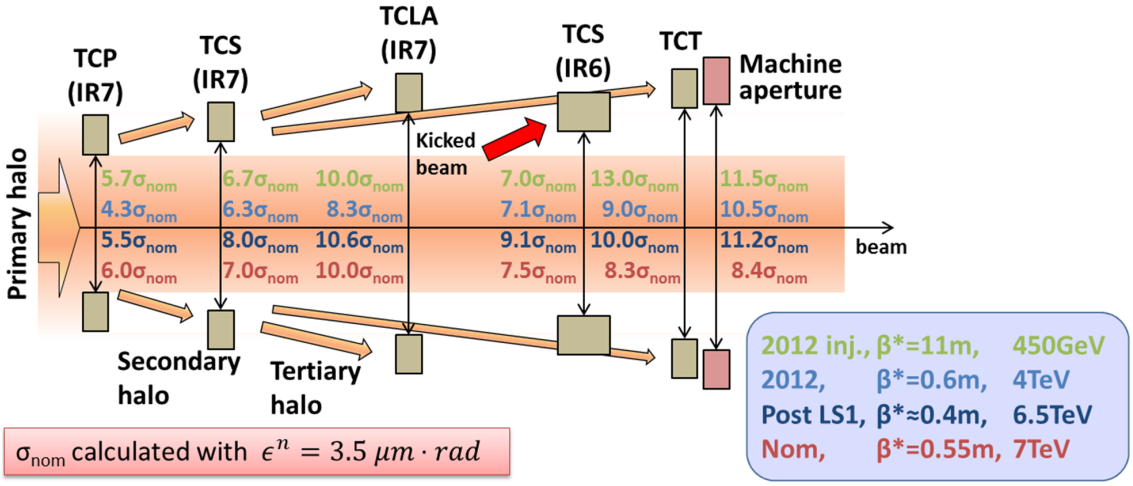


Figure 2.7.: Illustration of the LHC multi-stage betatron collimation system. The half-gaps of the betatron collimators (IR7), the dump protection collimators (IR6) and the tertiary collimators (TCTs) in the experimental IRs are given as multiples of the nominal transverse beam size $\sigma_{\text{nom}}$. The given values for post long shutdown 1 (LS1) represent one out of five proposed sets of settings (courtesy of R. Bruce and S. Redaelli [27, 28]).

noted that the betatron collimation system does not fully cover all oscillation phases and is thus a multi-turn collimation system[8].

Additional collimators are installed in IR3 to absorb particles with a longitudinal momentum error. Due to the specific optics in IR3 (large dispersion[9]), such particles have a larger transverse offset at the corresponding collimators.

Moreover, dedicated injection protection collimators in IR2 and IR8 with a half-gap down to $6.8\,\sigma_{\text{nom}}$ (2012 settings) are inserted during the injection process. Dedicated collimators in IR6 protect against beam losses from the beam dump process, as illustrated in Fig. 2.7 and discussed in Sec. 2.3.4.

### 2.3.3. Beam Loss Monitoring System

About 4000 beam loss monitors (BLMs) are installed around the LHC. Most of them are about 50 cm long ionization chambers filled with $N_2$ [31], which are installed on the outside of the cryostat as depicted in Fig. 2.8. Three ionization chambers per beam are installed in each standard arc half-cell, all around the quadrupole magnet. These ionization chambers have a time resolution of $40\,\mu s$ (about half of the LHC revolution period). The measured dose rates (in Gy/s) are averaged in 12 different

[8] See [29, pp. 32] for a detailed explanation.
[9] The concept of dispersion is explained in Sec. 3.1.1.

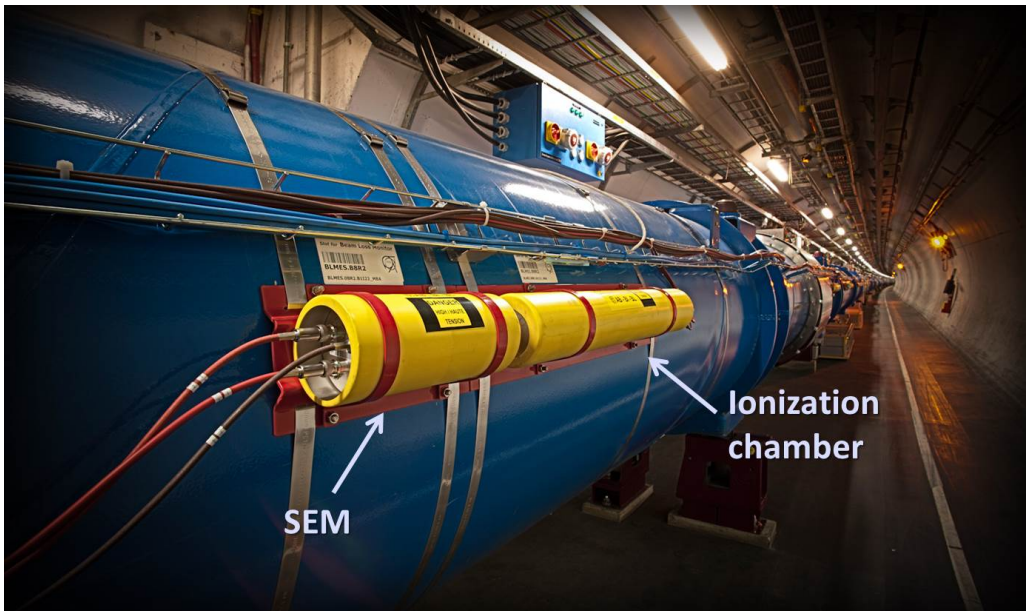


Figure 2.8.: Installation of an ionization chamber and a secondary emission monitor (SEM) at an LHC main dipole magnet (courtesy of A. Saba [30]).

running-sums with integration times between 40 $\mu$s and 83.8 s. If the dose rate in a single running-sum of a single BLM exceeds the corresponding threshold, a beam dump is triggered, as explained in Sec. 2.3.4.

The experience after the LHC start-up showed a remarkable reliability of the BLM system, including multiple redundancy for the protection against critical beam losses [32]. This is underlined by the complete absence of accidental beam induced magnet quenches at top energy throughout run 1.

For analysis and monitoring purposes, the maximum[10] of each running-sum within the last second is published and stored in a logging data base with 1 Hz repetition rate. In addition to that, around each beam dump the measured dose rates from each ionization chamber are stored with 40 $\mu$s resolution from the 81.9 ms long post mortem buffer. Similarly, a 20.5 ms long buffer with 40 $\mu$s resolution stores the dose rates around each beam injection for an injection quality check (IQC). From 2012 onwards, an additional 349.5 ms long study buffer with 80 $\mu$s resolution was used for specific studies (see Sec. 5.2.2).

Evacuated secondary emission monitors (SEMs, see Fig. 2.8) and little ionization chambers (LICs) are used to increase the dynamic range beyond the saturation limit of the ionization chambers [33]. For bunch-by-bunch beam loss diagnostics, diamond BLMs with nanosecond time resolution are installed at special locations, e.g. downstream of the primary betatron collimators in IR7 (see Sec. 5.1.3) [29].

[10]For the running-sums with an integration time above 1 s the last measured value is published.

### 2.3.4. Beam Dump System and Beam Interlock System

Several ten thousand interlock conditions are constantly evaluated by the LHC machine protection systems [34]. The LHC beam dump system (LBDS) and beam interlock system (BIS) are the backbone of the machine protection systems. For each beam, so-called beam interlock controller (BICs) are installed in each long straight section and are connected redundantly to one another in a loop around the LHC. Starting from IR6, two redundant beam permit signals per beam are transmitted in opposite directions around the LHC via these loops at a repetition rate of 10 MHz [11, p. 409]. The active protection systems (like quench protection system or BLM system) are redundantly connected to each beam permit loop via the BICs. A BIC has to receive an active signal at each of these inputs in order to transmit the beam permit signal along the ring[11]. If at least one of the two beam permit loops per beam is interrupted and the beam permit signal does not arrive in IR6 ("the beam permit is removed"), a beam dump is triggered for the concerned beam. The LBDS then fires the beam dump kicker magnets (MKDs, see Sec. 2.3.1) in IR6 synchronously with the next passage of the 3 $\mu$s long abort gap. The passing beam is hereupon extracted from the LHC via one of the two 750 m long beam dump transfer lines onto a beam dump absorber block [11, p. 441]. **However, it can take up to three LHC revolution periods after the detection of a failure until the beam is completely extracted from the LHC**[12].

The beam permit loops for the two beams are by design independent. However, for several systems like quench protection system or BLM system the same input signal is connected to the BICs for both beams. Furthermore, the beam permit loops can be logically linked, which implies a dump of both beams in case the beam permit of a single beam is removed. The beam permit loops are usually linked in regular operation above injection energy.

In the 2012 proton physics run, 598 beam dumps above injection energy were successfully executed, 255 out of these for beams with more than 100 MJ stored energy[13].

One of the most severe (but acceptable) LHC failure scenarios is a so-called asynchronous beam dump, for which the field rise-time of the beam dump kickers is not

[11] However, it is possible to deactivate (mask) specific BIC inputs for so-called setup beam conditions.

[12] Up to one LHC revolution period is needed for transmission of the signal to IR6 and signal processing. Up to one additional turn is needed for synchronization with the abort gap and up to one additional turn is needed for the complete extraction of the beam.

[13] Protection as well as programmed beam dumps are counted. The numbers are per dump of both LHC beams.

synchronized with the abort gap. Such a failure may happen due to e.g. a spontaneous triggering of the kicker magnet switches. Up to $\approx 120$ bunches are only partially deflected in this case and lead to significant beam losses within a single turn. The expected failure rate is one asynchronous beam dump per year. Dedicated dump protection collimators in IR6 protect the LHC aperture against this failure case, as shown in Fig. 2.7 [11, p. 445].

## 2.4. LHC Operation and Specific Challenges

An efficient operation of the LHC relies on a dependable interplay of all LHC subsystems. The typical operational cycle and the specific challenges are presented in the following.

### 2.4.1. LHC Operational Cycle

The LHC pre-accelerators are fast-cycling machines that repeat an operational cycle every few seconds. In contrast to that, the LHC is a storage ring which can store the beams for many hours (a so-called fill). The operational cycle typically starts with a beam dump, followed by a ramp down and setup period, during which the LHC is prepared for the next beam injection. Thereafter, low-intensity pilot bunches are injected into the two LHC rings, followed by intermediate and high-intensity bunch trains of up to 288 bunches (with 25 ns bunch-spacing) per injection. The magnet currents are then ramped up to increase the beam energy (up to 4 TeV per beam during the 2012/13 run). At top energy, the beam size at the interaction points is reduced during the squeeze. Hereupon, the until then separated beams are brought into collisions in the experimental interaction points. The full data taking of the experiments starts with the declaration of stable beams. Figure 2.9 illustrates a typical operational LHC cycle during the 2012 proton physics run.

In the 2012 proton physics run, stable beams were declared in 293 LHC fills. Whereas a record stable beams duration of over 25 hours was reached[14], most LHC fills are terminated by protection beam dumps; the average stable beams duration in 2012 was 6.5 hours[15]. In the absence of failures, the average turn-around-time, i.e. the time from beam dump until the declaration of stable beams, was about 2.5 hours in 2012 LHC operation [13, 35].

[14] LHC fill 2006 on 08.05.2011 had a stable beams duration of 25.4 hours.
[15] All proton-proton physics fills reaching stable beams with more than 1000 bunches are considered.

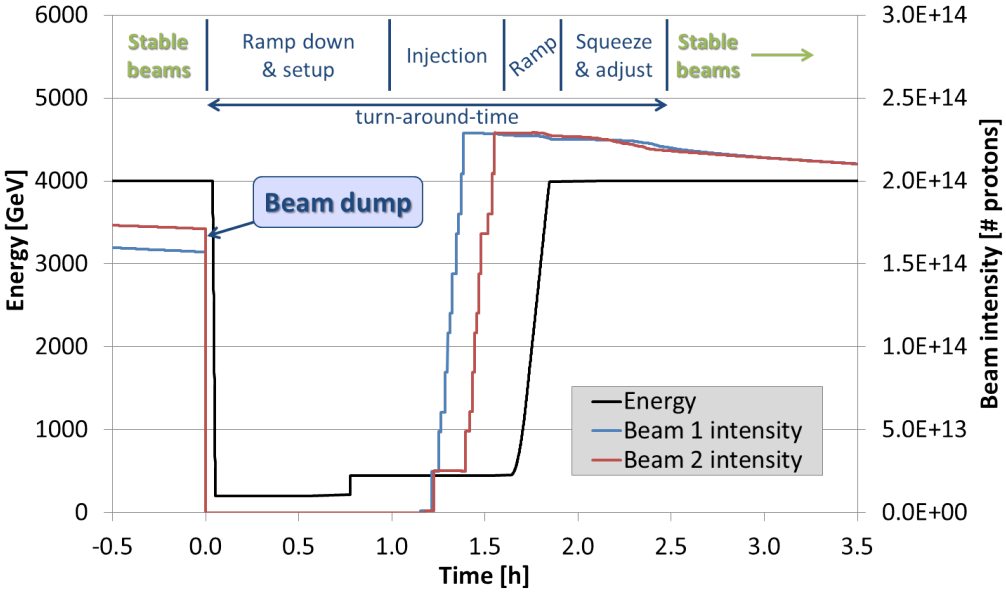


Figure 2.9.: Typical operational LHC cycle (LHC fill 3288 on 15.11.2012).

### 2.4.2. Specific Challenges

The complexity of the LHC sets tight constraints on the required availability and reliability of all systems. The downtime due to premature beam dumps resulting from system faults and unavailability of sub-systems amounts to a total of 2336 hours (about 98 days) in 2012 [35]. Concerning protection beam dumps, in particular radiation induced failures of electronics[16] are a critical limitation. They account for about 60 beam dumps in 2012 [36]. Extensive equipment-relocation and installation of radiation shielding is ongoing to minimize the radiation to electronics [37].

The energy stored in the superconducting circuits has with over 10 GJ for nominal operation a severe damage potential. This is underlined by the sector 34 incident, which happened on 19 September 2008: during the commissioning (without beam) of the sector 34 main dipole circuit, an electrical fault occurred on the interconnection between two superconducting cables. This led to a local energy dissipation of about 400 MJ which resulted in the release of about 6 t of helium, severe mechanical and electrical damage and the contamination of large parts of the vacuum chamber with soot and debris. 53 magnets had to be replaced. The repairs took over 14 months [38].

The 362 MJ nominal stored energy of the beams circulating inside the superconducting magnets limit the acceptable beam loss rates to a very low level, as explained

[16] These are typically so-called single event upsets (SEU), which are radiation induced bit-flips. If a SEU occurs in a critical system, the machine protection systems trigger a protection beam dump.

in Sec. 2.3.1. Foremost, this requires tight control of the beam dynamics, which includes in particular very tight beam position tolerances that are enforced by narrow collimator gaps, as discussed below. Moreover, beam losses due to macro particles interacting with the circulating beams were observed to be an important limitation which was not anticipated before the LHC start-up. This beam loss mechanism affected the LHC availability during run 1 and could be a major limitation for LHC operation at higher energy after LS1. This effect is discussed in detail in Chap. 5.

Moreover, beam-beam effects[17] are a known limitation for high-intensity particle colliders [39, pp. 169]. Related beam instabilities were observed regularly in the LHC and affected LHC operation [40]. An introduction is given in Sec. 3.2. A related ultra fast beam loss mechanism, which was not considered until its observation in July 2012, is discussed in Chap. 6.

Furthermore, the transverse beam stability is influenced by the (longitudinal) impedance of the vacuum chamber or the equipment surrounding the beam. This impedance perturbs the image currents and results in an effective voltage, which acts back on the beam and can cause transverse beam instabilities. Several such single-beam instabilities were observed in the LHC [41].

Another particularity of high-intensity accelerators with positively charged beams is the electron-cloud build-up. This effect occurs when an electron is released from the vacuum chamber wall/beam-screen and is accelerated by the electric field of the beam. The accelerated electron can then impact on the vacuum chamber again and release secondary electrons, which are accelerated by the electric field of subsequent bunches. This can lead to the build-up of an electron-cloud around the beam on microsecond timescales, which influences the beam dynamics and can lead to a significant heat-load for the cryogenics-system. The effect can be mitigated by trapping the electrons in a small solenoidal magnetic field. However, such solenoids are not practical in the main magnets, where the main mitigation strategy is a surface conditioning of the beam-screen due to operation with very high beam intensities, so-called scrubbing [42, 43].

A further important LHC limitation is beam-induced equipment heating. The RF field of the beam can couple to surrounding equipment and deposit energy due to the impedance of the equipment. For equipment which is insufficiently cooled, this can lead to malfunctioning or even damage due to overheating. This applies for example to the LHC injection kicker magnets, which partially heated up to 190°C in 2012 [44]. The injection had to be consequently delayed in several cases for cool-down of these magnets.

[17] The interaction of the two beams affects the beam dynamics. The resulting effects are called beam-beam effects.

### Beam Position Tolerances

Tight control of the transverse beam position is mandatory to limit the beam losses during normal LHC operation and in failure cases as well as to avoid significant beam losses at sensitive elements. Particularly critical are transient beam position perturbations on timescales which are similar to the reaction time of the machine protection systems. Such perturbations may be too fast for an active protection and imply a potential for severe equipment damage. The most important limitations for transient beam trajectory perturbations are:

- The collimation system is designed for ultra fast accidental beam losses of up to 1 MJ [45]. For transient trajectory perturbations with given amplitude and phase, the lost energy depends mainly on the collimator gaps, the transverse beam distribution and the stored beam energy. For the 2012 collimator settings (in stable beams), the half-gap of the primary collimators in IR7 corresponds to $\approx 5.1\,\sigma_{\mathrm{b}}$[18] (see Fig. 2.7). In the LHC, typically a Gaussian beam profile with highly overpopulated tails is observed. In dedicated halo scraping measurements in 2011, up to 4.5% of the total beam intensity was observed beyond $4\,\sigma_{\mathrm{b}}$ [46]; this is confirmed by additional measurements and studies in 2012 [47]. For a nominal stored beam energy of 362 MJ, this value corresponds to $\approx$ 16 MJ. This implies that **trajectory perturbations with amplitudes of the order of $1\,\sigma_{\mathrm{nom}}$ may result in critical beam losses** (for high intensity operation at top energy) which are **significantly beyond the specification of the collimation system and imply a serious damage potential.**
  A reliable "online" diagnostics for the transverse tail population of high intensity LHC beams is not available at present. This aspect is further discussed in Sec. 6.4 and Sec. 7.4.4.

- Sizable beam losses at the non-robust tertiary (tungsten) collimators (TCTs) must be avoided. According to experimental tests and simulations, the beam loss level for the onset of damage is about $5 \cdot 10^9$ protons (<5% of a nominal bunch) at 7 TeV (= 5.6 kJ) for a direct beam impact onto a TCT [48]. The nominal retraction of the TCTs w.r.t. the primary collimators is $2.3\,\sigma_{\mathrm{nom}}$ in stable beams ($\approx 4.5\,\sigma_{\mathrm{nom}}$ for operation after LS1), as shown in Fig. 2.7. As the LHC collimation system does not provide a full phase-space coverage [11, pp. 468], single-turn trajectory perturbations which exceed these am-

[18] $\sigma_{\mathrm{b}}$ denotes the transverse beam size of the beam (see Sec. 3.1.1). A normalized emittance of $\epsilon^{\mathrm{n}} = 2.5\,\mu\mathrm{m} \cdot \mathrm{rad}$ is assumed, which was a typical value in 2012 LHC operation. In contrast to that, $\sigma_{\mathrm{nom}}$ denotes the nominal transverse beam size with the nominal normalized transverse emittance of $\epsilon^{\mathrm{n}}_{\mathrm{nom}} = 3.5\,\mu\mathrm{m} \cdot \mathrm{rad}$.

plitudes[19] may lead to primary losses at the TCTs and consequent equipment damage.

- The beam dump transfer lines are designed for a beam trajectory perturbation of up to 4 mm ($\approx 9\,\sigma_{\mathrm{nom}}$ for the aperture limiting elements at 4 TeV, $\mathbf{\approx 3.0\,\sigma_{nom}}$ **at 450 GeV**) during the beam dump process [11, p. 442]. A dedicated hardware beam position interlock system triggers a beam dump if the beam position at one out of four beam position monitors (BPMs) per beam and plane deviates by more than 3 mm from the reference. This corresponds to $4.6\,\sigma_{\mathrm{nom}} - 4.8\,\sigma_{\mathrm{nom}}$ at 4 TeV and $\approx 1.6\,\sigma_{\mathrm{nom}}$ at 450 GeV for the BPMs at focusing quadrupole magnets. The interlock system has a reaction time of not more than 10 turns if at least 250 bunches are perturbed[20].

The typical operational margins are even tighter: during 2012 high intensity LHC operation at 4 TeV, transient trajectory perturbations with an amplitude of about $0.2\,\sigma_{\mathrm{nom}}$ - $0.3\,\sigma_{\mathrm{nom}}$ typically led to beam losses above the BLM dump thresholds in the betatron collimation region in IR7; a detailed example is described in Sec. 6.2.

At injection energy, slightly larger trajectory perturbations may be tolerated, since the main collimators are further retracted (see Fig. 2.7) and the stored beam energy is only $\frac{450\,\mathrm{GeV}}{7000\,\mathrm{GeV}} = 6.4\%$ of the nominal stored energy at flat top. The main limitation is given by the acceptance of the beam dump transfer lines ($\approx 3.0\,\sigma_{\mathrm{nom}}$) as discussed above. Typical oscillations during the injection process have amplitudes of up to $\approx 1.2\,\sigma_{\mathrm{nom}}$ in 2012. However, these apply only to the injected bunches with a total energy of up to $\approx$ 1.7 MJ for 2012 protons physics fills. Furthermore, dedicated injection collimators protect the LHC against too large injection oscillations, as described in Sec. 2.3.2.

## 2.5. LHC Outlook

The LHC is at present in the first long shutdown (LS1), during which it is prepared for operation at even higher energies of up to $\approx$ 6.5 TeV per beam. This involves mainly a consolidation of over 12'000 interconnections between superconducting cables, which were limiting the energy-reach during LHC run 1 [37]. Many other maintenance and upgrade activities are ongoing alongside, e.g. a relocation of

[19] Other deviations from the nominal parameters like beta-beating, closed orbit perturbations or drifts of the collimator jaws may further reduce the margins.

[20] The interlock system has two independent interlock conditions for each BPM: The beam dump is triggered if at least 70 measurements within 100 turns are outside the tolerances or if at least 250 measurements within 10 turns are outside the tolerances. The first and second interlock condition are evaluated once every 100 and 10 turns, respectively.

electronic equipment to mitigate radiation problems as explained in Sec. 2.4.2. The LHC is expected to resume beam operation in early 2015.

A second long LHC shutdown (LS2) is scheduled for 2018/19 and includes an upgrade of the LHC injectors, the LHC experiments and the installation of additional collimators [49].

About 15 years after the LHC start-up, a major LHC upgrade is foreseen during the third long shutdown (LS3) in 2022/23. The High-Luminosity LHC (HL-LHC) upgrade program aims at a 20-25 times increased (virtual[21]) peak collision rate. This implies major modifications of the collision regions, foremost an upgrade of the final focus triplet quadrupole magnets and the installation of crab cavities (see below) [49]. Moreover, a novel optics solution is proposed, which allows a reduction of the transverse beam size at the collision points by about a factor 4 [50]. An overview of the HL-LHC project phases is shown in Fig. 2.10 together with the project phases of the Large Electron-Positron Collider (LEP) and the LHC. At present, the construction and testing of HL-LHC prototype equipment is ongoing.

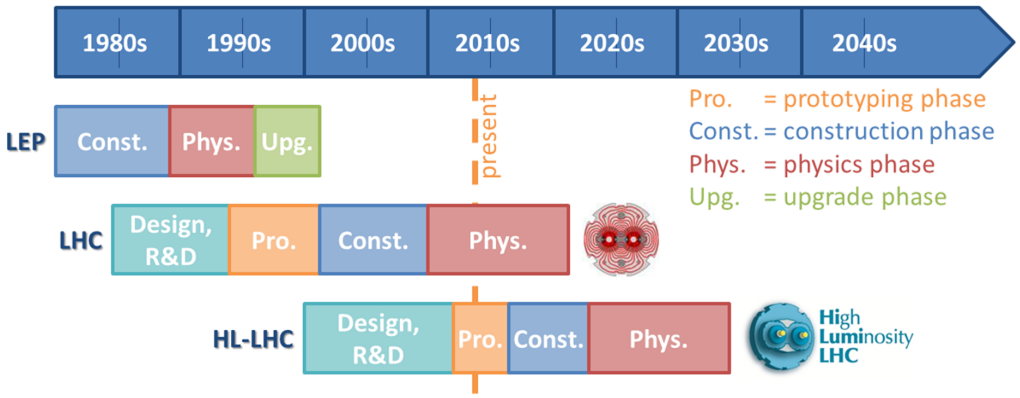


Figure 2.10.: Overview of the project phases of the Large Electron-Positron Collider (LEP), the Large Hadron Collider (LHC) and the High-Luminosity LHC (HL-LHC) project (courtesy of L. Rossi [51]).

Even upgrades beyond the HL-LHC era are currently developed. For example the High-Energy LHC (HE-LHC) project aims at proton-proton collisions with up to 33 TeV center-of-mass energy, based on the installation of 20 T dipole magnets in the LHC tunnel [51].

[21] Since this high collision rate exceeds the limitations of the LHC experiments, it is deliberately reduced by so-called luminosity leveling mechanisms in the beginning of a fill, as discussed in Sec. 3.2.

## LHC Crab Cavity Upgrade Program

In order to avoid parasitic collisions and to minimize beam-beam effects, the beams collide under a small crossing angle at the collision point. This leads to a geometric reduction of the collision rate, as discussed in Sec. 3.2. So-called crab cavities can compensate this effect. Hence, crab cavities can increase the collision rate without the need for an even higher stored beam energy. For the HL-LHC upgrade program, superconducting crab cavities will be installed around the ATLAS and CMS experiments.

Crab cavities are resonators for electromagnetic fields which deflect the passing particles in a transverse plane. Crab cavities were already successfully operated at the electron-positron collider KEKB [52]. However, the KEKB crab cavities with a transverse dimension of about 1 m are too large for the LHC, whose vacuum chambers have a nominal separation of 19.4 cm [11, p. 6]. Hence, compact crab cavities matching the LHC size constraints are required. Figure 2.11 illustrates the peak electric and magnetic fields for the so-called parallel-bar crab cavity. In this case, the transverse deflection is mainly due to the electric field component, as explained in Sec. 3.3. Since the fields oscillate in time, head and tail of a bunch can be deflected in opposite directions such that the bunches are rotated at the collision point in order to compensate the crossing angle[22]. A detailed explanation of the beam dynamics and the working principle of crab cavities is given in Sec. 3.2, Sec. 3.3 and Sec. 7.1.

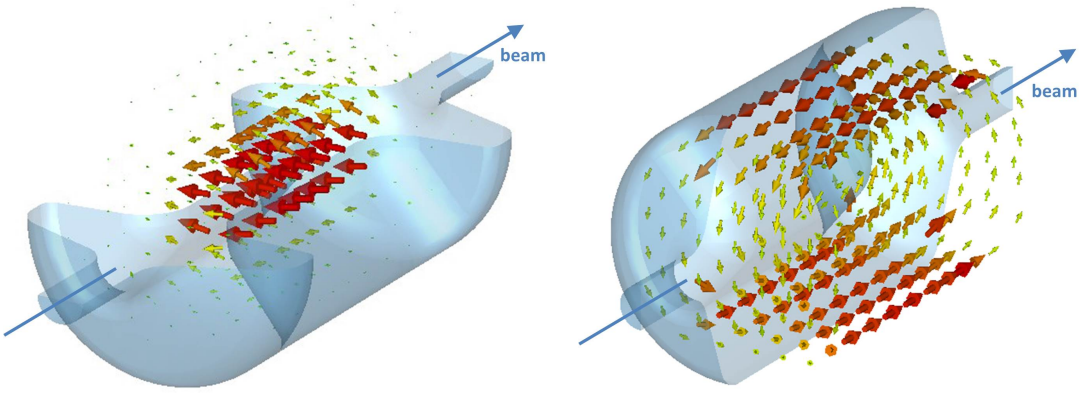


(a) Peak electric field.

(b) Peak magnetic field.

Figure 2.11.: Peak electric (a) and magnetic (b) field of the deflecting mode for the parallel-bar crab cavity (courtesy of S. U. De Silva et al. [53]).

[22]The resulting motion of the bunches towards the collision point looks like the side-stepping motion of a crab. Hence the name crab cavity.

Currently, three different HL-LHC crab cavity designs are under development:

- **Parallel-bar crab cavity:** the parallel-bar crab cavity design [54–56] is developed by a collaboration of Old Dominion University, Thomas Jefferson National Accelerator Facility and SLAC National Accelerator Laboratory (all USA). The total deflection is dominated by the electric field, the magnetic field is partially counteracting the transverse deflection, as explained in Sec. 3.3. The deflecting mode is the fundamental mode, i.e. the mode with lowest frequency. The higher order modes have at least 1.5 times the frequency of the fundamental mode and are extracted by two higher order mode couplers [57]. A prototype niobium cavity was fabricated. In first experimental tests, a transverse deflecting voltage of 7.0 MV was reached [56], which is almost a factor 2 beyond the requirements, as discussed in Sec. 7.1. The schematic layout and the prototype are shown in Fig. 2.12.
- **Four-rod crab cavity:** the four-rod crab cavity design [58–60] is developed by The University of Lancaster/The Cockcroft Institute (UK). In the deflecting mode both electric and magnetic field contribute to the total deflection. It is not the fundamental mode and has a lower order mode with about 0.9 times the frequency of the deflecting mode. A prototype niobium cavity was fabricated [59]. Whereas the design parameters are still to be demonstrated, first experimental tests show a good cavity performance [60]. The schematic layout and the prototype are shown in Fig. 2.13.
- **Double-quarter-wave crab cavity:** the double-quarter-wave crab cavity design [61–63] is developed by a collaboration of Brookhaven National Laboratory, Stony Brook University (both USA) and CERN. The deflection is mainly due to the electric field component of the fundamental mode. The next higher order mode has about 1.5 times the frequency of the fundamental mode. Different schemes for the extraction of the higher order modes were developed [62]. A prototype niobium cavity was fabricated [63] and first experimental tests were performed. However, the design parameters remain to be demonstrated [64]. Fig. 2.14 shows the schematic layout and the prototype.

The three designs follow conceptually very different approaches, which result in the different layouts as illustrated in Fig. 2.12, Fig. 2.13 and Fig. 2.14.

Before the installation of crab cavities in the LHC, all three designs will be tested in the Super Proton Synchrotron (SPS) at CERN in 2016/17. The technical integration is currently in preparation [65]. Further tests with individual crab cavities in the LHC are under discussion [66] and could be done after LS2 in 2019/20. The final installation in the LHC is scheduled during LS3 in 2022/23.

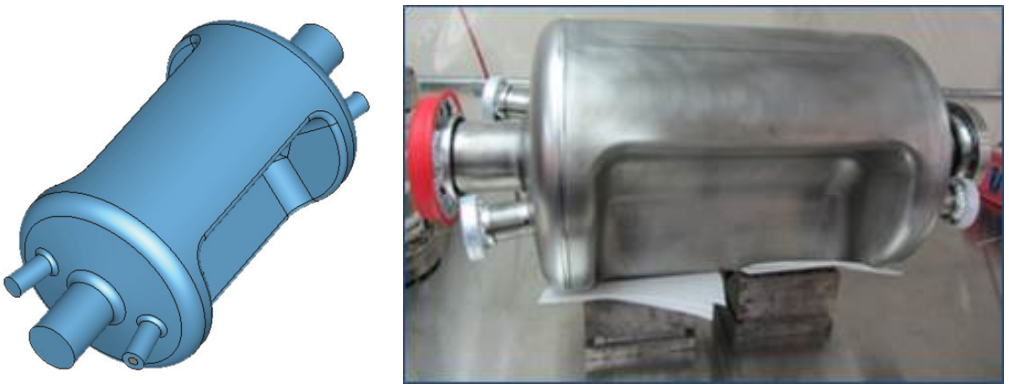

(a) Layout. (b) Prototype.

Figure 2.12.: Layout (a) and prototype (b) of the parallel-bar crab cavity (courtesy of J.R. Delayen, S.U. De Silva et al. [56, 67]).

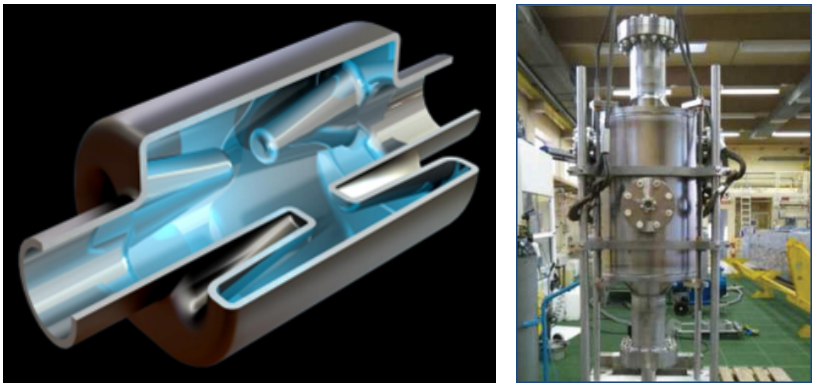

(a) Layout. (b) Prototype.

Figure 2.13.: Layout (a) and prototype (b) of the four-rod crab cavity (courtesy of G. Burt, P. Ambattu, et al. [60]).

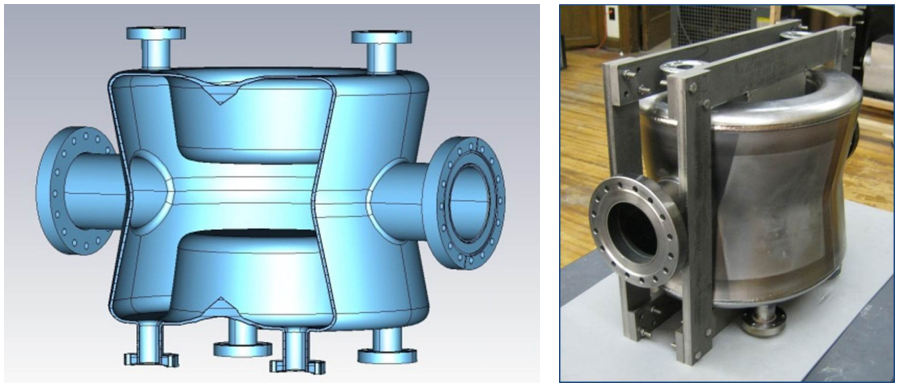

(a) Layout. (b) Prototype.

Figure 2.14.: Layout (a) and prototype (b) of the double-quarter-wave crab cavity (courtesy of B.P. Xiao, Q. Wu et al. [63, 68]).

# 3. Introduction to Accelerator Physics

This chapter gives a basic introduction to the theory of accelerator physics and to the formalisms used in this thesis. The transverse beam dynamics is explained, followed by an introduction to the concept of luminosity and a discussion of beam-beam interactions. The working principle of crab cavities is explained and basic crab cavity relations are derived. The chapter concludes with a discussion about beam losses.

## 3.1. Transverse Beam Dynamics

For the description of the particle trajectory in an accelerator, a co-moving coordinate system is used, as shown in Fig. 3.1. It is defined w.r.t. the nominal **design orbit** which describes the closed trajectory of an ideal particle in the ideal machine under design conditions. The transverse axis that is in the accelerator plane is defined as x-axis or horizontal axis. The y-axis or vertical axis is perpendicular to the accelerator plane. The global coordinate $s$ defines the zero-position of the co-moving coordinate system along the design orbit w.r.t. an arbitrary but fixed location in the global reference frame.

It is further distinguished between the design orbit and the **closed orbit**. The latter describes the closed trajectory of an ideal particle in the real accelerator. The closed orbit is dynamic and depends e.g. on the machine settings (in particular of the orbit corrector magnets), misalignments and magnetic field errors. The term **particle trajectory** refers to the trajectory of a single real particle in a real accelerator. As illustrated in Fig. 3.1, the particle trajectory is generally not closed around the accelerator. The term (single-turn) **beam trajectory** denotes the average trajectory of all particles, which is also generally not closed.

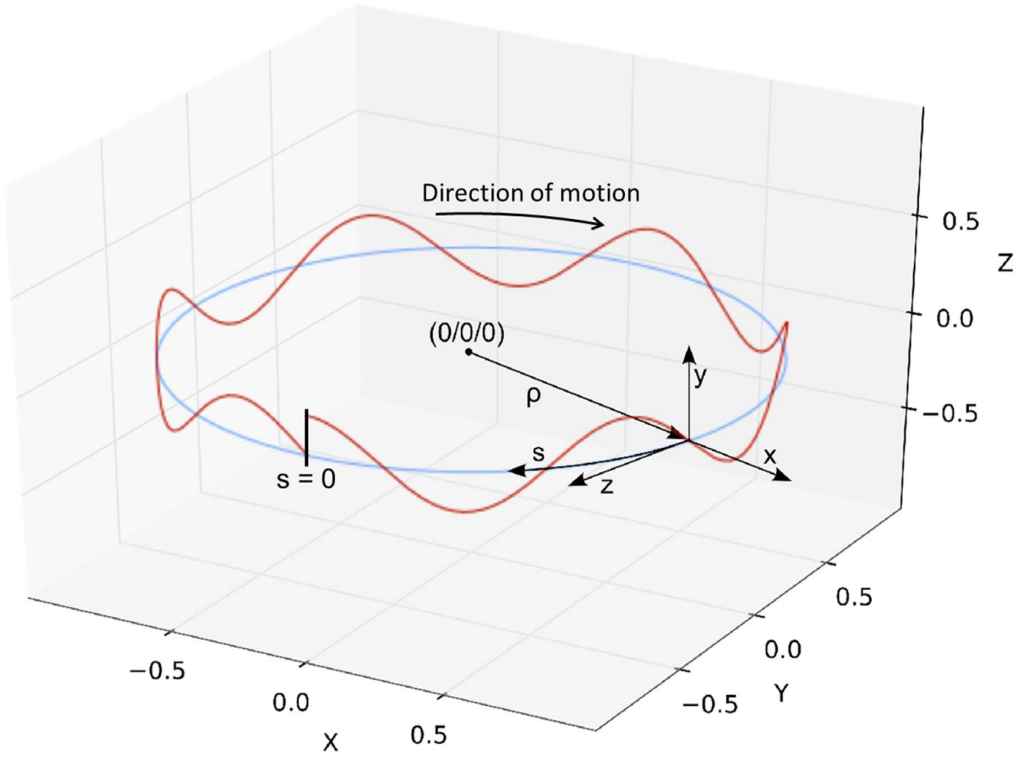


Figure 3.1.: The design orbit (blue) and the trajectory of a particle oscillating in the vertical plane (red) in a global coordinate system (X,Y,Z). A co-moving coordinate system (x,y,z) is also drawn (courtesy of K. Fuchsberger [69]).

### 3.1.1. Linear Equations of Motion

The motion of particles in a particle accelerator is mainly determined by electric and magnetic fields. Their influence on the momentum $\vec{p}$ of a particle with charge q and velocity $\vec{v}$ is given by the Lorentz force

$$\frac{d\vec{p}}{dt} = q \cdot (\vec{E} + \vec{v} \times \vec{B}) \tag{3.1}$$

with $\vec{E}$ and $\vec{B}$ being the electric and magnetic field vector, respectively.

In a synchrotron, the transverse motion is dominated by the magnetic field components, in particular by the dipole fields which are perpendicular to the direction of motion ($\vec{B} \perp \vec{p}$). The equilibrium of Lorentz force and centrifugal force leads to the definition of the beam rigidity [70, p. 82]:

$$B \cdot \rho = \frac{p}{q} \tag{3.2}$$

with $\rho$ being the bending radius, $B = |\vec{B}|$ and $p = |\vec{p}|$ .

By including also magnetic quadrupole fields and keeping only the leading terms in linear approximation, Eq. 3.1 can be rewritten as a differential equation of motion[1]:

$$\begin{aligned} x''(s) + k_x(s) \cdot x(s) &= \frac{1}{\rho(s)} \frac{\Delta p}{p} \\ y''(s) + k_y(s) \cdot y(s) &= 0 \end{aligned} \tag{3.3}$$

with $r'' = \frac{\partial^2 r}{\partial s^2}$ for $r = x, y$ and the relative momentum offset $\frac{\Delta p}{p}$. $k_x$ and $k_y$ are related to the strength $K(s)$ of the quadrupole fields[2]:

$$\begin{aligned} k_x &= \frac{1}{\rho^2} - K(s) = \frac{1}{\rho^2} + \frac{1}{B\rho} \frac{\partial B_y}{\partial x} \\ k_y &= K(s) = -\frac{1}{B\rho} \frac{\partial B_y}{\partial x}. \end{aligned} \tag{3.4}$$

The equations of motion for horizontal and vertical plane (Eq. 3.3) are independent[3]. Thus, both planes can be treated separately. The following discussion focuses on the horizontal plane, unless indicated otherwise.

For $\frac{\Delta p}{p} = 0$ the equations of motion (Eq. 3.3) are Hill-type differential equations[4]. By using Floquet's Theorem the general solution can be found [71, pp. 244]:

$$x(s) = \sqrt{\epsilon \cdot \beta(s)} \cdot \cos\left[\psi(s) - \psi(0)\right] \tag{3.5}$$

with $\epsilon$ and $\psi(0)$ being the initial conditions. $\beta(s)$ is introduced here as the periodic $\beta$-function or amplitude function, which is by definition always positive and in a regular FODO lattice (see Sec. 2.3.1) maximal at focusing quadrupole magnets and minimal at defocusing quadrupole magnets. $\psi(s)$ is the betatron phase and depends on the $\beta$-function

$$\psi(s) = \int_0^s \frac{d\bar{s}}{\beta(\bar{s})}. \tag{3.6}$$

Figure 3.2 shows the $\beta$-function and the betatron phase in a regular FODO structure in the LHC arcs.

The emittance $\epsilon$ is relevant for the amplitude $\sqrt{\epsilon \cdot \beta(s)}$ of the oscillation. It depends on the beam energy [69, pp. 13], which is why often the normalized emittance

[1] See for example [71, pp. 126] or [72, pp. 46] for a more detailed introduction.

[2] The sign of the quadrupole strength is arbitrary. Here K is chosen to be $< 0$ for quadrupoles which are focusing in the horizontal plane.

[3] In a real accelerator this is not completely true, as higher order fields imply a coupling between the two planes. However, the related effects are typically small in the LHC, especially when considering fast timescales.

[4] The Hill's equation is a homogeneous differential equation of second order without first order derivatives. It was first studied by the astronomer G. Hill to find a solution to the three-body problem [73].

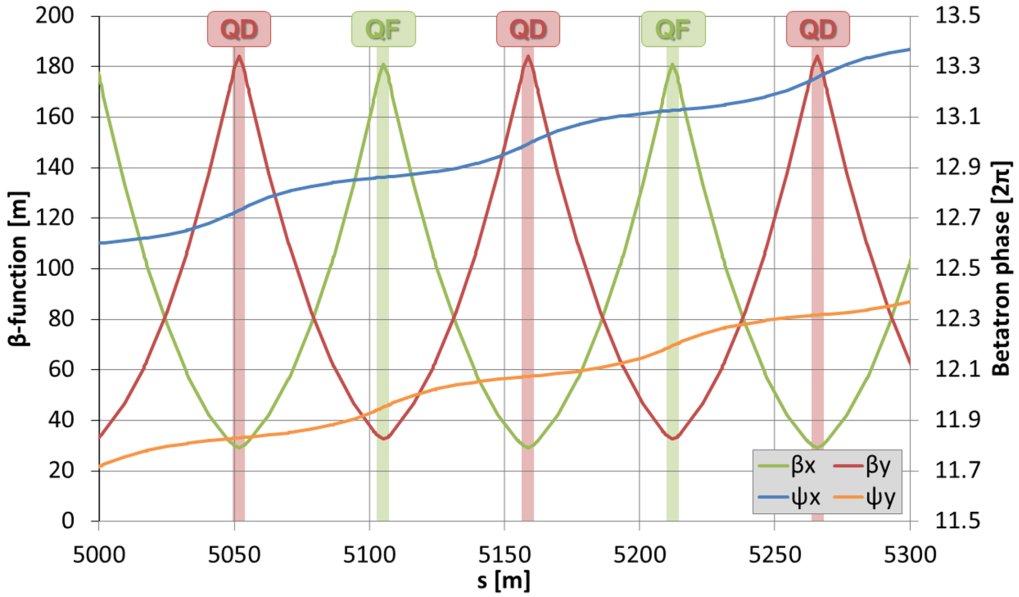


Figure 3.2.: $\beta$-function and betatron phase for the regular FODO structure of the LHC arcs. Per definition, $s$ is zero in IP1. QF and QD denote quadrupole magnets, which are focusing and defocusing in the horizontal plane, respectively.

$\epsilon^{\mathrm{n}} = \epsilon\beta_r\gamma_r$ is used[5]. For a beam with Gaussian particle distribution, the transverse RMS beam size is as derived in [71, p. 252] also given by

$$\sigma = \sqrt{\epsilon \cdot \beta(s)}.$$

As indicated by Eq. 3.3, the general solution to the horizontal equation of motion depends also on the momentum deviation $\frac{\Delta p}{p}$. In linear approximation, the solution to the inhomogeneous equation is given by

$$x(s) = x_\beta(s) + D_x(s) \cdot \frac{\Delta p}{p},$$

where $x_\beta(s)$ denotes the solution to the homogenous equation of motion given by Eq. 3.5. $D_x(s)$ is the linear dispersion function, which is defined as

$$D_x(s) = \frac{\partial x(s)}{\partial\left(\frac{\Delta p}{p}\right)}.$$

### 3.1.2. Betatron Oscillation, Tune and Chromaticity

Equation 3.5 shows that the particle trajectory has oscillatory behavior. These oscillations are called betatron oscillations, since they were first observed in betatron

[5] With the relativistic functions $\beta_r = \frac{v}{c}$ and $\gamma_r = \frac{1}{\sqrt{1-\beta_r^2}}$.

accelerators [74]. Figure 3.1 shows the trajectory of a particle oscillating in the vertical plane around the closed design orbit. The number of betatron oscillations per revolution is called tune[6]. Equation 3.6 leads to the following relation between tune $Q$ and beta function:

$$Q = \frac{1}{2\pi}[\psi(C) - \psi(0)] = \frac{1}{2\pi}\oint_C \frac{d\bar{s}}{\beta(\bar{s})} \tag{3.7}$$

with $C$ being the circumference of the accelerator. For the nominal LHC injection optics $Q_H = 64.28$ and $Q_V = 59.31$, for LHC collision optics $Q_H = 64.31$ and $Q_V = 59.32$.

Combining Eq. 3.2 and Eq. 3.4 shows that the strength $K(s)$ of quadrupole fields is inversely proportional to the particle momentum. This results in a momentum dependency of the tune. In a linear approximation, the chromaticity $\xi$ is defined as the proportionality factor between momentum offset and tune change:

$$\Delta Q = \xi \cdot \frac{\Delta p}{p}. \tag{3.8}$$

### 3.1.3. Transfer Matrices and Orbit Response

The particle accelerator elements can be characterized by a transfer matrix in order to calculate the beam position $x$ and its derivative $x' = \frac{\partial x}{\partial s}$ (the horizontal plane is discussed here again) for any location $s$ based on the initial conditions at location $s_0$:

$$\begin{pmatrix} x(s) \\ x'(s) \end{pmatrix} = R \begin{pmatrix} x(s_0) \\ x'(s_0) \end{pmatrix}. \tag{3.9}$$

The transfer matrix $R$ is typically parametrized by the betatron phase advance $\Delta\psi = \psi(s) - \psi(s_0)$, the $\beta$-function and the $\alpha$-function $\alpha(s) = -\frac{1}{2}\frac{\partial\beta(s)}{\partial s}$ [71, p. 263]:

$$R = \begin{pmatrix} \sqrt{\frac{\beta(s)}{\beta(s_0)}}\left[\cos(\Delta\psi) + \alpha(s_0)\sin(\Delta\psi)\right] & \sqrt{\beta(s_0)\beta(s)}\sin(\Delta\psi) \\ \frac{\alpha(s_0)-\alpha(s)}{\sqrt{\beta(s_0)\beta(s)}}\cos(\Delta\psi) - \frac{1+\alpha(s_0)\alpha(s)}{\sqrt{\beta(s_0)\beta(s)}}\sin(\Delta\psi) & \sqrt{\frac{\beta(s_0)}{\beta(s)}}\left[\cos(\Delta\psi) - \alpha(s)\sin(\Delta\psi)\right] \end{pmatrix}.$$

This shows directly that a dipole deflection $\Delta x'(s_0)$ leads to a downstream (single-turn) trajectory perturbation $\Delta x(s)$ which is given by the (1,2) element of the R-matrix:

$$\Delta x(s) = \sqrt{\beta(s_0)\beta(s)}\sin[\psi(s) - \psi(s_0)] \cdot \Delta x'(s_0). \tag{3.10}$$

Taking into account the circular boundary conditions for the corresponding effect on the closed orbit yields [71, p. 291]:

$$\Delta x(s) = \frac{\sqrt{\beta(s_0)\beta(s)}}{2\sin(\pi Q)}\cos[|\psi(s) - \psi(s_0)| - \pi Q] \cdot \Delta x'(s_0). \tag{3.11}$$

[6]The red particle in Fig. 3.1 makes 6.25 vertical betatron oscillations per turn. Thus, it has a vertical tune of $Q_V = 6.25$.

## 3.2. Luminosity and Beam-Beam Effects

As discussed in Sec. 2.1, the luminosity $L$ is a key performance quantity of a particle collider. It defines the event rate $\frac{dN_i}{dt}$ for a nuclear interaction process with cross section $\sigma_i$:

$$\frac{dN_i}{dt} = L \cdot \sigma_i.$$

For bunched counter-rotating beams with Gaussian transverse beam profile, it is given by

$$L = \frac{N_b^2 \cdot k_b \cdot f_{ref}}{4\pi \cdot \sigma_x^* \cdot \sigma_y^*} \cdot h, \tag{3.12}$$

where $N_b$ is the number of particles per bunch, $k_b$ the number of colliding bunches per beam, $f_{rev}$ the revolution frequency and $\sigma_x^*$ and $\sigma_y^*$ the horizontal and vertical beam size at the interaction point, respectively [71, pp. 73]. $h$ denotes a correction factor for higher order effects, as discussed below.

Whereas generally a high luminosity is desirable, this may lead to multiple simultaneous interactions per bunch-crossing, a so-called pile-up. If the pile-up is too high, the simultaneous interactions cannot be distinguished by the experimental detectors anymore. Therefore, the maximal acceptable pile-up defines an upper limitation for the desired peak luminosity[7]. In this case, luminosity leveling techniques, e.g. a transverse separation of the beams at the collision point, are applied to deliberately reduce the luminosity and to keep it at a constant level throughout the fill. In 2012 LHC operation, the average pile-up regularly exceeded 30 proton-proton interactions per bunch crossing in each high-luminosity experiment.

Apart from the nuclear interaction processes, two counter-rotating beams in a common vacuum chamber also interact via the Lorentz force given by Eq. 3.1. In first-order approximation, this results in a dipole deflection $\Delta\vec{r}'$, which is for bunches with Gaussian profile determined by the transverse separation of the bunch centers $\vec{d}$ and the bunch charge of the counter-rotating beam $N_b$:

$$\Delta\vec{r}' = -\frac{2N_b r_0}{\gamma_r} \cdot \frac{\vec{d}}{|\vec{d}|^2} \cdot \left[1 - \exp\left(-\frac{|\vec{d}|^2}{2\sigma^2}\right)\right] \tag{3.13}$$

with $r_0$ being the classical particle radius, the relativistic factor $\gamma_r$ and the transverse beam size $\sigma$ [75, p. 11]. In order to mitigate the beam-beam effects and to avoid parasitic head-on collisions, the beams are colliding under a small crossing angle $\Theta$, as illustrated in Fig. 3.3.

[7] In particular the longitudinal pile-up density, i.e. the pile-up divided by the longitudinal extension of the collision region, is limiting.

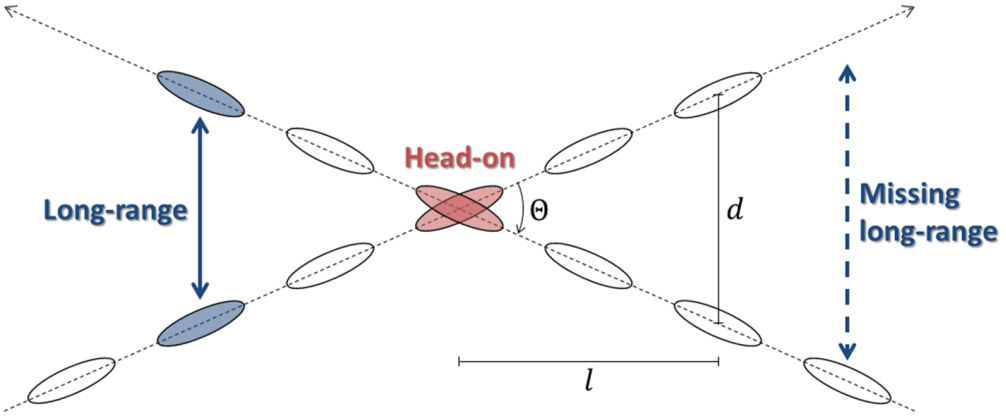


Figure 3.3.: Illustration of head-on and long-range beam-beam interactions for two beams colliding under the crossing angle Θ (courtesy of W. Herr [76]).

In the absence of external magnetic fields, the separation $d_i$ at the $i^{th}$ long-range beam-beam encounter is mainly given by the crossing angle:

$$d_i = 2 \cdot l_i \cdot \tan\frac{\Theta}{2},$$

where $l_i$ is the distance of the $i^{th}$ long-range encounter from the collision point. For small crossing angles and a $\beta$-function at the collision point $\beta^*$ which is small compared to $l_i$, this can be expressed as

$$d_i \approx \Theta\sqrt{\beta_{\mathrm{LR,i}} \cdot \beta^*} \tag{3.14}$$

with $\beta_{\mathrm{LR,i}}$ being the $\beta$-function at the $i^{th}$ long-range encounter [71, p. 262]. In order to keep the closed orbit distortion due to the long-range beam-beam deflections constant, one obtains with Eq. 3.11, Eq. 3.13 and Eq. 3.14 the scaling-law for the nominal crossing angle:

$$\Theta \propto \frac{1}{\sqrt{\beta^*}}. \tag{3.15}$$

As illustrated in Fig. 3.3, the bunches at the beginning and at the end of a bunch train, the so-called PACMAN bunches, have a reduced number of long-range encounters, resulting in a different closed orbit.

The crossing angle moreover implies a geometric reduction of the luminosity, as the bunches do not fully overlap during the bunch traversal at the collision point (see Fig. 3.3). For a small crossing angle, which is assumed without loss of generality to be in the horizontal plane, and bunches with a bunch length $\sigma_s \gg \sigma_x^*$, the correction factor $h$ in Eq. 3.12 can be written as [77]

$$h = \frac{1}{\sqrt{1+\Phi^2}}, \tag{3.16}$$

where $\Phi$ is the Piwinski angle which is defined as

$$\Phi = \frac{\Theta \cdot \sigma_s}{2\sigma_x^*}.$$

Figure 3.4 illustrates the resulting luminosity as function of $\beta^*$ for LHC parameters (see Tab. 2.1). Whereas for nominal LHC parameters with $\beta^* = 55\,\text{cm}$ the geometric luminosity reduction is below 20%, the effect cancels out most of the luminosity gain from a further reduction of $\beta^*$.

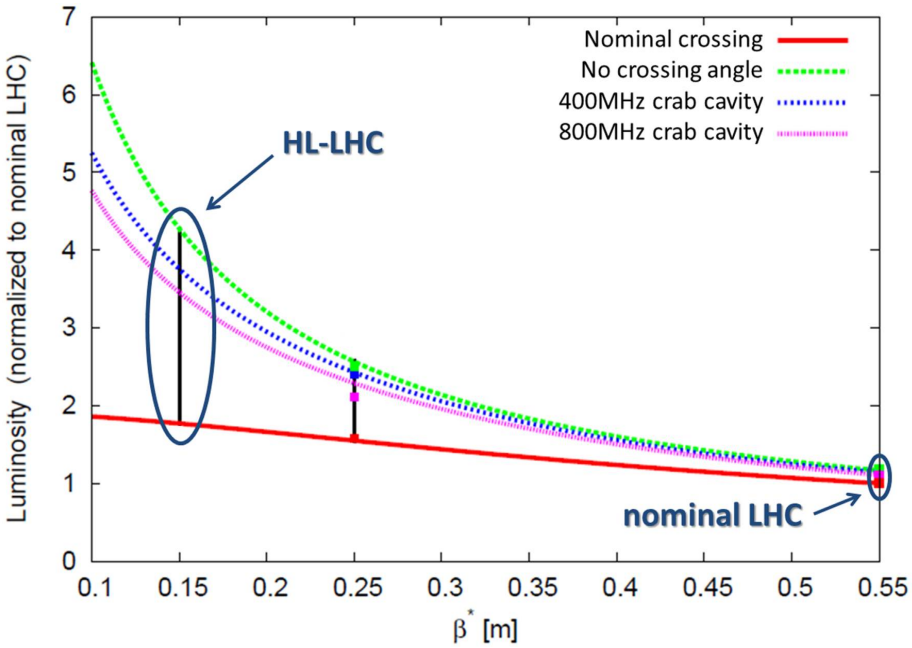


Figure 3.4.: Luminosity (normalized to nominal LHC) as function of $\beta^*$ with nominal crossing angle (red) and without crossing angle (green). The blue and magenta curves illustrate the luminosity gain by using 400 MHz and 800 MHz crab cavities, respectively (courtesy of R. Calaga et al. [78]).

Therefore, as part of the HL-LHC upgrade program, crab cavities will be installed in the LHC (see Sec. 2.5), which can compensate the geometric luminosity reduction. Crab cavities deflect the beam transversely, with an amplitude that depends on the longitudinal particle position w.r.t. the bunch center. This so-called tilt-kick rotates the bunches to reestablish a full overlap of the bunches at the collision point, as illustrated in Fig. 3.5. However, crab cavities cannot fully compensate the geometric luminosity reduction as shown in Fig. 3.4, since the tilt-kick has a sinusoidal shape (see Eq. 3.17). This RF curvature limits the tilt-kick for particles with large (longitudinal) distance from the bunch center [79]. In the so-called local scheme, crab cavities are installed upstream and downstream of each collision point such that the tilt-oscillations are confined within the insertion region (IR).

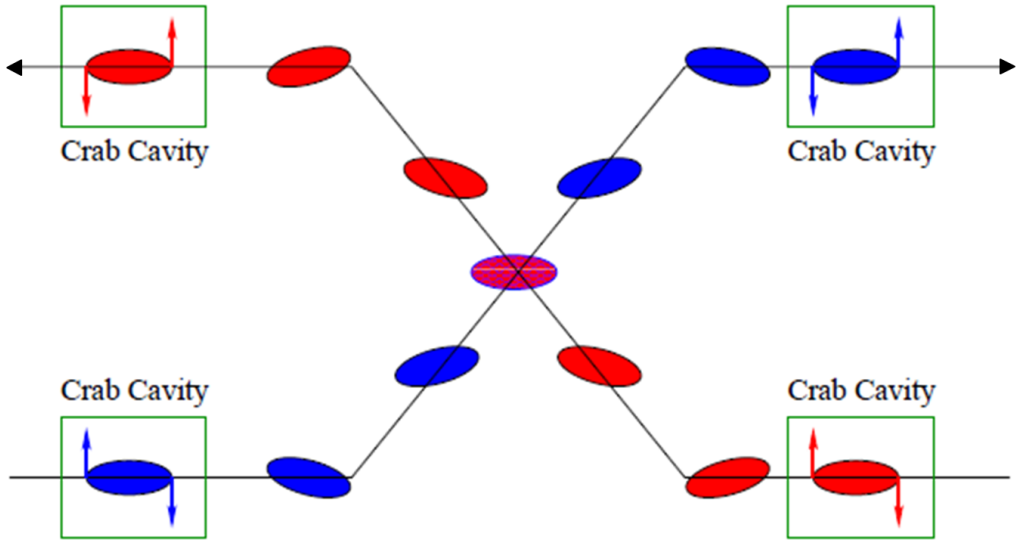


Figure 3.5.: Illustration of bunch-rotation by crab cavities in the local scheme. At the interaction point, quasi head-on collisions are reestablished (courtesy of R. Calaga et al. [80]).

## 3.3. Crab Cavity Theory

The basic crab cavity relations are introduced in analogy to the relations for accelerating cavities in this section. A more detailed introduction can be found in [81, 82].

A crab cavity is a resonator for electromagnetic waves, as illustrated in Fig. 2.11 for the parallel-bar crab cavity design. Figure 3.6 shows the corresponding transverse peak electric and magnetic field components on the beam axis which are relevant for a transverse deflection in the $x$-direction. Since the electric and magnetic fields are oscillating 90° out of phase, they are of the form

$$E_x(s,t) = E_x(s) \cdot \cos(2\pi f \cdot t)$$
$$B_y(s,t) = B_y(s) \cdot \sin(2\pi f \cdot t),$$

where $f$ is the oscillation frequency and $s$ denotes spatial coordinate in the direction of beam motion. With Eq. 3.1, the peak transverse deflection (for relativistic particles) can be characterized by a transverse deflecting voltage amplitude

$$V_{\perp,0} = \int_L \left[ E_x(s) \cdot \cos\left(2\pi f \cdot \frac{s}{c}\right) + cB_y(s) \cdot \sin\left(2\pi f \cdot \frac{s}{c}\right) \right] ds,$$

where $L$ denotes the longitudinal extension of the fields and $c$ is the speed of light [54]. Thus, for the fields illustrated in Fig. 3.6, the total transverse deflection is mainly due to the horizontal electric field with the vertical magnetic field counteracting the deflection. However, the effect of the magnetic field is comparatively small [54].

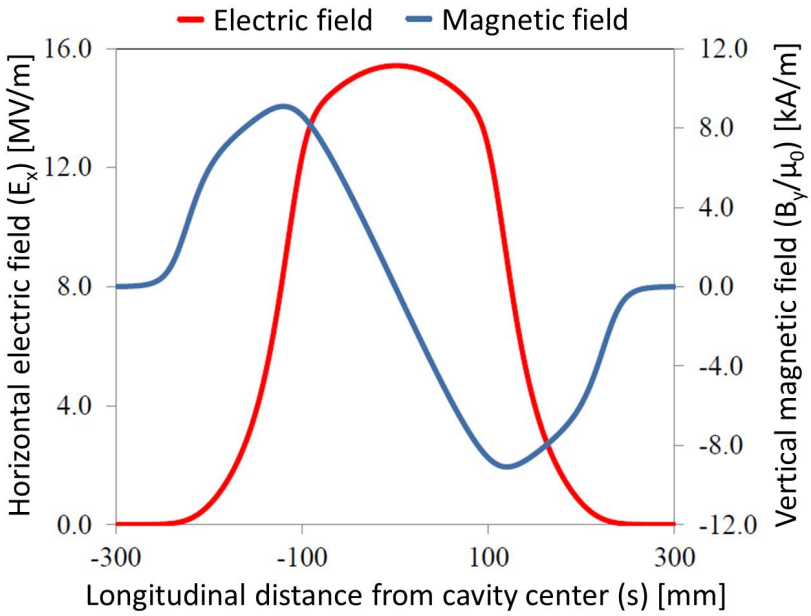


Figure 3.6.: Relevant peak transverse electric and magnetic field components on axis for a horizontal deflection of a parallel-bar crab cavity (courtesy of S. U. De Silva et al. [54]).
The values are for a 499 MHz crab cavity for the Jefferson Lab 12 GeV upgrade but they are qualitatively similar for the 400 MHz HL-LHC crab cavity. $\mu_0 = 4\pi \cdot 10^{-7} \frac{\mathrm{V \cdot s}}{\mathrm{A \cdot m}}$ denotes the vacuum permeability.

The time-dependent transverse deflecting voltage can then be written as

$$V_\perp = V_{\perp,0} \cdot \sin\left(\Phi + 2\pi f \cdot t\right). \tag{3.17}$$

For a pure crab cavity the nominal phase $\Phi = 0$, such that head and tail of a bunch are deflected in opposite direction to quasi rotate the bunches. The optimal voltage amplitude for nominal crab cavity operation is derived in Sec. 7.1.

Since the cavity (even a superconducting cavity) has a finite surface resistance $R_s$ for high-frequency fields, the energy $E_s$ stored in the electromagnetic field is dissipated in the cavity walls. The energy loss is characterized by the quality factor

$$Q_0 = 2\pi f \cdot \frac{E_s}{P_c}, \tag{3.18}$$

where $P_c$ is the power dissipated in the cavity walls [81, p. 45]. $Q_0$ can also be expressed in terms of the surface resistance $R_s$:

$$Q_0 = \frac{G}{R_s} \tag{3.19}$$

with the constant geometry factor $G$ [81, p. 45]. Another important quantity for the characterization of the energy loss in a cavity is the shunt impedance[8] [81, p. 47]:

$$R_a = \frac{V_{\perp,0}^2}{P_c}. \tag{3.20}$$

Combining Eq. 3.18 and Eq. 3.20 yields

$$\frac{R_a}{Q_0} = \frac{V_{\perp,0}^2}{2\pi f \cdot E_s}. \tag{3.21}$$

In order to excite the operating mode in the cavity and to compensate the internal power losses, energy from an RF power generator is coupled into the cavity via an input coupler. It is for now assumed that the RF power generator is switched off while the cavity is operated. In this case, the energy stored in the cavity leaks out through the input coupler. In analogy to $Q_0$, the external quality factor $Q_{\text{ext}}$ is defined as

$$Q_{\text{ext}} = 2\pi f \cdot \frac{E_s}{P_e}$$

with $P_e$ being the power dissipated through the input coupler [81, p. 146].

This can be generalized with the total power loss $P_{\text{tot}} = P_c + P_e + \cdots$ to define the loaded quality factor:

$$Q_L = 2\pi f \cdot \frac{E_s}{P_{\text{tot}}}. \tag{3.22}$$

The different quality factors are related by:

$$\frac{1}{Q_L} = \frac{1}{Q_0} + \frac{1}{Q_{\text{ext}}} + \cdots. \tag{3.23}$$

For a superconducting crab cavity $Q_0 \gg Q_{\text{ext}}$ and $Q_L \approx Q_{\text{ext}}$.

Equation 3.22 can be seen as the differential equation

$$\frac{dE_s}{dt} = -P_{\text{tot}} = -2\pi f \cdot \frac{E_s}{Q_L}.$$

Since $E_s \propto V_{\perp,0}^2$ (see Eq. 3.21), the solution implies an exponential decay of the transverse deflecting voltage amplitude:

$$V_{\perp,0}(t) = V_{\perp,0}(0) \cdot e^{-\frac{t}{\tau}} \tag{3.24}$$

with the time constant

$$\tau = \frac{Q_L}{\pi f}.$$

[8] The shunt impedance is also often defined as $R_a = \frac{V_{\perp,0}^2}{2 \cdot P_c}$ (for example in [82]). In the following, the definition given by Eq. 3.20 is used.

It is important to note that a beam which is centered in an ideal crab cavity is only subject to the transverse deflecting field components. Thus, the deflecting force is perpendicular to the direction of beam motion and there is no energy transfer from the crab cavity to the beam (no so-called beam-loading). This implies that the RF power $P_g$ (from the RF power generator) which is needed to maintain the crab cavity field is independent of the beam intensity and the phasing between crab cavity and beam. The required RF generator power is derived in [82, p. 15] and is given by

$$P_g = \frac{V_{\perp,0}^2}{4 \cdot R_a/Q_0} \cdot \frac{Q_{\text{ext}}}{Q_L^2}. \tag{3.25}$$

However, according to the Panofsky-Wenzel theorem[9] [82,83], the beam interacts with an additional accelerating field component, if it is transversely off-centered in the crab cavity by $\Delta x$. This can result in increased power requirements. As derived in [82, p. 19], this can be expressed by an additional voltage component $V_b$ which has to be added to $V_{\perp,0}$ in Eq. 3.25. For a crab cavity with phase $\Phi = 0$, this is given by

$$V_b = Q_{\text{ext}} \cdot \frac{R_a}{Q_0} \cdot I_b \cdot F_b \cdot \frac{2\pi f}{c} \cdot \Delta x \tag{3.26}$$

with $I_b$ being the beam current (in A) and $F_b$ being the relative bunch form factor, which is about 0.9 for LHC beams at top energy [82, p. 12].

Likewise, $P_g$ has to be increased if the cavity is slightly detuned by $\Delta f$ from the reference frequency. The additionally required power is given according to [82, p. 16] by

$$\Delta P_g = \frac{V_{\perp,0}^2}{R_a/Q_0} \cdot Q_{\text{ext}} \cdot \left(\frac{\Delta f}{f}\right)^2. \tag{3.27}$$

## 3.4. Beam Losses

The nominal stored beam energy in the LHC is more than two orders of magnitude higher than in other high-intensity accelerators like SPS, Tevatron or HERA. At the same time the superconducting magnets can be quenched by a beam loss corresponding to $10^{-8}$ - $10^{-7}$ of the stored beam energy (for nominal LHC operation) [84]. A beam loss of $5 \cdot 10^9$ protons (<5% of a single nominal bunch) at 7 TeV is already sufficient to damage a tertiary tungsten collimator [48]. Therefore, a very tight control of the beam losses is mandatory to ensure a safe LHC operation.

[9] The Panofsky-Wenzel theorem relates the transverse deflection to the (transverse) gradient of the longitudinal electric field. It is valid for any deflecting mode of arbitrary geometry under the assumption that the particle traverses the cavity at constant velocity on a straight line [54].

During regular operation, a major source of beam losses are the nuclear collisions for luminosity production. These lead mainly to localized losses in the experimental interaction regions. Further beam losses in regular operation are caused e.g. by elastic beam-beam scattering processes, intra-beam scattering and fluctuations of the closed orbit. Additional beam losses occur during the injection and extraction processes. Most of these beam losses are concentrated at the collimators, as described in Sec. 2.3.2. The steady beam losses are characterized by the beam intensity life time. Changes occur typically on timescales of seconds or even longer. The LHC collimation system is designed for beam losses of up to 500 kW for a duration of 10 s in nominal LHC operation, which corresponds to an intensity lifetime of 0.2 h [11, p. 468]. A performance allowing beam losses of up to 1 MW was successfully demonstrated in a dedicated test in February 2013 [85].

Most critical for the machine integrity are erroneous beam losses due to failures or abnormal behavior. These can be classified by the time between the start of the failure and the onset of significant beam losses:

- **Ultra fast:** beam loss scenarios which can lead to significant beam losses within the reaction time of the LHC beam interlock and beam dump system of up to 3 LHC revolution periods (see Sec. 2.3.4) are classified as ultra fast. Such failures are too fast to ensure an active protection by a protection beam dump. The only corresponding failure cases in the present LHC are injection or extraction failures (and similar fast kicker failures) [84]. The high dependability of injection and extraction systems ensures that these failures are very rare [4]. The LHC aperture is protected against such failures by dedicated injection and dump protection collimators (see Sec 2.3.4). Crab cavities may be an additional source of ultra fast failures, as discussed in Chap. 7. Moreover, previously unforeseen beam losses due to the missing long-range beam-beam deflections during the beam dump process fall into this category, as discussed in Chap. 6. However, this beam loss mechanism occurs regularly in routine operation and is therefore not regarded as a failure.

- **Very fast:** multi-turn beam loss scenarios which allow active protection by the fastest machine protection systems like beam loss monitors (see Sec. 2.3.3) or fast magnet current change monitors (see Sec. 2.3.1) are classified as very fast. The only equipment failures in this category are failures of normal-conducting magnets [84] or the transverse damper, as discussed in Chap. 4. Abnormal beam losses due to macro particles, which were not expected before the LHC start-up, also fall into this category, as discussed in Chap. 5. Furthermore, an erroneous behavior of crab cavities can lead to beam losses on this timescale, as discussed in Chap. 7.

- **Fast:** multi-turn beam loss scenarios which evolve over at least 15 ms are redundantly covered by multiple distributed machine protection systems, in particular the beam loss monitoring system and the quench protection system and are classified as fast. Many equipment failures fall into this category. Examples are a trip of the accelerating RF, a quench of a superconducting magnet or a powering failure of a superconducting circuit. The experience during run 1 showed that the LHC is well protected against such failure scenarios.
- **Slow:** Failures or abnormal conditions which evolve over timescales $> 1$ s allow a manual intervention and are classified as slow. Typical examples are problems of the cryogenic system, transverse beam instabilities (see Sec. 2.4.2) or a failure of the feedback system for tune or orbit. Like for fast beam losses, the LHC is well protected against these beam loss scenarios.

This classification is illustrated in Figure 3.7. **A redundant protection (typically by multiple systems) is required for all critical failure scenarios.** The focus of this thesis is on the critical ultra fast and very fast beam loss scenarios for the circulating beam[10].

[10] In particular injection and extraction failures are excluded from the further discussion, as explained in Chap. 1.

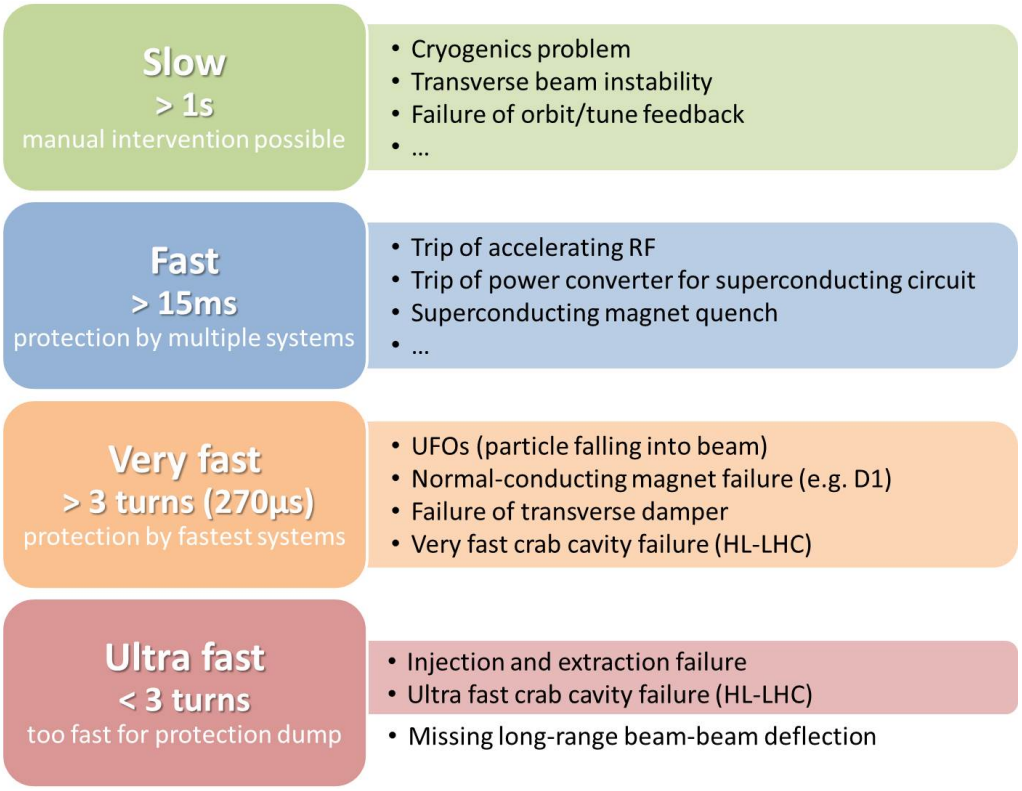


Figure 3.7.: Classification of beam loss scenarios in the LHC due to abnormal behavior or failures according to the time between the start of the failure and the onset of critical beam losses.
Ultra fast beam losses due to the missing long-range beam-beam deflection during the beam dump process are not regarded as abnormal beam loss scenario.

# 4. Very Fast Beam Losses due to Equipment Failures

As shown in Fig. 3.7, most equipment failures are relatively slow. The LHC is well protected against failures on the corresponding timescales e.g. by the beam loss monitoring system and the quench protection system, as discussed in Sec. 3.4. Apart from the fast kicker magnets with magnet rise-times in the order of $1\,\mu$s (see Sec. 2.3.1), failures of the normal-conducting separation dipole magnets (see Sec. 2.3.1) and the transverse damper [86] are most critical and can provoke beam losses on very fast timescales.

## 4.1. Warm Magnet Circuits

Failures of the normal-conducting magnet circuits were already extensively studied before the LHC start-up [21, 23, 87] and motivated the installation of fast magnet current change monitors (FMCMs) for 12 LHC circuits (see Sec. 2.3.1). Dedicated tests and the experience with protection dumps by FMCMs showed that failures in the powering of the normal-conducting magnets are always detected by the FMCMs well before any effect (position change or related beam losses) on the beam dynamics is observable.

Figure 4.1 illustrates a typical example of a FMCM protection beam dump: an electrical perturbation causes a voltage and current change of the RD1 separation dipole circuit in IR5. After about 8.6 ms, the FMCM signal[1] exceeds the dump threshold, as shown in Fig. 4.1a. The current change until the beam dump is $\approx 70\,\text{mA} = 0.02\%$. No effect on the beam trajectory and no increased beam losses are observable.

Electrical perturbations of the external power distribution, primarily caused by protection/reconfiguration actions in the high-voltage distribution network or flashes of lightning during thunderstorms, turned out to be the main reason for protection

[1] The FMCM estimates a filtered simulated current change. This signal is quantitatively different from the absolute current change of the circuit.

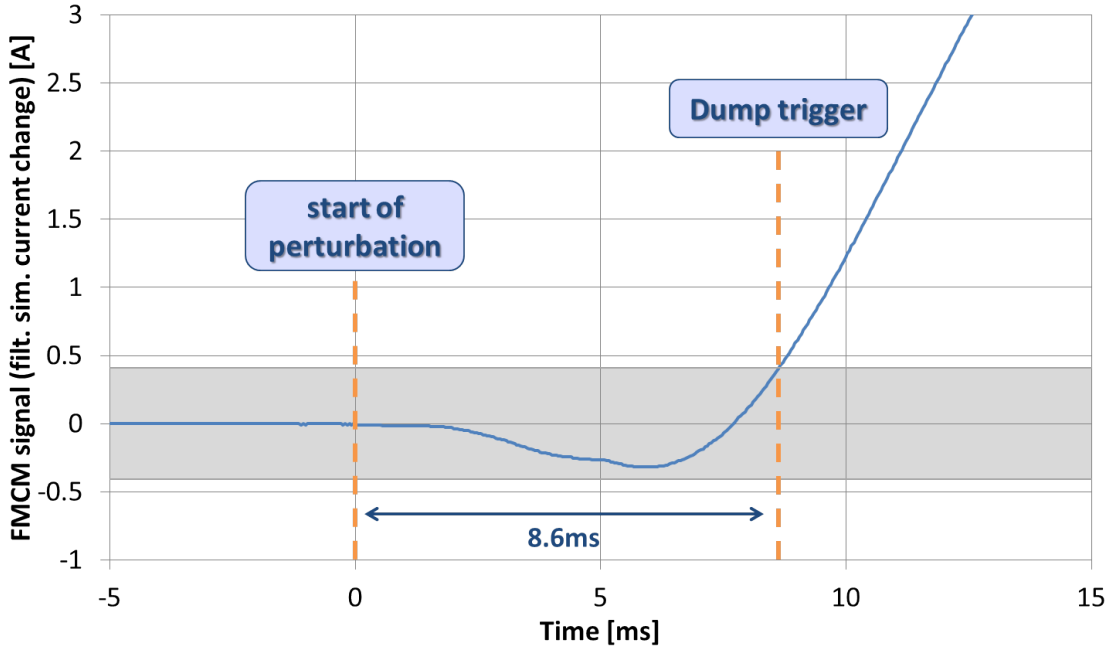


(a) FMCM signal.

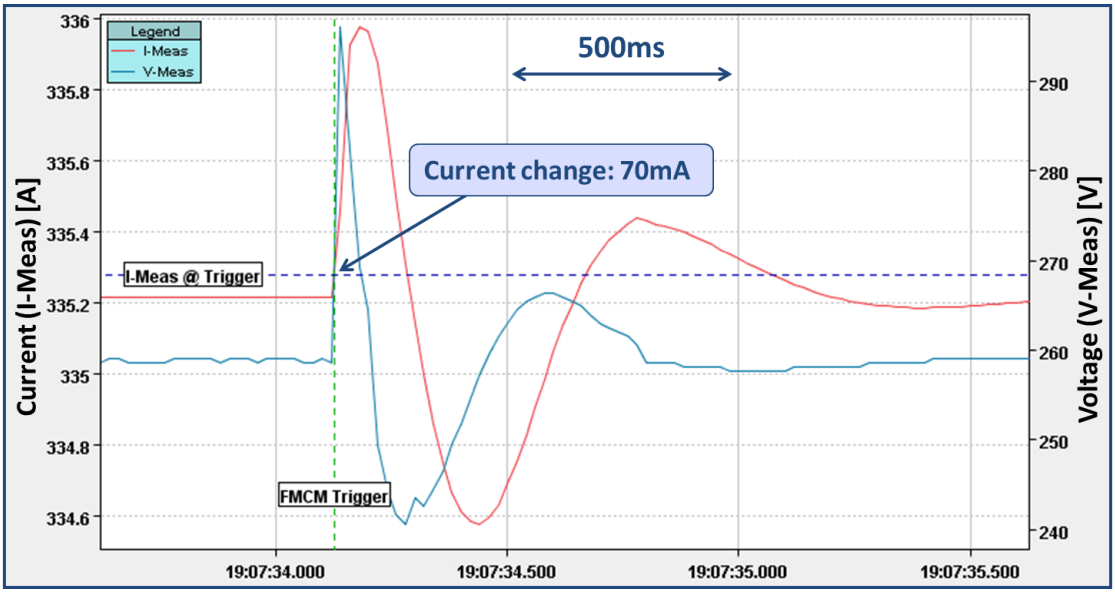


(b) Voltage and Current.

Figure 4.1.: FMCM signal (filtered simulated current change) during an electrical perturbation affecting the RD1 circuit in IR5 (a). The beam dump is triggered after 8.6 ms, when the signal exceeds the thresholds indicated by the gray area. The current changes by $\approx 70$ mA until the beams are dumped (b).
Measurement on 23.07.2011 19:07. Beam energy: 3.5 TeV, $\beta^* = 1.5$ m.

beam dumps by FMCMs. These perturbations often lead to temporary oscillations of voltage and current in the affected circuits, as illustrated in Fig. 4.1b). In particular small electrical perturbations, which remained within the tolerances of the power converters[2] and did not affect other systems but exceeded the FMCM thresholds, had an impact on LHC availability during run 1. Figure 4.2 shows the amplitude of the current changes for such small perturbations and the corresponding FMCM signal relative to its threshold for various normal-conducting dipole magnet circuits.

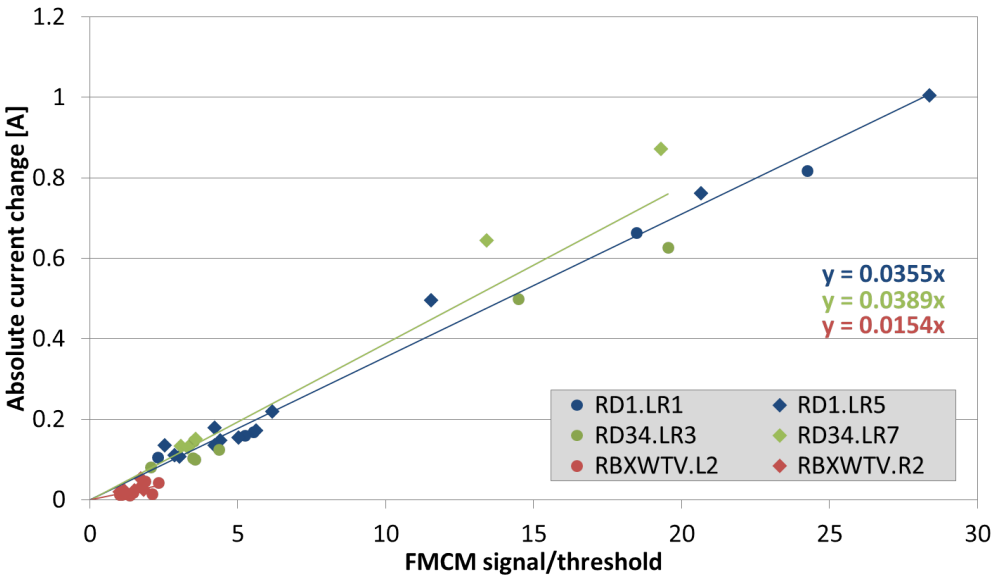


Figure 4.2.: The amplitude of the current change versus the FMCM signal relative to its threshold for different temporary electrical perturbations in 2011. The electrical perturbations of the illustrated cases exceeded the FMCM thresholds but remained within the tolerances of the power converters and did not affect other systems.

The possibility of threshold increases in order to avoid unnecessary beam dumps while keeping the FMCM thresholds low enough to protect against critical failures was evaluated in the context of this thesis. Dedicated MAD-X [88] simulations based on the operational settings used throughout the 2012 proton physics run were performed. Since the typical perturbations occur on timescales of many turns, adiabatic changes of the closed orbit are assumed in the following.

[2]Large voltage oscillations beyond the power converter tolerances may also cause a protective power abort by the power converter.

### 4.1.1. Simulation of RD1 Perturbation

Since the nominal betatron phase advance from IR1 to IR5 is exactly 360°, the effects of the RD1 separation dipole circuits in IR1 and IR5 add up maximally in case of a synchronous perturbation [26]. Figure 4.3 depicts the beam 1 closed orbit perturbation resulting from a simultaneous 100 mA current change of the RD1 circuits in IR1 and IR5 in 2012 stable beams conditions. The horizontal perturbation in the arc between IR5 and IR1 reaches a maximum of $\Delta x_{\mathrm{max}} \approx 130\,\mu\mathrm{m} = 0.34\,\sigma_{\mathrm{nom}}$ (in the regions with high $\beta$-function, the perturbation amplitude in millimeter is even larger). Such a perturbation is not critical, but would typically lead to beam losses above the dump thresholds of the beam loss monitoring (BLM) system, as explained in Sec. 2.4.2. A comparison with Fig. 4.2 shows that there is therefore no margin for a significant increase of the RD1 FMCM thresholds in 2012 operational conditions.

The simulation result can be easily scaled to another beam energy or operational configuration ($\beta^*$) by

$$\frac{\Delta x_{\mathrm{max}}}{\sigma_{\mathrm{nom}}} \propto \frac{\Delta I}{\sqrt{E \cdot \beta^*}}, \tag{4.1}$$

where $\sigma_{\mathrm{nom}}$ denotes the transverse beam size for a nominal (normalized) emittance of $\epsilon^{\mathrm{n}}_{\mathrm{nom}} = 3.5\,\mu\mathrm{m} \cdot \mathrm{rad}$, $\Delta I$ the current change, $E$ the beam energy and $\beta^*$ the $\beta$-function at the interaction point (IP).

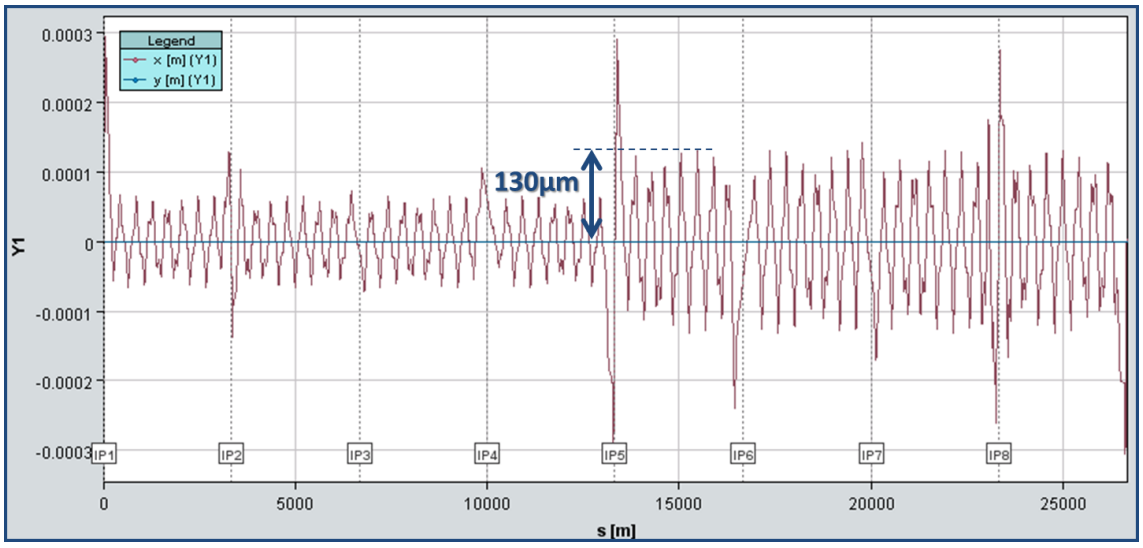


Figure 4.3.: Simulated closed orbit perturbation for beam 1 due to 100 mA current change of RD1 circuits in IR1 and IR5. Only the horizontal plane is affected.
Beam energy: 4 TeV, $\beta^* = 60$ cm.

### 4.1.2. Simulation of RD34 Perturbation

For the normal-conducting dipole circuits RD34 in IR3 and IR7, the orbit effects of synchronous current perturbations also add up partially. Since, in contrast to the experimental insertion areas, the optics in IR3 and IR7 remain rather constant throughout the operational cycle, the scaling of the orbit deviation is given by:

$$\frac{\Delta x_{\max}}{\sigma_{\text{nom}}} \propto \frac{\Delta I}{\sqrt{E}}. \tag{4.2}$$

Thus, the largest normalized orbit deviation is given for an electrical perturbation at injection energy. Figure 4.4 shows the orbit deviation for a corresponding current change of 100 mA of the RD34 circuits in IR3 and IR7. The maximal orbit deviation in the arc is $\Delta x_{\max} \approx 43\,\mu\text{m} = 0.04\,\sigma_{\text{nom}}$.

Since this value is far below any critical value, as discussed in Sec. 2.4.2 (injection oscillation have amplitudes of up to $\approx 1.2\,\sigma_{\text{nom}}$), the corresponding FMCM thresholds were increased by up to a factor three throughout the 2012 run [89]. A similar increase was possible for the FMCM thresholds of the ALICE spectrometer compensator dipole magnets [26, 89].

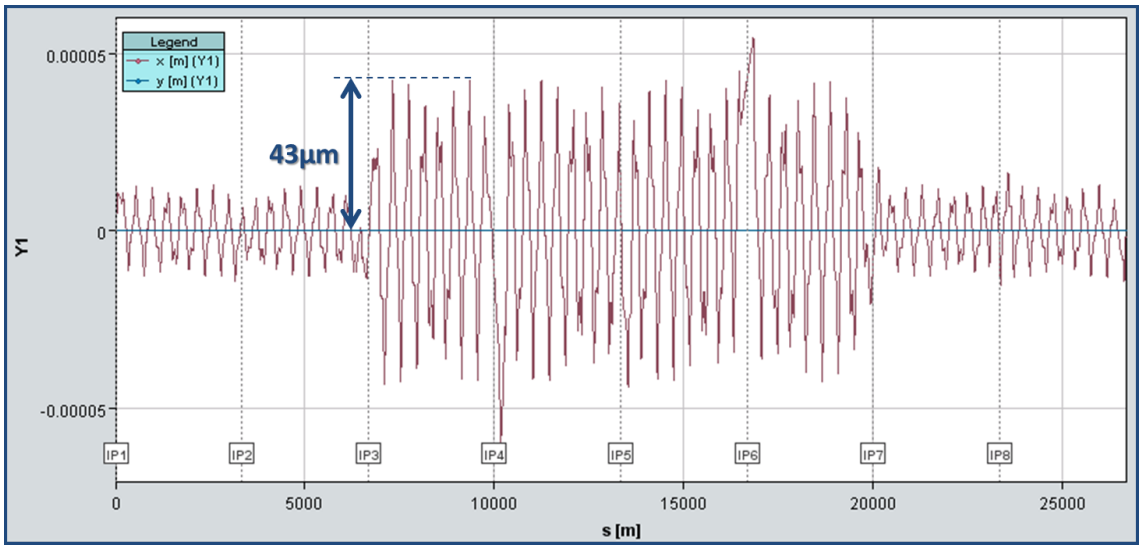


Figure 4.4.: Simulated orbit perturbation for beam 1 due to 100 mA current change of RD34 circuits in IR3 and IR7.
Beam energy: 450 GeV.

### 4.1.3. Outlook and Protection for HL-LHC

As explained above, the LHC availability in run 1 was affected by electrical perturbations of the external power distribution which exceeded the thresholds of the fast magnet current change monitors (FMCMs). The MAD-X simulations demonstrated the possibility of threshold increases for some circuits to reduce the number of unnecessary beam dumps. In order to further reduce the sensitivity to such electrical perturbations, the power converter regulations for the most critical RD1 and RD34 circuits are modified during the first long shutdown (LS1). This should stabilize the magnet circuits against external electrical perturbations [90] and reduce the associated number of beam dumps.

Since the impact of failures of warm magnet circuits depends particularly on the $\beta$-function at the concerned magnets, the RD1 circuits with $\beta$-functions of up to $\approx 3500\,\mathrm{m}$ (nominal LHC optics, $\beta^* = 55\,\mathrm{cm}$) are particularly critical. With the HL-LHC upgrade, the optics in the insertion regions will significantly change and the $\beta$-function at the D1 separation dipole magnets in IR1 and IR5 will increase up to $\approx 17000\,\mathrm{m}$ (ATS optics *SLHCV3.1b* [50], $\beta^* = 15\,\mathrm{cm}$). At the same time a replacement of the D1 separation dipole magnets by superconducting magnets is proposed. This would increase the time constants of the circuits significantly (see Sec. 2.3.1), which would mitigate any fast changes.

In case the D1 separation dipole magnets remain normal-conducting, the increased $\beta$-functions imply an increased sensitivity of the beam to corresponding current changes. Figure 4.5 illustrates the orbit perturbation for a 100 mA current change of the RD1 circuits in IR1 and IR5. The maximal orbit deviation in the arc is $\Delta x_{\mathrm{max}} \approx 230\,\mu\mathrm{m} = 0.43\,\sigma_{\mathrm{nom}}$, i.e. about 25% larger than in 2012 stable beams conditions. Since with this particular optics the phase advance from IP1 to IP5 is not 360°, the orbit perturbation is below the simulation result presented in Sec. 4.1.1 scaled with Eq. 4.1 ($\Delta x_{\mathrm{max}} = 0.34\,\sigma_{\mathrm{nom}} \cdot \sqrt{\frac{4\,\mathrm{TeV}\cdot 60\,\mathrm{cm}}{7\,\mathrm{TeV}\cdot 15\,\mathrm{cm}}} = 0.51\,\sigma_{\mathrm{nom}}$).

In case of a fast power abort (e.g. due to a power converter trip), the circuit current $I$ can be approximated by an exponential decay:

$$I(t) = I_0 \cdot e^{-\frac{t}{\tau}},$$

where $I_0$ is the nominal current and $\tau$ the time constant of the circuit [21]. Hence, the fastest current decay[3] is given by

$$\left.\frac{dI}{dt}\right|_{t=0} = -\frac{I_0}{\tau}. \tag{4.3}$$

[3] This is a worst-case approximation. Typically, the current change is initially slower than given by Eq. 4.3.

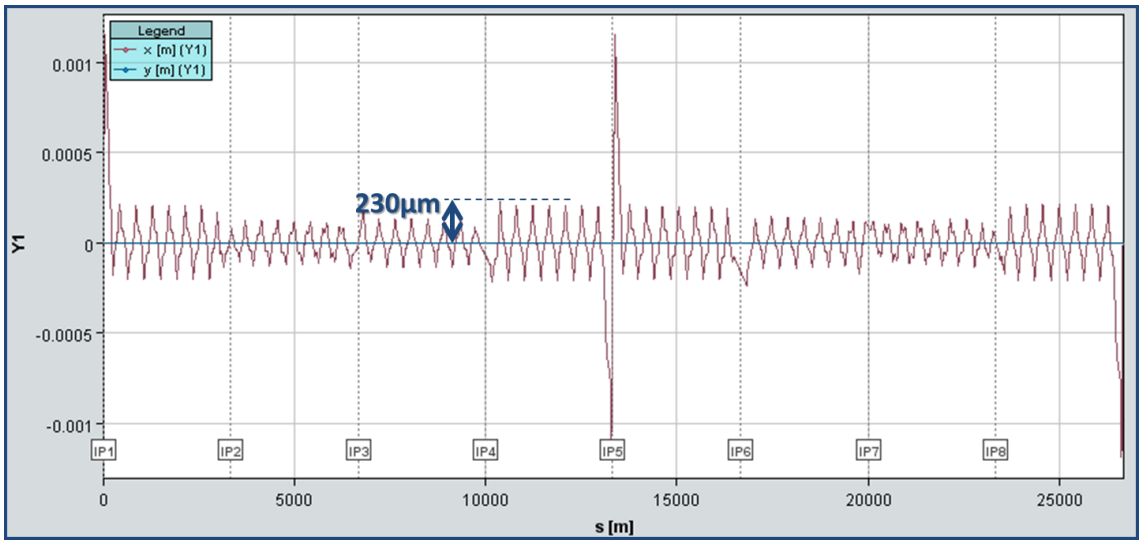


Figure 4.5.: Simulated orbit perturbation for beam 1 due to 100 mA current change of RD1 circuits in IR1 and IR5 with the *SLHCV3.1b* upgrade optics [50]. Beam energy: 7 TeV, $\beta^* = 15$ cm.

The time constant of the normal-conducting RD1 circuits is $\tau = 2$ s (see Sec. 2.3.1). Thus, the fastest current decay is $\frac{dI}{dt}\big|_{t=0} = -29.9$ mA per turn[4]. Together with the simulated orbit deviation of $0.43\,\sigma_{\text{nom}}$ for a simultaneous 100 mA current change of the RD1 circuits in IR1 and IR5, **the orbit perturbation increases by up to $0.13\,\boldsymbol{\sigma_{\text{nom}}}$ per turn.**

As discussed in Sec. 2.4.2, this could lead to beam losses above the BLM dump thresholds ($\approx 0.2\,\sigma_{\text{nom}}$) within below 2 turns and a machine critical oscillation amplitude of $\approx 1\,\sigma_{\text{nom}}$ in about 8 turns[5]. Whereas this is a very fast failure scenario, the present machine protection systems are fast enough to protect against this failure case, as described in Sec. 3.4. However, next to the BLMs, a failure detection by a redundant systems is needed. **The required FMCM detection level is $10^{-4} \cdot \mathbf{I_0}$ =67 mA with a reaction time of about 100 $\boldsymbol{\mu}$s**[6]. This is beyond the specification for the RD1 FMCMs (relative detection level of $3.5 \cdot 10^{-4}$ with a detection time of 900 $\mu$s [26]) but within the operational reach of the present FMCM system.

[4] With $I_0 = 670$ A at 7 TeV and the LHC revolution frequency $f_{\text{rev}} = 11'245$ Hz.

[5] An adiabatic orbit change is assumed here. The durations are slightly larger when considering the nominal betatron phase advance of the D1 separation dipole magnets to the collimators.

[6] With these values, a beam dump is triggered by the FMCM after not more than $\frac{67\,\text{mA}}{29.9\,\text{mA}}$ turns $+100\,\mu$s $= 3.4$ turns. Up to about 3 additional turns are needed until the beam is completely extracted from the LHC (see Sec. 2.3.4).

## 4.2. Failure of Transverse Damper

The LHC transverse damper system (ADT) is a high-frequency beam position feedback system. It is based on a bunch-by-bunch beam position measurement and a central signal processing. The output signal is amplified and fed back to the beam by capacitive high-voltage deflectors with a delay down to a single turn [11, p. 140]. It is designed to damp transverse oscillations (e.g. injection oscillations) within a few ten turns [86]. In a failure case, e.g. a sign or phase error, the ADT can excite the beam with the same time constant. Dedicated machine development tests were performed in 2012 to characterize the beam excitation with the ADT [91]. In February 2013, the ADT was used to create very fast beam losses for a beam induced magnet quench test [92]. These tests provide valuable information for machine protection considerations, which are discussed in the following.

### 4.2.1. Excitation Measurements

An example of the ADT excitation strength is illustrated in Fig. 4.6, which shows the horizontal root-mean-square (RMS, see Appendix A) position of beam 2 for 100 turns[7]. At turn 40, the beam is excited with the tune kicker (MKQ), resulting in a global betatron oscillation. 11 turns later, the ADT is activated with inverse sign and continuously excites the oscillation. Due to the large initial oscillation, the ADT feedback chain is directly saturated and the RMS position increases linearly with $\approx 76.4\,\mu$m per turn until the beam is dumped after turn 80 due to too high beam losses in the betatron collimation region.

In a similar test at 4 TeV, a RMS position rise-time of $\approx 8.3\,\mu$m per turn was observed[8]. The difference is consistent with the $\frac{4\,\mathrm{TeV}}{450\,\mathrm{GeV}} \approx 9$ times increased beam rigidity.

As shown in Fig. 4.7, the available kick strength of the ADT depends on the bunch-spacing configuration. For the measurements presented above, the 50 ns configuration was used. The excitation increases by about a factor 3 for a mode adopted to a larger bunch-spacing. Figure 4.8 shows the RMS position for a measurement at 4 TeV, with the 625 ns ADT mode. Since the initial excitation by the MKQ is reduced due to the increased beam rigidity, the ADT reaches saturation only about

[7] The horizontal excitation of beam 2 is discussed in the following, as this configuration was used in most of the beam-based tests. However, the $\beta$-function is largest at the vertical ADT unit for beam 2, leading to an about 23% larger amplification of the ADT deflection compared to the horizontal plane for beam 2.

[8] Measurement on 13.10.2012 at 05:56:11.

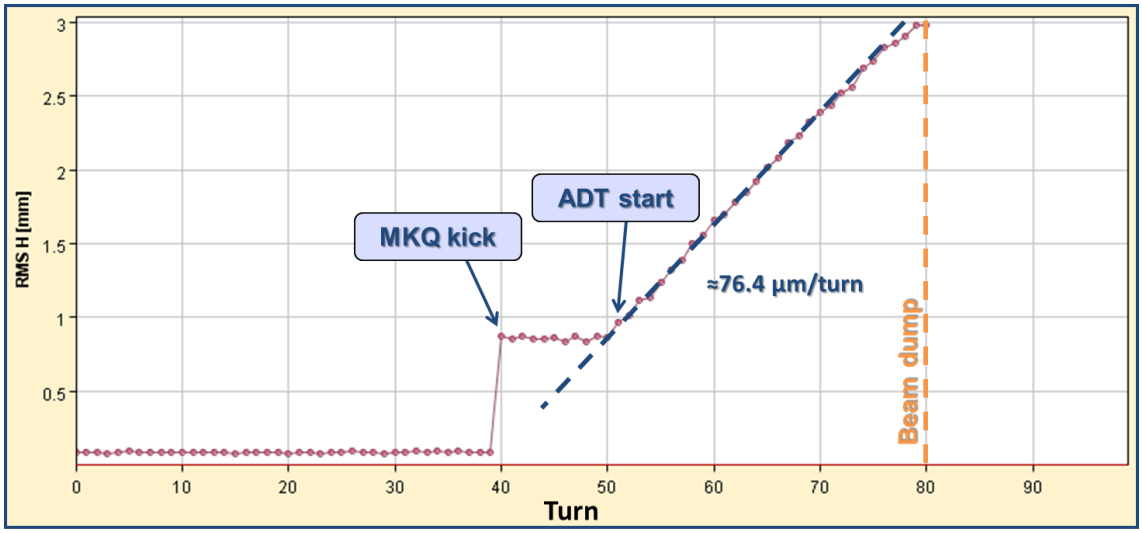


Figure 4.6.: Turn-by-turn RMS position after initial excitation by tune kicker (MKQ) at turn 40 and continuous excitation by ADT from turn 51 onwards. All horizontal arc beam position monitors (BPMs) for beam 2 between IR4 and IR8 are considered.
Measurement on 13.10.2012 03:35:58. Beam energy: 450 GeV, bunch intensity B2: $\approx 1 \cdot 10^{10}$ protons, single bunch. MKQ gain: 100%, ADT gain: 400%, 50 ns mode.

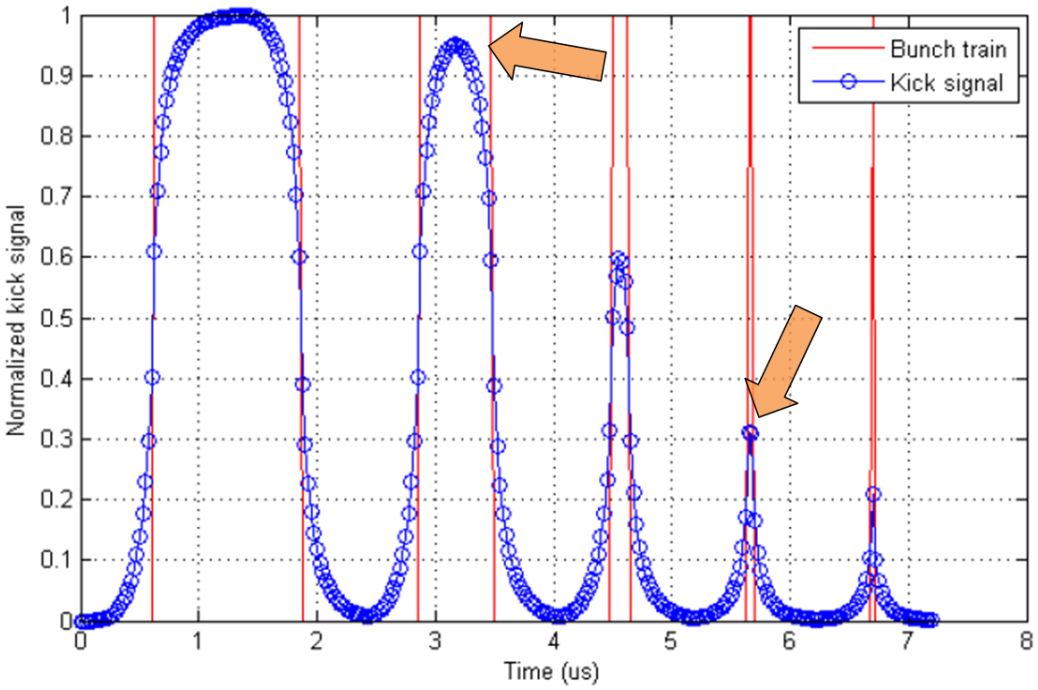


Figure 4.7.: Available kick strength from the ADT as a function of the bunch-spacing configuration. From left to right: 1250 ns, 625 ns, 150 ns, 50 ns and 25 ns mode. The orange arrows indicate the settings used for Fig. 4.6 and Fig. 4.8 (courtesy of W. Höfle and D. Valuch [93]).

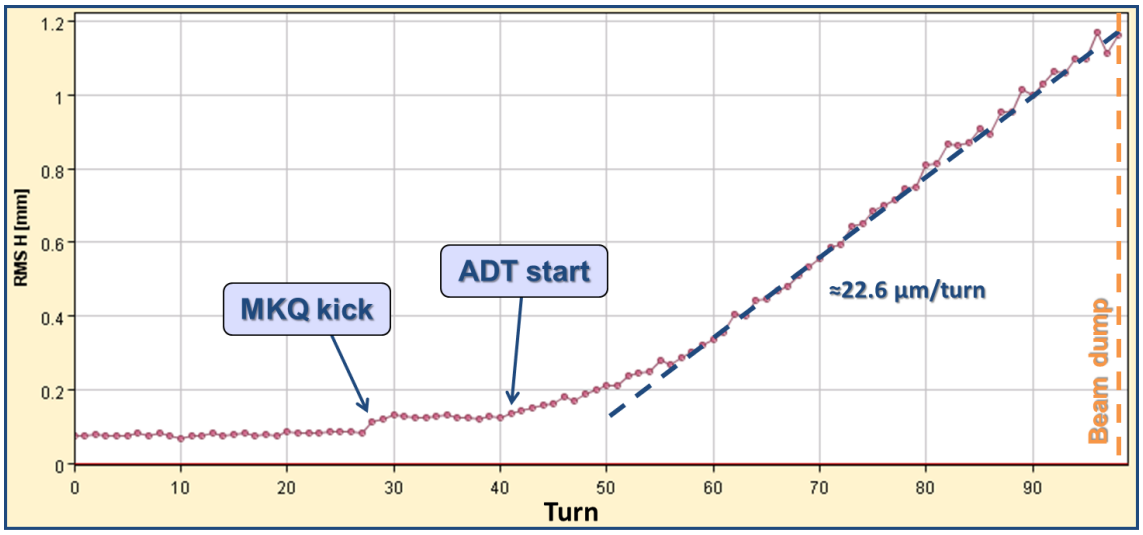


Figure 4.8.: Horizontal turn-by-turn RMS arc position after initial excitation by tune kicker (MKQ) at turn 28 and continuous excitation by ADT from turn 41 onwards. Only one bunch is excited and measured.
Measurement on 13.10.2012 06:30:30. Beam energy: 4 TeV, bunch intensity B2: $\approx 1 \cdot 10^{10}$ protons, 10 bunches. MKQ gain: 100%, ADT gain: 400%, 625 ns mode.

15 turns after the activation of the ADT. The increased available normalized kick strength results in a RMS position increase of $\approx 22.6\,\mu$m per turn until the beam is dumped at turn 100 due to too high losses.

The corresponding deflection amplitude of the ADT (per turn) can be derived with Appendix A. It is given by[9]

$$\Delta x' = \frac{22.6\,\mu\text{m} \cdot 2}{0.64 \cdot \sqrt{\beta_{\text{ADT}} \cdot (\beta_{\text{BPM,l}} + \beta_{\text{BPM,s}})}}.$$

With $\beta_{\text{ADT, B2H}} = 199\,\text{m}$, $\beta_{\text{BPM,l}} = 171.0\,\text{m}$ and $\beta_{\text{BPM,s}} = 30.9\,\text{m}$ for this case, $\Delta x' = 0.35\,\mu$rad. This corresponds to $0.35\,\mu\text{rad} \cdot \frac{4000\,\text{GeV}}{450\,\text{GeV}} = 3.13\,\mu$rad at injection energy. This value is very consistent with the expected maximal deflection amplitude of $\approx 3\,\mu$rad[10].

[9] With $\beta_{\text{ADT}}$ being the $\beta$-function at the ADT deflector, $\beta_{\text{BPM,l}}$ and $\beta_{\text{BPM,s}}$ being the $\beta$-functions at arc beam position monitors (BPMs) with large and small $\beta$-function respectively. The factor 0.64 accounts for the phase advance between the oscillations from deflections in consecutive turns. It is determined by (linear) numerical simulations for a fractional tune of $Q_x = 0.28$.

[10] The design deflection of the ADT at 450 GeV is $2\,\mu$rad with a nominal deflecting voltage of $\pm 7.5$ kV [11, p. 141]. At the moment of the test the ADT power amplifiers were new and a deflecting voltage of about $\pm 10.5$ kV is expected. Moreover, the deflection is slightly increased due to an optimized design of the deflector electrodes [94]. Hence, a maximal deflection amplitude of about $3\,\mu$rad is expected.

### 4.2.2. Conclusions and Extrapolation

The experimental studies demonstrated that the transverse damper (ADT) can excite transverse beam oscillations on very fast timescales. However, the time constant of the excitation is limited by the (mode-dependent) ADT saturation limit.

The amplitude of the initial oscillation due to the tune kicker at 450 GeV shown in Fig. 4.6 is similar to typical injection oscillations. The measured RMS position increase of $\approx 76.4\,\mu$m per turn by the ADT corresponds to an increase of the oscillation amplitude by $1\,\sigma_{\mathrm{nom}}$ in $\approx 8$ turns[11]. The situation is even more critical when considering the full (single bunch) ADT kick strength and the larger $\beta$-functions at the vertical beam 2 ADT unit ($\beta_{\mathrm{ADT,\ B2V}} = 302\,\mathrm{m}$ instead of $\beta_{\mathrm{ADT,\ B2H}} = 199\,\mathrm{m}$) for the injection of a high intensity bunch train. Then, the ADT could increase the amplitude of the injection oscillations by $1\,\sigma_{\mathrm{nom}}$ in $\approx 2.2$ turns. **The acceptance of the beam dump transfer lines ($\approx 3.0\,\sigma_{\mathrm{nom}}$) could be exceeded within $\approx 4$ turns.** This is very close to the reaction time of the machine protection systems. Thus, it is proposed to implement an automatic verification of the ADT configuration (in particular sign and bunch-spacing configuration) prior to each injection, e.g. in the software interlock system[12]. Such a check was not available during run 1.

For operation at about 6.5 TeV after the first long shutdown (LS1), the maximal increase of the oscillation amplitude is in single bunch mode limited to about $22.6\,\mu\mathrm{m} \cdot 1.88 \cdot \frac{4\,\mathrm{TeV}}{6.5\,\mathrm{TeV}} = 26.1\,\mu\mathrm{m} = 0.09\,\sigma_{\mathrm{nom}}$ per turn, based on the excitation measurement shown in Fig. 4.8. Considering the larger $\beta$-function at the vertical beam 2 ADT unit implies an increase of the oscillation amplitude by up to $0.11\,\sigma_{\mathrm{nom}}$ per turn. This is very similar to a fast power abort of the RD1 circuits with HL-LHC parameters, as discussed in Sec. 4.1.3 and can lead to a **machine critical oscillation amplitude of about $1\,\sigma_{\mathrm{nom}}$ in 9 turns.** The present machine protection systems are fast enough to protect against this failure case. However, the timescale indicates that this failure scenario is among the fastest equipment failures in the LHC. Thus, it is recommended to investigate interlock mechanisms which are redundant to the BLM system. For example the hardware beam position interlock (see Sec. 2.4.2) could provide this redundancy with an improved reaction time (turn-by-turn) and adequate thresholds for position changes on this timescale ($< 1\,\sigma_{\mathrm{nom}}$ at top energy)[13].

[11] $\frac{1.15\,\mathrm{mm}}{1.88 \cdot 76.4\,\mu\mathrm{m/turn}} \approx 8$ turns, with the nominal beam size of 1.15 mm at maximum arc $\beta$-function and 450 GeV beam energy. The scaling-factor 1.88 is needed to determine the oscillation amplitude based on the RMS position measurement, as derived in Appendix A.

[12] The injection software interlock system (injection SIS) is a comprehensive machine protection framework which allows the evaluation of complex interlock conditions prior to each injection.

[13] A turn-by-turn interlocking of the beam position difference w.r.t. the closed orbit rather than the absolute beam position may be more robust. Moreover, energy-dependent thresholds may be needed to allow typical injection oscillations while ensuring adequate protection at top energy.

# 5. Beam Losses due to Macro Particles

(Un)identified falling objects (UFOs) are one of the most relevant surprises after the LHC start-up. They have significantly affected the LHC availability and may become a major performance limitation for future LHC operation. UFOs are most likely micrometer-sized dust particles which lead to very fast beam losses with a duration of a few turns when they interact with the beam.

In 2011/12, the diagnostics for UFO events were significantly improved, dedicated experiments and measurements in the LHC and in the laboratory were made and complemented by MAD-X [88] and FLUKA [95, 96] simulations and theoretical studies. This allows extrapolations for future LHC operation and the development of dedicated mitigation measures.

## 5.1. Observations and UFO Detection

Since July 2010, in total **58 LHC fills** (see Appendix B) were prematurely terminated by the beam loss monitoring (BLM) system due to sudden beam losses with similar characteristics:

- The temporal loss profile has an (asymmetric) **Gaussian shape** with a width that is of the order of 100 $\mu$s ($\approx$ 1 LHC turn).
- The major beam losses are often **localized at unusual loss locations** with large aperture, e.g. in the arcs or at the injection kicker magnets (MKIs).
- The beam losses are not correlated to perturbations of the beam dynamics and appear often **suddenly** throughout the whole LHC cycle.

Such events were observed in the whole machine (warm and cold) and for both beams, for proton as well as for lead ion operation. They are thought to be caused by so-called (un)identified falling objects (UFOs) which are most likely micrometer-sized macro particles that lead to beam losses when they interact with the beam,

as discussed later in this chapter. Figure 5.1 shows spatial and temporal beam loss profile of a typical UFO event.

An overview of the location of the 58 UFOs that caused a beam dump is given in Tab. 5.1. More than one out of three events occurred at the MKIs, as discussed in Sec. 5.3. The number of UFO events in the arcs and the dispersion suppressors[1] could be mitigated from 2011 onwards by large-scale increases (up to a factor 5) and optimizations of the BLM dump thresholds [97].

| Run | Arc | MKI | Coll. & RP | Exp. | Other | Total |
|---|---|---|---|---|---|---|
| 2010 | 5 | 2 | 2 | 2 | 7 | 18 |
| 2011 | 2 | 11 | 0 | 5 | 0 | 18 |
| 2012/13 | 1 | 8 | 5 | 5 | 3 | 22 |
| Total | 8 | 21 | 7 | 12 | 10 | 58 |

Table 5.1.: Number of beam dumps due to UFOs in the arcs ($\geq$ half-cell 12), at the injection kicker magnets (MKIs), at collimators and roman pots[2] (while moving), at experiments (dump trigger by experiments) and at other locations (long straight sections and dispersion suppressors).

### 5.1.1. UFO Detection

Most UFO events lead to beam losses well below the BLM dump thresholds. These events are detected in real time by the *UFO Buster* application which was developed in the course of this thesis. The detection algorithm is based on the requirement that at least 2 BLMs of the same beam within a distance of 40 m measure a signal of at least $1 \cdot 10^{-4}$ Gy/s in the 640 $\mu$s running-sum[3]. In addition, each BLM signal has to pass a noise filter which requires the ratio of the loss rates in the 80 $\mu$s over the 40 $\mu$s running-sum to exceed 0.55 and the loss rates in the 320 $\mu$s over the 40 $\mu$s running-sum to exceed 0.3[4].

[1] The dispersion suppressors are the outer parts of the insertion regions. The regular dispersion function in the arcs is reduced to about zero at the interaction points in these regions.

[2] Roman pots are movable detectors that are installed around the main experiments ATLAS and CMS.

[3] The noise level is about $2 \cdot 10^{-5}$ Gy/s in the 640 $\mu$s running-sum for the arc BLMs. Some BLMs with higher noise level or background losses have an increased detection threshold or are even excluded from the UFO detection.

[4] In 2011 slightly different parameters were used for the UFO detection [98], which requires corresponding corrections when correlating data from 2011 and 2012.

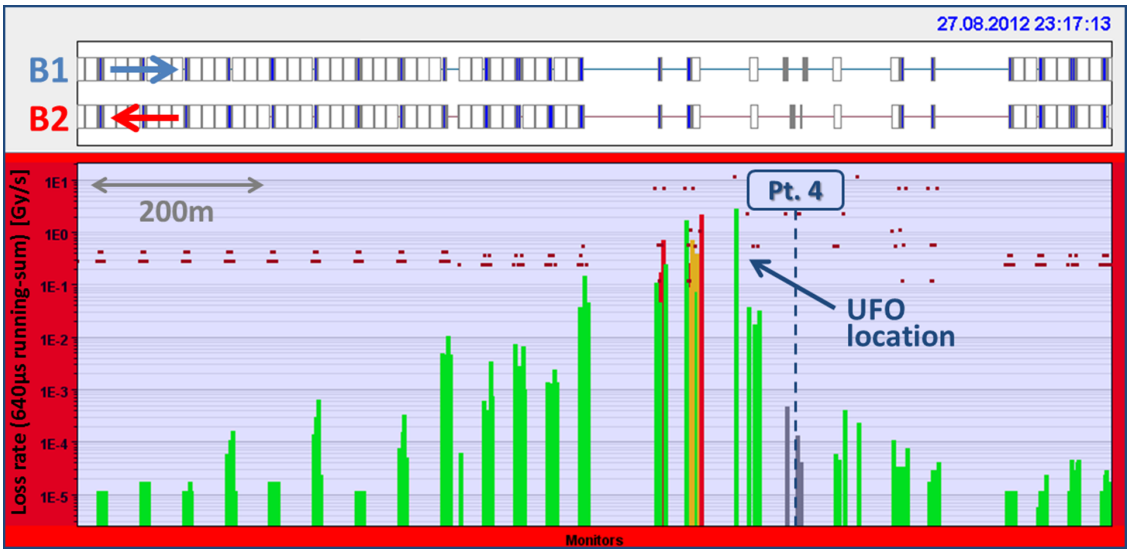


(a) Spatial loss profile.

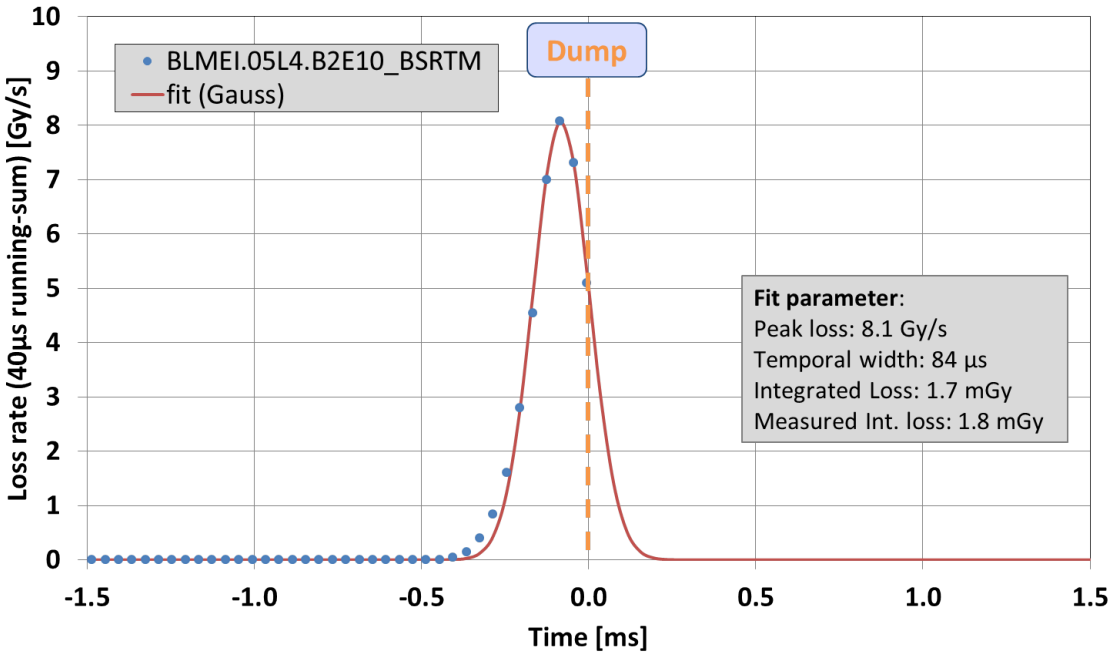


(b) Temporal loss profile.

Figure 5.1.: Spatial (a) and temporal (b) loss profile of an UFO event on beam 2 around the synchrotron light monitor (BSRT) during stable beams, measured by the LHC ring BLMs (ionization chambers). The beam losses in the 40 $\mu$s - 10 ms running-sums reached up to 219% of the corresponding thresholds when the beams were dumped.
Measurement on 27.08.2012 23:17:13. Beam energy: 4 TeV, bunch intensity: $1.6{\cdot}10^{11}$ protons, 1374 bunches per beam.

The detection thresholds are set rather wide in order to record all potentially interesting events. This results in an occasional false detection of non-UFO events. Thus, depending on the analysis, additional cuts are used which are benchmarked against a manually verified collection of reference datasets [99].

Since 2011, more than **30,000 candidate UFO events** were detected with this approach.

### 5.1.2. Spatial UFO Distribution

The spatial distribution of the UFO events shown in Fig. 5.2 underlines that UFOs occur all around the LHC. The general pattern is very similar for 2011 and 2012 data. Many events occur especially at the MKIs (see Sec. 5.3). Similarly, there is a significantly increased UFO activity in some arc half-cells, typically only for one beam; no direct correlation with the sector 34 incident (see Sec. 2.4.2) or its repair works was found. Table 5.2 gives an overview of the locations with particularly high UFO activity.

| Location | Number of UFOs in 2011 | Number of UFOs in 2012 |
|---|---|---|
| MKI.5L2.B1 | 239 | 422 |
| MKI.5R8.B2 | 248 | 343 |
| 25R3.B2 | 155 | 69 |
| 19R3.B1 | 126 | 165 |
| 28R7.B2 | 119 | 82 |
| 28L6.B2 | 73 | 33 |
| 26L3.B1 | 73 | 32 |
| 31L7.B2 | 74 | 58 |
| 28L8.B1 | 69 | 62 |
| 13R3.B1 | 69 | 53 |
| 16L3.B2 | 68 | 24 |
| 32L5.B1 | 62 | 22 |
| 25R8.B2 | 56 | 30 |

Table 5.2.: Locations with high UFO activity at top energy (more than 50 UFOs per half-cell in one year).
Only UFOs with signal in 640 $\mu$s running-sum $> 2 \cdot 10^{-4}$ Gy/s. In half-cell 19R3, additional BLMs were installed in the winter technical stop 2011/12, resulting in an increased UFO detection efficiency in this region.

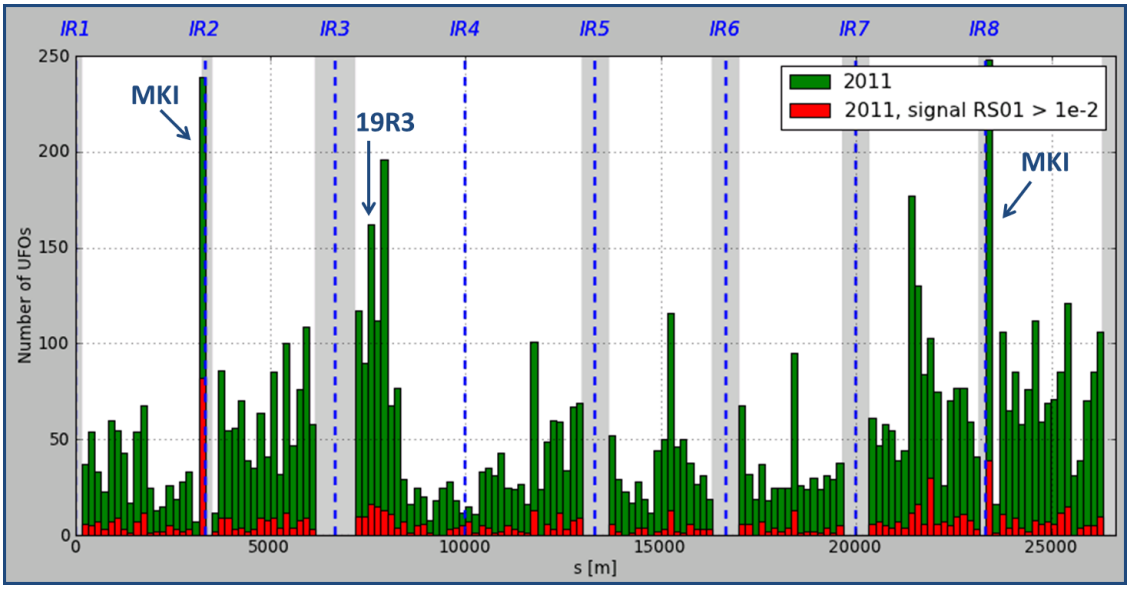


(a) 2011

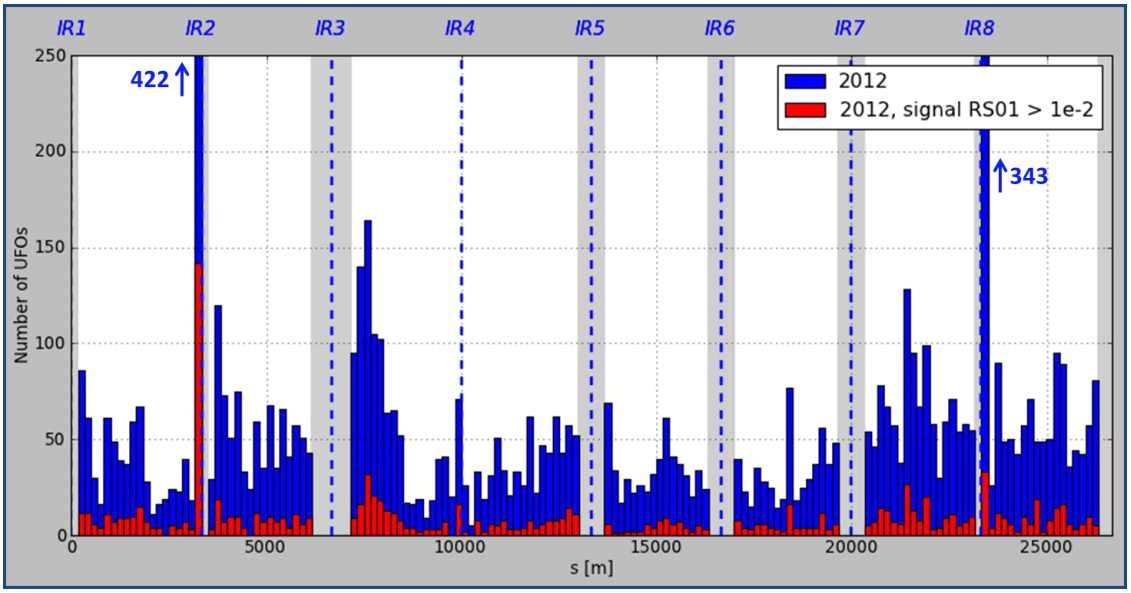


(b) 2012

Figure 5.2.: The spatial distribution around the LHC of 7430 UFOs at 3.5 TeV in 2011 (a) and 7171 UFOs at 4 TeV in 2012 (b).
UFO events during the proton runs with at least $2 \cdot 10^{-4}$ Gy/s in the 640 $\mu$s running sum are considered. The bins have a width of 167 m $\hat{=}$ 3.1 arc half-cells. The dashed blue lines indicate the centers of the insertion regions. Gray areas are excluded from the analysis.

### 5.1.3. Bunch-by-Bunch Diagnostics

About one third of the protons that interact with a dust particle are subject to elastic scattering processes (see Sec. 5.3.5). These particles are typically deflected under a small angle, such that beam losses can be observed at all aperture restrictions, mainly the betatron collimation region in IR7. The results of related simulations are discussed in Sec. 5.3.5. Dedicated diamond BLMs in IR7 (see Sec. 2.3.3) are used since May 2012 to improve the temporal resolution for UFO events. Figure 5.3 shows a corresponding measurement of the temporal loss profile of the UFO shown in Fig. 5.1 with nanosecond time resolution. Figure 5.3a confirms that the losses are decreasing in the turn before the beam dump. Figure 5.3b shows that all bunches contribute equally to the beam losses, as expected for a macro particle interaction.

## 5.2. UFOs in the LHC Arcs

In particular, UFOs in the LHC arcs could be a major limitation for future LHC operation (see Sec. 5.4). A detailed analysis of the observations and the main studies are presented in this section.

### 5.2.1. UFO Statistics

UFOs are the only significant beam loss mechanism in the LHC arcs ($\geq$ half-cell 12) for normal proton operation. Thus, arc UFO events can be very clearly detected by the approach explained in Sec. 5.1.1. During 2011/2012 proton operation, in total 6321/6237 arc UFO events[5] below the BLM dump thresholds were recorded.

Figure 5.4a shows the distribution of the dose of the UFO events; **the number of UFOs with a dose above a certain threshold is seen to be inversely proportional to this threshold**[6]. Since the maximal observable dose is limited by the BLM dump thresholds, the number decreases rapidly above $\approx 10^{-4}$ Gy. A similar distribution is measured for the volume of dust particles in the magnet test halls (see Fig. 5.4b). Since according to the theoretical model [102], dust particle volume and resulting beam losses are almost proportional, **the observed UFO event distribution is consistent with the distribution of dust particles.**

The evolution of the arc UFO rate in stable beams from April 2011 until the end of the first LHC run is shown in Fig. 5.5. Whereas the beam intensity was increased

[5] Signal in 640 $\mu$s running-sum $> 2 \cdot 10^{-4}$ Gy/s, beam intensity $> 10^{11}$ protons.
[6] This distribution is very constant over time [98, 100, 101].

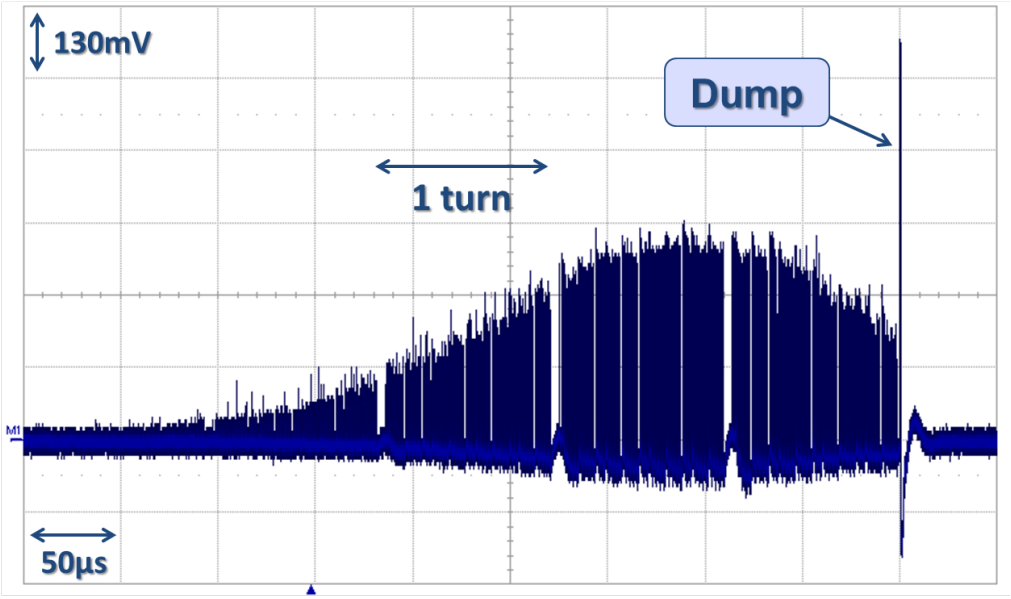


(a) 50 $\mu$s/div.

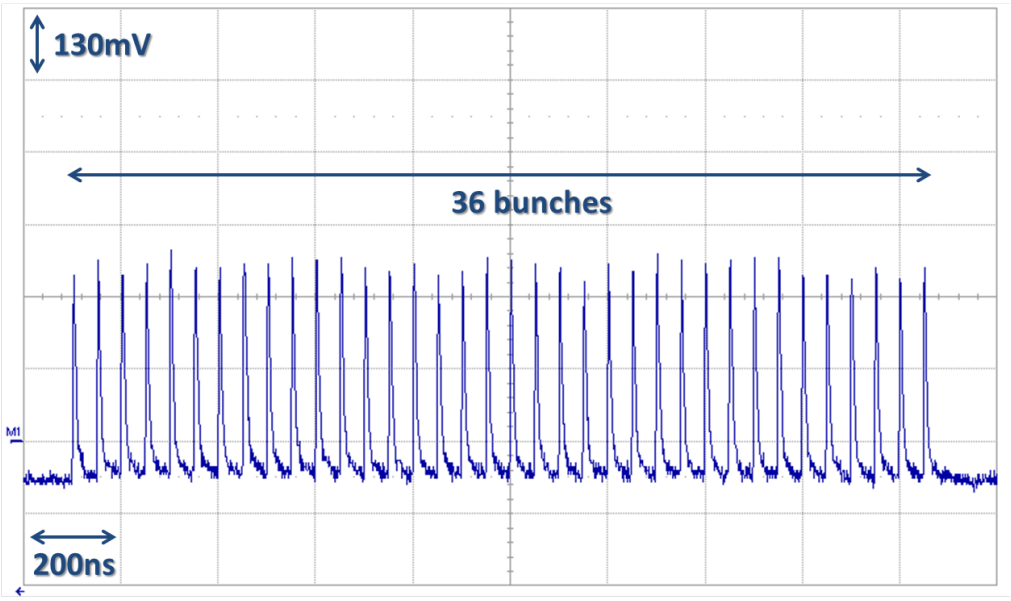


(b) 200 ns/div.

Figure 5.3.: Signal of beam 2 diamond BLM in IR7 versus time with nanosecond resolution for the UFO shown in Fig. 5.1. The losses start about 5 turns before the beam dump. The beam free abort gap is clearly visible (a). The zoom (b) shows that all bunches contribute equally to the beam losses, as expected for a macro particle interaction.
Measurement on 27.08.2012 23:17:13. Beam energy: 4 TeV, bunch intensity: $1.6{\cdot}10^{11}$ protons, 1374 bunches per beam.

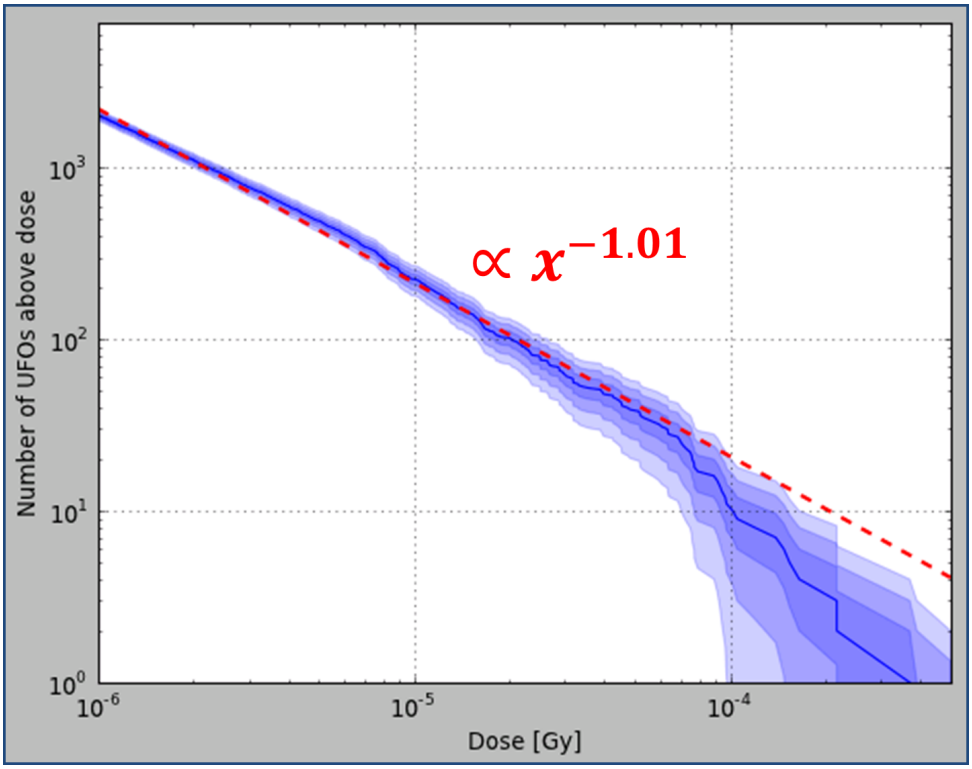


(a) Dose distribution of UFO events.

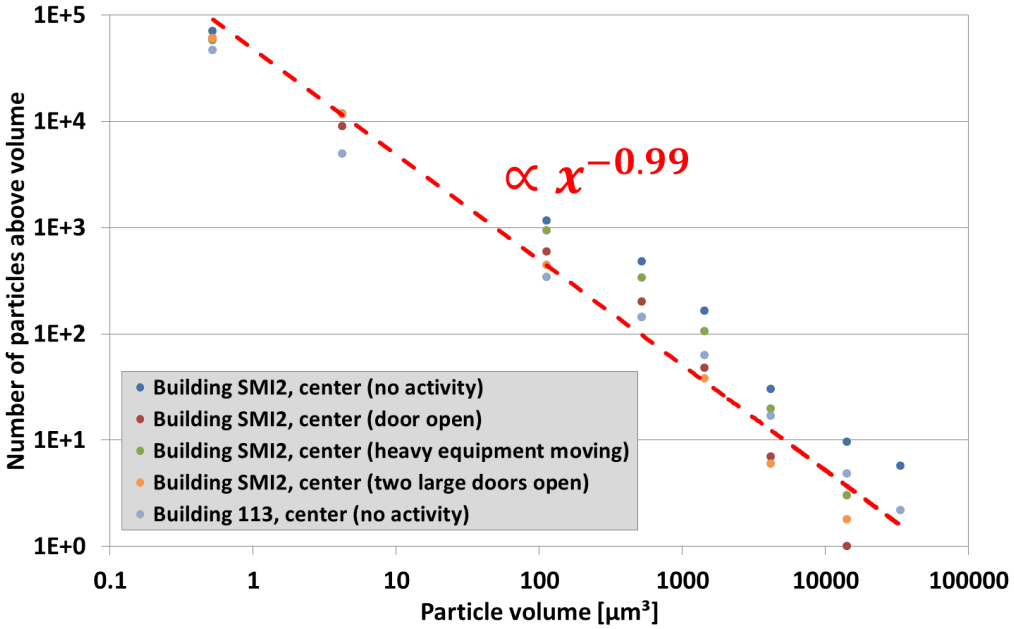


(b) Distribution of dust particle size (based on data from J.M. Jimenez).

Figure 5.4.: The number of UFOs with a dose exceeding the value on the horizontal axis (a) and the distribution of the volume of dust particles in the magnet test halls (b).

For (a) 6416 arc UFOs ($\geq$ half-cell 12) at flat top in fills with 1374/1380 bunches between 14.04.2011 and 06.12.2012 are considered. For the fit, only UFO events with a dose $< 10^{-4}$ Gy are taken into account. The blue areas indicate a fluctuation of 1, 2 and 3 standard deviations around the observed distribution.

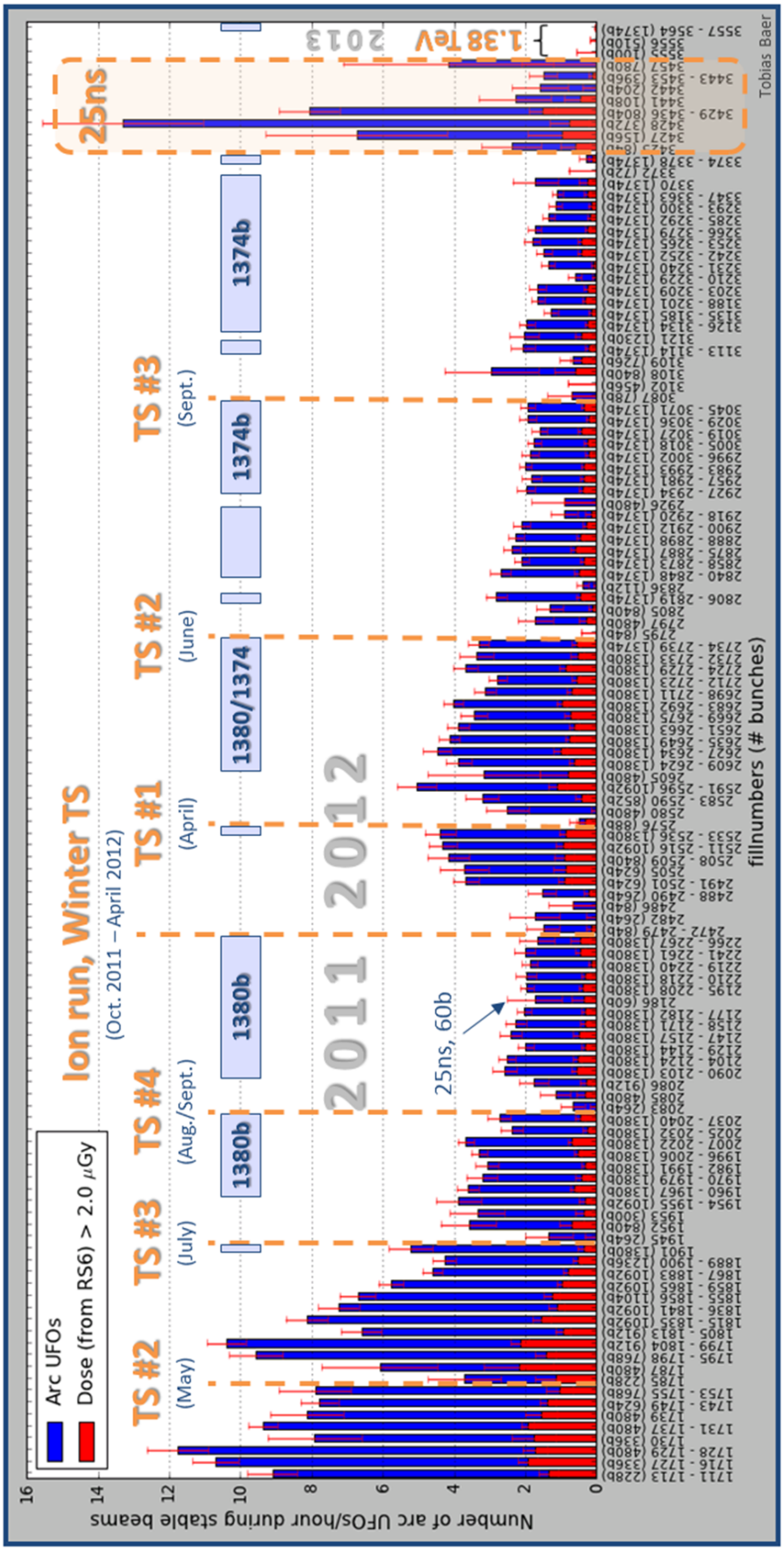


Figure 5.5.: The arc UFO ($\geq$ half-cell 12) rate in stable beams. A clear conditioning effect is observable throughout 2011 and 2012 with a deconditioning over the 2011/12 winter technical stop. The rate is decreased in the intermediate intensity fills after the technical stops (TS). The 25 ns fills have a significantly increased UFO activity. No UFO was observed during the 1.38 TeV run in February 2013.

9406 UFOs in all proton-proton fills with at least one hour of stable beams since 14.04.2011 until the end of the 2012/13 run are taken into account. Up to 5 consecutive fills with the same number of bunches are grouped. Signal in 640 $\mu$s running-sum $> 2 \cdot 10^{-4}$ Gy/s. Only UFOs with signal in 320 $\mu$s running-sum / signal in 80 $\mu$s running-sum $\geq 0.45$ to correct for algorithm changes (see Sec. 5.1.1).

from 228 to 1380 bunches throughout 2011, a **clear conditioning effect** is observable, which leads to a decrease of the arc UFO rate from $\approx$ 10 events/hour to $\approx$ 2 events/hour. **Over the winter technical stop 2011/12, a deconditioning is observable** leading to a $\approx$ 2.5 times increased arc UFO rate in the beginning of 2012[7]. Throughout 2012, the arc UFO rate decreased from $\approx$ 5 events/hour to $\approx$ 1 event/hour. In the fills with 25 ns bunch-spacing, the UFO activity is significantly increased, as discussed in Sec. 5.4.2. During the intermediate energy run in 2013, not a single UFO was observed in about 17.5 hours at 1.38 TeV with 1374 bunches. This indicates a strong scaling of the UFO activity with beam energy, as discussed in Sec. 5.4.3.

During a fill, the arc UFO rate remains almost constant in stable beams with a slight tendency to increase throughout the fill, as shown in Fig. 5.6[8].

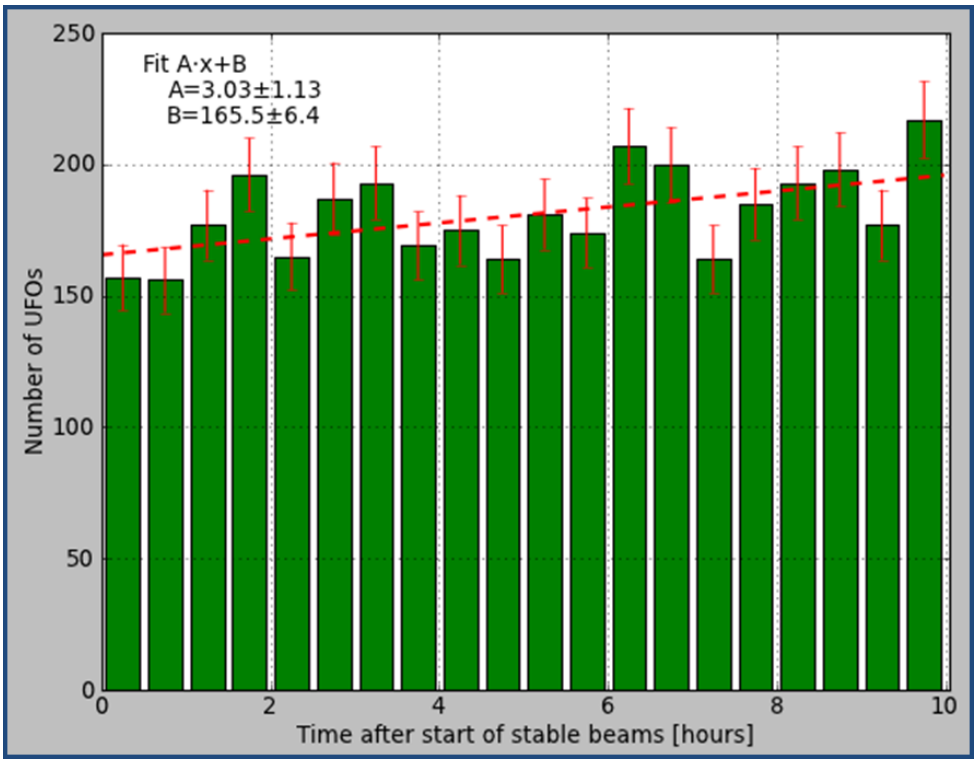


Figure 5.6.: The arc UFO ($\geq$ half-cell 12) activity throughout stable beams.
3856 arc UFOs in 108 proton fills with at least 10 hours of stable beams and over 500 bunches per beam between 14.04.2011 and 06.12.2012 are taken into account. Only UFOs with signal in 640 $\mu$s running-sum $> 2 \cdot 10^{-4}$ Gy/s.

[7] The increase in top beam energy from 3.5 TeV in 2011 to 4 TeV in 2012 can, according to the FLUKA simulations (see Sec. 5.2.3), only explain an increase of the UFO rate of about 30%. Over the winter technical stop 2011/12, the cold machine parts were warmed up to about 80 K; the beam vacuum was (with few exceptions) constantly maintained.

[8] Throughout stable beams the most relevant changes are a decrease of beam intensity and an increase of the transverse emittance. The latter implies an increase of the UFO rate [103].

The dependence of the UFO rate on the beam intensity can be determined from the fast intensity ramp up achieved in 2012 without being biased by the conditioning effect discussed above. In agreement with previous studies [97], **the rate of detectable UFO events is proportional to the beam intensity for small intensities. Above several hundred bunches, the effect saturates** as shown in Fig. 5.7. This is qualitatively consistent with the theoretical model [102]. An influence of the bunch intensity on the UFO rate (apart from the described effect on the total intensity) was not observed [104].

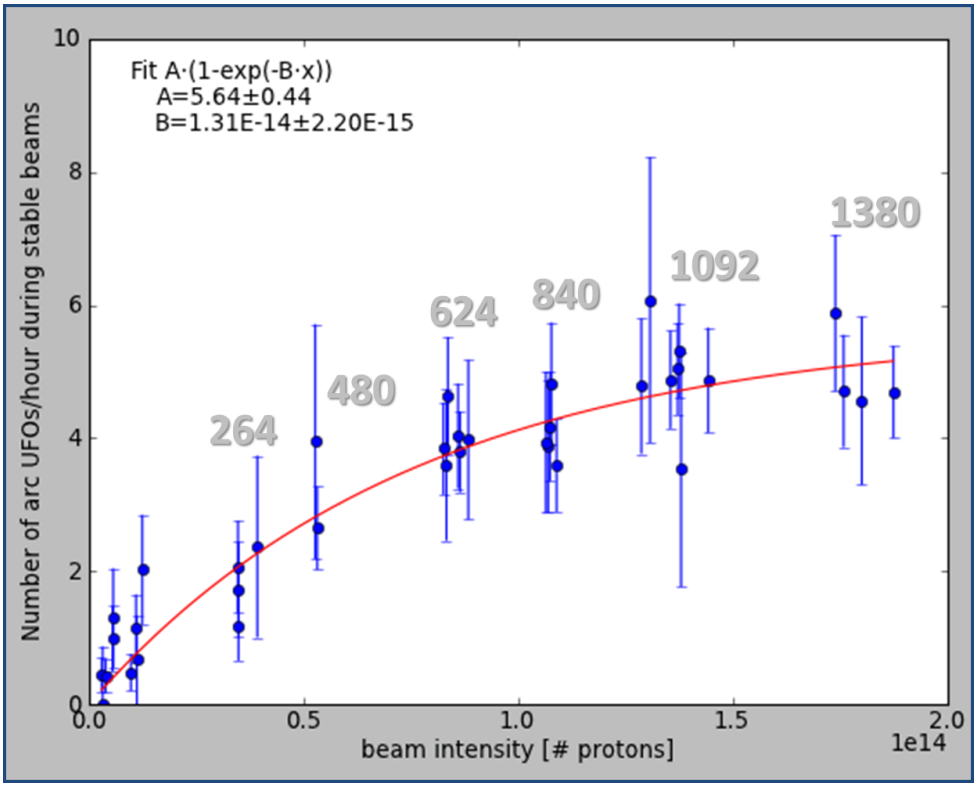


Figure 5.7.: The arc UFO ($\geq$ half-cell 12) rate as a function of the beam intensity (intensity at start of stable beams, averaged over both beams). The gray numbers indicate the number of bunches.
667 UFOs in 37 fills with at least 1 hour of stable beams during the intensity ramp up between 05.04.2012 and 10.05.2012 are taken into account. Only UFOs with signal in 640 $\mu$s running-sum $> 2 \cdot 10^{-4}$ Gy/s.

The temporal structure of the UFO events can be determined from the various running-sums of the BLM data. As shown in Fig. 5.1b (and discussed in more detail in Sec. 5.2.2), typically an (asymmetric) Gaussian loss profile is observed and expected. Figure 5.8 shows the distribution of the temporal width of UFO events assuming a Gaussian loss profile. For many UFOs, the temporal width is in the order of an LHC revolution period (89 $\mu$s), or even faster, making UFOs one of the fastest beam loss mechanisms in the LHC (see Sec. 3.4).

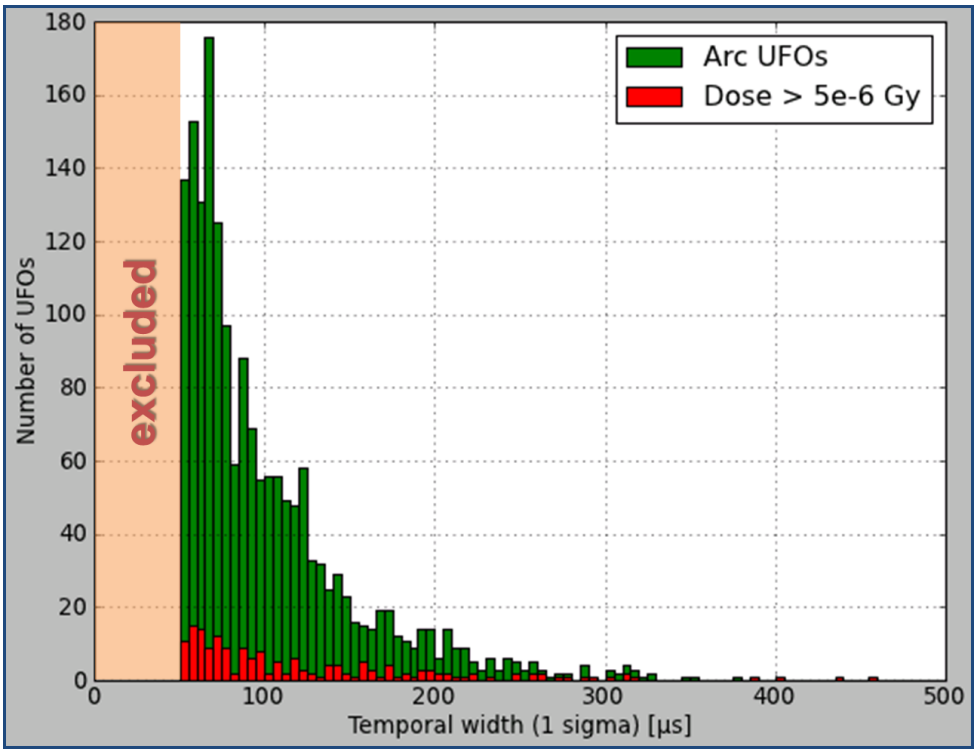


Figure 5.8.: Distribution of temporal width from Gaussian fit of UFO events.
1753 arc UFOs ($\geq$ half-cell 12) at 4 TeV operation with 1374/1380 bunches are taken into account. UFO events with a temporal width $< 50\,\mu$s or a peak loss rate of the fit $< 1 \cdot 10^{-3}\,$Gy/s are excluded from the analysis to avoid bias from the noise filter (see Sec. 5.1.1).

### 5.2.2. Macro Particle Model

These observations can be explained by macro particles that lead to beam losses when they interact with the beam (see Sec. 5.2.4 for alternative attempts to explain the observations). Beam losses due to interactions with macro particles were observed at many electron and antiproton storage rings, e.g. PF-AR [105], HERA and DORIS [106], PEP-II [107], CESR [108], TRISTAN [109], and others [110]. Since macro particles are ionized by the beam (resulting in a positive charging of the macro particle), they are attracted by a negatively charged beam. This can eventually lead to a stable accumulation of macro particles around the beam and result in a constant reduction of the beam lifetime. For positively charged beams, indications for beam losses due to macro particles were observed for example at ISR [111] but had (before the LHC) never been a limitation for beam operation.

The contamination of the LHC vacuum chamber with macro particles is generally expected, especially after the sector 34 incident [112]. However, the distribution of UFOs around the whole LHC, the missing correlation of the UFO activity with the sector 34 repairs (see Sec. 5.1.2), the continuous UFO activity even 3 year after the

LHC start-up and the dependence on bunch-spacing (see Fig. 5.5) indicate a beam related production mechanism of UFOs. For the LHC arcs two main production mechanisms are imaginable:

- **Electric discharges/sparking:** Electric discharges/sparking are a known production mechanism for macro particles: high-intensity bunches can induce strong electromagnetic fields in the vacuum chamber walls. This may lead to sparking at electrical incontinuities or sharp edges and a consequent detaching of particles from the surface. In the PF-AR electron storage ring, macro particles were deliberately generated for study purposes by electric discharges [105]. In particular the RF fingers[9] installed in between all LHC magnets are a likely location for electric sparking.
- **Particles frozen to the beam-screen:** Since the vacuum chamber in the LHC arcs is at cryogenic temperatures, particles that are frozen to the aperture may be released e.g. by beam induced heating.

Other known macro particle sources, which are not present in the LHC arcs, are distributed ion pumps [106], movable devices (also observed at LHC, see. Tab. 5.1) and the LHC injection kicker magnets (see Sec. 5.3).

A macro particle that is released from the aperture and is accelerated towards the beam only by gravitation with $g = 9.81\,\frac{\mathrm{m}}{\mathrm{s}^2}$, would reach the beam center (distance $s = 22\,\mathrm{mm}$) after $t = \sqrt{\frac{2 \cdot s}{g}} = 67\,\mathrm{ms}$ with a velocity $v = g \cdot t = 0.66\,\frac{\mathrm{m}}{\mathrm{s}}$. Assuming that the particle just falls through the beam would result in a Gaussian temporal loss-profile with a width between 190 $\mu$s and 590 $\mu$s[10]. As depicted in Fig. 5.8, UFOs with a temporal width down to 50 $\mu$s were observed, which indicate a **more complex macro particle dynamics.**

Dedicated simulations of the dynamics and interactions of macro particles falling into the circulating LHC proton beam were performed [102]. An important conclusion is that the macro particles are charged up positively by the proton beam and are therefore deflected or even repelled by the beam. Many predictions are described in [102], among them that the typical loss duration is of the order of 1 ms and that the temporal loss profile has an asymmetry due to the deflection of the macro particle by the beam, which increases with the macro particle size, as shown in Fig. 5.9a.

[9] RF fingers are sliding electrical contacts between the beam screens of neighboring LHC magnets to ensure continuous electrical conductivity.

[10] Assuming a Gaussian transverse beam distribution with a normalized emittance between 2.0 $\mu\mathrm{m} \cdot \mathrm{rad}$ and 3.5 $\mu\mathrm{m} \cdot \mathrm{rad}$ and $\beta$-functions between 32.5 m and 184.0 m, which is the typical parameter-range for the LHC.

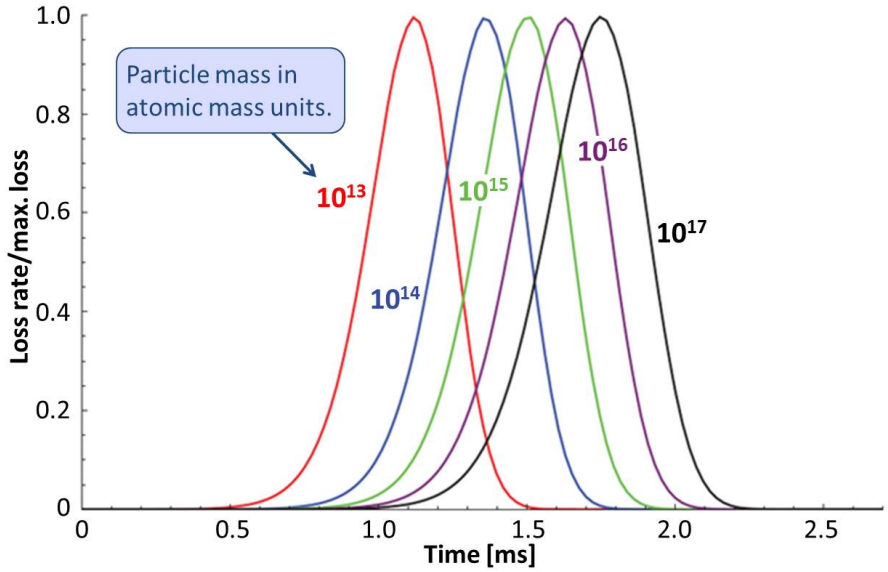


(a) Temporal loss profiles as predicted by the theoretical model (courtesy of N. Fuster Martinez et al. [102]).

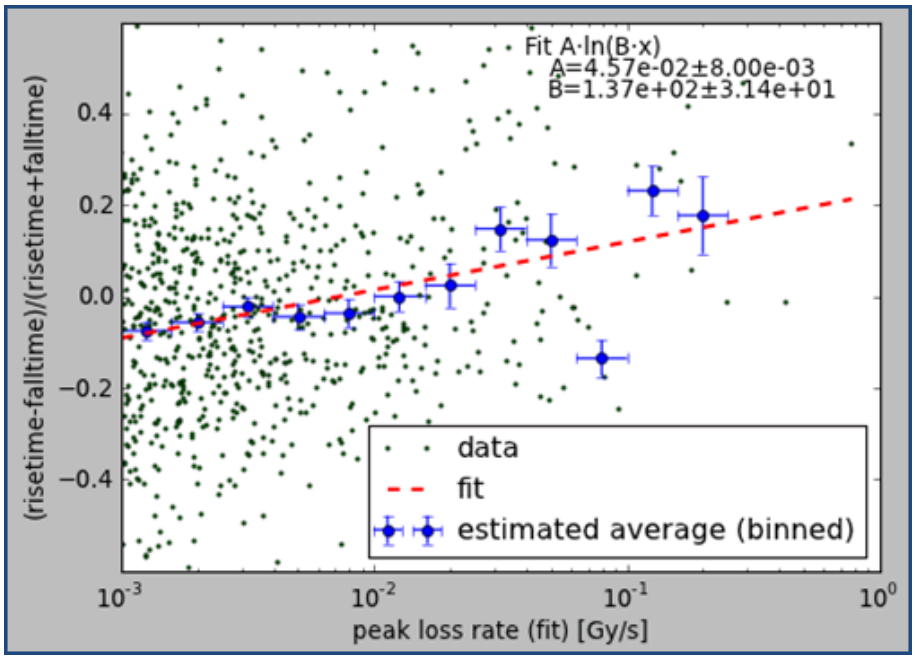


(b) Measured asymmetry.

Figure 5.9.: Normalized beam loss rate for macro particles with different masses and a beam intensity of $1.6 \cdot 10^{14}$ protons as predicted by the theoretical model (a). Measured asymmetry as function of the peak loss rate (b). For (b) 699 arc UFOs ($\geq$ half-cell 12) at 4 TeV operation with 1374/1380 bunches are taken into account (green dots). Only UFO events with an average temporal width $> 50\,\mu$s and a peak loss rate of the fit $> 1 \cdot 10^{-3}$ Gy/s are considered. The blue points (with horizontal and vertical bars) indicate the arithmetic average of the data within the bins defined by the horizontal bars. The vertical bars indicate the statistical $1\,\sigma$ uncertainty of the estimated average. The fit is based on the data represented by the green dots.

From the beginning of 2012, the BLM study buffer with 80 $\mu$s time resolution was used (see Sec. 2.3.3) to observe the predicted asymmetry for UFO events below the BLM dump thresholds. To quantify the observations, an asymmetric Gaussian function with different temporal widths $\sigma_r$ for the rising edge and $\sigma_f$ for the falling edge were fitted to the measured loss profiles[11]. The asymmetry ($\frac{\sigma_r-\sigma_f}{\sigma_r+\sigma_f}$) is plotted in Fig. 5.9b as a function of the peak loss rate of the UFO events. As predicted by the theoretical model, the average asymmetry increases with the peak loss rate (which increases with the macro particle mass, as shown in [102]).

### 5.2.3. FLUKA Simulations

Simulations of the (inelastic) interactions between protons and UFOs[12] and the induced particle showers were performed using the multi-particle transport code FLUKA [95, 96, 113]. In Fig. 5.10, typical BLM dose patterns measured by the standard BLMs at the arc quadrupoles are compared to simulation results. The simulations reveal that with the standard BLM distribution of six BLMs at each arc quadrupole magnet the precise UFO location within a half-cell cannot be localized. To improve the spatial resolution, four additional BLMs were installed at the three dipole magnets in half-cell 19R3 in early 2012. As indicated by the simulations, with these new BLMs, significant differences in spatial loss patterns can be observed for different loss locations (see Fig. 5.10). UFO events observed in half-cell 19R3 in 2012 indeed exhibit different loss patterns, suggesting that **UFOs originate from various positions across the arc half-cell** [104]. In particular, loss pattern suggesting UFO locations close to the magnet interconnections were observed as well as loss pattern suggesting UFO locations inside dipole magnets [114].

The FLUKA simulations moreover predict the density of the energy deposited in the superconducting magnet coils due to the proton-UFO interaction. Figure 5.11 shows the peak energy density per inelastic proton-UFO interaction at *Pos #1* (see layout in Fig. 5.10) in the downstream dipole magnets. The highest energy density is caused by the neutral collision products of the proton-UFO interactions [113], which impact the magnet $\approx 11$ m downstream of the UFO location due to the geometrical bending of the magnet and explain the peak at $\approx 842$ m in Fig. 5.11. Fig. 5.11 also shows that **the peak energy density per inelastic proton-UFO interaction is about a factor 4.2 higher for 7 TeV operation than for 3.5 TeV operation.**

The peak energy density in the magnet coils is compared to the magnet quench level in Sec. 5.4.3.

[11] The measured loss profiles are corrected for the BLM time response.
[12] For the FLUKA simulations Fe-particles are assumed.

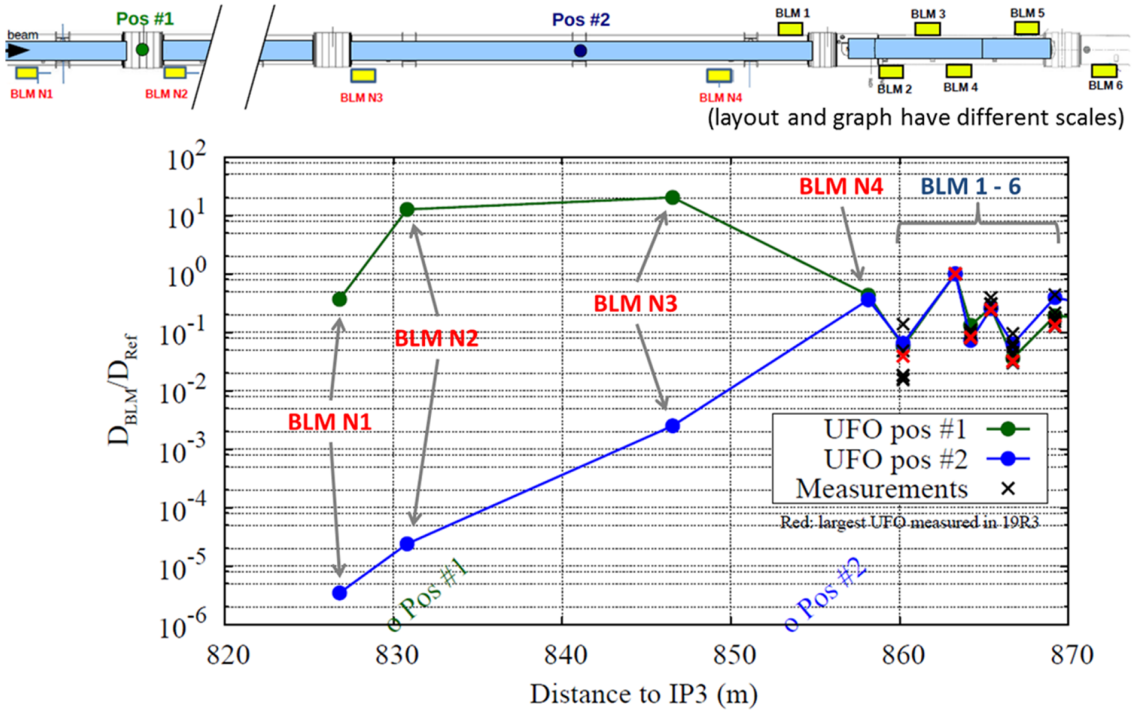


Figure 5.10.: Simulated and measured BLM dose patterns for UFO-induced beam losses in standard arc half-cell 19R3. Simulations for two potential UFO locations (*Pos #1*, *Pos #2*) are shown. The signals at the standard quadrupole BLMs (BLM 1 - 6) and the additional diagnostics BLMs (BLM N1 - N4) are normalized to the highest quadrupole BLM signal (courtesy of A. Lechner et al. [113]).

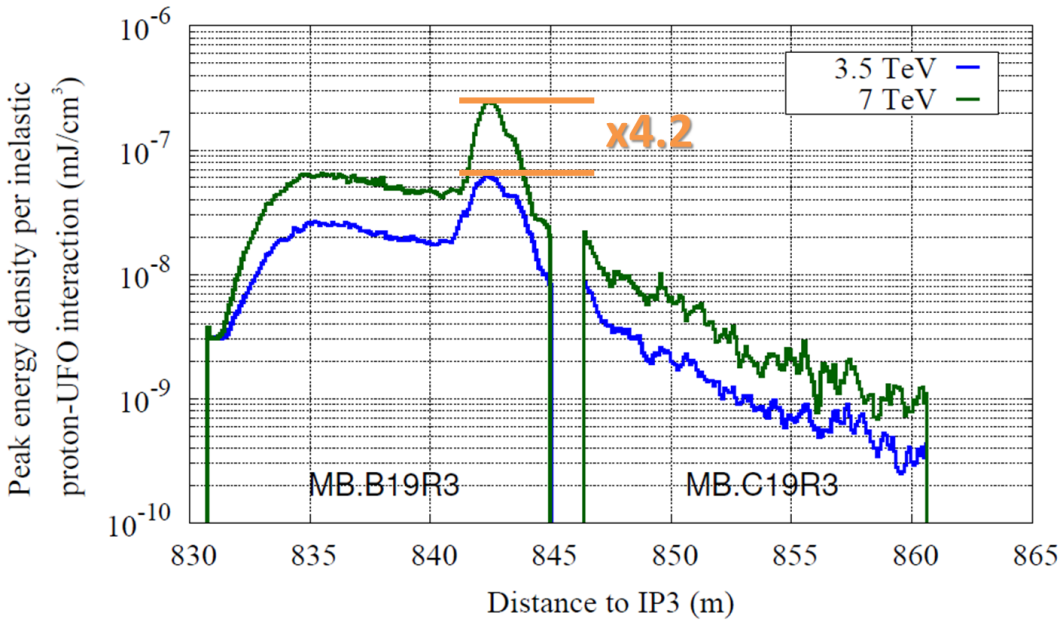


Figure 5.11.: Peak energy density per inelastic proton-UFO interaction at *Pos #1* (see Fig. 5.10) in the downstream dipole magnets simulated with FLUKA (courtesy of A. Lechner et al. [113]).

### 5.2.4. Alternative Attempts of Explanation

UFO events were not anticipated before the start-up of the LHC and various explanations for the fast beam loss events were investigated when the first UFO events occurred.

In the LHC arcs, the available aperture at 4 TeV exceeds $55\,\sigma_{\mathrm{nom}}$ everywhere. With the global limitation of the aperture by the collimators to $4.3\,\sigma_{\mathrm{nom}}$ in 2012 and the available beam instrumentation, a local impact of primary protons on the aperture in the LHC arcs as explanation of the UFO events can be excluded with certainty.

In order to explain the UFO events by an increased vacuum pressure, an enormous pressure rise would be required: for the UFO event on 05.10.2012 at 06:19:41 (see Appendix B) a peak loss of 0.74 Gy/s was measured by the BLMs. According to FLUKA simulations of beam-gas interactions, a uniform hydrogen density of $\frac{N_{H_2}}{V} = 2.4 \cdot 10^{20}\,\frac{\mathrm{H_2}}{\mathrm{m^3}}$ is needed to explain this BLM signal[13] [115]. This corresponds to a pressure (at $T = 5\,\mathrm{K}$) of

$$p = \frac{N_{H_2}}{V} \cdot k \cdot T \approx 1.7 \cdot 10^{-4}\,\mathrm{mbar}, \tag{5.1}$$

where $k$ is the Boltzmann-constant.

Typically, the pressure in the LHC arcs is of the order of $10^{-10} - 10^{-9}$ mbar, and the nominal $H_2$ density is below $1 \cdot 10^{15}\,\frac{\mathrm{H_2}}{\mathrm{m^3}}$ [11, p. 340]. Typical time constants for pressure changes during stable beams are in the order of a second. There is no known mechanism which could explain very fast pressure perturbations by many orders of magnitude in the LHC arcs during stable beams, as needed to explain the beam losses from UFO events. Consequently, pressure perturbations are not considered as explanation for the observed UFO events.

As explained in Sec. 2.4, an electron-cloud can build up on $\mu s$ timescales in the LHC arcs and lead to subsequent beam losses. However, an electron-cloud builds up along the bunch trains and significantly decays in gaps in the filling pattern, resulting in bunch-to-bunch variations of the beam losses [116]. As shown in Fig. 5.3, this is not the case for UFO events, where all bunches contribute equally to the beam losses.

In summary, apart from the dust particle model there are no (known) plausible explanations for the UFO observations.

[13] With $N_p = 1.96 \cdot 10^{14}$ protons beam intensity for the UFO event. The value is slightly overestimated by about 20% - 30%, because the FLUKA simulations are for 3.5 TeV beam energy, whereas the UFO occurred at 4 TeV.

## 5.3. UFOs at the Injection Kicker Magnets

With 21 beam dumps since 2010 (see Tab. 5.1), the UFOs at the injection kicker magnets (MKIs, see Sec. 2.3.1) had the largest impact on LHC operation. Thus, an intensive study program was launched in 2011. The main observations and results are presented in the following. The mitigation strategies are discussed in Sec. 5.5.

### 5.3.1. UFO Statistics

Out of the 21 MKI UFO events that caused a beam dump, 16 occurred at top energy, but only 5 during stable beams (see Sec. 2.4.1). 17 events occurred at MKID in IR2 (MKID.5L2, see Annex B).

During 2011/12 proton operation, in total 2041/1953 UFO events[14] below the BLM dump thresholds were recorded at the MKIs, which represent about 0.06% of the LHC length, compared to 6321/6237 UFO events in the LHC arcs ($\geq$ half-cell 12), which represent 72% of the LHC length (see Sec. 5.2.1) [117]. This underlines that there is a particularly high UFO activity around the MKIs, as also indicated by Tab. 5.2 and Fig. 5.2.

Out of the 3994 MKI UFO events, 2026 (51%) were recorded at injection energy, 1054 (26%) during the ramp and 914 (23%) at top energy. 1375 events (34%) occurred at the MKIs for beam 1 in IR2 and 2619 (66%) at the beam 2 MKIs in IR8. The spatial BLM patterns show clearly that the MKI UFOs occur always on the beam passing through the magnet (beam 1 in IR2 and beam 2 in IR8)[15] [104].

Figure 5.12 shows the number of MKI UFOs per fill in proton operation between 2011 and 2013. A conditioning of the MKI UFO rate from about 8 MKI UFOs per fill in 2011 to about 2 MKI UFOs per fill at the end of 2012 is observable[16].

In contrast to arc UFOs (see Fig. 5.6), **most MKI UFOs occur in the beginning of a fill; typically within $\approx$ 30 minutes after the last injection**, as illustrated in Fig. 5.13. Throughout stable beams, the MKI UFO events are rather rare.

[14] Signal in 640 $\mu$s running-sum $> 2 \cdot 10^{-4}$ Gy/s, beam intensity $> 10^{11}$ protons.

[15] This excludes e.g. the nearby vacuum valves as potential UFO source, as they are installed on the beam pipes for both beams.

[16] Around technical stop #3 in 2011, the UFO activity at the MKID.5L2 was temporarily strongly increased, leading to three beam dumps on 16.07.2011. No apparent reason for the increased activity could be identified [118].

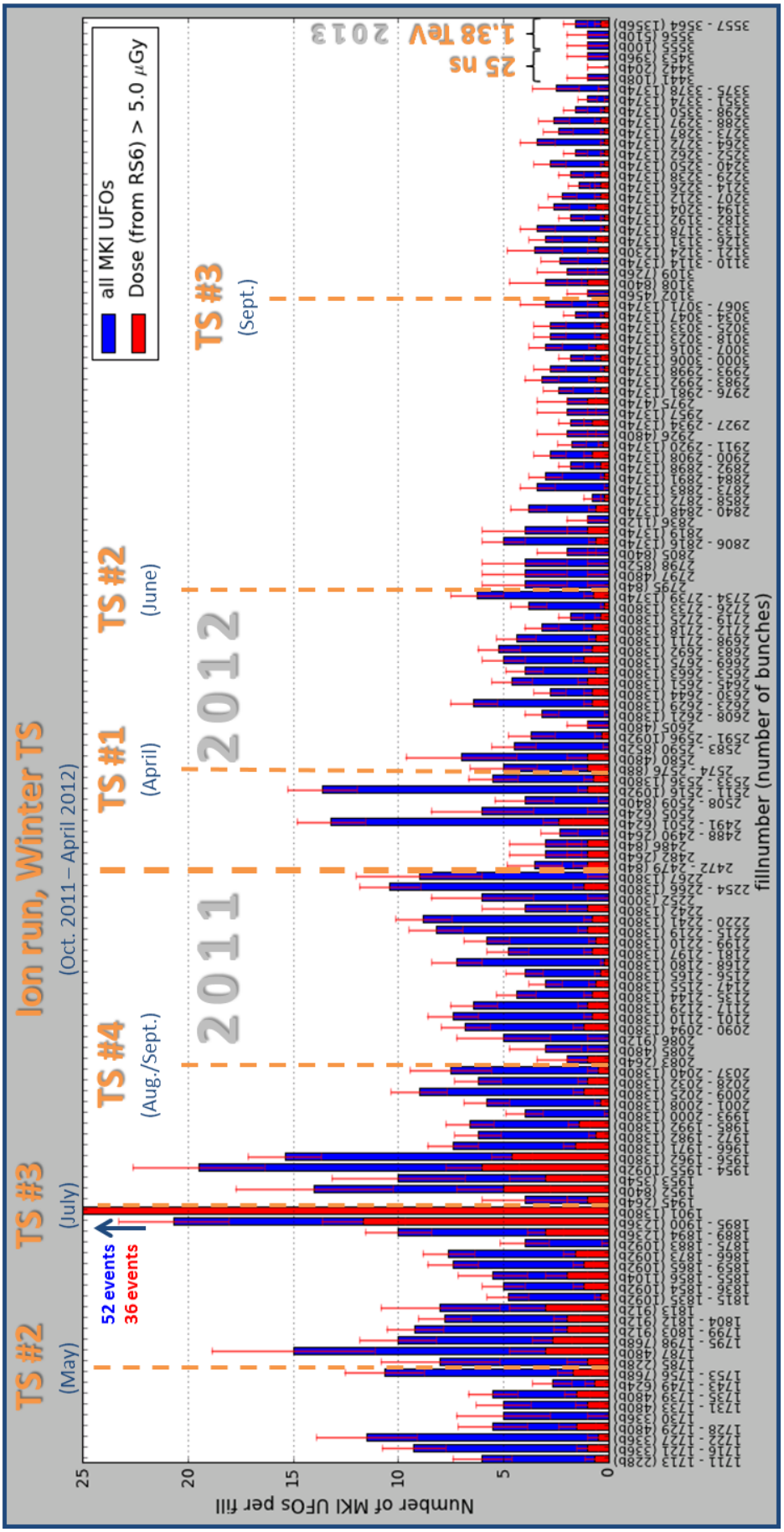


Figure 5.12.: The number of MKI UFOs per fill. A conditioning effect from 2011 to the end of 2012 is observable. No particularly high MKI UFO activity is observed in the 25 ns physics fills.
2349 MKI UFOs in all proton physics fills with at least 3 hours at top energy since 14.04.2011 until the end of the 2012/13 run are taken into account. Only UFOs with signal in 640$\mu$s running-sum $> 2 \cdot 10^{-4}$ Gy/s and with signal in 320$\mu$s running-sum / signal in 80$\mu$s running-sum $\geq 0.45$. Since technical stop #3 in 2011, 8 additional BLMs are installed to improve the diagnostics for MKI UFOs.

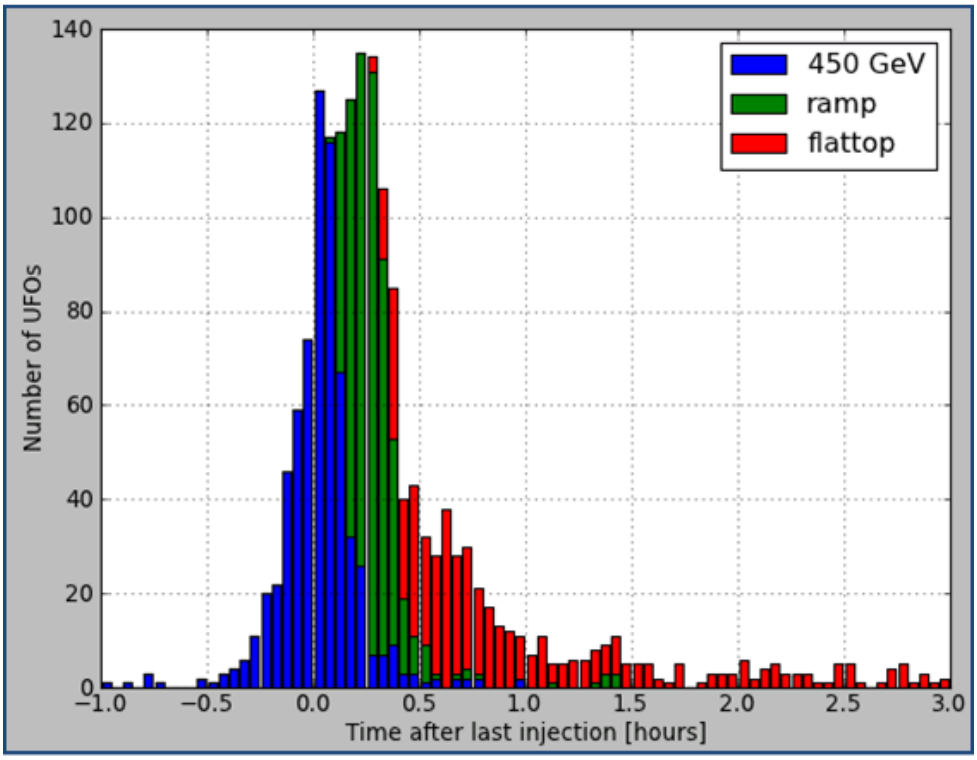


Figure 5.13.: The time of the occurrence of MKI UFOs w.r.t the last injection.
1694 MKI UFOs in 319 proton physics fills between 14.04.2011 and 06.12.2012 are taken into account. Only fills which lasted at least 3 hours after the last injection are considered. Only UFOs with signal in 640 $\mu$s running-sum $> 2 \cdot 10^{-4}$ Gy/s and beam intensity $> 10^{11}$ protons.

This implies a difference in the production mechanisms of MKI UFOs and arc UFOs, which is underlined by a different dose distribution of the UFO events: as shown in Fig. 5.4a, the number of arc UFOs $N_{\mathrm{UFO}}(d)$ with a dose $> d$ is observed to be inversely proportional to this dose: $N_{\mathrm{UFO}}(d) \propto d^{-1}$. In contrast to that, the number of MKI UFOs scales with $d^{-0.38}$ and $d^{-0.70}$ in IR2 and IR8, respectively. As illustrated in Fig. 5.14 this dose distribution results in a particularly large number of UFO events with high BLM signal for IR2 and leads to the large number of beam dumps due to UFOs at the IR2 MKIs.

In order to improve the diagnostics for MKI UFOs, four additional BLMs were installed around the MKIs for each beam in the third technical stop in 2011, resulting in a very dense BLM distribution around the MKIs, as illustrated in Fig. 2.5. This allows (together with the FLUKA simulation explained in Sec. 5.3.4) to determine in which particular MKI an UFO occurred. Figure 5.15 shows the distribution of UFOs among the different MKI magnets in IR2 and IR8. Whereas the UFO activity in IR2 is dominated by UFO events in MKID, the distribution is more balanced among the four MKIs in IR8.

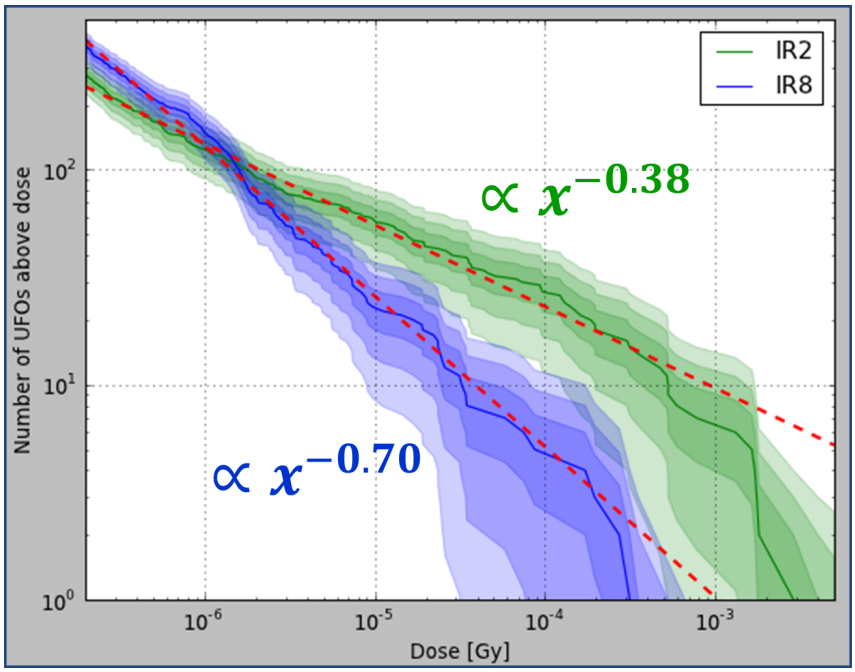


Figure 5.14.: Dose distribution of MKI UFO events in IR2 and IR8 at top energy. Since the maximum observable dose is limited by the BLM dump thresholds, the number decreases rapidly above $\approx 5 \cdot 10^{-4}$ Gy.
278/378 MKI UFOs in IR2/IR8 between technical stop (TS) #3 in 2011 and TS #3 in 2012 are considered. For the fits (red dashed lines), only UFO events with a dose $< 10^{-4}$ Gy are taken into account. The color-shades indicate a fluctuation of 1, 2 and 3 standard deviations around the observed distribution.

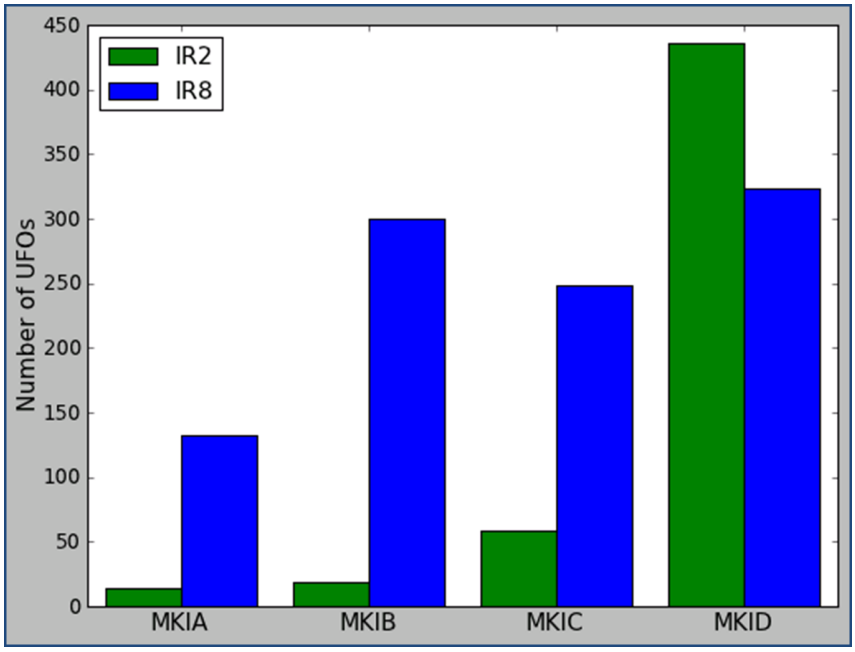


Figure 5.15.: Distribution of UFOs among the individual MKI magnets in IR2 and IR8.
528/1005 UFOs around the MKIs in IR2/IR8 between 10.07.2011 and 20.09.2012 are considered. Only UFOs with signal in 640 $\mu$s running-sum $> 5 \cdot 10^{-4}$ Gy/s.

### LHC Experiments

Several dedicated machine development sessions (MDs) were performed in 2011 and 2012 to study the production mechanism and the dynamics of MKI UFOs [119, 120]. During these MDs, the injection kicker magnets (MKIs) were repeatedly pulsed (without injecting beam) in a gap in the partly filled LHC. **A clear correlation between pulsing the MKIs and the occurrence of MKI UFOs was found;** many UFO events were observed within a few hundred milliseconds after pulsing the MKIs. Figure 5.16a shows the distribution of the time when the UFO events occur (w.r.t. the time of the MKI pulse). Following this observation the BLM IQC buffer with 40 $\mu$s temporal resolution (see Sec. 2.3.3) was adjusted for an improved detection of MKI UFOs around normal beam injections. As a result UFOs around the MKIs could be regularly traced shortly after a beam injection. Figure 5.16b shows the corresponding distribution of the time when the UFO events occur (w.r.t. the time of the injection[17]).

Assuming that a macro particle is released from the aperture at the moment of the kicker pulse and accelerated towards the beam only by gravitation, the expected delay until the particle reaches the beam center (distance $s = 19\,\text{mm}$) is 62.2 ms (see calculation in Sec. 5.2.2). However, many events with a shorter delay were observed; the shortest observed delay[18] is 2.0 ms, which would require a constant acceleration of the particle by $\approx 9500\,\text{m/s}^2$. Hence, **the particle dynamics cannot be explained by the gravitational force alone**, and it is believed that the macro particle is accelerated towards the beam by electric fields as well. This aspect is discussed further in Sec 5.3.3.

During the MD on 01.11.2011 the production of UFOs by pulsing the tune kickers[19] (MKQs) [121] was studied. The design of the MKQs is similar to the MKIs (see Sec. 2.3.1), but the MKQs have a metalized ceramic tube and are almost never used during nominal high intensity operation. During the MD, the MKQs were pulsed as often as the MKIs, but **not a single UFO event around the MKQs was observed** [120].

[17] The beam injection itself and the pulsing of the MKIs induce (non UFO-like) ultra fast losses in the injection regions which are clearly visible in the BLM data. Thus, the temporal uncertainty is small and is mainly determined by the temporal resolution of the BLM buffer.

[18] UFO in MKIC.5L2 after injection on 10.08.2011 at 04:57:19.550.

[19] Four tune kicker magnets (MKQ) per beam are installed in IR4 to deliberately excite the beam or deflect it even to the aperture (in aperture kicker mode).

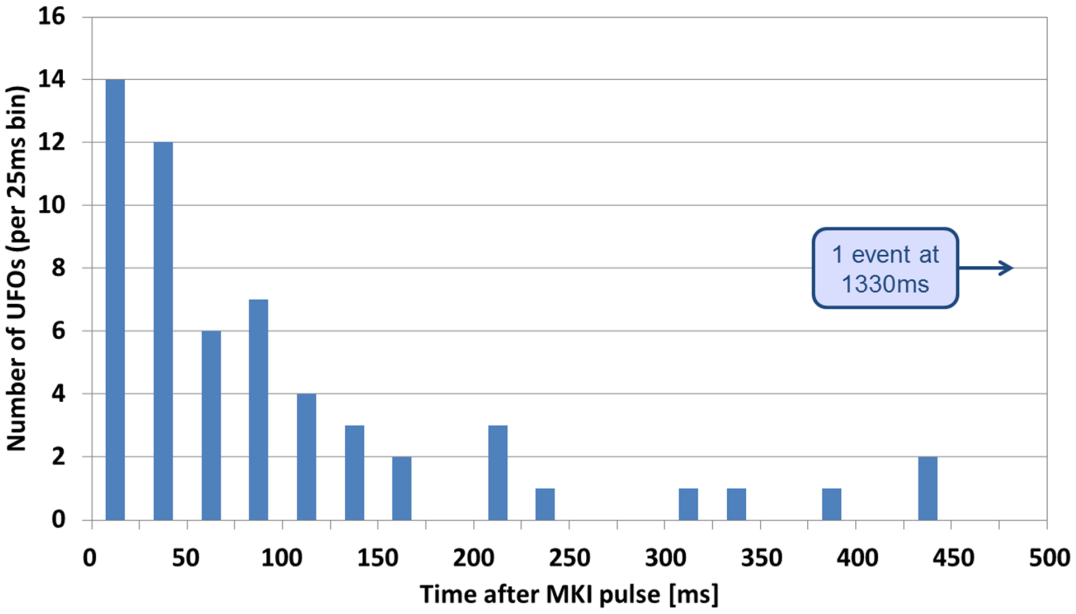


(a) UFOs after MKI pulses during MD.

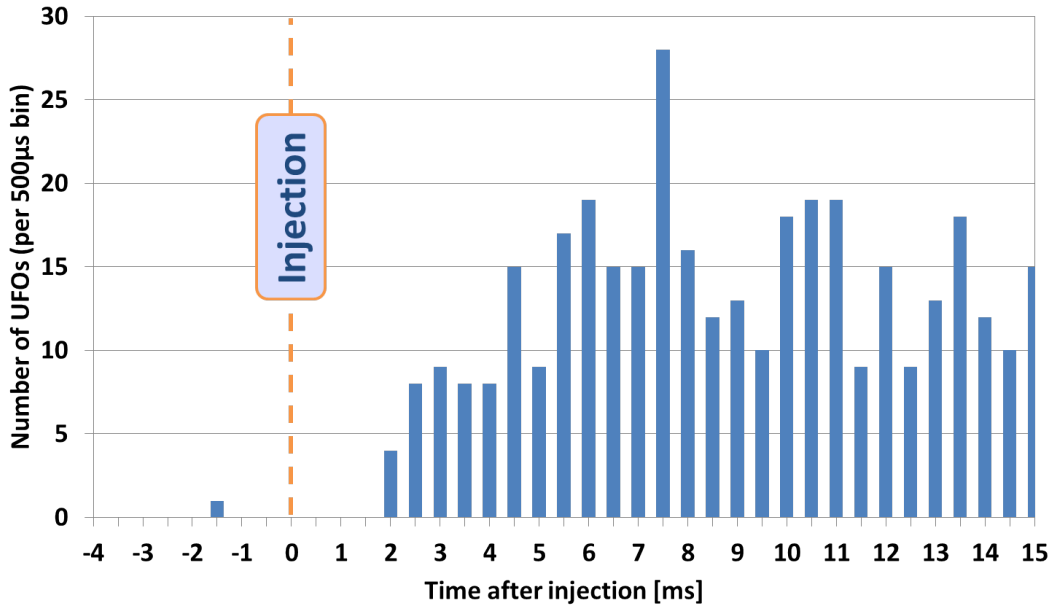


(b) UFOs after normal proton injections.

Figure 5.16.: The distribution of the occurrence of MKI UFOs after pulsing the MKIs during the MD on 01.11.2011 [119] (a) and the distribution after proton injections (b). For (a) the BLM study buffer was used with a duration of 11.2 s and a temporal resolution of 2.56 ms. (b) is based on data from the BLM IQC Buffer with a duration of 20.5 ms and a temporal resolution of 40 $\mu$s (see Sec. 2.3.3).
For (b) 364 MKI UFOs in IR2 and IR8 between 27.07.2011 and 17.12.2012 are considered. An (asymmetric) Gaussian function is fitted to the temporal loss profile of each UFO event. The times of the peak loss rates from the fits are shown here.

### 5.3.2. Macro Particle Inspection

In the winter technical stop 2010/11 the MKIB in IR2 was removed and replaced. This tank was opened in October 2011 and inspected for macro particles. In a standardized procedure the ceramic tube was flushed with $N_2$ to sample macro particles on a filter [122]. In reference measurements with clean room air 100, with a new ceramic tube 10'000 macro particles were found on the filter. **After the inspection of the removed MKI 5'000'000 particles were found on the filter.** Most of these particles are of micrometer size, but **particles with a diameter of up to about 100 $\mu$m were found.** Figures 5.17a and 5.17b show electron microscope pictures of macro particles found in the MKI. An energy-dispersive X-ray spectroscopy (EDS) showed that the particles consist mainly of Al and O, suggesting that **the macro particles originate from the $Al_2O_3$ ceramic tube** shown in Fig. 2.6b.

### 5.3.3. Macro Particle Model

The presented studies provide strong evidence that the UFO events around the MKIs are caused by the $Al_2O_3$ macro particles originating from the ceramic tube. As discussed in Sec. 5.3.1, some of these particles are expected to be accelerated by electric fields towards the beam. Thus, it is believed that those particles are negatively charged up by impinging electrons from an electron-cloud, which is known to build up in the regions of the MKIs during high intensity proton operation [42, 43, 123]. The particles are then detached by the electric field on the inner surface of the ceramic tube during the MKI pulse [117], the electric beam potential and/or mechanical vibrations. In dedicated laboratory measurements, vibrations of the MKI tank and the ceramic tube were observed when pulsing a MKI[20] [117,124]. Charged macro particles are then accelerated towards the beam by gravitation and the electric fields from the MKI and the beam, as illustrated in Fig. 5.18.

The macro particle dynamics model described in Sec. 5.2.2 was extended for MKI UFOs to take into account also the electrical field during the MKI pulse and initially charged particles [125]. An important conclusion is that particles cannot be picked up from the bottom of the ceramic tube, but must be detached from the top [117]. To explain a delay of a few milliseconds between the MKI pulse and the moment when the particle reaches the beam center, the ratio of the initial particle charge $Q$ and its mass $A$ (in atomic mass units) must be $Q/A \approx -10^{-8}$ e [117]. Thus, for an $Al_2O_3$ particle with 50 $\mu$m radius, an initial charge of about $-10^{10}$ e is required.

[20] Electrical noise and spurious vibrations complicated the measurements, but vibrations with small amplitudes of $\approx 10$ nm in the 60 to 300 Hz range could be identified.

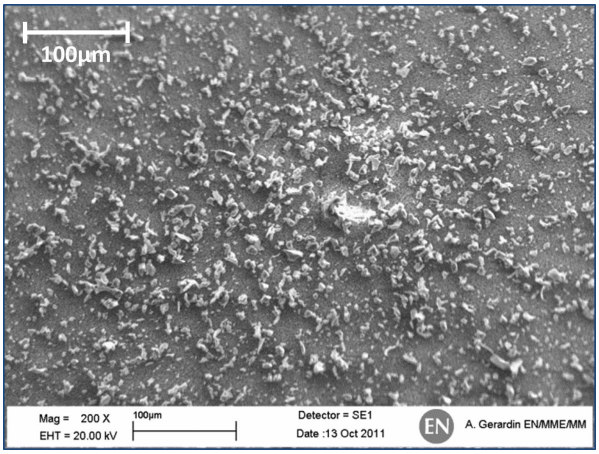


(a) Macro particles on filter.

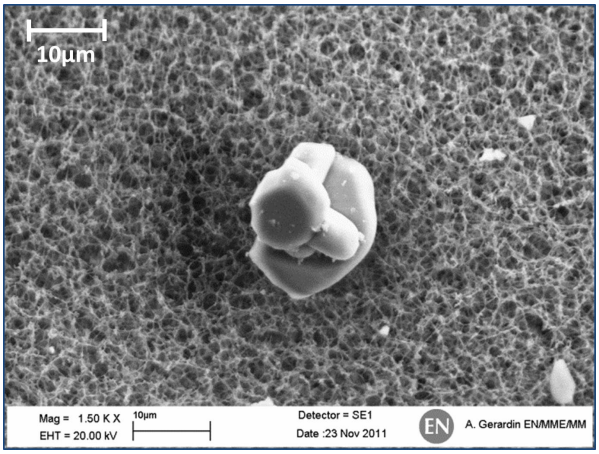


(b) Zoom of a macro particle.

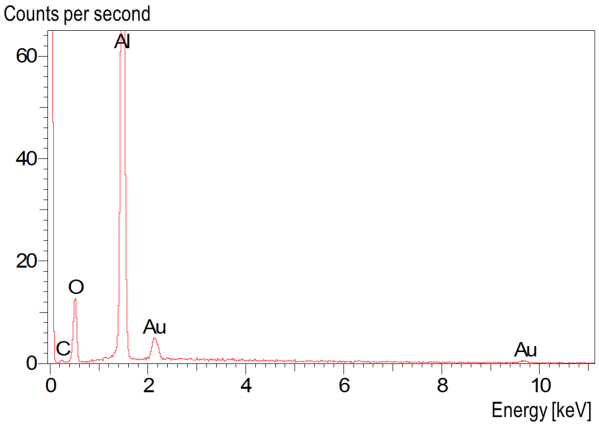


(c) Energy-dispersive X-ray spectrum of particle in b.

Figure 5.17.: About 5'000'000 particles were found on the filter after flushing the MKI which was removed from the LHC in the winter technical stop 2010/11 (a, b). The EDS spectra of the samples (c) reveal that most particles consist of Al and O (courtesy of A. Gérardin et al. [122]). Traces of gold in the EDS spectra result from gold which is sputtered on the filters after sampling the macro particles to ensure electrical conductivity for the microscopic investigation.

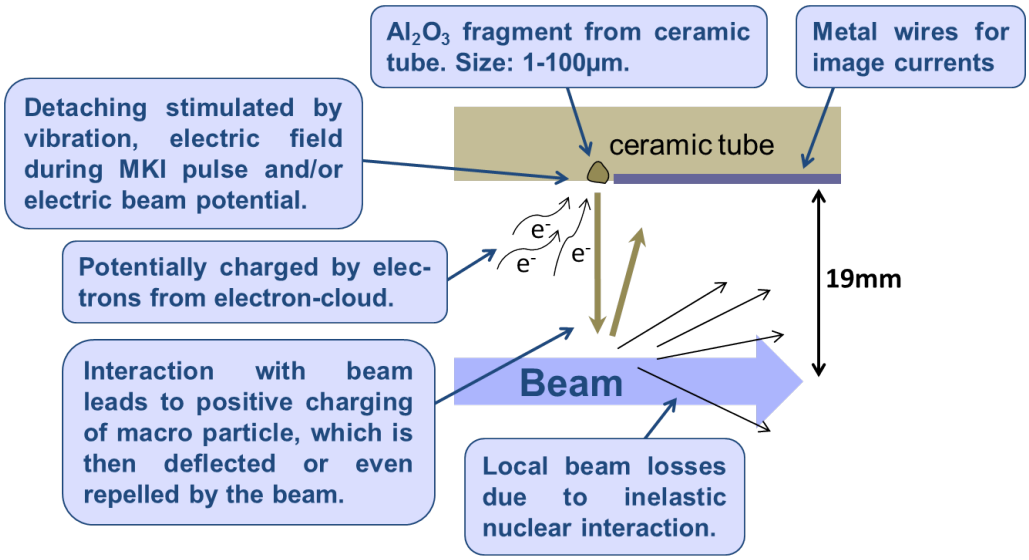


Figure 5.18.: Illustration of macro particle model, dynamics and interactions for UFOs at the injection kicker magnets (MKIs).

### 5.3.4. FLUKA Simulations

Similar to the FLUKA simulations for arc UFOs (see Sec. 5.2.3), dedicated FLUKA simulations for UFOs at the MKIs in IR2 were made [126]. The simulated BLM dose patterns shown in Fig. 5.19 underline that **the UFO location must be in (or very close to) the MKIs** in order to explain the observed loss patterns.

The simulations [126] indicate that about $\dot{N}_{p,\max} = 6.1 \cdot 10^{12}$ inelastic proton-UFO interactions per second are needed to explain the measured peak beam loss rate of the largest observed UFO at MKID.5L2[21] [100]. Assuming a macro particle in the beam center with a radius $r$, which is small compared to the horizontal and vertical beam size $\sigma_x$ and $\sigma_y$, $\dot{N}_{p,\max}$ is (in accordance with [102]) given by

$$\dot{N}_{p,\max} = \frac{N_p \cdot f_{\text{rev}}}{2\pi\sigma_x\sigma_y} \cdot \frac{A \cdot u}{l \cdot \rho} \tag{5.2}$$

with $N_p$ being the number of protons in the beam, $f_{\text{rev}} = 11'245\,\text{Hz}$ the revolution frequency of the LHC, $A$ the macro particle mass in atomic mass units $u$, $l$ the inelastic nuclear interaction length of the macro particle's material and $\rho$ the mass density of the macro particle. For an $Al_2O_3$ macro particle ($l = 24.8\,\text{cm}$, $\rho = 3970\,\text{kg/m}^3$) and $N_p = 1.01 \cdot 10^{14}$, $\sigma_x = 325\,\mu\text{m}$ and $\sigma_y = 140\,\mu\text{m}$ for the example case, a macro particle mass $A = 9.1 \cdot 10^{17}$ is needed to explain the observed $\dot{N}_{p,\max}$. This corresponds to a **radius of 45 µm for a spherical particle** [100]. This result has to

[21] The event occurred on 16.07.2011 at 05:52:33. A peak beam loss rate of 15.3 Gy/s was measured at the BLM directly downstream of the MKID. Each inelastic nuclear proton-UFO interaction leads to a signal of $\approx 2.5 \cdot 10^{-12}$ Gy in this BLM [126].

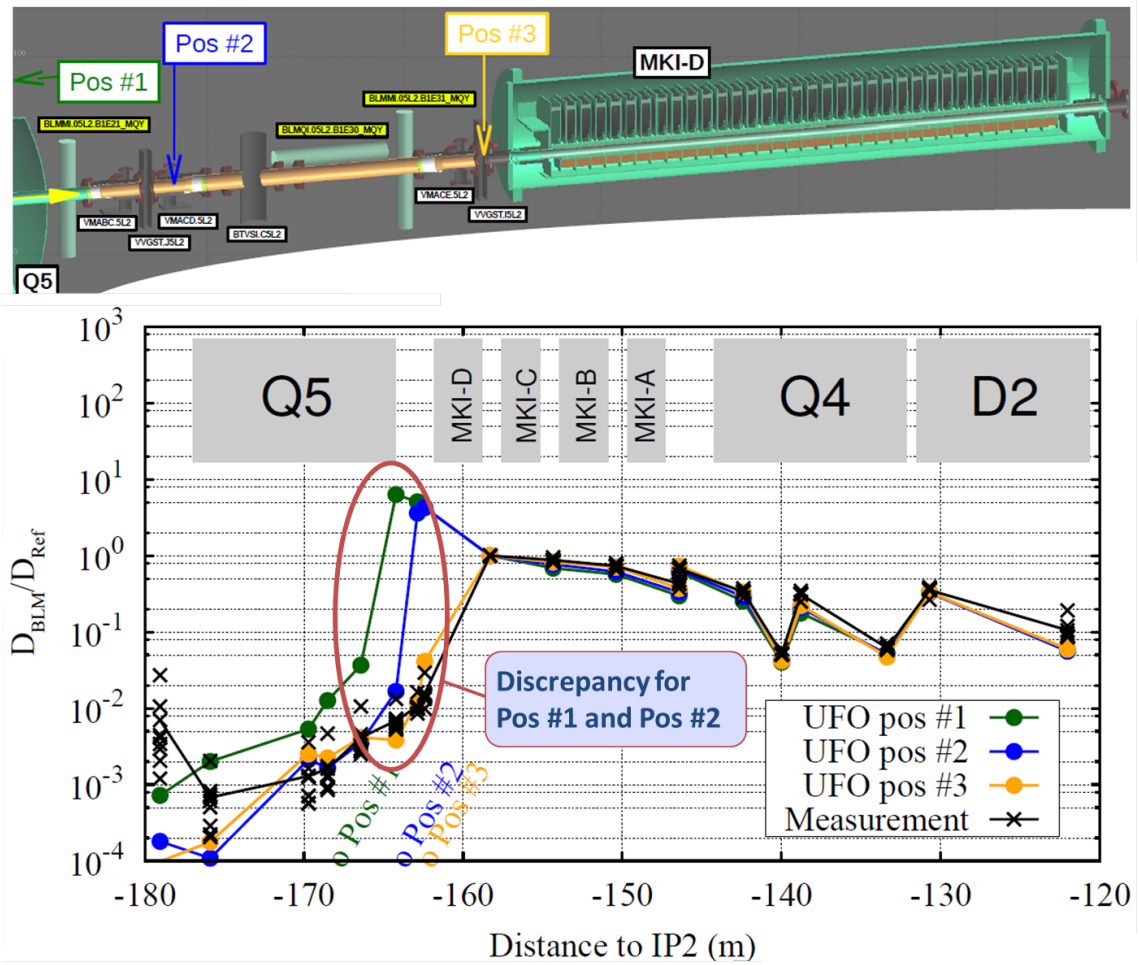


Figure 5.19.: The interaction of the proton beam with a macro particle was simulated at different locations (*Pos #1* - *Pos #3*) around the MKID.5L2 using FLUKA. The comparison of the expected BLM dose patterns and typical measured loss patterns for UFO events at MKID shows discrepancies for UFOs occurring too far upstream of the MKI (courtesy of A. Lechner et al. [126]).

be understood as the minimum particle radius needed to explain the measured peak beam loss rate of the largest observed MKI UFO event. This value is consistent with the size of the largest $Al_2O_3$ particles found in the MKI macro particle inspection (see Sec. 5.3.2).

Since the MKIs are operated at ambient temperature, they are insensitive to the beam losses from typical UFO events (they do not quench). The most critical elements are the downstream superconducting quadrupole magnet (Q4) and dipole magnet (D2). As for the arc UFOs, the density of the energy deposited in the coils of the downstream magnets due to the (inelastic) proton-UFO interactions is estimated based on the FLUKA simulations. Figure 5.20 shows the peak energy density per

inelastic proton-UFO interaction at MKID.5L2 in the Q4 and D2 magnet. The highest energy density (at top energy) is expected to be at the end of the D2 due to the D2 dipole field [126]. Fig. 5.20 also illustrates that **the peak energy density per inelastic proton-UFO interaction is over 50 times higher at 3.5 TeV compared to injection energy and another factor 3.4 higher for operation at 7 TeV.**

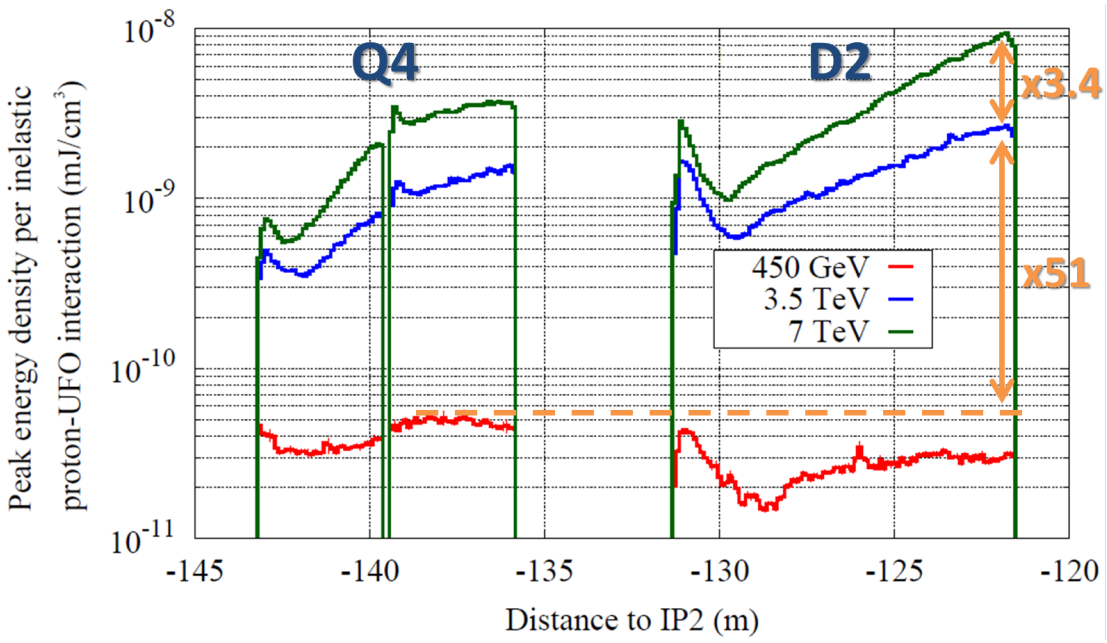


Figure 5.20.: Peak energy density per inelastic proton-UFO interaction in MKID.5L2 in the coils of the downstream superconducting quadrupole and dipole magnets simulated with FLUKA (courtesy of A. Lechner et al. [126]).

### 5.3.5. MAD-X Simulations

For the FLUKA simulations described above, only inelastic nuclear interactions, which lead to nearby beam losses, are taken into account. About one third of the protons interacting with a macro particle are subject to elastic scattering processes and are deflected under small angles. These particles lead to beam losses at aperture limiting elements all around the LHC. Simulations combining FLUKA simulations of the elastic scattering processes and tracking of the deflected protons with MAD-X were performed [29]. Figure 5.21 shows the loss locations of the scattered protons: all scattered protons are lost at collimators in IR2, IR3, IR6 and IR7.

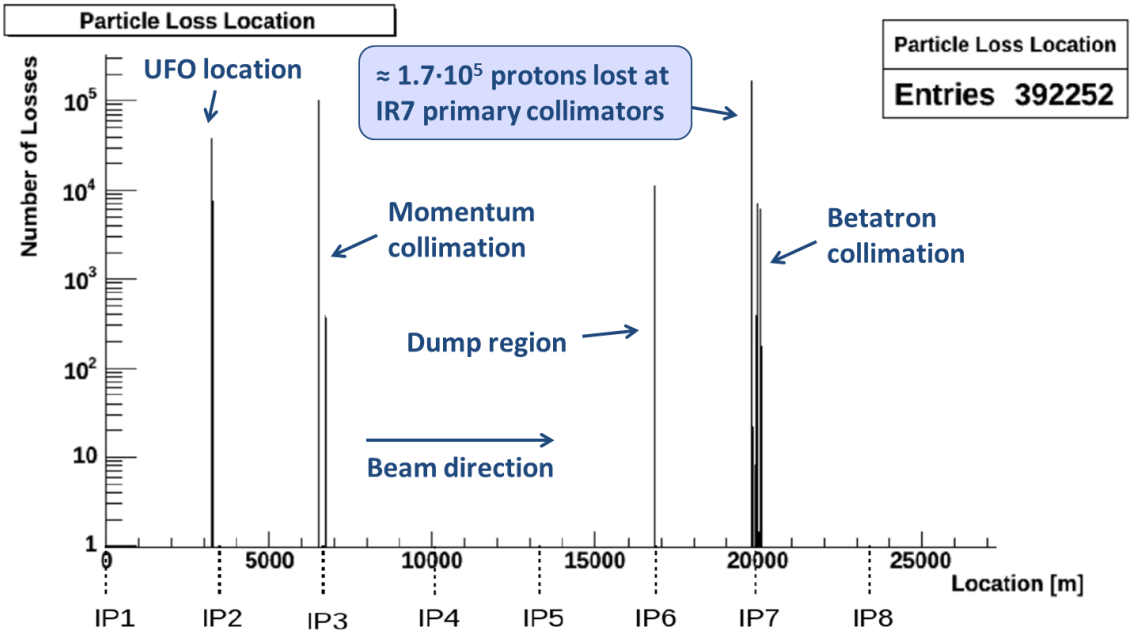


Figure 5.21.: Distribution of the proton losses around the LHC for an UFO event at MKID.5L2. The elastic nuclear interactions of 600'000 protons with an Al macro particle is simulated with FLUKA, the deflected protons are tracked with MAD-X for up to 10 turns (courtesy of M. Hempel et al. [29]).

For the largest UFO at MKID.5L2[22], a peak beam loss rate of 2.93 Gy/s was measured at the BLM BLMEI.06L7.B1E10_TCHSH.6L7.B1, which is located 5 m - 10 m downstream of the primary beam 1 betatron collimators. Based on a calibration for this BLM (see Appendix C), this BLM signal corresponds to a loss of $6.15 \cdot 10^{11}$ protons per second at the primary betatron collimators[23]. The MAD-X simulations (see Fig. 5.21) indicate that about 28% of the elastically scattered protons are lost at the primary collimators in IR7. Thus, for the example UFO event, about $\dot{N}_{p,\mathrm{max}} = 2.2 \cdot 10^{12}$ elastic nuclear proton-UFO interactions per second are needed to explain the measured BLM signal at the primary collimators in IR7. With Eq. 5.2 and the elastic nuclear interaction length for $Al_2O_3$ $l = 49.3\,\mathrm{cm}$, the observed loss rate would be explained by a macro particle with mass $A = 6.5 \cdot 10^{17}$, which corresponds to a radius of 40 $\mu$m for a spherical macro particle. This is within about 10% consistent with the value calculated in Sec. 5.3.4.

[22]Event on 16.07.2011 at 05:52:33. See Sec. 5.3.4 for operational conditions.

[23]The value is expected to be slightly underestimated, because the BLM calibration is based on data from 4 TeV operation, whereas the UFO event occurred at a beam energy of 3.5 TeV.

## 5.4. Mid-Term Extrapolation

Between 2010 and the end of the 2012/13 LHC run, the number of beam dumps due to UFOs remained, thanks to large-scale increases and optimizations of the BLM dump thresholds [97], rather constant at about 20 beam dumps per year (see Tab. 5.1). After the first long shutdown (LS1), several operational parameters which affect the UFO activity will change (see Tab. 2.1):

- The **beam intensity** may increase by about 50% up to $3.2 \cdot 10^{14}$ protons.
- It is foreseen to operate the LHC with **25 ns** bunch-spacing.
- The top energy will increase to about **6.5 TeV** per beam.

The impact of these changes on the UFO activity is discussed in the following.

Furthermore, **during LS1 the cold parts of the LHC are warmed up to room temperature and the beam vacuum is opened in many areas. A related deconditioning of the UFO activity is expected,** which is for the arc UFOs at least similar to the deconditioning observed over the 2010/11 winter technical stop (about a factor 2.5, see Sec. 5.2.1), but may lead to an increased UFO activity on a level similar to the beginning of 2011 (about 10 times higher UFO activity than at the end of 2012), or even higher.

### 5.4.1. Intensity Extrapolation

As shown in Fig. 5.7, for beam intensities above several hundred bunches, the arc UFO activity does not depend strongly on the beam intensity. Based on the fit in Fig. 5.7, for a beam intensity of $3.2 \cdot 10^{14}$ protons, the UFO activity is only about 4% higher than with $2.2 \cdot 10^{14}$ protons.

### 5.4.2. 25ns Operation

In ten intermediate intensity fills between 13.12. and 17.12.2012, the LHC was operated with 25 ns bunch-spacing at 4 TeV to study possible operational limitations such as UFOs or electron-cloud [43]. Whereas the arc UFO rate was about 1 UFO event per hour during the 50 ns fills with 1374 bunches at the end of 2012 (see Fig 5.5), a significantly higher UFO activity was observed in the 25 ns fills, as illustrated in Fig. 5.22a. Figure 5.22b shows the arc UFO rate scaled to the intensity level of 1374 bunch fills. This illustrates that **the arc UFO rate with 25 ns bunch-spacing**

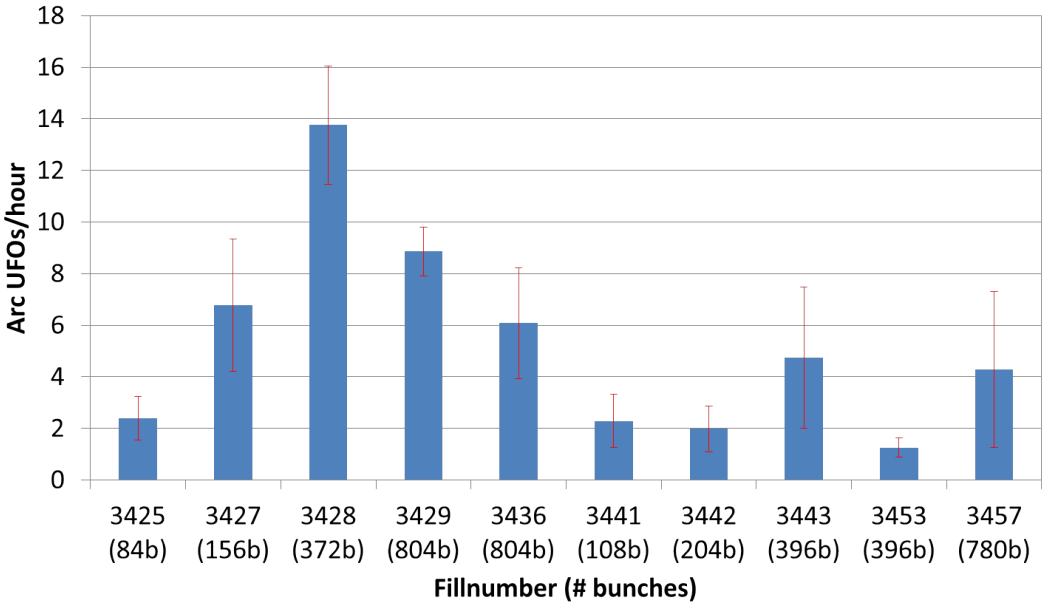


(a) Arc UFO rate.

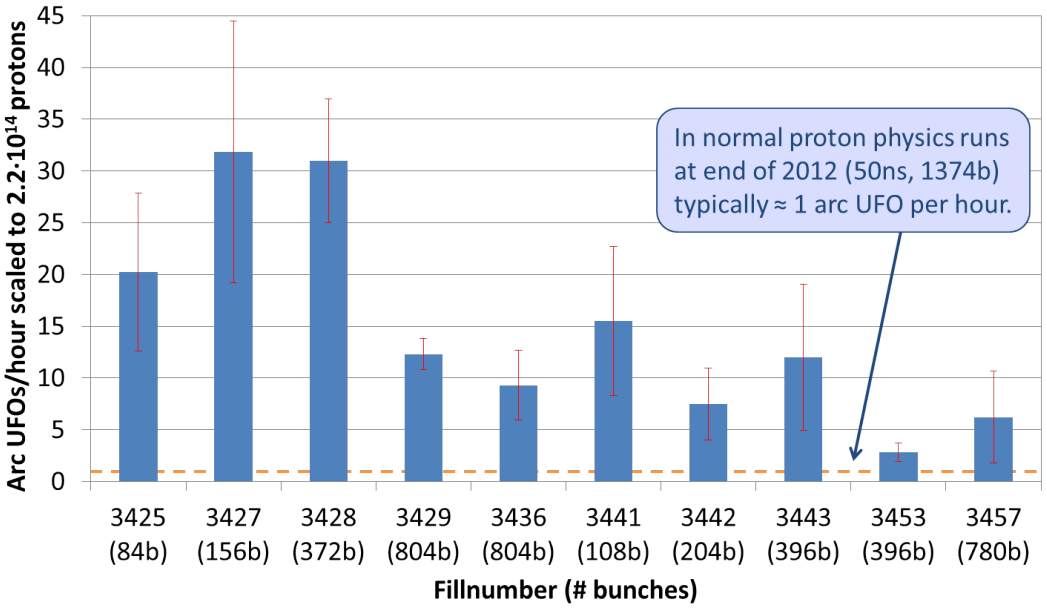


(b) Arc UFO rate scaled to $2.2. \cdot 10^{14}$ protons.

Figure 5.22.: Arc UFO rate at 4 TeV during the 25 ns fills at the end of 2012 (a). For (b) the intensity is scaled based on the fit shown in Fig 5.7 to an intensity of $2.2 \cdot 10^{14}$ protons.
Only UFOs with a signal in 640 $\mu$s running-sum $> 2 \cdot 10^{-4}$ Gy/s are taken into account.

**was initially over 10 times higher** than with 50 ns spacing[24]. Figure 5.22b also shows a **tendency for a decrease of the initially high arc UFO rate** within only five days[25].

The dependence of the arc UFO activity on the bunch-spacing can be explained for example by assuming macro particles that are frozen to the beam-screen and are released by beam-induced heating (see Sec. 5.2.2), which is increased for 25 ns operation due to electron-cloud activity [43].

As shown in Fig. 5.12, no particularly high MKI UFO activity was observed in the 25 ns physics fills. In contrast to that, during the 450 GeV scrubbing run[26] in December 2012, 221 MKI UFOs were observed in 13 fills with a peak beam intensity above $10^{14}$ protons. This corresponds to 17 MKI UFOs per fill (compared to about 2 MKI UFOs per fill at the end of the 2012 proton physics run).

### 5.4.3. Energy Extrapolation

The beam losses due to UFOs increase with beam energy. As illustrated in Fig. 5.11 and Fig. 5.20, for 7 TeV operation the peak density of the energy deposited in the superconducting magnets is about a factor 4.2 higher for arc UFOs and a factor 3.4 higher for MKI UFOs[27] compared to operation at 3.5 TeV. Moreover, due to higher currents, the magnet quench margin is lower for higher beam energy (about a factor 4-5 for main dipole magnets at 7 TeV compared to 3.5 TeV).

Based on the FLUKA simulations for arc UFOs (see Sec. 5.2.3), about $1.3 \cdot 10^8$ inelastic proton-UFO interactions are needed to explain the beam losses for the largest arc UFO observed so far[28]. An UFO event at *Pos #1* (see layout in Fig. 5.10) with the same number of inelastic proton-UFO interactions would according to Fig. 5.11 imply a peak energy density in the dipole magnet of $\approx 7.8\,\mathrm{mJ/cm^3}$ for 3.5 TeV operation and $\approx 32.5\,\mathrm{mJ/cm^3}$ for 7 TeV operation. These values are compared in Fig. 5.23 to the expected quench margin for the LHC arc dipole magnets. With

[24] Of particular significance is fill 3429 (804 bunches) with 87 arc UFOs in almost 10 hours at 4 TeV.

[25] In fill 3453 (396 bunches) only 11 arc UFOs were observed in almost 9 hours at 4 TeV.

[26] During a scrubbing run, the accelerator is operated with highest possible intensity deliberately above the electron-cloud limit. This conditions the vacuum chamber surface and increases the intensity limit for electron-cloud build-up (see Sec. 2.4.2).

[27] The scaling is geometry dependent. A scaling of a factor 3 was found from wire scanner measurements at different energies [97].

[28] The event occurred on 05.10.2012 at 06:19:41 (see Appendix B). Beam losses of 0.67 mGy were measured by BLM 2 (see layout in Fig. 5.10). It is assumed that the UFO occurred at *Pos #2*, i.e. close to the quadrupole magnet. According to the FLUKA simulations for 3.5 TeV, each inelastic nuclear proton-UFO interaction at *Pos #2* leads to a signal of $\approx 5.2 \cdot 10^{-12}$ Gy in BLM 2 [113].

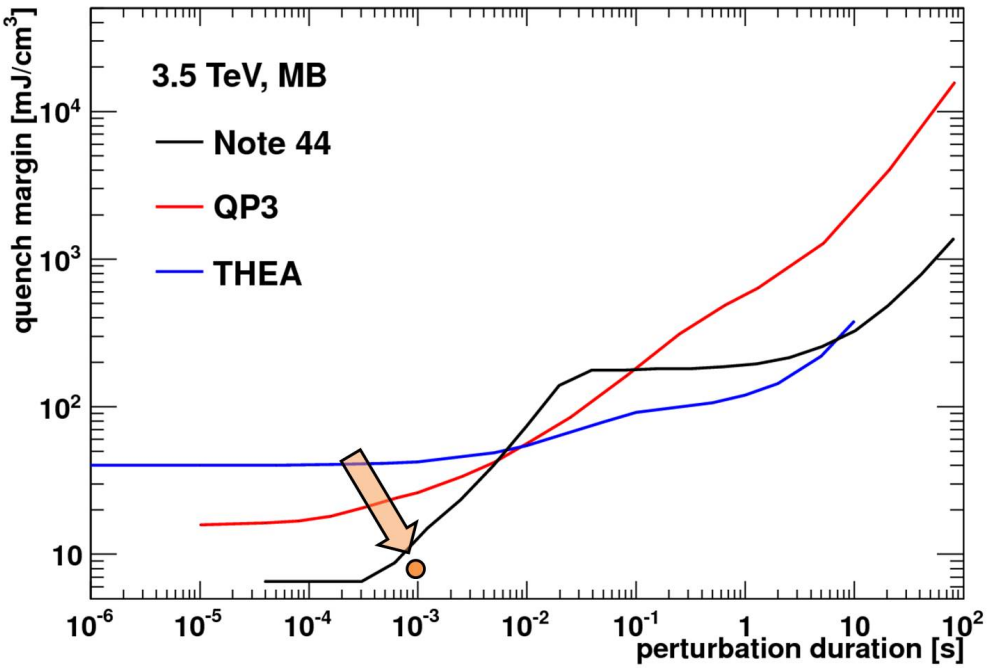


(a) Quench margin at 3.5 TeV.

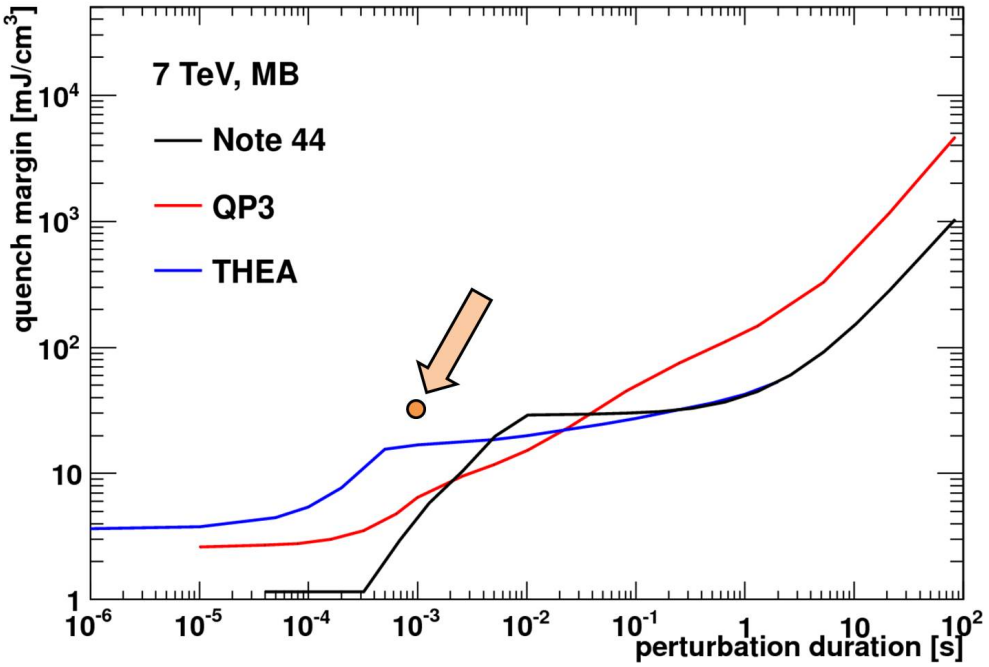


(b) Quench margin at 7 TeV.

Figure 5.23.: The estimated quench margin of the LHC main dipole magnets as function of the beam loss duration from LHC Project Note 44 [19], the QP3 model [127] and the THEA model [128] for operation at 3.5 TeV (a) and 7 TeV (b). The orange points indicate the peak energy density in the magnet for $1.3 \cdot 10^8$ inelastic nuclear proton-UFO interactions at *Pos #1* (see layout in Fig. 5.10) as estimated from the FLUKA simulations [113] (based on material from M. Sapinski).

respect to the quench margin estimate from the QP3 model [127] (which is presently assumed to be the most accurate model), **the beam losses reach about 30% of the quench margin for 3.5 TeV operation, but are a factor 5 above the quench margin for 7 TeV operation.**

The BLM dump thresholds are set to decrease with beam energy according to the magnet quench margin. The corresponding scaling of BLM signal/BLM threshold for UFO events is shown in Figure 5.24. When the BLM signals and thresholds of all arc UFO events recorded in 2012 are scaled, one predicts **91 beam dumps** if the LHC would have been operated at 7 TeV instead of 4 TeV (**112 beam dumps from 2011 arc UFOs**). An additional **21 beam dumps** would have been caused by MKI UFOs (**27 beam dumps from 2011 MKI UFOs**)[29]. These numbers have to be compared to one actual beam dump by arc UFOs and 8 dumps by MKI UFOs in 2012 (2011: 2 dumps by arc UFOs, 11 dumps by MKI UFOs). For operation at 6.5 TeV the expected number of beam dumps is about 30% lower for arc UFOs and 15% lower for MKI UFOs (see Fig. 5.24).

The extrapolation shows that whereas in LHC run 1 most beam dumps were caused by MKI UFOs (see Tab. 5.1), for operation at higher energies the arc UFOs are expected to become more critical. This is partly due to the different dose distributions (see Fig. 5.4a and Fig. 5.14) and the different scaling of beam losses and BLM thresholds with energy (see Fig. 5.11 and Fig. 5.20) but also because the MKI UFOs occur typically in the beginning of a fill (see Fig. 5.13), thus only a fraction is affected by a higher flat top beam energy.

In February 2013, a dedicated magnet quench test with beam losses on UFO-timescales was performed. The targeted main quadrupole magnet quenched with beam induced losses of about $8 \cdot 10^8$ primary protons impacting the aperture (below 1% of a single nominal bunch) [92]. The initial analysis indicates that the quench margin for arc quadrupole and dipole magnets is about a factor 6-13 above the expected level [129], which would allow for large-scale increases of the arc BLM thresholds and would significantly reduce the expected number of UFO related beam dumps. The expected reduction can be extracted from Fig. 5.25, which shows the number of UFO related beam dumps as function of the BLM signal/BLM threshold scaling factor. For example, the BLM signal/BLM threshold scaling factor for arc UFOs at 6.5 TeV is about 15, which corresponds to 62 related beam dumps based on the 2012 data. A factor 5 increase of the BLM thresholds would result in a

[29] The extrapolation assumes (apart from the beam energy) identical running conditions as in 2011/12. Excluded are potential further increases of the BLM thresholds, a deconditioning over LS1, the increased UFO rate at 25 ns operation and changes in beam intensity and beam size. Concerning the MKI UFOs, only the BLM thresholds at the superconducting elements are assumed to be limiting.

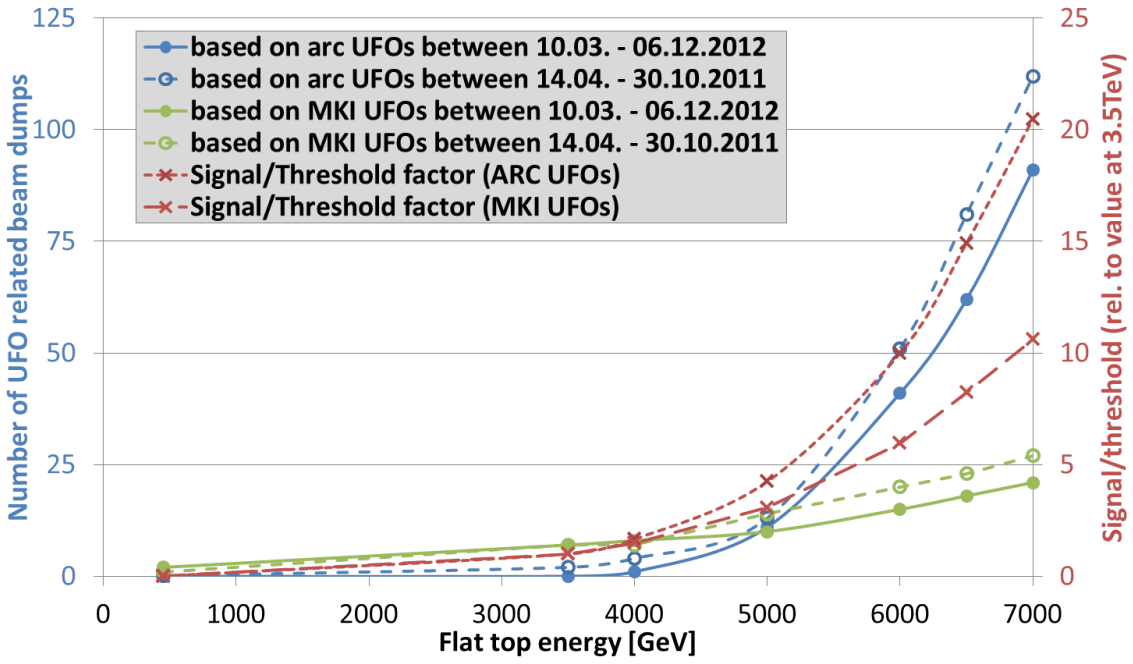


Figure 5.24.: The expected number of beam dumps by arc and MKI UFOs and the expected scaling of BLM signal/BLM threshold as function of the beam energy (based on [97, 113, 126]).

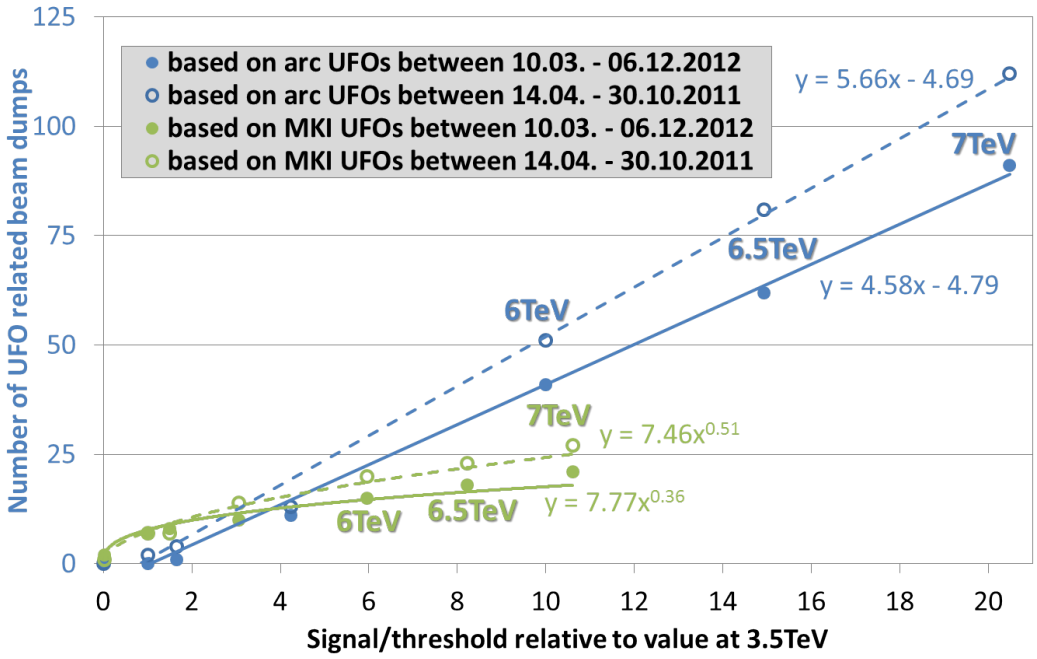


Figure 5.25.: The expected number of beam dumps by arc and MKI UFOs as function of the scaling of BLM signal/BLM threshold (based on [97, 113, 126]).

signal/threshold factor of 3, which corresponds to roughly 9 expected beam dumps due to arc UFOs based on the 2012 data. A detailed analysis of the quench test including MAD-X, FLUKA and Geant4 [130] simulations is currently ongoing.

Besides increased beam losses, a higher beam energy also implies smaller transverse emittances; thus, it is expected that the duration of the beam losses is shorter for UFO events at higher beam energies. The macro particle dynamics model predicts that transverse beam size and beam loss duration are directly proportional [102]. Hence, it is expected that the temporal width of UFO events is about $1-\sqrt{\frac{4\,\mathrm{TeV}}{6.5\,\mathrm{TeV}}} \approx 20\%$ shorter for operation at 6.5 TeV compared to 4 TeV. This implies that **some UFO events may be too fast for active protection by the BLM system and may lead to magnet quenches** (see also Fig. 5.8 and Sec. 2.3.4)[30].

## 5.5. Mitigation Strategies

Energy dependence, bunch-spacing dependence and expected deconditioning over LS1 indicate that UFOs could be a major performance limitation for LHC operation after LS1. Thus, various mitigation strategies were investigated.

### 5.5.1. Mitigation of UFOs at the Injection Kicker Magnets

UFOs at the injection kicker magnets (MKIs) are identified as macro particles originating from the $Al_2O_3$ ceramic tube (see Sec. 5.3.2) and many mitigation measures are in preparation during LS1 [131]:

- All MKI magnets will be equipped with 24 instead of 15 screen conductors (see Sec. 2.3.1). This reduces the electric field by a factor 7 during the majority of the MKI pulse [117]. As explained in Sec. 5.3.3, the electric field is thought to be important for the detachment of macro particles from the ceramic tube.
- An improved cleaning procedure will be applied to all MKIs. This is expected to reduce the initial macro particle contamination by a factor 5-7 [117].
- The MKI interconnects, bypass tubes and nearby equipment will be NEG[31] coated. This mitigates electron-cloud activity and improves the vacuum in the

[30] As illustrated in Fig. 5.8, also UFO events with high beam losses and short temporal width have been observed.

[31] Non-Evaporable-Getter (NEG) materials can absorb gas molecules and increase the intensity threshold for electron-cloud build-up. In the LHC, most of the warm vacuum chambers in the long straight section are coated with NEG [132].

MKIs. Electron-cloud and high vacuum pressure are expected to enhance the UFO activity as explained in Sec. 5.3.3 and [104].

- A coating of the ceramic tube, possibly with carbon or $Cr_2O_3$, is under investigation. This would reduce electron-cloud activity and the risk of surface flash-overs in the MKIs and could seal the surface of the ceramic tube.

The effectiveness of some of these mitigation measures was already successfully demonstrated: in the technical stop in September 2012 (TS #3), the MKID in IR8 was replaced by an improved version which had been subject to the improved cleaning procedure and is equipped with 19 instead of 15 screen conductors [131]. Figure 5.26 shows the distribution of UFOs among the different MKIs in IR8 before and after TS #3. Whereas before TS #3, the highest UFO activity was observed in MKID (and MKIB), the UFO activity in MKID is lowest after the replacement. The number of UFOs per fill at MKID is reduced by $(72 \pm 11)\%$ compared to an average reduction (due to the conditioning effect, see Sec. 5.3.1) of $(33 \pm 12)\%$ at the other MKIs.

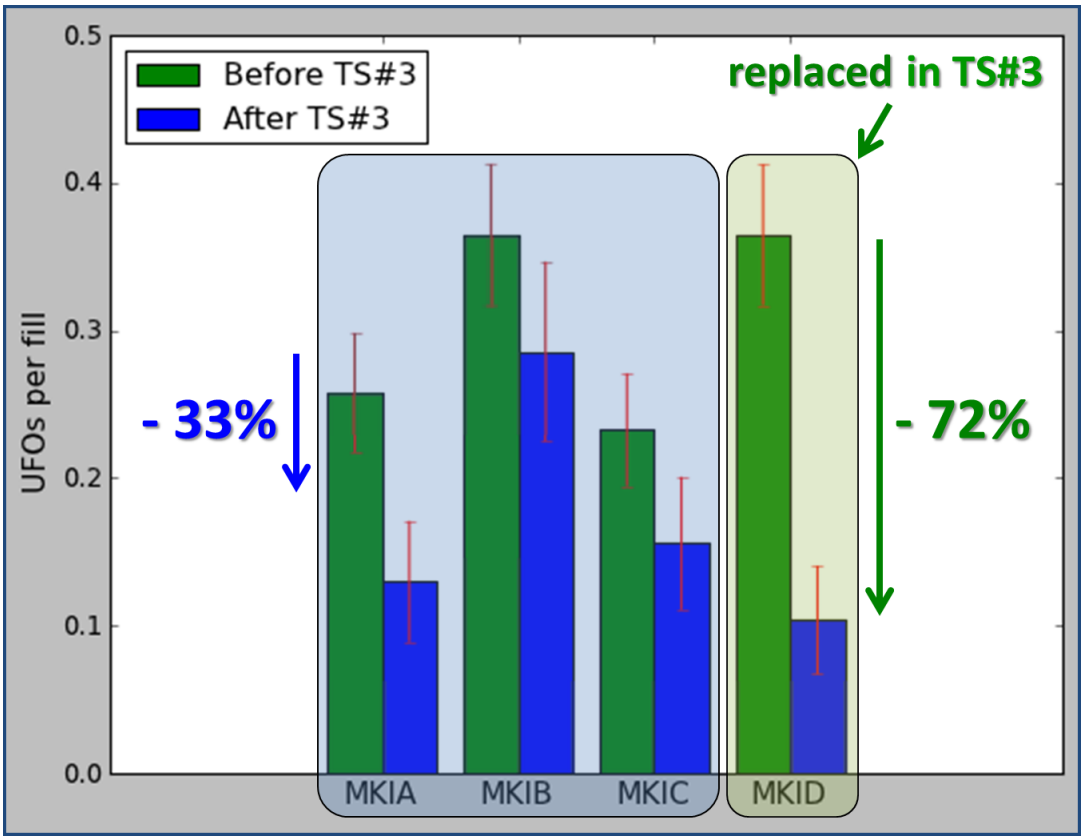


Figure 5.26.: Distribution of UFOs among the individual MKI magnets in IR8 before and after technical stop (TS) #3 in 2012.
194/52 UFOs in 159/77 fills with stable beams and at least 1000 bunches before/after TS #3 are taken into account. Only UFOs with signal in 640 $\mu$s running-sum $> 5 \cdot 10^{-4}$ Gy/s.

Other mitigation measures were studied as well, but were found to be unfeasible:

- Based on the experimental studies with the tune kickers (see Sec. 5.3.1) the effect of a titanium coating of the ceramic tube was investigated. However, dedicated simulations show that this would result in an unacceptably long rise-time of the MKI field of 4.5 $\mu$s instead of $\approx$ 900 ns [117].
- A modified design of the ceramic tube in which the screen conductors are completely enclosed by the ceramic tube was investigated. However, the design was found to be impractical since the manufacturing is extremely difficult[32] [117].

During the period with strongly enhanced UFO activity at MKID.5L2 around TS #3 in 2011 (see Sec. 5.3.1), the energy ramp was delayed by up to one hour after the last injection to reduce the sensitivity to MKI UFOs. Since most MKI UFOs occur within about 30 minutes after the last injection (see Fig. 5.13) and the beam losses and BLM thresholds depend strongly on the beam energy (see Fig. 5.20 and Sec. 5.4.3), this approach mitigates the problem, but implies also a significantly increased turn-around-time.

### 5.5.2. Mitigation of UFOs in the LHC Arcs

The main mitigation strategy for arc UFOs is to increase the BLM thresholds towards the magnet quench limit and to profit from the conditioning effect. In particular, the higher UFO activity and possibly faster conditioning with 25 ns bunch-spacing (see Sec. 5.4.2) indicate that an extended scrubbing run (see Sec. 2.4.2) after LS1 can reduce the UFO activity. If the initial impact of UFOs on LHC operation after LS1 is too severe, a (temporary) operation with 50 ns bunch-spacing or ultimately a (temporary) physics run at reduced top energy (around $5 - 5.5$ TeV) could mitigate the problem.

Nevertheless, the FLUKA simulations and the additional instrumentation in half-cell 19R3 (see Sec. 5.2.3) show that the current BLM distribution is highly inefficient for protection against beam losses due to UFOs at the dipole magnets [134]. Furthermore, the current BLM distribution is over-redundant for protection against beam losses at the quadrupole magnets. Thus, the arc BLMs are systematically relocated during LS1 [135]: two BLMs of each half-cell are removed from the quadrupole and are positioned vertically above the dipole-dipole interconnections as illustrated in Fig. 5.27.

[32] Moreover, the modification may also increase the imaginary part of the longitudinal beam coupling impedance, as explained in [133, pp. 207].

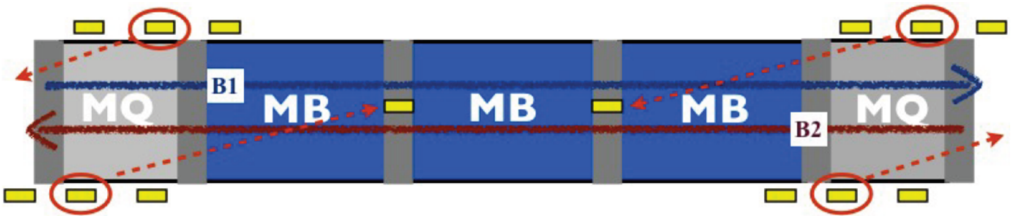


Figure 5.27.: Relocation of BLMs during LS1 as seen from the top (courtesy of E. Nebot del Busto [135]).

A complementary approach is to add a few bunches with large emittance to the filling scheme for UFO detection well before the macro particle reaches the center of the beam. This could allow a detection of very fast UFO events at higher energies in time to dump the beam before the beam losses exceed the magnet quench margin (see also Sec. 5.4.3). Furthermore, an interaction of a macro particle with these large-emittance bunches would lead to an ionization of the macro particle and a deflection of the particle by the electrical field of the full beam. A related machine development study was foreseen in 2012 but not conclusive due to (unrelated) technical problems. For quantitative estimates, further experimental studies and simulations of the dust particle dynamics are proposed.

### 5.5.3. Mitigation of UFOs at Other Locations

About 20% of the UFO related beam dumps are caused by the protection systems of the main experiments (see Tab. 5.1). These UFO events typically cause no (or very small) beam losses in the ionization chambers of the main BLM system [98]. As the beam dump thresholds from the main experiments are mostly independent of the beam energy, the scaling of the impact on LHC operation with beam energy is less severe for these events than for arc UFOs or MKI UFOs. Furthermore, there may be some margins for increases and optimizations of the corresponding beam dump thresholds. FLUKA simulations are required to improve the understanding of UFOs around the experiments.

UFOs are regularly observed when moving collimators. Especially the beam losses from UFO events at collimators which are close to superconducting elements (as TCL.5L5, see also Appendix B) can be critical. To reduce the impact of these UFOs, the movement of the collimators should be done at lowest possible energy and be reduced to a minimum at top energy.

## 5.6. Summary and Conclusions

Between 2010 and 2013, 58 LHC fills were terminated by UFO events. Thus, extensive studies were made, which include improvements of the diagnostics and intensive data analysis, dedicated experiments in the LHC [119,120] (including a magnet quench test [92]) and in the laboratory [122,124], FLUKA [113,114,126] and MAD-X simulations [29], and theoretical studies [102,125]. As a result, fundamental correlations were found, the macro particle dynamics are characterized, the response of the BLM system is understood and the source of the UFO events at the MKIs is identified. This allows for mid-term extrapolations.

In particular the energy and bunch-spacing dependence and the expected deconditioning over LS1 imply that UFOs could be a major performance limitation for LHC operation after LS1. Thus, various mitigation measures for MKI UFOs are ongoing and a large-scale relocation of the arc BLMs during LS1 is in preparation to allow a better protection against magnet quenches due to arc UFO events while minimizing the number of unnecessary beam dumps.

Moreover, during LS1, several magnets will be replaced, which allows an endoscopic inspection of three locations with particularly high UFO activity (16L3.B2, 25R3.B2, 28R7.B2).

For future high-intensity accelerators, macro particles have to be considered as a potentially significant performance limitation, also for superconducting accelerators with positively charged beams. An initial macro particle contamination should be avoided wherever possible. Brittle materials should be coated, all sources of sparking should be avoided. As for the LHC, ion pumps should be shielded from the beam and special care concerning the design and integration of movable devices should be taken.

# 6. Missing Beam-Beam Deflection during Beam Dump Process

In July 2012 an unconsidered single-turn beam loss mechanism was observed in the LHC. For a quantitative analysis, experimental studies and dedicated MAD-X [88] simulations were performed. The observations and the loss mechanism are presented in the following and the results from the simulations are compared to the experimental studies. Extrapolations for LHC operation in the mid-term and long-term future are discussed.

## 6.1. Observations and Introduction

In the context of this thesis, the acquisition chain for diamond BLMs was improved in 2012 for a better diagnostics of very fast beam losses (see Sec. 2.3.3). Subsequently, in July 2012 several beam dump events with **significant beam losses in the turn directly before the beam dump were observed.** Figure 6.1 shows the measured beam losses from beam 1 at the IR7 collimators for such a case. The losses from the dump of beam 1 itself lead to a sharp loss spike with a typical duration of 200 ns [29].

In this case, a dump of beam 2 had been initiated first due to an interlock of the beam 2 RF system[1]. Since the beam permit loops for the two beams were logically linked (see Sec. 2.3.4), beam 1 was subsequently dumped with a delay of 1.25 turns[2]. Thus, in the last turn of beam 1, many bunches were no longer colliding in the experimental interaction points (IPs), since the corresponding collision partners had already been extracted from the machine. Figure 6.2 illustrates the position of the abort gaps $\frac{1}{8}$ turn after firing the beam 2 dump kickers; there are no collisions in IP5 anymore. In particular, the long-range beam-beam deflections (see Sec. 3.2) are suddenly absent in such a case. This results in an instantaneous perturbation of the

[1] A problem with the cryogenics system for the beam 2 RF had been detected. Until the beam dump, no effect on the beam was expected or observed.

[2] Since the first bunches after the abort gaps are set to collide in IP1 and IP5, the beam 1 abort gap reaches the dump region in IR6 0.25 turns after the beam 2 abort gap. Due to the internal processing time of the beam interlock system, beam 1 was dumped with a delay of 1.25 turns [136].

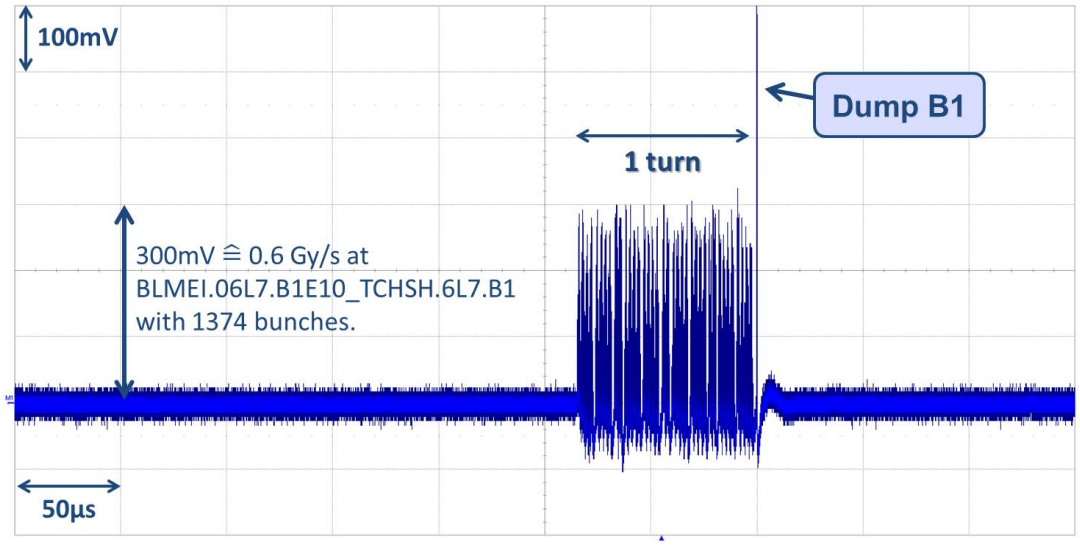


Figure 6.1.: Signal of beam 1 diamond BLM in IR7 versus time. Significant beam losses occur in the last turn before the beam dump.
Measurement on 08.07.2012 20:46:04. Beam energy: 4 TeV, bunch intensity: $1.4{\cdot}10^{11}$ protons, 1374 bunches per beam. For the used configuration, a diamond signal amplitude of 300 mV for 1374 circulating bunches corresponds to a beam loss rate of about 0.6 Gy/s at BLMEI.06L7.B1E10_TCHSH.6L7.B1.

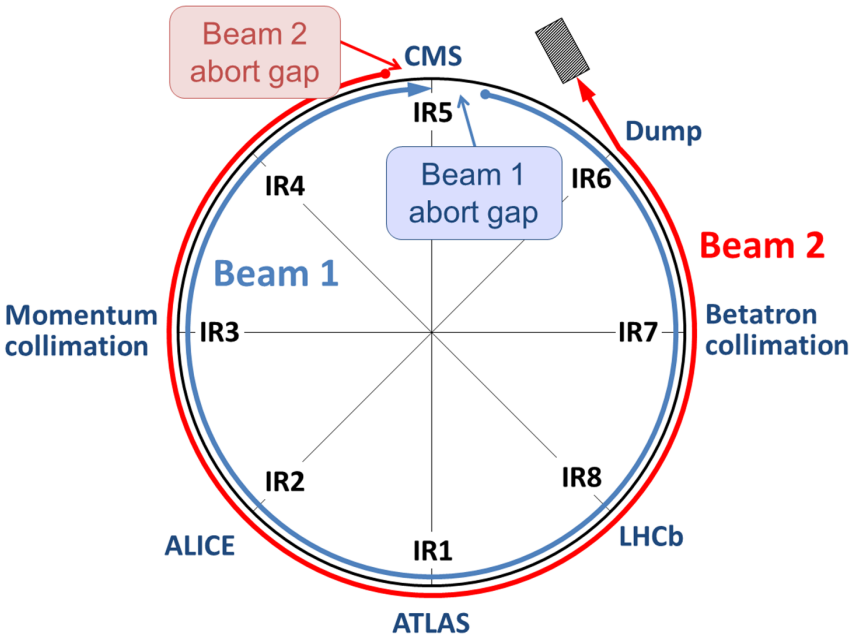


Figure 6.2.: $\frac{1}{8}$ turn after the firing of the beam 2 dump kickers, the first bunches of beam 1 no longer encounter any beam 2 collision partners in IP5. The arrows indicate the position of bunch number 1 for each beam, the dots the position of the last bunches before the abort gaps.
Unlike illustrated, the beams change between internal and external aperture at each collision point, as shown in Fig. 2.2).

trajectory as shown in Fig. 6.3 and corresponding beam losses at the collimators as illustrated in Fig. 6.1[3]. Since the crossing angle orbit bump in IR5 is in the horizontal plane (and so are the long-range beam-beam deflections), only the horizontal plane is affected directly downstream of IP5. The crossing angle bump in IR8 (and IR1 and IR2) is in the vertical plane[4], thus the vertical trajectory is affected at a later stage (see Fig. 6.3).

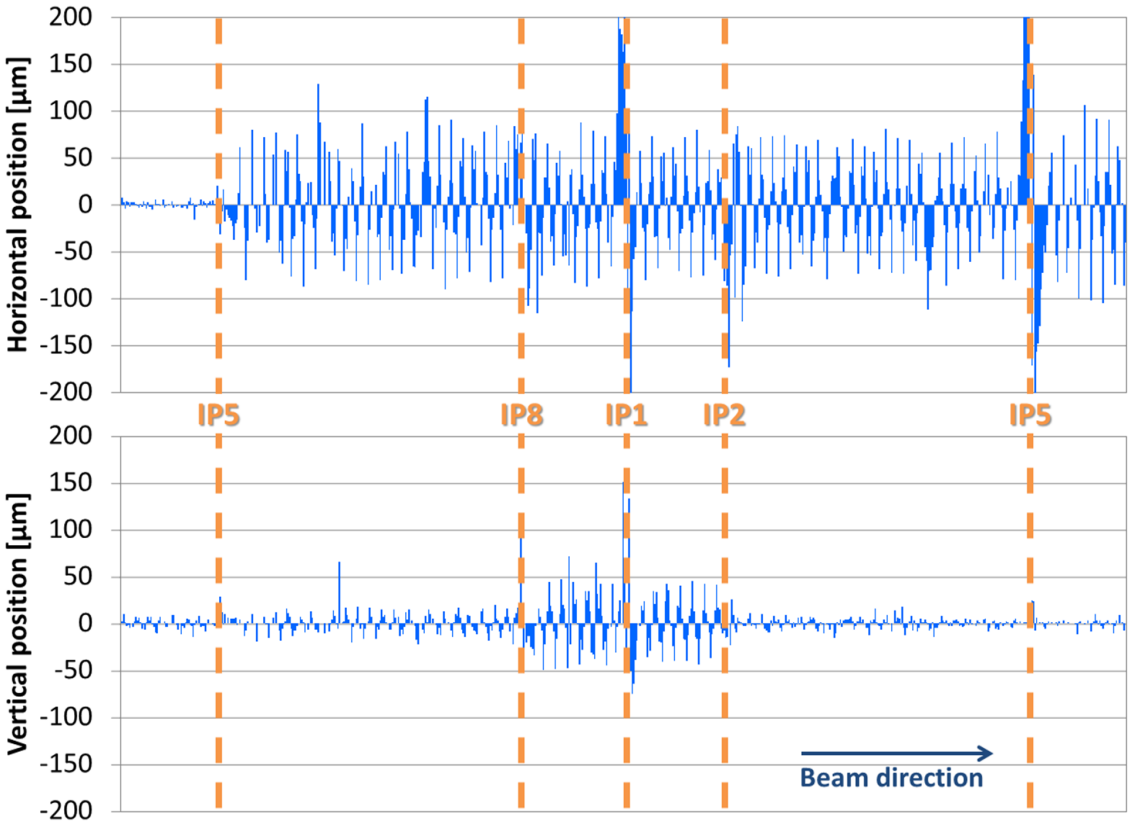


Figure 6.3.: Horizontal and vertical beam trajectory perturbation of beam 1 as measured by the ring beam position monitors (BPMs) in the turn directly after the beam 2 dump kickers were fired (post-mortem data). The measurement is a convolution of all bunches.
Measurement on 08.07.2012 20:46:04. Beam energy: 4 TeV, bunch intensity: $1.4{\cdot}10^{11}$ protons, 1374 bunches per beam. The beam position measurements w.r.t. the initial closed orbit before the beam dump are shown.

[3] A more detailed explanation of the event sequence is given in [136].

[4] In addition to the external crossing angle bumps, the beam-beam separation is affected by the experimental spectrometers around IP2 (vertical plane) and IP8 (horizontal plane). Furthermore, the beams are transversely separated in IP8 (in a skew plane) and IP2 (horizontal plane) to level the luminosity.

## 6.2. Experimental Studies

Two experimental tests with additional instrumentation for a better diagnostics of the beam 1 perturbations were performed in the LHC on 02.10.2012 and 13.12.2012. In both cases the beam permit loops for beam 1 and beam 2 were unlinked[5] and beam 2 was dumped first; the test conditions are summarized in Tab. 6.1.

| | **50 ns test** | **25 ns test** |
|---|---|---|
| Date | 02.10.2012 12:44:33 | 13.12.2012 08:26:54 |
| Fill | 3121 | 3425 |
| Bunch-spacing | 50 ns | 25 ns |
| Bunches per beam | 1230 | 84 |
| Average bunch intensity B1/B2 [$10^{11}$ protons] | 1.09/1.00 | 0.85/0.96 |
| Number of collisions IP1/2/5/8 | 1224/0/1224/992 | 72/0/72/0 |
| Half (external) crossing angle and plane IP1/2/5/8 [$\mu$rad] | -145v/145v/145h/90v | -80v/145v/68h/-220h |
| $\beta^*$ in IP1/2/5/8 [cm] | 60/300/60/300 | 100/300/100/300 |

Table 6.1.: Summary of conditions for the dedicated tests.

In the first test with a bunch-spacing of 50 ns, the beam losses due to the trajectory perturbations exceeded the BLM dump thresholds in IR7 and resulted in a subsequent dump of beam 1 after 4.25 turns. To reduce the losses while improving the signal-to-noise ratio, for the second test only 72 colliding bunches with 25 ns bunch-spacing and reduced crossing angles in IP1 and IP5 were used. The targeted half crossing angles were set to $\frac{\Theta}{2} = \mp 65\,\mu$rad instead of $\mp 145\,\mu$rad. However, this value is not consistent with the measured beam-beam separation at the BPMs close to IP1. As illustrated in Fig. 6.4a, the measured beam-beam separation is well reproduced by simulation with a vertical half crossing angle of $-80\,\mu$rad in IP1. In IP5, the measured beam-beam separation is reproduced best with a half crossing angle of $68\,\mu$rad, as shown in Fig. 6.4b. In the following, the latter values are used[6] and the results from the 25 ns test are presented (unless indicated otherwise).

[5] When the beam permit loops are unlinked, they are logically independent and the two beams can be dumped individually, as explained in Sec. 2.3.4.

[6] The nominal crossing angles for the 50 ns test (see Tab. 6.1) are within the measurement uncertainty consistent with the measured beam-beam separations.

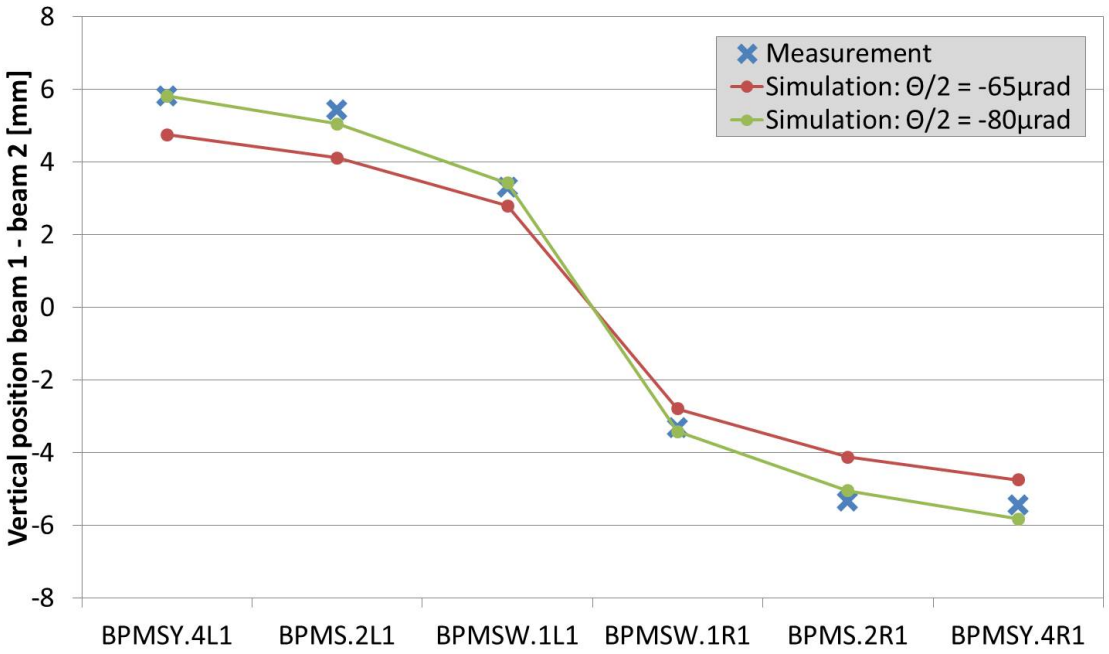


(a) Measured vertical beam-beam separation at BPMs in the common beam pipe around IP1 and simulated separations with half crossing angles of $\frac{\Theta}{2} = -65\,\mu$rad and $\frac{\Theta}{2} = -80\,\mu$rad in IP1.

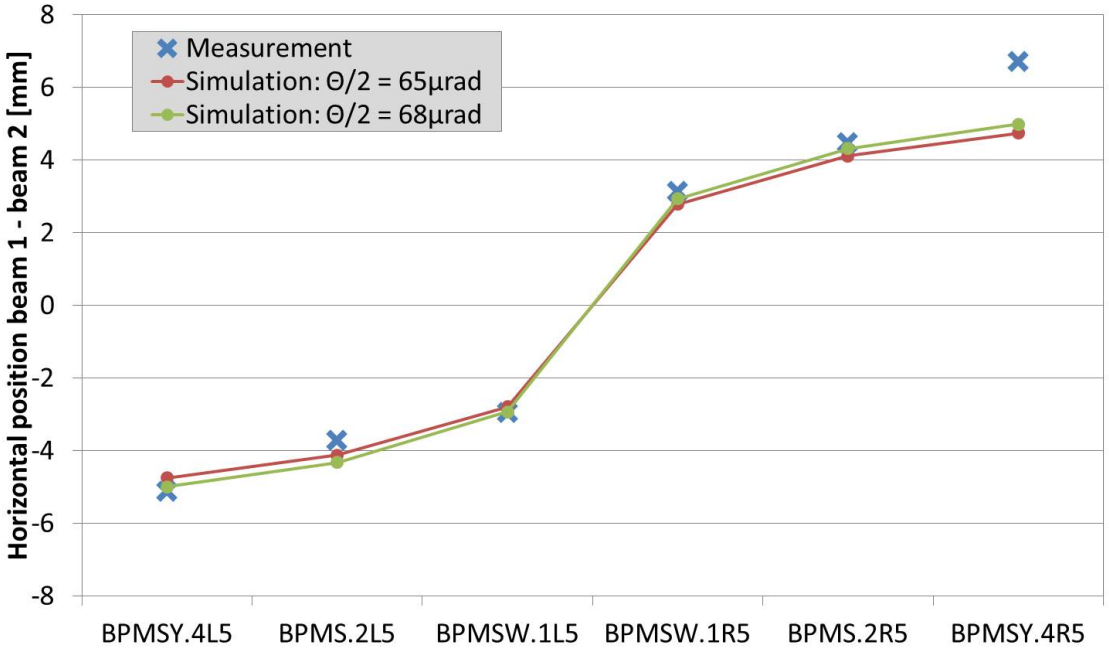


(b) Measured horizontal beam-beam separation at BPMs in the common beam pipe around IP5 and simulated separations with half crossing angles of $\frac{\Theta}{2} = 65\,\mu$rad and $\frac{\Theta}{2} = 68\,\mu$rad in IP5.

Figure 6.4.: Comparison of the measured beam-beam separation at BPMs around IP1 (a) and IP5 (b) with the simulated separations for different crossing angles.

Measurement on 13.12.2012 08:26:23. Beam energy: 4 TeV, bunch intensity B1/B2: $0.85/0.96 \cdot 10^{11}$ protons. Only the bunches 322-351 with full long-range encounters are taken into account.

As illustrated in Figure 6.5a, the absence of the long-range beam-beam deflections leads to a closed orbit perturbation. Fig. 6.5b shows the oscillation amplitude in the arcs from betatron fits of the closed orbit perturbations for each bunch. The amplitude of the closed orbit perturbation is about $150\,\mu\text{m} = 0.39\,\sigma_{\text{nom}}$ in the horizontal plane and $120\,\mu\text{m} = 0.31\,\sigma_{\text{nom}}$ in the vertical plane for the bunches with full long-range encounters. As shown in Fig. 6.5b, the effect is reduced for the PACMAN bunches (see Sec. 3.2).

As illustrated in Fig. 6.6a, the horizontal trajectory perturbation is even larger in the turn directly after the beam 2 dump kickers have been fired, with up to $230\,\mu\text{m} = 0.60\,\sigma_{\text{nom}}$ in the arcs and $-130\,\mu\text{m} = -0.37\,\sigma_{\text{nom}}$ at the primary horizontal collimator (TCP.C) in IR7. Fig. 6.6b shows that the **largest oscillation amplitude of $\approx 290\,\mu\text{m}$=$0.75\,\sigma_{\text{nom}}$** is reached in the fourth turn after the firing of the beam 2 dump kickers. The transverse damper then damps the oscillation and the beam stabilizes around the new closed orbit. The corresponding maximal arc oscillation amplitude in the vertical plane is $\approx 230\,\mu\text{m} = 0.60\,\sigma_{\text{nom}}$.

For the 50 ns test, peak oscillation amplitudes of $105\,\mu\text{m} = 0.27\,\sigma_{\text{nom}}$ (horizontal) and $100\,\mu\text{m} = 0.26\,\sigma_{\text{nom}}$ (vertical) were measured in the arcs.

The trajectory perturbation in the collimation region results in beam losses as shown in Fig. 6.7a, with the PACMAN structure being clearly visible. Since the losses are caused by coherent transverse betatron oscillations of the beam, the temporal beam loss evolution is modulated with the tune. The bunch-by-bunch tunes can be estimated via a fast Fourier-transformation (FFT) of the turn-by-turn beam loss evolution for each bunch. The FFT spectrum for each bunch is fitted with a modified Lorentz-function to increase the tune resolution as shown in Fig. 6.7b. The average fractional tune for the bunches with full long-range encounters is $0.3069 \pm 0.0003$[7]. A comparison with the fractional tunes measured by the base-band tune measurement system[8] ($Q_H = 0.307$, $Q_V = 0.320$) reveals that the tune estimated from the beam losses corresponds to the horizontal tune, indicating that the losses in the horizontal plane are dominant. This is in agreement with the larger oscillation amplitudes observed in the horizontal plane (see Fig. 6.5b and Fig. 6.6b).

[7] The FFT resolution is presently limited to about $3 \cdot 10^{-3} f_{\text{rev}}$ due to the limited length of the diamond BLM acquisition buffer (about 360 turns, for Fig. 6.7b only 200 turns are used). The resolution of the tune estimate can be improved by a fit as shown in Fig. 6.7b. The acquisition buffer length could be increased to about 10'000 turns during the first long shutdown (LS1), which would allow an FFT resolution of about $10^{-4} f_{\text{rev}}$. See [137] and [138] for a more detailed explanation.

[8] The base-band tune measurement system (BBQ) is the standard tune measurement system in the LHC [139].

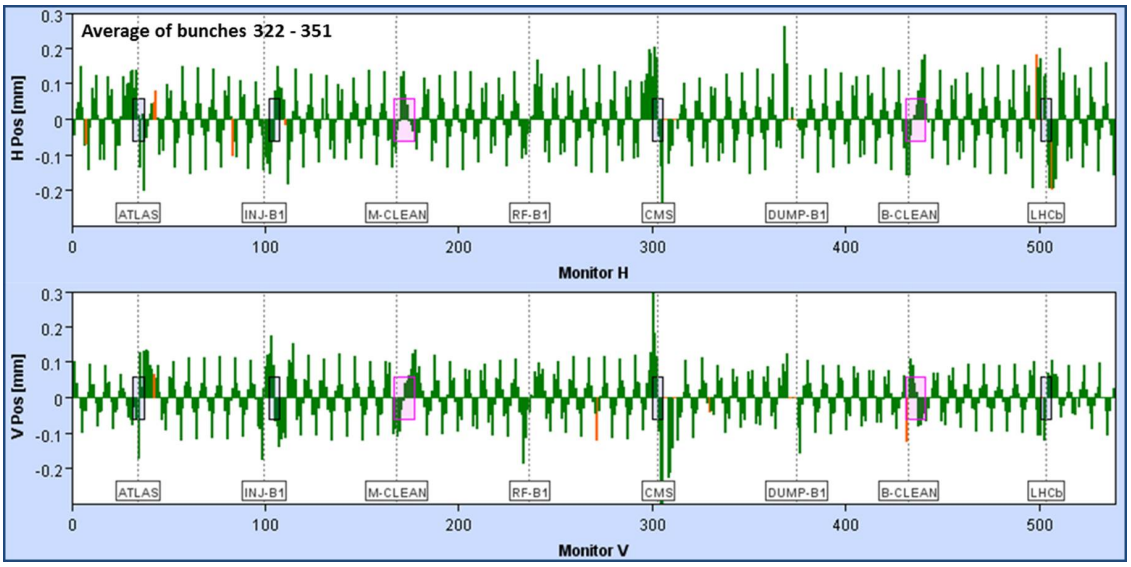


(a) Beam 1 closed orbit perturbation after the dump of beam 2 for the 30 bunches with full long-range encounters.

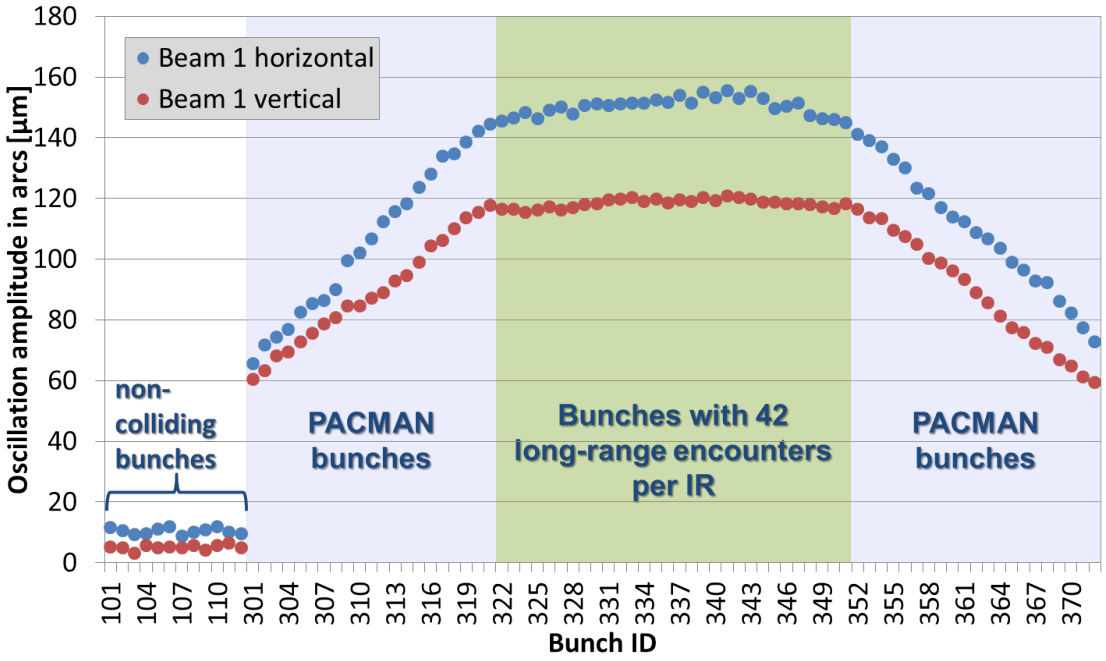


(b) Bunch-by-bunch amplitude of closed orbit perturbation from betatron fits.

Figure 6.5.: Beam 1 closed orbit perturbation after the dump of beam 2 for the bunches with full long-range encounters (a) and the amplitude of the closed orbit perturbation for each bunch (b).
Measurement on 13.12.2012 08:27:13. Beam energy: 4 TeV, bunch intensity B1: $0.85 \cdot 10^{11}$ protons. The bunch-by-bunch closed orbit measurements w.r.t. the initial bunch-by-bunch closed orbits before the beam dump are shown.

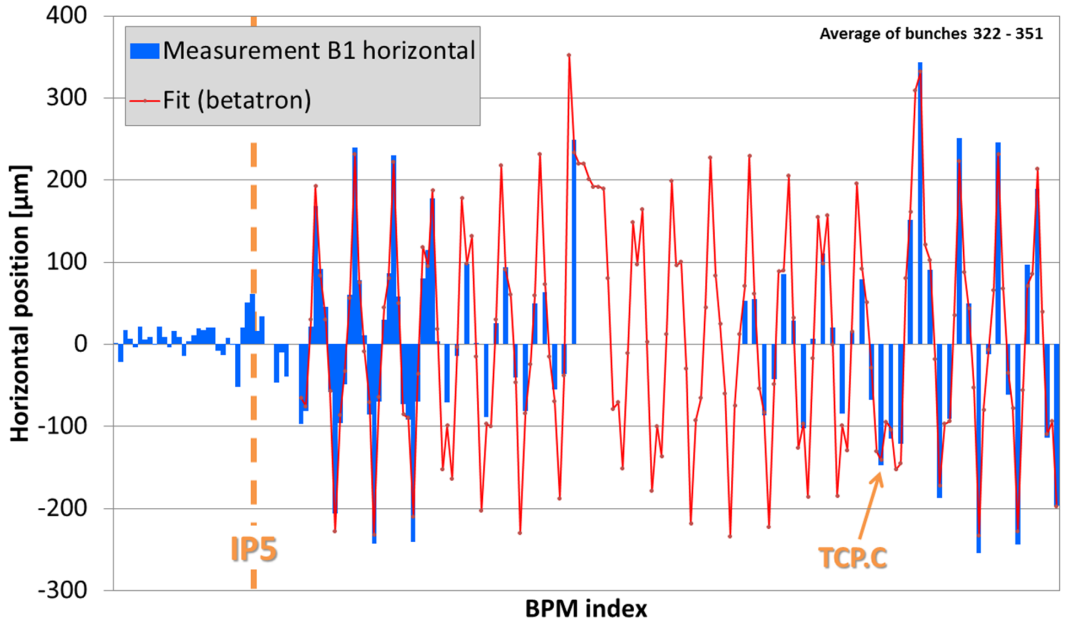


(a) Beam 1 horizontal position perturbation of the bunches with full long-range encounters for the turn directly after firing the beam 2 dump kickers. The red line is a fit of the betatron oscillation.

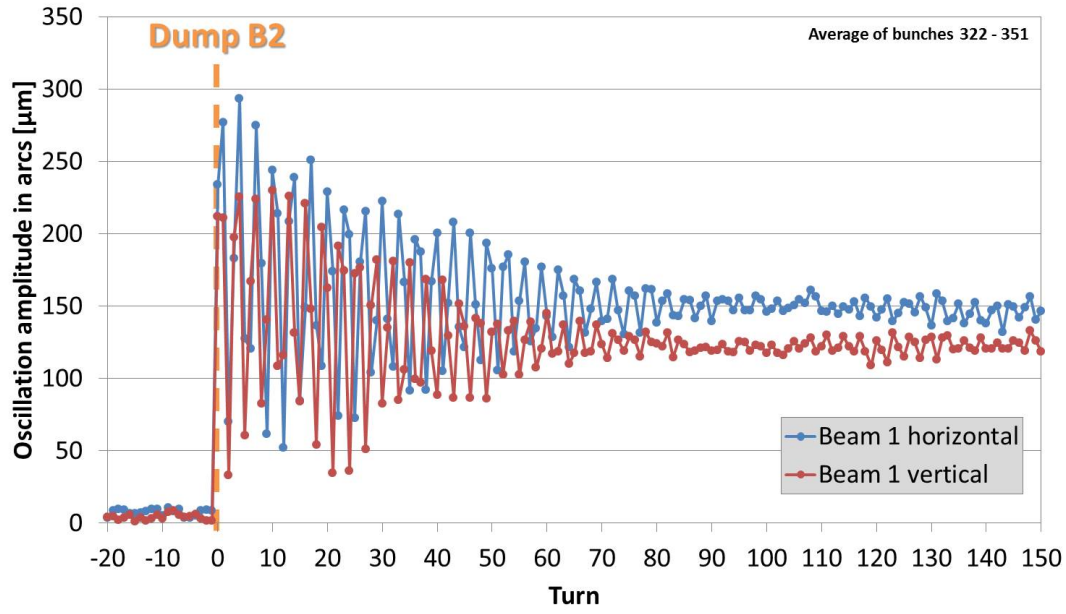


(b) Turn-by-turn oscillation amplitude of the position perturbation from a betatron fit for bunches with full long-range encounters.

Figure 6.6.: Beam 1 horizontal position perturbation of the bunches with full long-range encounters in the turn directly after firing the beam 2 dump kickers (a). The oscillation is damped by the transverse damper within about 80 turns and a new closed orbit is established (b).
Measurement on 13.12.2012 08:26:54. Beam energy: 4 TeV, bunch intensity B1: $0.85 \cdot 10^{11}$ protons. For several BPMs no acquisition data is available. The beam position measurements w.r.t. the initial closed orbit before the beam dump are shown.

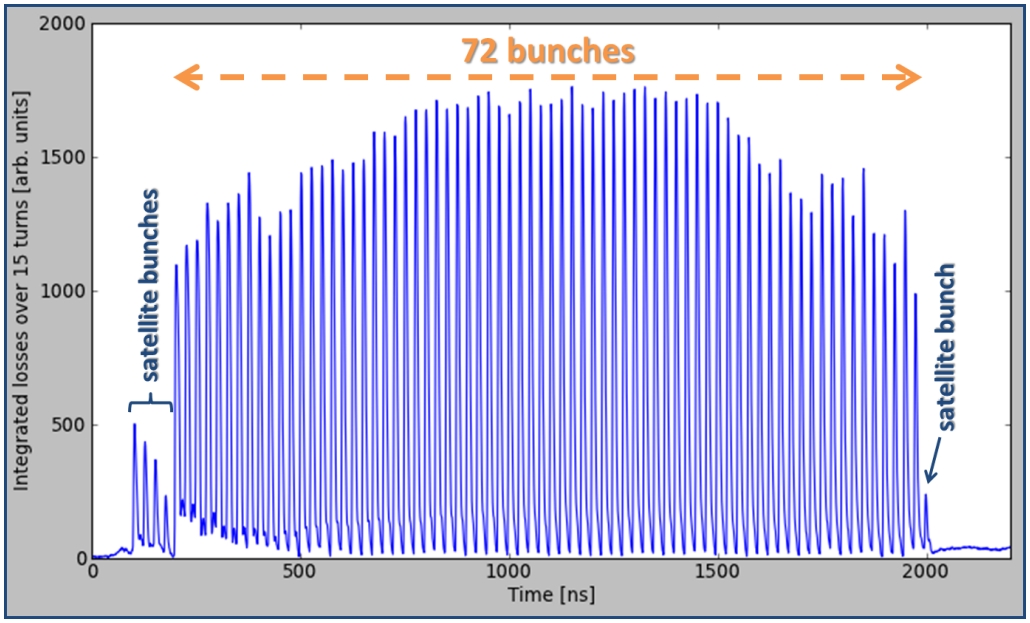


(a) Beam losses along the train of 72 colliding bunches after the dump of beam 2 measured with the beam 1 diamond BLM in IR7. The losses are integrated over 15 turns. Losses outside of the main bunch train which are consistent with the 25 ns bunch-spacing are believed to be caused by satellite bunches.

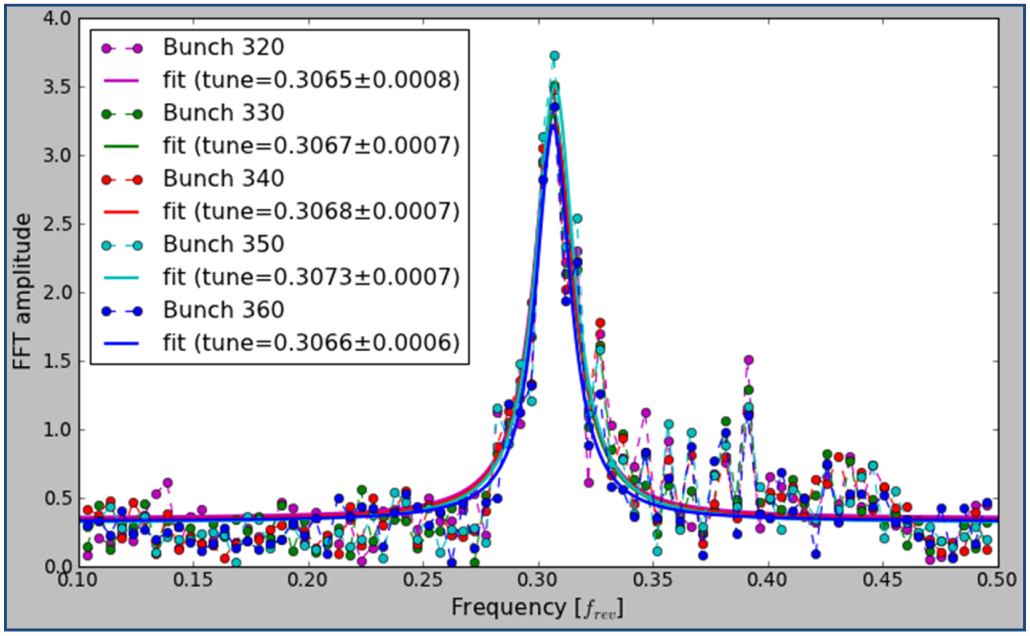


(b) FFT of the turn-by-turn beam loss evolutions in the first 200 turns after the dump of beam 2 (in units of the revolution frequency $f_{\text{rev}} = 11'245\,\text{Hz}$) for selected bunches. The FFT spectra are fitted with a modified Lorentz-function $y(x) = \frac{B^2}{(x-A)^2+B^2} \cdot C + D$ with the fit parameters $A$, $B$, $C$ and $D$; $A$ represents the tune.

Figure 6.7.: Beam losses along the train of 72 colliding bunches after the dump of beam 2 (a). FFT spectra of temporal beam loss evolutions and tune estimates (b).

Measurement on 13.12.2012 08:26:54. Beam energy: 4 TeV, bunch intensity B1: $0.85 \cdot 10^{11}$ protons.

## 6.3. Simulations

Dedicated simulations based on the particle accelerator simulation code MAD-X [88] were performed for a quantitative comparison of the experimental results and extrapolations for LHC operation after LS1 and in the HL-LHC era. The simulations are based on a particle tracking for beam 1 of either one particle in the center of the bunch or multiple particles in a Gaussian distribution[9] for about 30 turns. After 10 initial revolutions without beam-beam interactions, all long-range and head-on beam-beam interactions are activated (using the MAD-X BEAMBEAM module[10] [88]) with negative sign to simulate the sudden absence of these interactions. In Fig. 6.8 and Fig. 6.9 the simulated trajectory in the turn after the activation of the beam-beam interactions (w.r.t. the initial closed orbit) is shown for both tests[11] together with the BPM measurements for the bunches with full long-range encounters, as presented in Fig. 6.6a.

As illustrated in Fig. 6.8 and Fig. 6.9, the average trajectory perturbation of the simulated particle ensemble agrees well with the simulated perturbation of the bunch center. This shows that for this effect the non-linear influence of the beam-beam force on the particle ensemble can be neglected for large separations[12] (see also Sec. 3.2).

For all cases, the phases of the simulated oscillations are very consistent with the measurements. The measured oscillation amplitudes are between 5% and 15% smaller than the simulated amplitudes. This discrepancy is within the expected accuracy of simulations and measurements.

Among the most important uncertainties are the exact crossing angles. A measurement with higher precision could be done for example by the LHCb experiment via primary vertex reconstruction of beam-gas interactions [140]. Moreover, the simulations assume an ideal machine: misalignments, field errors and the corresponding corrections are not included.

Another particularity of the long-range beam-beam deflections is that they imply a small bunch-dependent closed orbit perturbation with an amplitude of up to

[9] The particles are distributed according to a six dimensional Gaussian distribution (position and momentum in horizontal, vertical and longitudinal plane) with a transverse normalized emittance of $\epsilon^{\mathrm{n}}_{\mathrm{x,y}} = 3.5\,\mu\mathrm{m}\cdot\mathrm{rad}$ (50 ns test) and $\epsilon^{\mathrm{n}}_{\mathrm{x,y}} = 3.15\,\mu\mathrm{m}\cdot\mathrm{rad}$ (25 ns test), a $(4\,\sigma)$ bunch length of 1.2 ns and a momentum spread of $\frac{\Delta p}{p} = 1.129\cdot 10^{-4}$.

[10] For beam 2, a Gaussian transverse distribution with same emittances as for beam 1 is assumed.

[11] For the multi-particle simulations, the average trajectory of all particles (w.r.t. the initial closed orbit) is shown.

[12] In the simulations shown in Fig. 6.8 and Fig. 6.9, the transverse separation of all long-range encounters is $\geq 3.7\,\sigma$ and $\geq 6.4\,\sigma$, respectively.

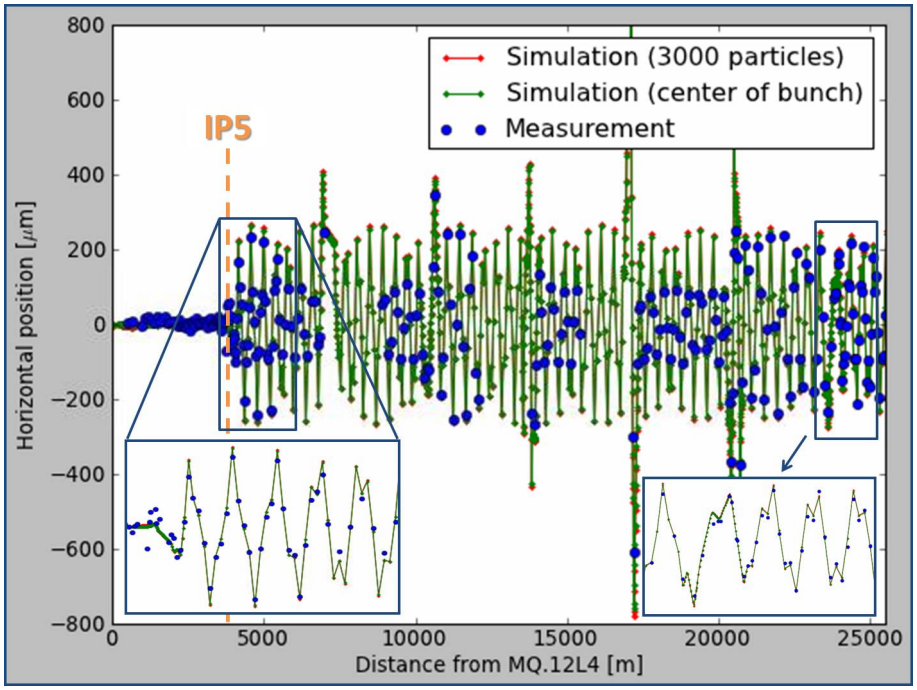


(a) 25 ns test, horizontal plane.

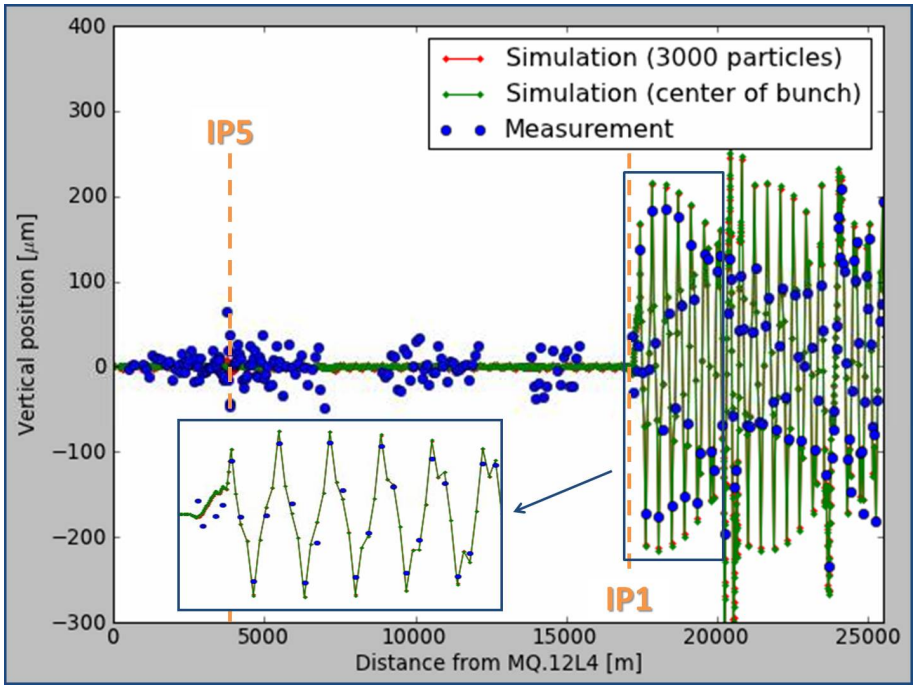


(b) 25 ns test, vertical plane.

Figure 6.8.: Simulated trajectory perturbation of beam 1 in the turn directly after the firing of the beam 2 dump kickers for horizontal (a) and vertical plane (b) and the measured perturbations for bunches with full long-range encounters for the 25 ns test.

Simulated and measured trajectories are w.r.t. the (simulated/measured) closed orbit before the dump of beam 2. There is for several BPMs no acquisition data available, as illustrated in Fig. 6.6a. In some regions, this concerns systematically only the BPMs at large or small $\beta$-function.

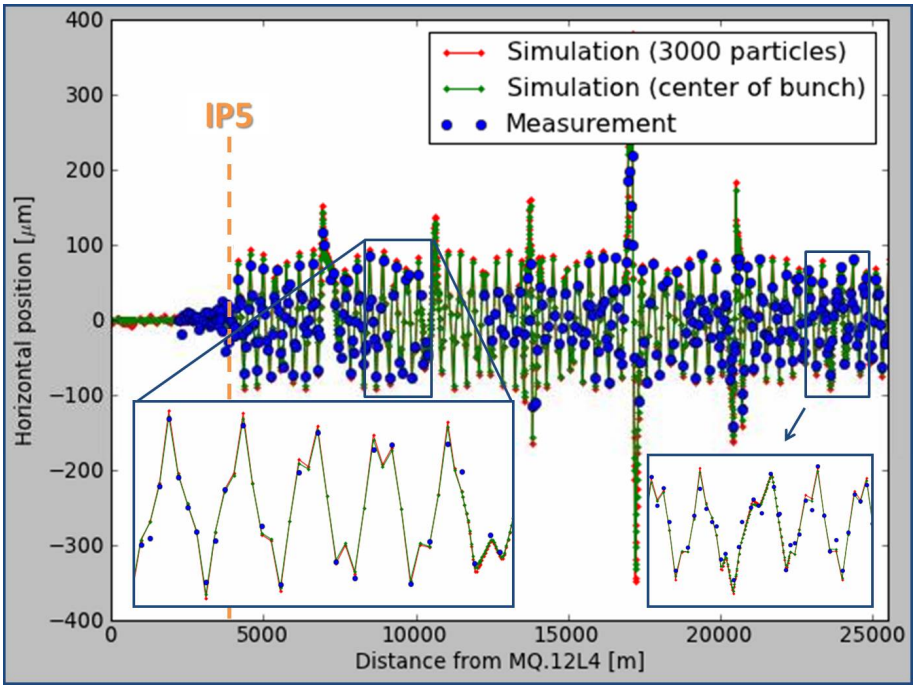


(a) 50 ns test, horizontal plane.

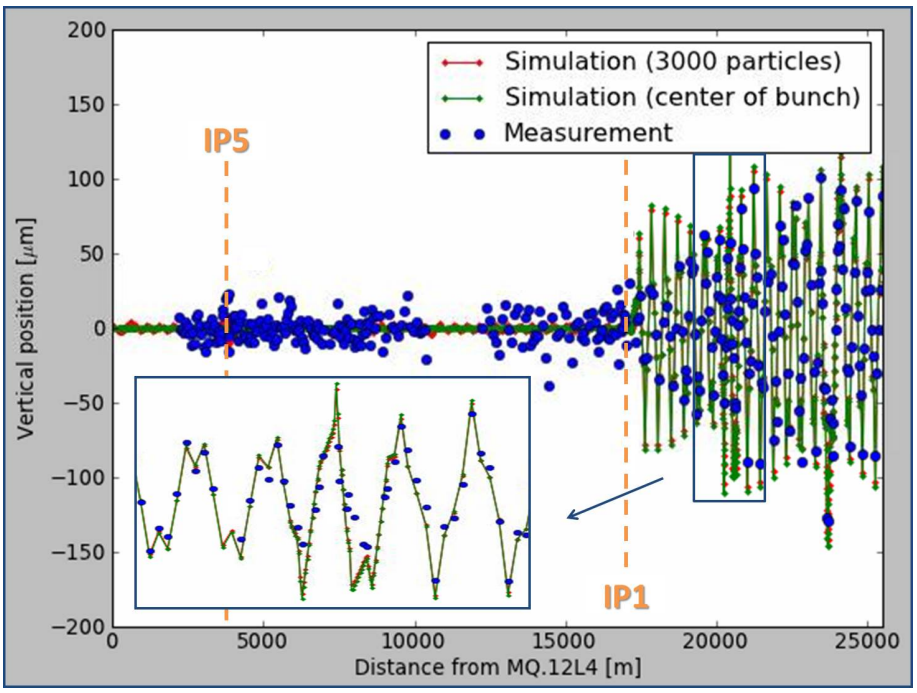


(b) 50 ns test, vertical plane.

Figure 6.9.: Simulated trajectory perturbation of beam 1 in the turn directly after the firing of the beam 2 dump kickers for horizontal (a) and vertical plane (b) and the measured perturbations for bunches with full long-range encounters for the 50 ns test.

Simulated and measured trajectories are w.r.t. the (simulated/measured) closed orbit before the dump of beam 2. There is for several BPMs no acquisition data available, as illustrated in Fig. 6.6a. In some regions, this concerns systematically only the BPMs at large or small $\beta$-function.

$0.3\,\sigma_{\mathrm{nom}}$ - $0.4\,\sigma_{\mathrm{nom}}$ in case of the 25 ns test, as shown in Fig. 6.5. This affects the beam-beam separation at the long-range encounters. This is partially accounted for by matching the crossing angles in the simulations to the measured beam-beam separations at the BPMs around the IPs, as illustrated in Fig. 6.4. Nevertheless, the exact effect (on a bunch-by-bunch bases) is not taken into account in the simulations. However, for the 50 ns test, the expected closed orbit perturbation of about $0.1\,\sigma_{\mathrm{nom}}$ - $0.2\,\sigma_{\mathrm{nom}}$ is small compared to the separation at the long-range encounters of at least $6.4\,\sigma_{\mathrm{nom}}$. Thus, in particular for the 50 ns test, this effect can be neglected. Dedicated simulations with a self-consistent closed orbit based on the simulation program TRAIN [88] are envisaged for a further quantification of this effect.

## 6.4. Extrapolation and Conclusions

The experimental studies demonstrated that the sudden absence of the long-range beam-beam encounters after the dump of a single beam can result in significant trajectory perturbations of the counter-rotating beam and consequent beam losses within a single turn. The measured trajectory perturbations are quantitatively consistent with MAD-X simulations. This allows extrapolations for LHC operation after LS1 and in the HL-LHC era.

Under the simplified assumption that the deflections from all $N_{\mathrm{LR}}$ long-range encounters have a betatron phase advance of 90° from the IP, the normalized[13] oscillation amplitude due to the missing long-range beam-beam deflections of each IR is with Eq. 3.10 given by[14]

$$\frac{\Delta r_{\mathrm{max}}}{\sigma_{\mathrm{nom}}} = \sum_{i=1}^{N_{\mathrm{LR}}} \Delta r_i' \cdot \frac{\sqrt{\beta_{\mathrm{LR,i}} \cdot \gamma_r}}{\sqrt{\epsilon_{\mathrm{nom}}^{\mathrm{n}}}}. \tag{6.1}$$

With Eq. 3.13 and Eq. 3.14, the normalized oscillation amplitude is given by

$$\frac{\Delta r_{\mathrm{max}}}{\sigma_{\mathrm{nom}}} \propto \sum_{i=1}^{N_{\mathrm{LR}}} \frac{N_b}{\gamma_r \cdot d_i} \cdot \frac{\sqrt{\beta_{\mathrm{LR,i}} \cdot \gamma_r}}{\sqrt{\epsilon_{\mathrm{nom}}^{\mathrm{n}}}} \propto N_{\mathrm{LR}} \cdot \frac{N_b}{\Theta} \cdot \frac{1}{\sqrt{\beta^* \gamma_r \epsilon_{\mathrm{nom}}^{\mathrm{n}}}}. \tag{6.2}$$

The scaling of the normalized oscillation amplitudes as given by Eq. 6.2 is summarized in Tab. 6.2 for the operational parameters after the first long shutdown (LS1)

[13] In the following, all oscillation amplitudes are normalized to the beam size with the same nominal (normalized) emittance $\epsilon_{\mathrm{nom}}^{\mathrm{n}} = 3.5\,\mu\mathrm{m} \cdot \mathrm{rad}$.

[14] $\beta_{\mathrm{LR,i}}$ is the $\beta$-function at long-range encounter number $i$, $\beta^*$ the $\beta$-function at the IP, $\gamma_r$ the relativistic gamma factor, $N_b$ the bunch intensity of the counter-rotating beam and $\Theta$ the full crossing angle.

| | **w.r.t. 50 ns test** | **w.r.t. 25 ns test** | **w.r.t. 2012 operation** |
|---|---|---|---|
| Post LS1 | 2.1 | 0.7 (H) / 0.8 (V) | 1.3 |
| HL-LHC | 3.8 | 1.2 (H) / 1.4 (V) | 2.4 |

Table 6.2.: Scaling factors of the normalized oscillation amplitudes as given by Eq. 6.2 for the operational parameters after LS1 and in the HL-LHC era relative to the test conditions in the 50 ns test and the 25 ns test (see Tab. 6.1) and typical operational conditions at the end of the 2012 physics run (see Tab. 2.1). The different scaling factors for horizontal (H) and vertical plane (V) in case of the 25 ns test account for the different crossing angles, as given in Tab. 6.1.

and in the HL-LHC era[15] w.r.t. the test conditions and typical 2012 operational conditions.

For operation **after LS1**, the effect increases by about 30% w.r.t. 2012 operation. The corresponding maximal oscillation amplitudes are expected to increase up to $\mathbf{0.5\,\sigma_{nom}}$ **-** $\mathbf{0.6\,\sigma_{nom}}$[16]. As described in Sec. 2.4.2, the resulting beam losses may, depending on the transverse tail distribution, reach critical levels. Therefore, regular tail population measurements e.g. by collimator scraping tests [46] or an analysis of the beam losses throughout the operational cycle [47] are strongly recommended (as long as no dedicated diagnostics for the transverse tail population is available). For a similar transverse tail population as in 2012, no critical increase of the beam losses due to the described effect is expected (despite the increased stored beam energy), since the proposed collimator positions for after LS1 imply a retraction of the primary collimators (in IR7) by $1.2\,\sigma_{\mathrm{nom}}$ w.r.t. the 2012 positions[17] (see Fig. 2.7).

For operation in the **HL-LHC** era, oscillation amplitudes of up to $\mathbf{0.9\,\sigma_{nom}}$ **-** $\mathbf{1.1\,\sigma_{nom}}$ within the first few turns after the beam dump are expected. Figure 6.10 shows the simulated beam 1 oscillation amplitudes for HL-LHC optics with nominal HL-LHC crossing angles and parameters in the first 20 turns after the dump of beam 2.

The simulated vertical peak oscillation amplitude within the first 5 turns after the dump of beam 2 is $0.84\,\sigma_{\mathrm{nom}}$. With the measured oscillations amplitudes in the 25 ns

[15] Extensive layout-changes of the interaction regions are foreseen for the HL-LHC upgrade, which include a different positioning of the separation dipole magnets. This increases the number of relevant long-range beam-beam interactions $N_{\mathrm{LR}}$ by about 15%.

[16] Depending on the reference test and the applied scaling factors of Tab. 6.2.

[17] The retraction is the same in millimeter, but is reduced in $\sigma_{\mathrm{nom}}$ due to the higher top beam energy.

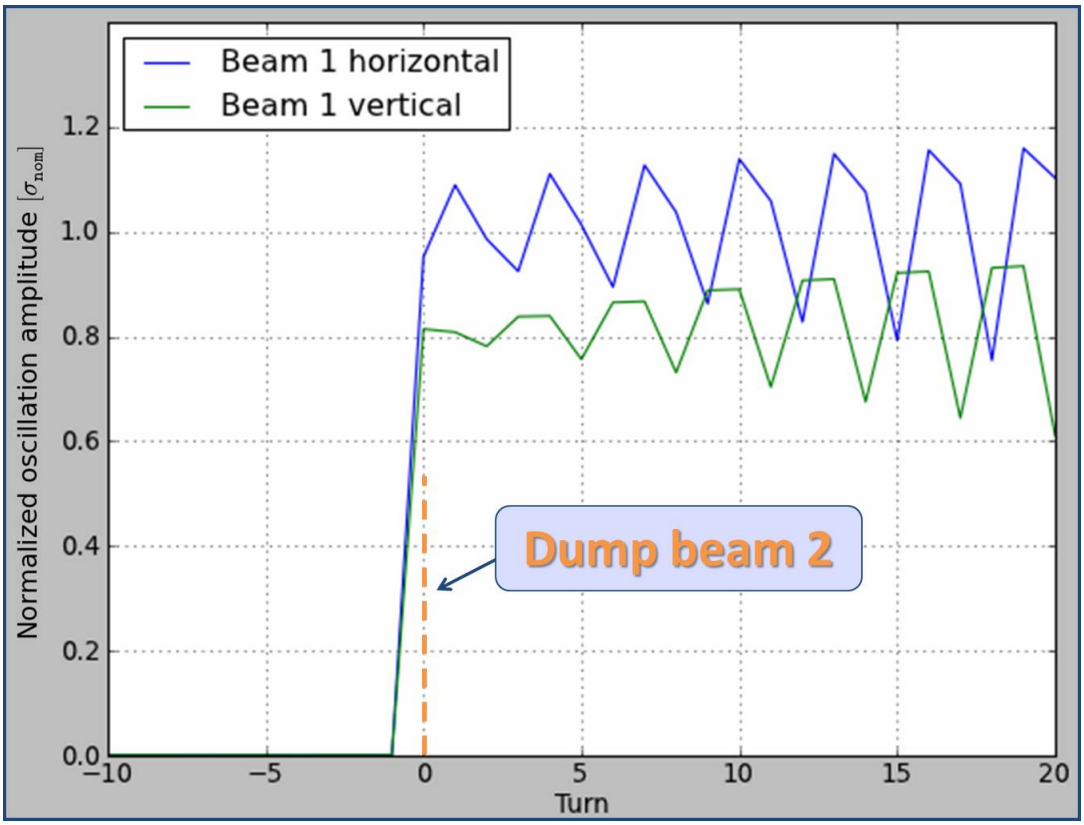


Figure 6.10.: Normalized oscillation amplitude of the horizontal and vertical trajectory perturbations due to the missing long-range beam-beam deflections for HL-LHC.
The simulations are based on the *SLHCV3.1b* upgrade optics [50] and the HL-LHC parameters given in Tab. 2.1. The oscillation amplitudes are normalized to the nominal beam size $\sigma_{\text{nom}}$ with a nominal (normalized) emittance of $3.5\,\mu\text{m}\cdot\text{rad}$. Only the long-range beam-beam deflections in IR1 and IR5 are considered. The simulation does not include the effect of the transverse damper. The perturbation in the horizontal plane is larger due to the horizontal separation downstream of the D1 separation dipole magnets in IR1 and IR5 (see Sec. 2.3.1).

test and the scaling factors in Tab. 6.2, the same value of $0.60\,\sigma_{\text{nom}} \cdot 1.4 = 0.84\,\sigma_{\text{nom}}$ is predicted.

For the horizontal plane a peak oscillation amplitude of $0.75\,\sigma_{\text{nom}} \cdot 1.2 = 0.90\,\sigma_{\text{nom}}$ is expected from the scaling of the 25 ns test results to HL-LHC parameters. However the simulated peak oscillation amplitude within the first 5 turns after the dump of beam 2 is $1.11\,\sigma_{\text{nom}}$ (see Fig. 6.10). This discrepancy results from the horizontal separation of the beams downstream of the D1 separation dipole magnets in IR1 and IR5 (see Sec. 2.3.1), which leads to an in total 6% larger perturbation in the horizontal plane for the 25 ns test. With the HL-LHC IR layout and parameters this effect increases, which is taken correctly into account in the simulations but not by the simple scaling with Eq. 6.2.

As discussed in Sec. 2.4.2, with the present transverse beam distribution, single turn trajectory perturbations with amplitudes of about $1\,\sigma_{\mathrm{nom}}$ can lead to beam losses which are far beyond the specifications of the collimation system and imply a significant damage potential.

Since the described effect occurs regularly during normal LHC operation, a fast and reliable diagnostics (and interlocking) of the transverse tail population is essential for safe operation in the HL-LHC era. Such a diagnostics could e.g. be based on the synchrotron light monitor (BSRT) - related studies are strongly encouraged.

Furthermore, a depletion of the transverse tail population may be required. A hollow electron-lens [141] would provide this functionality. Dedicated studies are presently ongoing and are strongly supported [142]. This aspect is discussed further in Sec. 7.4.4.

# 7. Crab Cavity Failures

With the HL-LHC upgrade program, crab cavities will be installed in the LHC to compensate the geometric luminosity loss due to the crossing angle as described in Sec. 2.5 and Sec. 3.2. The baseline is a local scheme with crab cavities around the ATLAS and CMS experiments. In the event of a failure (e.g. a control-logic failure or a cavity quench), the voltage and/or phase of a crab cavity can change significantly within the reaction time of the LHC machine protection systems of up to about three LHC turns. This can lead to large, global betatron oscillations of the beam.

The impact of crab cavities on the beam dynamics, in particular for failure cases, is discussed and the results of dedicated simulations are presented. Strategies for the detection of crab cavity failures, the protection of the LHC and the mitigation of the failure impact to an acceptable level are proposed.

## 7.1. Crab Cavity Operation

Crab cavities induce a transverse dipole deflection of the beam with a sinusoidal modulation that is determined by the deflecting voltage amplitude $V_{\perp,0}$, the cavity frequency $f$ and the phase $\Phi$, a so-called tilt-kick. For a relativistic beam, this transverse deflection is with Eq. 3.1 and Eq. 3.17 given by

$$\Delta r' = -\frac{q}{E} \cdot V_{\perp,0} \cdot \sin\left(\Phi + 2\pi f \cdot \frac{z}{c}\right), \tag{7.1}$$

where $q$ is the particle charge, $E$ the particle energy, $z$ the longitudinal particle position w.r.t. the bunch center and $c$ the velocity of light [79]. The transverse displacement at the experimental interaction point (IP), $\Delta r_{\mathrm{IP}}(z)$, which is required to compensate for the crossing angle $\Theta$ can be derived from the geometry of the crossing at the IP:

$$\Delta r_{\mathrm{IP}}(z) = z \cdot \tan\left(\frac{\Theta}{2}\right).$$

Thus, the transverse deflection at the position of the crab cavity upstream of the IP, which is needed to compensate for the crossing angle is with Eq. 3.10 given by

$$\Delta r'(z) = \frac{\Delta r_{\mathrm{IP}}(z)}{\sqrt{\beta^* \beta_u} \cdot \sin(\Delta\psi) \cdot n_{cc}} = \frac{z \cdot \tan(\frac{\Theta}{2})}{\sqrt{\beta^* \beta_u} \cdot \sin(\Delta\psi) \cdot n_{cc}} \tag{7.2}$$

with $\beta^*$ and $\beta_u$ being the $\beta$-functions at the IP and at the concerned crab cavity upstream of the IP, respectively. $\Delta\psi$ is the betatron phase advance from the crab cavity to the IP and $n_{cc}$ the number of crab cavities per beam on either side of the IP. From Eq. 7.1 and Eq. 7.2 the theoretically optimal ($z$-dependent) amplitude of the transverse deflecting voltage to compensate the crossing angle can be derived:

$$V_{\perp,0}(z) = -\frac{E \cdot z \cdot \tan(\frac{\Theta}{2})}{q \cdot \sin\left(\Phi + 2\pi f \cdot \frac{z}{c}\right) \sqrt{\beta^* \beta_u} \cdot \sin(\Delta\psi) \cdot n_{cc}}.$$

Since the voltage amplitude $V_{\perp,0}$ is constant along the bunch during normal operation, it is optimized for a particle in the bunch center. Assuming a nominal crab cavity phase of $\Phi = 0$, the linear approximation yields:

$$\lim_{z \to 0} V_{\perp,0}(z) = -\frac{c \cdot E \cdot \tan(\frac{\Theta}{2})}{q \cdot 2\pi f \cdot \sqrt{\beta^* \beta_u} \cdot \sin(\Delta\psi) \cdot n_{cc}}. \tag{7.3}$$

In the local crab cavity scheme (see Sec. 3.2), the tilt-kick is locally compensated by crab cavities downstream of the IP. For an optimal compensation of the tilt-kick, the betatron phase advance between the crab cavities upstream and downstream of the IP should be $\Delta\psi_{cc} = 180°$. The optimal transverse deflecting voltage amplitude of the downstream crab cavities can be calculated with Eq. 3.9 and is given by:

$$\tilde{V}_{\perp,0} = -\sqrt{\frac{\beta_u}{\beta_d}} \cos\left(\Delta\psi_{cc}\right) \cdot V_{\perp,0} \tag{7.4}$$

with $\beta_d$ being the $\beta$-function at the concerned downstream crab cavity[1].

For the HL-LHC, a dedicated upgrade optics which includes crab cavities is proposed [50]: the *SLHCV3.1b* optics has a symmetric $\beta^*_{x,y} = 15\,\text{cm}$ and a half crossing angle of $\frac{\Theta}{2} = 295\,\mu\text{rad}$ (see Tab. 2.1). Furthermore, the layout of IR1 and IR5 is significantly modified to allow the installation of new (and longer) final focus triplet quadrupoles. In order to simplify the alignment of the crab cavities, the crossing angle bumps will be closed on the IP-side of the crab cavities, which requires additional orbit corrector magnets. Given the demonstrated performance of the crab cavity prototypes (see Sec. 2.5), at least $n_{cc} = 2 - 3$ crab cavities per beam on either side of each IP are needed in order to obtain the required transverse deflection. However, for machine protection considerations (which are discussed later in

[1] It is often stated in literature that $\tilde{V}_{\perp,0} = -R_{22} \cdot V_{\perp,0}$ is optimal, with $R_{22}$ being the (2,2) element of the transfer matrix (see Sec. 3.1.3) from the crab cavity upstream of the IP to the crab cavity downstream of the IP [79]. With $\Delta\psi_{cc} = 180°$, this is equal to Eq. 7.4. However, with $\Delta\psi_{cc} \approx 181.6°$ and $\alpha_d \approx 48$ at the downstream crab cavity (*SLHCV3.1b* optics), the resulting $\tilde{V}_{\perp,0}$ is about 65% smaller than given by Eq. 7.4 and and the deflection of the upstream crab cavity is no longer optimally compensated. In the general case, Eq. 7.4 is optimal to minimize the betatron oscillation amplitude outside of the IR.

this chapter), the baseline is $n_{cc} = 3$. The corresponding transverse deflecting crab cavity voltages, as given by Eq. 7.3 and Eq. 7.4 are shown in Tab. 7.1 together with a summary of the design parameters for the LHC crab cavities.

| | | |
|---|---|---|
| Frequency of crab cavities | [MHz] | 400.79 |
| Number of crab cavities per beam on either side of IP ($n_{cc}$) | | 3 |
| $\beta$-function at crab cavities | [m] | 2800 - 3700 |
| Peak transverse deflecting voltage ($V_{\perp,0}$, $\tilde{V}_{\perp,0}$) | [MV] | 3.5 - 4.0 |
| $R_a/Q_0$ | [Ω] | 300 - 900 |
| $Q_0$ | | $\geq 1 \cdot 10^{10}$ |
| External quality factor[2] ($Q_{\text{ext}}$) | | $1 \cdot 10^5$ - $1 \cdot 10^6$ |
| Available RF power ($P_{g,\max}$) | [kW] | $\approx 80$ |

Table 7.1.: Summary of operational and design parameters for LHC crab cavities [65]. See Sec. 3.3 for explanations.

The required RF generator power $P_g$ per crab cavity is for centered beams and tuned cavities ($\Delta f = 0$) according to Eq. 3.25 about 10 kW (with $Q_{\text{ext}} = 1 \cdot 10^6$, $R_a/Q_0 = 300\,\Omega$ and $V_{\perp,0} = 3.5\,\text{MV}$). However, $P_g$ increases according to Eq. 3.26 up to about 30 kW for a 1 mm transverse offset and a nominal beam current of 1.1 A with HL-LHC parameter (see Tab. 2.1). For a slightly detuned cavity, the required RF power increases further (see Eq. 3.27) by about 23 kW for $\Delta f = 300\,\text{Hz}$. In order to provide additional operational margins, the installation of RF power generators with a peak output power of $P_{g,\max} \approx 80\,\text{kW}$ for each cavity is foreseen (see Tab. 7.1).

The effect of the crab cavities is only needed when the beams are in collisions. Thus, the crab cavities are detuned and operated at very low voltage when they are not needed, to make them transparent for the beams [143]. Throughout collisions, the crab cavities are operated at nominal voltage to compensate the geometric luminosity loss due to the crossing angle (see Sec. 3.2).

It has been proposed to use crab cavities for luminosity leveling [65, 79, 144]. However, a crab cavity operation with reduced transverse deflecting voltage implies a longitudinal shortening of the luminous region [145] and (for $\Theta \ll \pi$) the peak longitudinal pile-up density remains constant, as illustrated in Fig. 7.1. The longitudinal pile-up density is one of the main luminosity limitations though (see Sec. 3.2). In this context, an operation with nominal crab cavity voltage (full compensation of the crossing angle) and luminosity leveling by e.g. $\beta^*$-reduction is preferable [145].

[2] $Q_{\text{ext}}$ is adjusted such that $Q_{\text{ext}} \cdot R_a/Q_0$ is constant. The value is defined by the available RF generator power and the beam loading tolerances [65, p. 4].

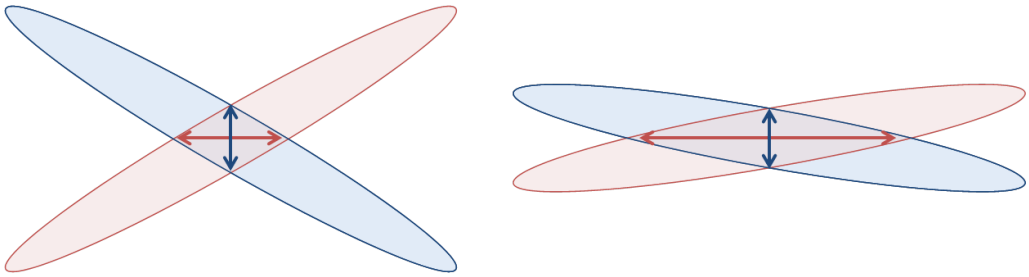

Figure 7.1.: Illustration of bunches interacting under different angles at the IP. The longitudinal size of the overlapping (luminous) region, indicated by the red arrow, is larger for smaller angles. However, the maximal number of interactions per unit length (longitudinal pile-up density), represented by the blue arrow, remains almost constant (for small angles).

### Beam Dynamics of Crab Cavity Failures

In case of a failure of a single crab cavity, i.e. a change of voltage and/or phase, the tilt-kick of the crab cavities is no longer locally compensated which results in a global betatron oscillation. With Eq. 3.10, Eq. 7.1 and the transverse deflecting voltage given by Eq. 7.3, the transverse displacement of a particle (in the first turn) at the longitudinal position $s$ due to the uncompensated kick of a single crab cavity is given by[3]

$$\begin{aligned}\frac{\Delta r(s,\Phi,z)}{\sigma_{\text{nom}}(s)} &= \frac{\sqrt{\beta_u}}{\sqrt{\epsilon_{\text{nom}}}} \cdot \Delta r'(\Phi,z) \cdot \sin\left(\Delta\psi_s\right) \\ &= \frac{c \cdot \tan(\frac{\Theta}{2})}{2\pi f \cdot \sigma^*_{\text{nom}} \cdot \sin(\Delta\psi) \cdot n_{cc}} \cdot \sin\left(\Phi + 2\pi f \cdot \frac{z}{c}\right) \cdot \sin\left(\Delta\psi_s\right). \end{aligned} \tag{7.5}$$

The transverse position perturbation is maximal at locations with $|\sin(\Delta\psi_s)| = 1$. Values for nominal LHC optics and the *SLHCV3.1b* optics (see Tab. 2.1) are given in Tab. 7.2.

## 7.2. Crab Cavity Failure Scenarios

Various failures can occur during the operation of crab cavities. The possible failure scenarios can be classified as slow/fast (external) failures, very fast (external) failures and ultra fast (internal) failures, as illustrated in Fig. 7.2. This categorization is described in the following.

[3] A crab cavity upstream of the IP is considered here. $\Delta\psi_s$ is the betatron phase advance from the crab cavity to the longitudinal position $s$, $\epsilon_{\text{nom}}$ is the nominal transverse emittance, $\sigma_{\text{nom}}(s) = \sqrt{\beta(s) \cdot \epsilon_{\text{nom}}}$ the nominal transverse beam size at the longitudinal position $s$ and $\sigma^*_{\text{nom}} = \sqrt{\beta^* \cdot \epsilon_{\text{nom}}}$ the nominal transverse beam size at the IP.

| | nominal LHC | HL-LHC |
|---|---|---|
| Particle with $z = 7.55\,\text{cm}$ $(= 1 \cdot \sigma_z)$ | $0.21\,\sigma_{\text{nom}}$ | $0.83\,\sigma_{\text{nom}}$ |
| Maximal displacement with $\sin\left(\Phi + 2\pi f \cdot \frac{z}{c}\right) = 1$ | $0.35\,\sigma_{\text{nom}}$ | $1.40\,\sigma_{\text{nom}}$ |
| Maximal displacement from all six crab cavities | $2.12\,\sigma_{\text{nom}}$ | $8.39\,\sigma_{\text{nom}}$ |

Table 7.2.: Transverse displacement amplitudes due to the uncompensated kick of a single or all six crab cavities for one beam and IR for nominal LHC optics and the *SLHCV3.1b* optics, as given by Eq. 7.5.
With $f = 400\,\text{MHz}$, $n_{cc} = 3$, $\Delta\psi = 90°$, $\sin(\Delta\psi_s) = 1$ and a nominal (normalized) transverse emittance of $\epsilon^{\text{n}}_{\text{nom}} = \epsilon_{\text{nom}}\beta_r\gamma_r = 3.5\,\mu\text{m} \cdot \text{rad}$ with $\beta_r\gamma_r = 7461$.
Nominal LHC optics: $\beta^* = 55\,\text{cm}$, $\Theta = 285\,\mu\text{rad}$.
HL-LHC optics: $\beta^* = 15\,\text{cm}$, $\Theta = 590\,\mu\text{rad}$.

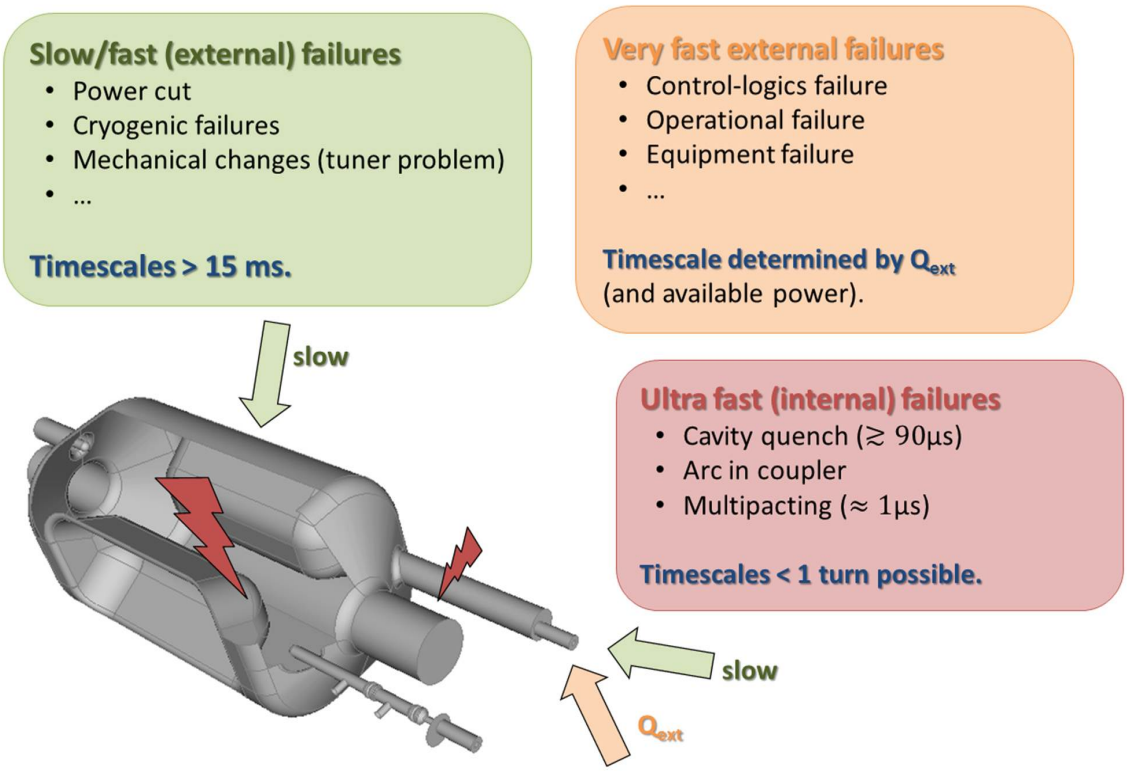


Figure 7.2.: Schematic overview of crab cavity failure categories.
The schematic layout of the parallel-bar crab cavity is used for illustration purposes only (courtesy of J. R. Delayen et al. [146]).

### 7.2.1. Slow/Fast (External) Failures

For example a power cut, thermal problems or mechanical changes (e.g. by the tuner) lead to failures on timescales above 15 ms [147]. The protection against failures of this category is not expected to be a fundamental problem. The present beam loss monitoring system and ultimately the quench protection system provide redundant protection of the LHC against such failure scenarios (see Sec. 3.4). Nevertheless, additional protection to avoid damage of the crab cavities and related equipment may be required.

### 7.2.2. Very Fast (External) Failures

For example a failure of the low-level RF feedback, an operational failure or an equipment failure (e.g. a fast abort of the RF power generator) can lead to voltage and/or phase changes of the crab cavities with a time constant $\tau$ that is determined by $Q_{\text{ext}}$: $\tau = \frac{Q_{\text{ext}}}{\pi \cdot f}$ (see Sec. 3.3). For a 400 MHz crab cavity with $Q_{\text{ext}} = 1 \cdot 10^6$ (see Tab 7.1), the **time constant $\tau \approx 800\,\mu$s $\approx$ 9 turns.**

For an initial transverse deflecting voltage amplitude $V_1$ and a target voltage level $V_2$ (for the same frequency and phase), the voltage amplitude at time $t$ is in analogy to Eq. 3.24 given by

$$V_{\perp,0}(t) = V_1 \cdot e^{-\frac{t}{\tau}} + V_2 \cdot (1 - e^{-\frac{t}{\tau}}) = V_2 + (V_1 - V_2) \cdot e^{-\frac{t}{\tau}}. \tag{7.6}$$

When additionally the target phase changes from $\Phi_1$ to $\Phi_2$, the transverse deflecting voltage is accordingly given by

$$\begin{aligned} V_\perp(t,z) &= V_1 \cdot \sin\left(\Phi_1 + 2\pi f \cdot \frac{z}{c}\right) \cdot e^{-\frac{t}{\tau}} + V_2 \cdot \sin\left(\Phi_2 + 2\pi f \cdot \frac{z}{c}\right) \cdot (1 - e^{-\frac{t}{\tau}}) \\ &= V(t) \cdot \sin\left(\Phi(t) + 2\pi f \cdot \frac{z}{c}\right) \end{aligned} \tag{7.7}$$

with [148, p. 84]

$$V^2(t) = V_1^2 \cdot e^{-2\frac{t}{\tau}} + V_2^2 \cdot (1 - e^{-\frac{t}{\tau}})^2 + 2V_1V_2 \cdot (e^{-\frac{t}{\tau}} - e^{-2\frac{t}{\tau}}) \cdot \cos(\Phi_2 - \Phi_1) \text{ and}$$

$$\Phi(t) = \arctan\left(\frac{V_1 \cdot e^{-\frac{t}{\tau}} \cdot \sin(\Phi_1) + V_2 \cdot (1 - e^{-\frac{t}{\tau}}) \cdot \sin(\Phi_2)}{V_1 \cdot e^{-\frac{t}{\tau}} \cdot \cos(\Phi_1) + V_2 \cdot (1 - e^{-\frac{t}{\tau}}) \cdot \cos(\Phi_2)}\right).$$

The peak voltage $V_{\max}$ is limited by the available RF power $P_{g,\max}$. With Eq. 3.25, the peak voltage of a single crab cavity for a centered beam is $V_{\max} = 9.8$ MV (with $P_{g,\max} = 80$ kW, $R_a/Q_0 = 300\,\Omega$, $Q_{\text{ext}} = 1 \cdot 10^6$ and $\Delta f = 0$).

Corresponding failure simulations are presented in Sec. 7.3.1.

### 7.2.3. Ultra Fast (Internal) Failures

Arcing in the coupler/waveguide, a quench of a crab cavity or sudden strong multipacting[4] are examples for potentially ultra fast failures since $Q_{\text{ext}}$ is not directly involved.

An electric arc in the coupler or waveguide can develop on timescales of about $1\,\mu$s [149]. Such a failure can be seen as a short-circuit that inhibits any energy-transmission through the coupler. This is equivalent to $Q_{\text{ext}} = \infty$ and leads to a decay of the transverse deflecting voltage in the cavity with a time constant $\tau = \frac{Q_0}{\pi \cdot f}$ (see Sec. 3.3). With $Q_0 \geq 10^{10}$ (see Tab. 7.1), the time constant $\tau \geq 8\,\text{s}$. Thus, the corresponding crab cavity field changes on a slow timescale and this failure case is not expected to be particularly critical for the LHC[5].

In case of a crab cavity quench, the energy stored in the cavity can dissipate in the cavity walls on ultra fast timescales, resulting in associated voltage and/or phase changes. Figure 7.3 illustrates the behavior of crab cavity voltage and phase in case of a quench at KEKB [150]. **The cavity voltage decays completely in $100\,\mu$s $\approx$ 1 LHC turn. The cavity phase oscillates by 50° in $50\,\mu$s.** Another example is illustrated in Fig. 7.4, which shows the **decay of the peak magnetic field within $100\,\mu$s** in a dedicated cavity quench test of a 1.3 GHz pure Nb cavity [151].

A cavity quench can be described by a decrease of $Q_0$, such that $Q_L$ is according to Eq. 3.23 dominated by $Q_0$. The decay time constant of the transverse deflecting voltage is then given by $\tau = \frac{Q_0}{\pi \cdot f}$. $Q_0$ is according to Eq. 3.19 determined by the geometry factor $G$ (for LHC type crab cavities $G \approx 100\,\Omega$ [56, 60]) and the surface resistance $R_s$. The surface resistance for a given frequency $f$ can be approximated by

$$R_s = \sqrt{\frac{\pi \cdot f \cdot \mu_0}{\sigma}}, \tag{7.8}$$

where $\mu_0 = 4\pi \cdot 10^{-7}\,\frac{\text{V·s}}{\text{A·m}}$ is the vacuum permeability and $\sigma$ is the electrical surface conductivity [81, p. 79]. For a completely quenched (i.e. normal-conducting) cavity at cryogenic temperatures, the electrical conductivity $\sigma_{0\,\text{K}}$ is given by $\sigma_{300\,\text{K}} \cdot RRR$, with the residual-resistance ratio $RRR = \frac{\sigma_{0\,\text{K}}}{\sigma_{300\,\text{K}}} \geq 300$ for LHC crab cavities [65] and $\sigma_{300\,\text{K}} = 6.58 \cdot 10^6\,\frac{\text{A}}{\text{V·m}}$ for niobium. With these values, $R_s = 894\,\mu\Omega$ for a 400 MHz

[4] An electron can be accelerated by the electromagnetic field of the cavity. The accelerated electron can then impact on the cavity wall again and release secondary electrons, which are also accelerated by the RF field. This process can repeat, resulting in an avalanche effect (so-called multipacting) and a large number of produced electrons. Since each electron is accelerated by the RF field, this may result in a significant dissipation of energy from the RF field.

[5] However, arcing may lead to a degradation or even damage of the coupler or waveguide.

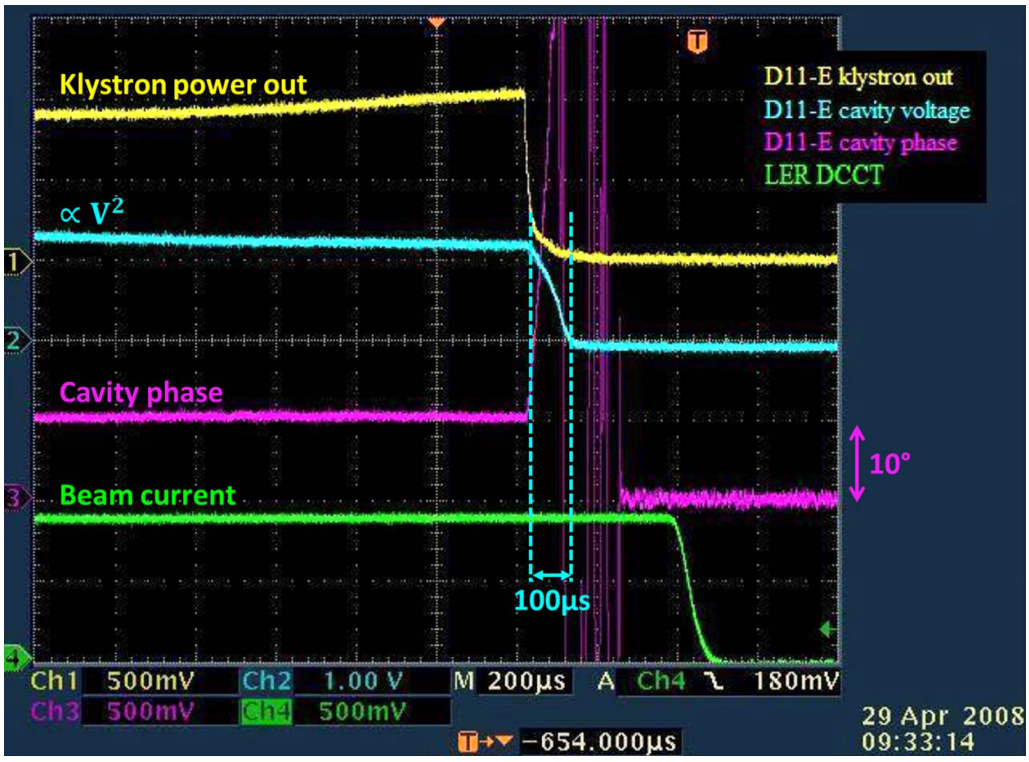


Figure 7.3.: Quench of a crab cavity at KEKB. The cavity voltage decays completely within 100 $\mu$s after a fast protection abort of the RF power generator (klystron). Large oscillations of the cavity phase are observed (courtesy of K. Nakanishi et al. [150]).

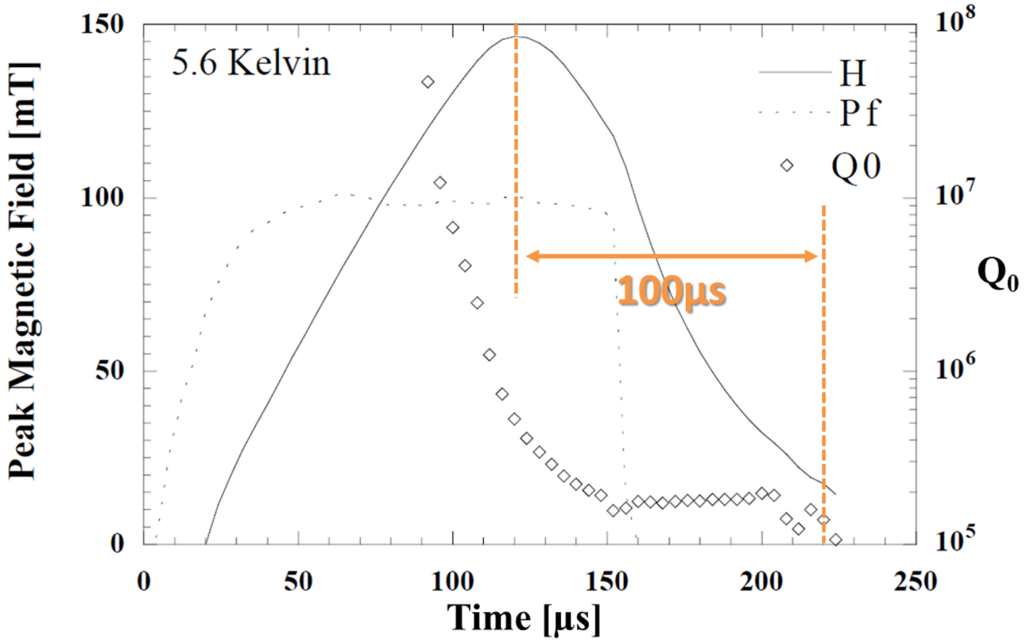


Figure 7.4.: Transient behavior of a 1.3 GHz pure Nb cavity during a deliberate quench test. The peak magnetic field $H$ decays completely in $\approx 100\,\mu$s (courtesy of T. Hays et al. [151]).
Pf denotes the forward power (towards the cavity) through the input coupler.

cavity and $Q_0 = 1.1 \cdot 10^5$. Thus, $\boldsymbol{\tau = 89\,\mu s = 1\,LHC\ turn}$[6]. Dedicated simulations of the transient phase behavior during a crab cavity quench are ongoing. Intermediate results indicate that for the quench of an LHC crab cavity the phase change on the relevant timescales is very small [152]. As mitigation of a quench, the low-level RF feedback typically increases initially the RF generator power (up to the limitation of the RF power generator) to maintain the deflecting voltage in the cavity. This is shown in Fig. 7.3 by the increase of the klystron power output before the RF abort. Whereas this delays the voltage decay, it also complicates the quench detection and may delay a protection beam dump, since the cavity voltage remains initially constant [149]. Possible quench detection and reaction strategies are discussed in Sec 7.4.

Apart from a cavity quench, also sudden multipacting could lead to ultra fast voltage changes of a crab cavity. Intensive multipacting studies are performed, typically with the focus on the ability to ramp up the deflecting voltage to the nominal level [56–59,61,62]. However, it is also imaginable that multipacting suddenly starts during standard operation, due to a change of external conditions [149] (e.g. changes of the bunch shape, the beam dynamics, deconditioning of the cavity surface or mechanical changes). For example at the Diamond Light Source ultra fast trips of the 500 MHz superconducting RF system are regularly observed, which are believed to be caused by multipacting [153]. **A corresponding collapse of the cavity field within 4.8 $\mu$s was observed** [154].

In case of a sudden start of multipacting, the number of electrons multiplies in each RF cycle with the so-called secondary electron yield ($SEY$). Assuming that each electron is accelerated by the RF field to the kinetic energy $E_e$, the stored energy in the cavity is consequently reduced in $n$ RF cycles by $SEY^n \cdot E_e$. With an $SEY$ of 1.1 and $E_e = 100\,\mathrm{eV}$[7], **the complete stored energy** of typically about 2 J - 10 J in an LHC-type crab cavity [56, 60, 63] **can dissipate within about 400 RF cycles = 1 $\mu$s.**

Whereas the calculations are merely simplified estimates, the examples indicate that in case of a crab cavity quench or sudden multipacting changes of the crab cavity voltage on timescales $\lesssim$ 1 LHC turn may be possible[8]. Corresponding failure simulation are presented in Sec. 7.3.2.

[6] This assumes that the cavity is completely quenched but remains at cryogenic temperatures. The time constant can be even faster if the temperature increases significantly [152]. For a temperature rise to room temperature, $Q_0 = 3324$ was measured for the prototype four-rod crab cavity [59], resulting in $\tau \approx 2.6\,\mu s \ll 1$ LHC turn.

[7] Typical values for niobium can range up to $SEY = 1.5$ and $E_e = 1.5\,\mathrm{keV}$ [57,153].

[8] Ultra fast (significant) changes of the cavity phase are not assumed to be possible, since external excitations or the resonance frequency of cavities typically change on longer timescales.

## 7.3. Failure Simulations

In the following, the results of MAD-X tracking studies of dynamic and instantaneous crab cavity failures are presented[9]. The simulations are based on the *SLHCV3.1b* optics [50] with a half crossing angle of $\frac{\Theta}{2} = 295\,\mu\text{rad}$ and symmetric $\beta^*_{x,y} = 15\,\text{cm}$ and the HL-LHC parameter given in Tab. 2.1. Complementary failure studies with nominal LHC optics are presented in [80]. In the simulations different failures of a single or multiple crab cavities for beam 1 around IP5 are assumed.

In order to isolate the effect of the crab cavity failures on the beam dynamics, the (normalized) amplitude of the transverse displacement

$$\frac{\Delta x_{\text{max}}}{\sigma_{\text{nom}}} = \frac{1}{\sigma_{\text{nom}}}\sqrt{(\Delta x_\beta)^2 + \left(\alpha \cdot \Delta x_\beta + \beta \cdot \Delta x'_\beta\right)^2} \tag{7.9}$$

with $\Delta x_\beta = \Delta x - D_x \frac{\Delta p}{p}$ and $\Delta x'_\beta = \Delta x' - D_{x'} \frac{\Delta p}{p}$ is considered in the following[10]. $\frac{\Delta x_{\text{max}}}{\sigma_{\text{nom}}}$ is apart from the interaction regions constant around the accelerator and is in particular (to first approximation) independent of the transverse beam distribution and the momentum deviation $\frac{\Delta p}{p}$ for the concerned failure scenarios. Thus, the initial tracking parameters are selected to correspond to the closed orbit of the bunch center (without crab cavities) and only the longitudinal position w.r.t. the bunch center is varied. Typically the particles are tracked for about 10 turns with nominal crab cavities operation (to verify the initial parameters and check the consistency of the simulation setup) and for about 20 more turns after the start of the failure.

### 7.3.1. Very Fast (External) Failures

For very fast external crab cavity failures, the time constant is determined by $Q_{\text{ext}}$. Such failures can lead to voltage and/or phase changes, which are discussed in the following.

[9] The crab cavity implementation in MAD-X allows to simulate the effect of crab cavity parameter changes on the beam dynamics. Beam-loading effects are not included.

[10] $\Delta x$ denotes the transverse particle position w.r.t. the initial closed orbit, $\Delta x'$ the transverse momentum divided by the longitudinal momentum (w.r.t. the initial closed orbit), $D_x$ and $D_{x'}$ the corresponding dispersions, $\frac{\Delta p}{p}$ the momentum deviation, $\sigma_{\text{nom}}$ the transverse beam size with nominal (normalized) emittance $\epsilon^{\text{n}}_{\text{nom}} = 3.5\,\mu\text{m} \cdot \text{rad}$ and $\alpha$ the $\alpha$-function (or $\alpha$ Twiss parameter) as defined in Sec. 3.1.3.

### Voltage Failure

When a single crab cavity has a non-nominal voltage, the tilt-kick of the crab cavity is no longer locally compensated. A typical failure scenario is a fast abort of the RF power generator. In this case the deflecting voltage amplitude is according to Eq. 7.6 given by $V_{\perp,0}(t) = V_1 \cdot e^{-\frac{t}{\tau}}$. Figure 7.5 illustrates the corresponding transverse displacement amplitude, as defined by Eq. 7.9, as function of the longitudinal particle position (w.r.t. the bunch center). The RF power for one out of the six beam 1 crab cavities around IP5 is suddenly aborted. Particles at $\pm\frac{c}{4f} = 2.5\,\sigma_z$ have the largest displacement of up to $\approx 0.4\,\sigma_{\text{nom}}$ within 5 turns after the failure. The longitudinal bunch center is not displaced. The illustrated displacement amplitudes before the start of the failure (turn -1 and turn -2) represent the non-closure of the tilt-kick in static operation[11]. When the RF power is simultaneously aborted for all three crab cavities on one side of the IP, the trajectory perturbation is a factor 3 larger.

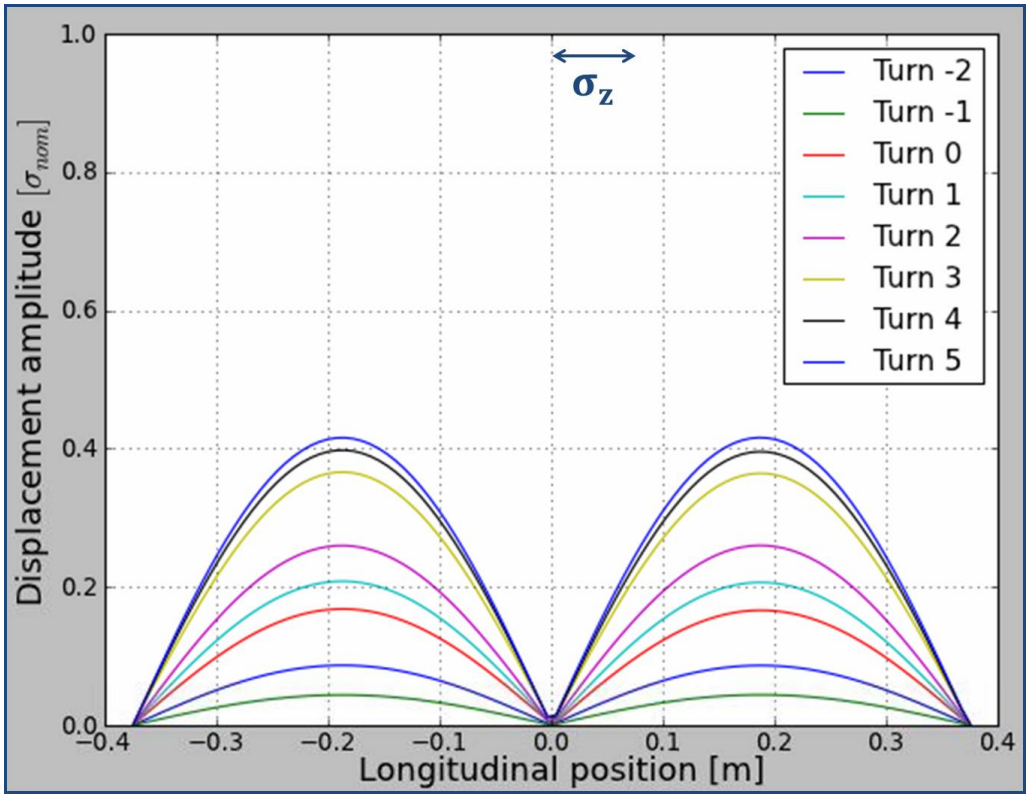


Figure 7.5.: Simulated displacement amplitude as function of the longitudinal position (w.r.t. the bunch center) for a dynamic voltage failure, which represents the sudden abort of the cavity power supply for one out of the six beam 1 crab cavities around IP5.
$Q_{\text{ext}} = 1{\cdot}10^6$. The failure starts at turn 0. The displacement amplitude is normalized to the nominal beam size with $\epsilon^{\text{n}}_{\text{nom}} = 3.5\,\mu\text{m} \cdot \text{rad}$.

[11] As the betatron phase advance between the crab cavities upstream and downstream of the IP is slightly larger than 180° the tilt-kick cannot be completely compensated (see also Sec. 7.1).

Figure 7.6 illustrates the transverse displacement amplitude for the case that the RF generator power for one crab cavity is suddenly increased to the maximum of $P_{g,\max} = 80\,\mathrm{kW}$ (see Tab. 7.1). The deflecting voltage amplitude is for this case according to Eq. 7.6 given by

$$V_{\perp,0}(t) = V_{\max} + (V_1 - V_{\max}) \cdot e^{-\frac{t}{\tau}}$$

with $V_{\max} = 9.8\,\mathrm{MV}$ (see Sec. 7.2.2). It is assumed that the crab cavity maintains the increased voltage $V_{\perp,0}$ in the first turns without quench. The corresponding transverse displacement amplitude of the final state (at $t = \infty$) is about

$$\frac{V_{\max} - 2 \cdot V_1}{V_1} = \frac{9.8\,\mathrm{MV} - 2 \cdot 3.5\,\mathrm{MV}}{3.5\,\mathrm{MV}} = 80\%$$

larger than for the case discussed above.

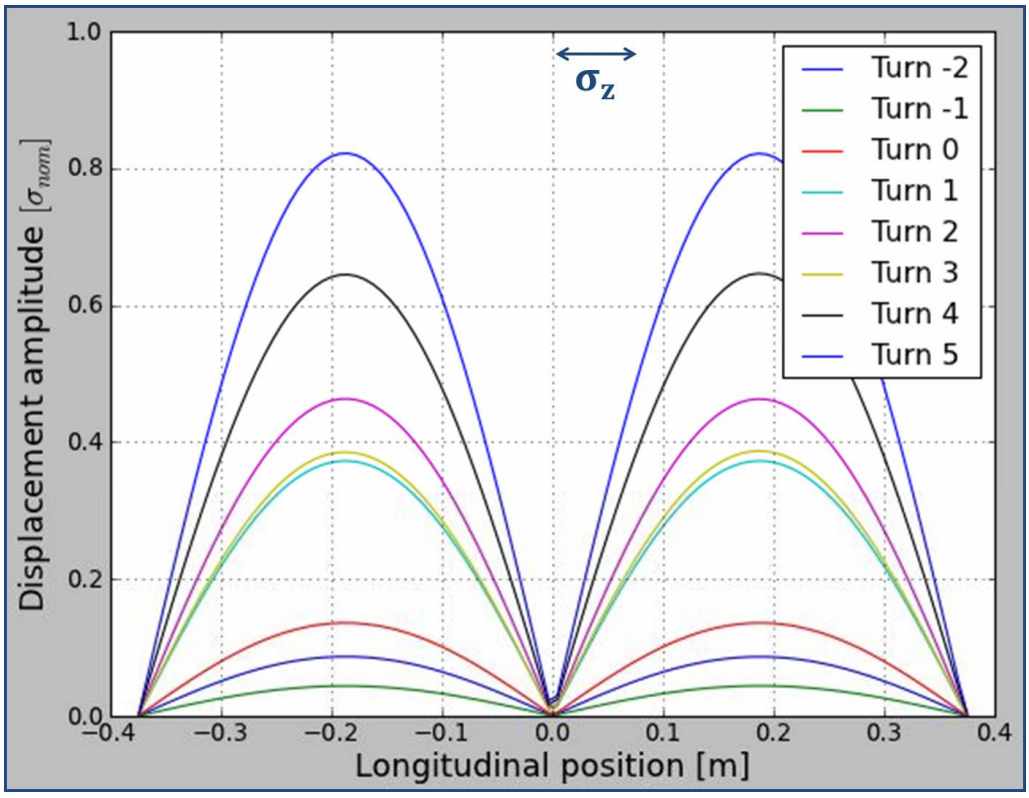


Figure 7.6.: Simulated displacement amplitude as function of the longitudinal position (w.r.t. the bunch center) for a dynamic voltage failure, which represents the sudden increase of the RF generator power to 80 kW for one out of the six beam 1 crab cavities around IP5.
$Q_{\mathrm{ext}} = 1{\cdot}10^6$. The failure starts at turn 0. The displacement amplitude is normalized to the nominal beam size with $\epsilon^{\mathrm{n}}_{\mathrm{nom}} = 3.5\,\mu\mathrm{m} \cdot \mathrm{rad}$.

### Phase Failure

In case of a phase error, the crab cavity no longer tilt-kicks the bunch, but kicks also the densely populated (longitudinal) bunch center. When the phase of the RF excitation (through the input coupler) changes by 90°, the phase in the cavity changes by up to

$$\arctan\left(\frac{1-e^{-\frac{t}{\tau}}}{e^{-\frac{t}{\tau}}}\right) = 6.7^\circ$$

in the first turn (with the LHC revolution period $t = 89\,\mu$s and $\tau = 800\,\mu$s, as calculated in Sec. 7.2.2) [155]. The failure is worst and the bunch center is maximally displaced, when the crab cavities upstream and downstream of the IP change phases in opposite directions. Figure 7.7 illustrates that in this case the bunch center is displaced by up to $2.7\,\sigma_{\text{nom}}$ within 5 turns[12].

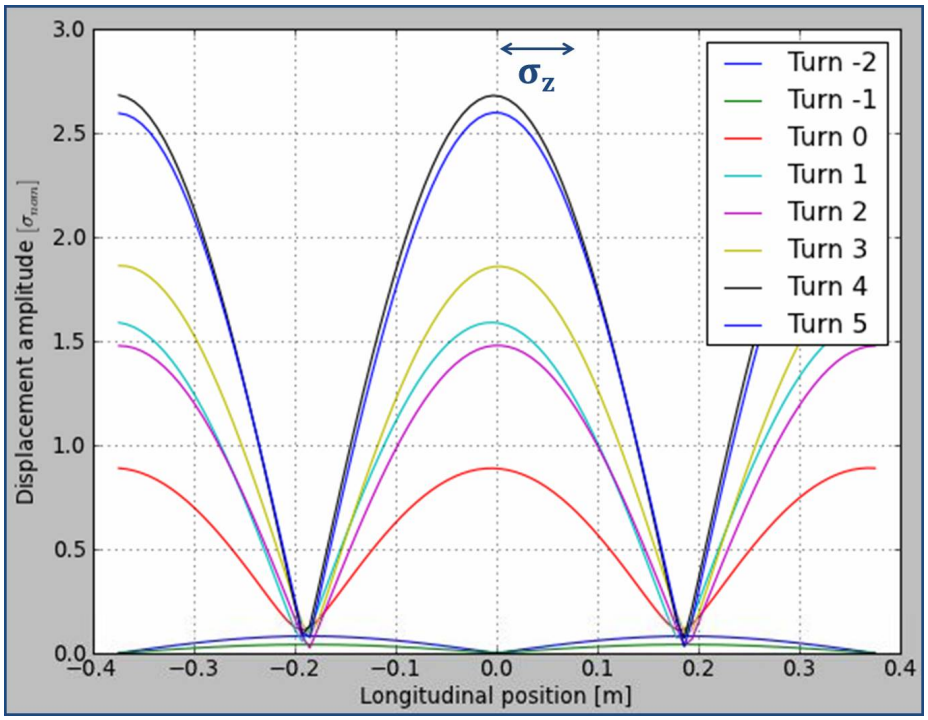


Figure 7.7.: Simulated displacement amplitude as function of the longitudinal position (w.r.t. the bunch center) for a dynamic phase failure. The phases of all crab cavities upstream and downstream of the IP are changed in opposite directions.
$Q_{\text{ext}} = 1{\cdot}10^6$. The failure starts at turn 0. The displacement amplitude is normalized to the nominal beam size with $\epsilon^{\text{n}}_{\text{nom}} = 3.5\,\mu\text{m}\cdot\text{rad}$.

[12] The beam displacement at the location of the crab cavity after the first turn changes the required RF generator power. With Eq. 3.25 and Eq. 3.26 a coherent beam displacement between $-4.7\,\sigma_{\text{nom}}$ and $+2.2\,\sigma_{\text{nom}}$ can be maintained at an ideal cavity with the parameters given in Tab. 7.1. It is therefore assumed that sufficient RF power is available in the first few turns and beam loading is neglected here.

Since all six crab cavities are affected in this case, the maximal displacement amplitude is about six times larger than for the case illustrated in Fig. 7.5.

Figure 7.8 shows the temporal evolution of the maximum displacement amplitude for different values of $Q_{\text{ext}}$. As illustrated, the transverse displacement increases much faster with smaller $Q_{\text{ext}}$ and saturates at about $8\,\sigma_{\text{nom}}$ for $Q_{\text{ext}} = 10^5$.

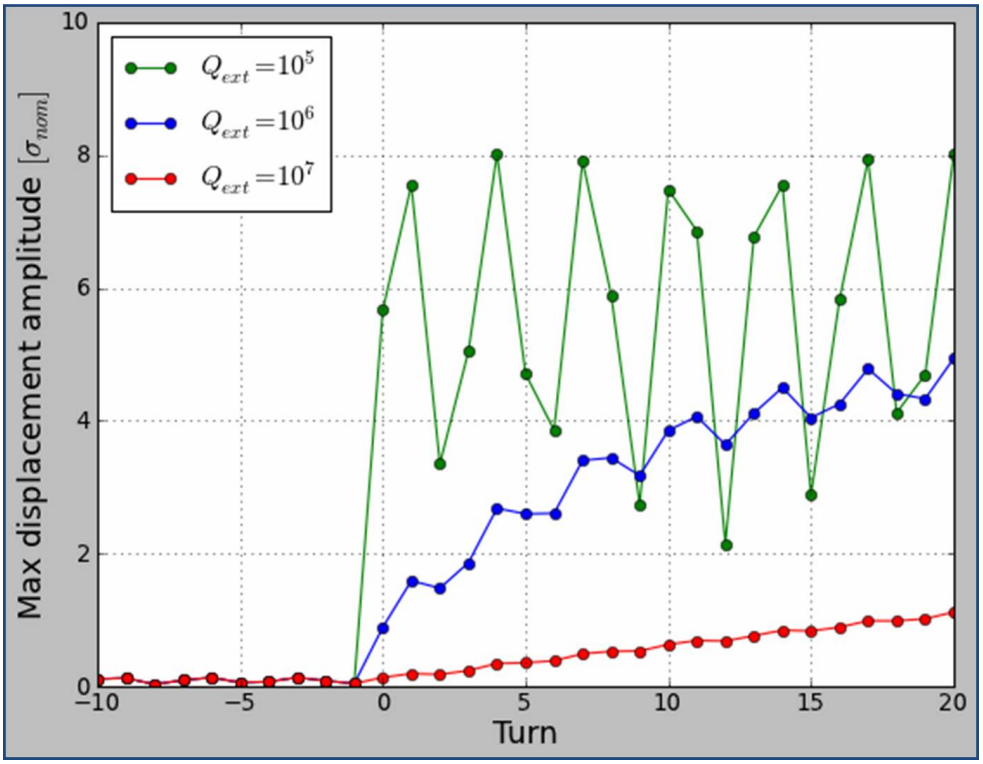


Figure 7.8.: The maximum of the displacement amplitudes shown in Fig. 7.7 for each turn and different values of $Q_{\text{ext}}$. The phases of all crab cavities upstream and downstream of the IP are changed in opposite directions. The failure starts at turn 0. The displacement amplitude is normalized to the nominal beam size with $\epsilon^{\text{n}}_{\text{nom}} = 3.5\,\mu\text{m} \cdot \text{rad}$.

### 7.3.2. Ultra Fast (Internal) Failures

For failures with time constants $\tau < 1\,\text{turn}$, the maximum displacement amplitude for one erroneous crab cavity (out of six crab cavities per beam around each IP) is $\approx 1.4\,\sigma_{\text{nom}}$ in the first turn (see Tab. 7.2). Since the fractional tunes ($Q_x = 0.31$, $Q_y = 0.32$) are close to the third order resonance, the effect partially cancels out after three consecutive revolutions[13]. Figure 7.9 shows the evolution of the maximal displacement amplitude after a drop of the deflecting voltage to zero within a single turn.

[13] Under the assumption that the failure remains constant (e.g. at $V_{\perp,0} = 0\,\text{V}$) after an instantaneous change of the crab cavity properties.

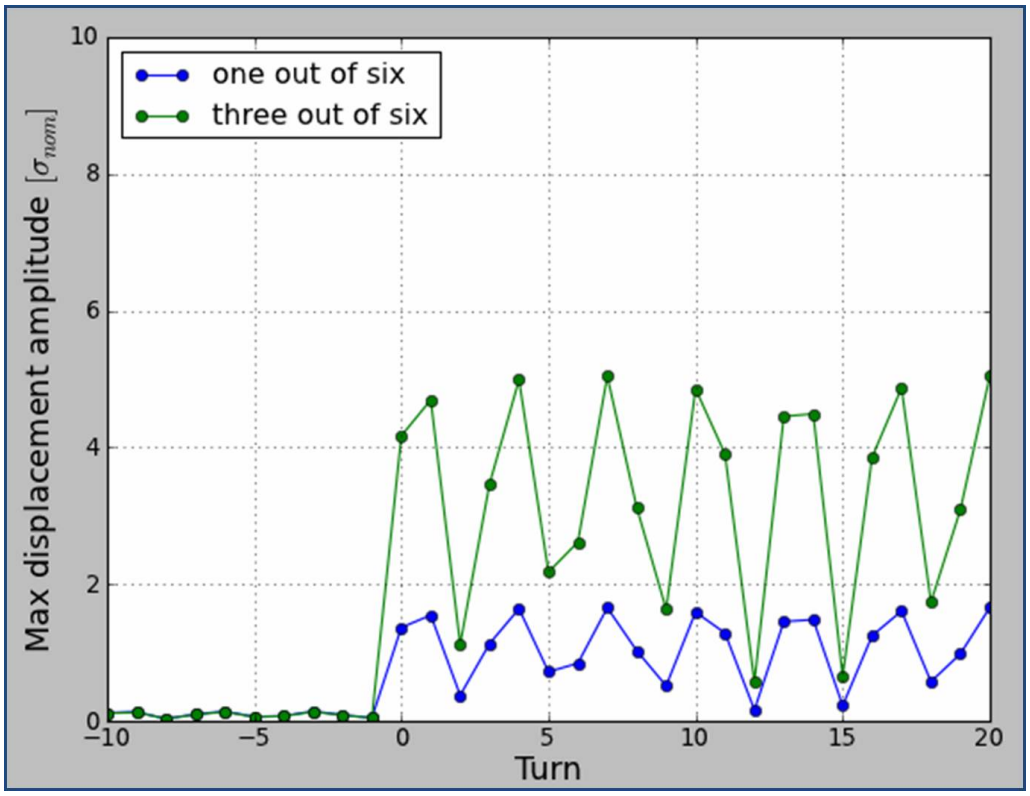


Figure 7.9.: The maximal displacement amplitude for each turn after an instantaneous drop of the deflecting voltage to zero for a failure of one crab cavity and of all three crab cavities on one side of IP5.
The failure starts at turn 0. The displacement amplitude is normalized to the nominal beam size with $\epsilon^{\mathrm{n}}_{\mathrm{nom}} = 3.5\,\mu\mathrm{m}\cdot\mathrm{rad}$.

## 7.4. Interlock and Mitigation Strategies

As illustrated by the simulations, crab cavity failures can imply large global betatron oscillations on very/ultra fast timescales. For amplitudes above about $1\,\sigma_{\mathrm{nom}}$, such oscillations can lead to critical beam losses, due to the highly overpopulated transverse tails in the LHC; an intensity corresponding to $\approx 31\,\mathrm{MJ}$ for HL-LHC parameters was observed beyond $4\,\sigma$ as described in Sec. 2.4.2. Ultra fast beam losses on this level are significantly beyond the specification of the collimation system of up to 1 MJ for fast accidental beam losses [45].

SIXTRACK[14] [156, 157] crab cavity failure simulations with an improved transverse beam distribution model are ongoing for a further quantification of the beam

[14]SIXTRACK is a six-dimensional particle tracking code for accelerator physics applications. It also includes elastic scattering processes and is therefore often used to simulate spatial beam loss pattern around the LHC.

losses. Intermediate results confirm beam losses of up to about 12 MJ at the collimators[15] [158].

The relevant strategies and options for the detection and mitigation of crab cavity failures are discussed in the following.

### 7.4.1. Failure Detection, Interlock and Post Mortem

A fast, reliable and redundant detection and interlock-processing of a crab cavity failure on a timescale $< 1$ LHC turn is vital to ensure a beam dump in not more than $\approx 3$ LHC turns (see Sec. 2.3.4). Possible fast failure detection mechanisms are:

- **RF field monitor probe:** the transverse deflecting voltage amplitude and the corresponding phase is measured with a RF field monitor probe and can be compared to reference signals. Such hardware machine protection systems have a typical processing time of a few $\mu$s.
  The measured phase can be compared to the reference phase of the main RF system[16] [65]. In order to limit the maximal transverse displacement to $0.5\,\sigma_{\mathrm{nom}}$, the phase may not change by more than 3.4° for each crab cavity according to Eq. 7.5 for nominal *SLHCV3.1b* optics. If such a significant phase change is detected, next to a beam dump trigger, an immediate fast, controlled and simultaneous RF power abort is required for all crab cavities for the corresponding beam and IR. This avoids further dephasing of the crab cavities. A corresponding low-level RF architecture is described in Sec. 7.4.3.
  The determination of a fail-safe reference signal for the deflecting voltage amplitude is much more complicated as a larger flexibility is needed: the deflecting voltage amplitude changes throughout the cycle and depends for example on the $\beta$-functions at the crab cavities (see Eq. 7.3 and Eq. 7.4) which change with the $\beta$-function at the collision point $\beta^*$, especially when considering luminosity leveling by $\beta^*$. Thus, it is believed that an interlock on fast changes of the voltage amplitude (rather than the absolute value) is more robust and less error-prone. A FMCM-like system (see Sec. 2.3.1 and Sec. 4.1) could provide this functionality. In order to limit the maximal transverse displacement

[15] The transverse beam distribution for these simulations is based on a measurement of the luminous region by the CMS experiment in 2011. A simplified crab cavity failure model is used.

[16] In certain conditions, e.g. when the cavities are detuned in order to be transparent (see Sec. 7.1) the reference phase has to be adjusted accordingly or the interlock has to be deactivated. Similarly, a bunch-by-bunch phase modulation of the accelerating RF by about 8.5° may be required in the HL-LHC era [65, p. 21]. This would imply a corresponding bunch-by-bunch adjustment of the reference phase.

to $0.5\,\sigma_{\mathrm{nom}}$ within 10 LHC turns, the relative change of the deflecting voltage of each crab cavity may not exceed 0.6% per turn[17].

- **Power transmission through input coupler:** as explained in Sec. 7.2.3, in case of an internal failure, the low-level RF feedback will initially maintain the deflecting voltage amplitude by increasing the RF generator power. As this excludes a failure detection based on the RF field monitor probe signal, the power transmission through the input coupler must be kept under tight surveillance. For crab cavity operation with nominal frequency and centered beams, the RF generator power $P_g$ is given by Eq. 3.25. As $R_a/Q_0$ and $Q_{\mathrm{ext}}$ are constant, a measurement of $P_g$ and the deflecting voltage amplitude $V_{\perp,0}$ (via the RF field monitor probe) allows to determine $Q_L$, which is for normal operation with centered beams dominated by $Q_{\mathrm{ext}}$. A significant drop of $Q_L$ below $Q_{\mathrm{ext}}$ is a clear indication for an abnormal energy-loss, for example due to an internal crab cavity failure (quench or multipacting). As explained in Sec. 7.2.3, for a completely quenched crab cavity, $Q_L$ is dominated by $Q_0$ and drops to below $1.1 \cdot 10^5$. Similarly, an erroneous increase of $P_g$ could also result in an increase of $V_{\perp,0}$ above the nominal level. This failure case can be detected by the same technique. However, as described in Sec. 3.3, $P_g$ also increases significantly when the beam has a transverse offset at the crab cavity or when the cavity is slightly detuned. Thus, also here an interlock on fast changes of the (average and peak) transmitted power may be more robust and may increase the operational flexibility.

- **Head-tail monitor:** considering the quite severe worst case failure scenarios, a redundant failure detection mechanism is required. A monitoring (with interlock functionality) of the global betatron oscillations outside the IR is desirable. As the oscillation amplitude changes along each bunch and is for a crab cavity voltage failure zero on average (head and tail are deflected in opposite directions), an intra-bunch detection like a head-tail monitor [159] is required. The internal reaction time[18] needs to be $\ll 1$ LHC turn and transverse oscillation amplitudes of about $0.1\,\sigma_{\mathrm{nom}}$ should be detectable. As the frequency of the transverse displacement is given by the crab cavity frequency (400 MHz), the present LHC multiband-instability-monitor [159], which is by design only sensitive to frequencies higher than 400 MHz, is not applicable for this.

[17] Assuming a simultaneous voltage change of all cavities (upstream and downstream cavities in opposite directions), the maximal transverse displacement given by Eq. 7.5 is with these values $8.4\,\sigma_{\mathrm{nom}} \cdot \frac{6 \cdot 10^{-3}}{1\,\mathrm{turn}} \cdot 10\,\mathrm{turns} = 0.5\,\sigma_{\mathrm{nom}}$.

[18] The total reaction time of the interlock system is increased by up to $\approx 1$ LHC turn for the flight-time of the perturbed bunches from the erroneous crab cavity to the head-tail monitor.

Each interlock system shall be connected to the beam interlock system and immediately trigger a beam dump in case the interlock condition is fulfilled.

In order to allow an adequate failure analysis, excellent post mortem functionality is required: in a failure case a bunch-by-bunch history of voltage and phase of all crab cavities needs to be stored together with the relevant information to reconstruct the behavior of the low-level RF feedback and the power generators. The LHC post mortem system [160] provides a standardized framework, including the possibility to execute automated post operational checks after each fill.

### 7.4.2. Operational Parameter

The maximal transverse displacement for a failure of a single crab cavity (with a voltage that is set to completely compensate the crossing angle) is proportional to the constant pre-factor in Eq. 7.5:

$$\frac{\Delta r_{\max}}{\sigma_{\text{nom}}} \propto \frac{c \cdot \tan(\frac{\Theta}{2})}{2\pi f \cdot \sigma^*_{\text{nom}} \cdot \sin(\Delta\psi) \cdot n_{cc}}. \tag{7.10}$$

For a small crossing angle $\Theta$ and $\Delta\psi = 90°$, this can be simplified with Eq. 3.15 to

$$\frac{\Delta r_{\max}}{\sigma_{\text{nom}}} \propto \frac{1}{f \cdot \beta^* \cdot n_{cc}}.$$

This important scaling law points out that the impact of a crab cavity failure is determined by the crab cavity frequency, $\beta^*$ and the number of independent crab cavities on either side of the IP. For a simultaneous failure of multiple crab cavities, the maximal transverse displacement amplitude multiplies with the number of erroneous crab cavities. Figure 7.10 illustrates the maximal transverse displacement amplitude as a function of $\beta^*$.

A flat optics at the IP with larger $\beta^*$ in the crossing plane [161] would reduce the required transverse deflecting voltage. The impact of a crab cavity failure is mitigated correspondingly without decreasing the peak luminosity. According to Eq. 7.10, the impact of a crab cavity failure could be further reduced by the use of beam-beam wire compensators, which would allow for a reduced beam-beam separation and a corresponding reduction of the crossing angle $\Theta$ (see Sec. 3.2) [15].

Equation 7.10 also underlines that reducing the number of crab cavities below $n_{cc} = 3$ per beam on either side of each IP increases the impact of a single crab cavity failure correspondingly. The crab cavities should be as independent as possible to avoid any fast common-cause failure scenarios, as illustrated in Fig. 7.10. Thus, independent power supplies and cryostats for each cavity are foreseen, which exclude many ultra fast common-cause failures of multiple crab cavities. A simultaneous

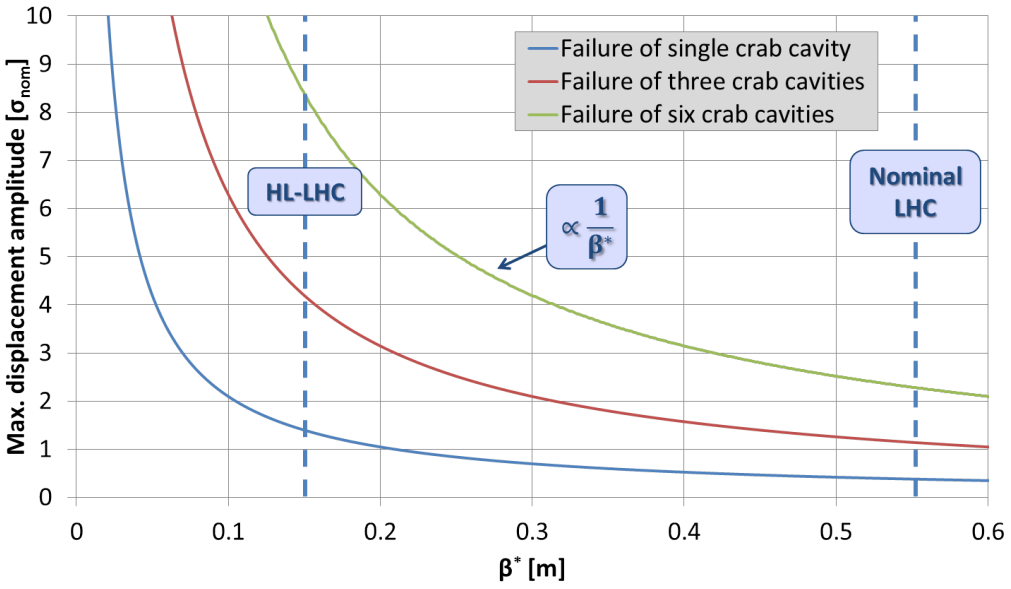


Figure 7.10.: The maximal transverse displacement amplitude as a function of $\beta^*$ for the failure of one or multiple crab cavities which are tuned to compensate the crossing angle.
For three 400 MHz crab cavities per beam on either side of the IP.

quenching of the crab cavities due to beam losses has to be avoided by a local beam loss monitoring with adequate beam dump thresholds.

Nevertheless, it cannot be excluded that multiple crab cavities are simultaneously affected by external failures, e.g. operational failures, control-logic/RF feedback failures, etc. Thus, it is important to keep the time constant for crab cavity failures as slow as possible. This implies that $Q_{\text{ext}}$ should not be below $10^6$ as underlined by Fig 7.8. A further increase of $Q_{\text{ext}}$ is not practical, as it requires even tighter limits on the frequency stability of the crab cavities, since the needed RF generator power for a slightly detuned cavity is according to Eq. 3.27 proportional to $Q_{\text{ext}}$. The available RF generator power should be limited to the necessary level on the other hand. As shown in Sec. 7.3.1, a significantly over-dimensioned power generator allows much faster voltage and phase changes and may imply even larger maximal transverse displacement amplitudes than given in Tab. 7.2.

In order to increase the field decay time constant in case of a cavity quench, niobium coated copper cavities are being investigated. This could increase $Q_0$ for a completely quenched crab cavity by about a factor 3 compared to a pure niobium cavity[19] and the corresponding field decay time constant to $\tau = 267\,\mu$s, compared to $\tau = 89\,\mu$s (see Sec. 7.2.3).

[19] With Eq. 3.19, Eq. 7.8 and $\sigma_{300\,\text{K}} = 59.1 \cdot 10^6\,\frac{\text{A}}{\text{V}\cdot\text{m}}$ for copper, $Q_0 = 3.4 \cdot 10^5$.

### 7.4.3. Active Protection

A coupling of the crab cavities upstream and downstream of the IP by the low-level RF feedback is proposed [65, p. 20]. With this approach, erroneous voltage and phase changes of a single crab cavity could be compensated by the other crab cavities. The proposed layout is illustrated in Fig. 7.11. The timescale for the corresponding field corrections is limited by $Q_{\text{ext}}$ and the available RF generator power, as given by Eq. 3.25 and Eq. 7.7. Hence, changes of the crab cavity field on ultra fast timescales can only be partly compensated by this approach. It is foreseen to develop and test the mechanism and to demonstrate its reliability in dedicated crab cavity tests in the CERN Super Proton Synchrotron (SPS).

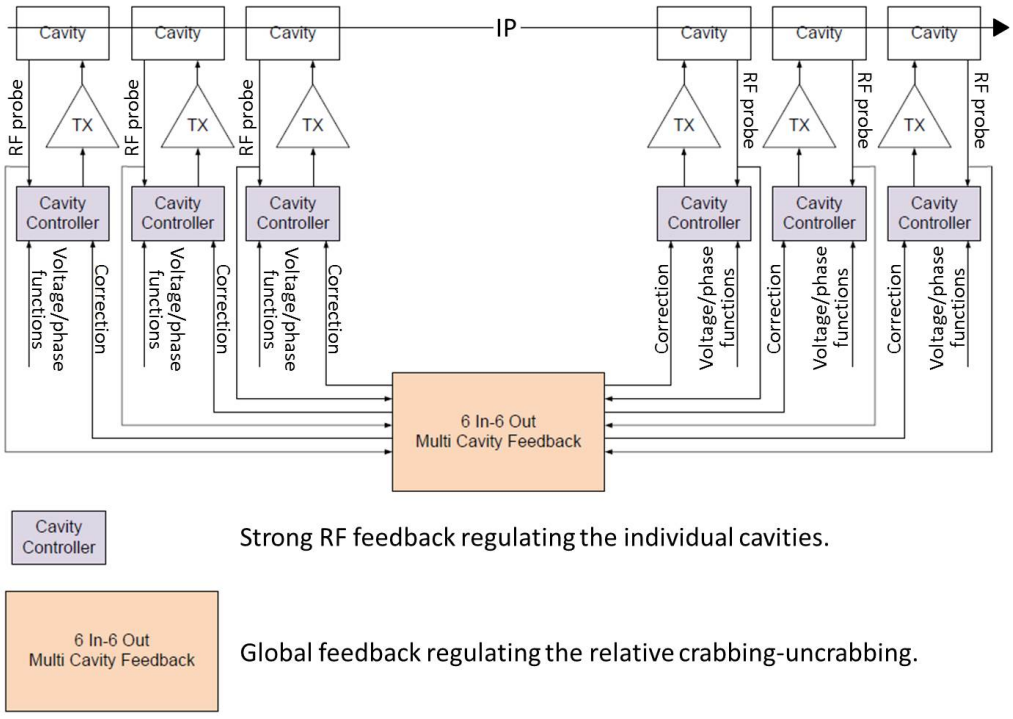


Figure 7.11.: Proposed low-level RF architecture for the crab cavities for one beam around one IP (courtesy of P. Baudrenghien [65]).

### 7.4.4. Passive Protection and Hollow Electron-Lens

As explained above, an ultra fast failure of a single crab cavity can lead to a transverse beam trajectory perturbation with a maximal displacement amplitude of up to $1.4\,\sigma_{\text{nom}}$ in the turn directly after the failure (see Tab. 7.2) and up to $1.7\,\sigma_{\text{nom}}$ within the first 5 LHC turns[20] (see Fig. 7.9). It has to be ensured that in such a

[20] It is believed that the maximal displacement amplitudes for external failure scenarios can be restricted to smaller values by the aforementioned interlock and mitigation strategies.

failure case the beam losses stay below the damage limit of the collimation system. This requires an active control and a reliable "online" diagnostics (with interlock functionality) of the transverse tail population.

The required diagnostics could be for example based on the monitoring of synchrotron light from the transverse beam halo [162]. Alternative intercepting approaches (like wire-scanners) cannot be used, as the high beam intensity is significantly above the typically damage level of the corresponding devices. Moreover, these approaches imply a transverse emittance blow-up when being continuously inserted.

For a transverse tail depletion many options are imaginable. For example a scraping with collimators or movable obstacles, a reduction of the dynamic aperture, e.g. by a reduced crossing angle [15] or a beam-beam wire compensator [163, 164], a removal of trapped halo particles by tune modulation [165, 166] or a beam excitation by an AC dipole or the transverse feedback [164]. Apart from the beam-beam wire compensator, which is not available at the LHC at present, these approaches could be implemented with the available hardware. Corresponding tests can be foreseen as soon as a diagnostics for the tail population is available.

However, all these approaches affect also the beam core and/or imply a significant complication of operation with high-intensity beams. In order to avoid transverse emittance blow-up and to minimize the impact on routine beam operation as well as machine protection issues, it is preferable to have a dedicated mechanism for transverse tail depletion, which does not affect the beam core.

Hence, the installation of a hollow electron-lens is proposed to deplete the transverse tails [142]. Figure 7.12 illustrates the working principle: in a dedicated area a hollow electron beam is superimposed to the proton beam. Tail particles of the proton beam, which exceed the inner diameter of the hollow electron beam are deflected transversely by the electron beam. Thus, the betatron oscillation amplitude increases for these particles until they are lost at the collimators. The beam core is in first approximation not affected by the hollow electron-lens [141]. This allows to deplete the transverse tails of the beam distribution in a controlled way, as illustrated in Fig. 7.13. A hollow electron-lens was successfully in operation at the Tevatron collider[21] [141]. Figure 7.14 shows a typical measurement of the current density profile of the Tevatron electron-lens.

For a protection against ultra fast failures of a single LHC crab cavity, the beam intensity in the last $1.7\,\sigma_{\mathrm{nom}}$ before the collimator needs to be reduced below a stored

[21] The Tevatron hollow electron-lens could be operated continuously, as well as in a pulsed operation mode, gated on selected bunches [141].

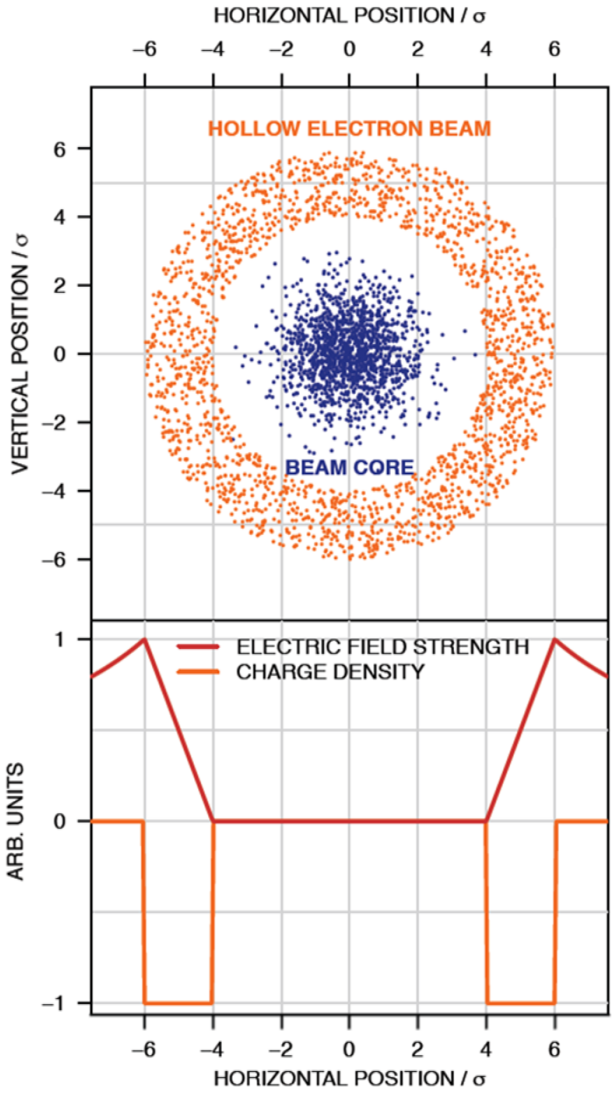


Figure 7.12.: Illustration of the hollow electron beam around the beam core and the resulting electric field strength (courtesy of G. Stancari [167]).

energy of 1 MJ (about 1.4‰ of the total stored energy for HL-LHC parameter). Thus, an operation of the hollow electron-lens between $4\,\sigma_{\text{nom}}$ and $6\,\sigma_{\text{nom}}$ with a nominal primary collimator half gap of $x_c = 6\,\sigma_{\text{nom}}$ as illustrated in Fig. 2.7, Fig. 7.12 and Fig. 7.13 is a reasonable choice of parameters. The corresponding inner and outer radius of the hollow electron beams for HL-LHC parameter at 7 TeV operation is between 1 mm and 2.5 mm for all beams and planes at the proposed location in IR4 [168]. This is very similar to the operational parameter of the Tevatron hollow electron-lens [141, 169]. SIXTRACK simulations to study the efficiency of the tail depletion are currently ongoing [170].

[22] The transverse diffusion coefficient $D(x)$ defines the beam (intensity) loss rate $\frac{dI}{dt}$ at the aperture limiting collimators for a given transverse beam distribution $f(x,t)$: $\frac{dI}{dt} \propto -D \cdot \frac{df(x,t)}{dx}\Big|_{x=x_c}$ [167].

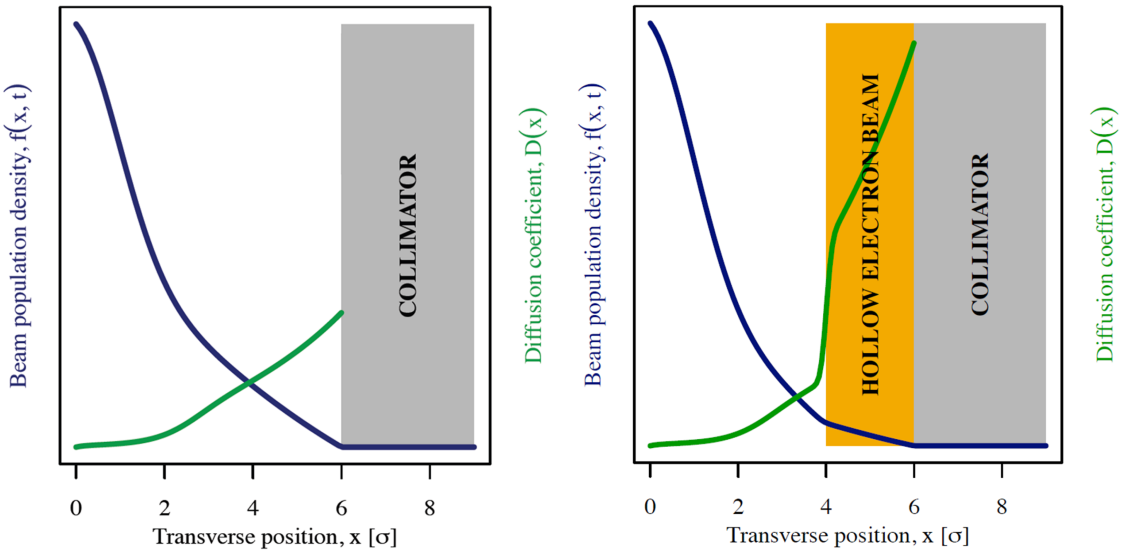


(a) Without hollow electron-lens (b) With hollow electron-lens.

Figure 7.13.: Illustration of the transverse beam profile and the transverse diffusion coefficient[22] without hollow electron-lens (a) and with hollow electron-lens (b). As for the nominal LHC, the collimator half gap in the illustration is $x_c = 6\,\sigma$. The hollow electron beam is between $4\,\sigma$ and $6\,\sigma$ as illustrated in Fig. 7.12 (courtesy of G. Stancari [167]).

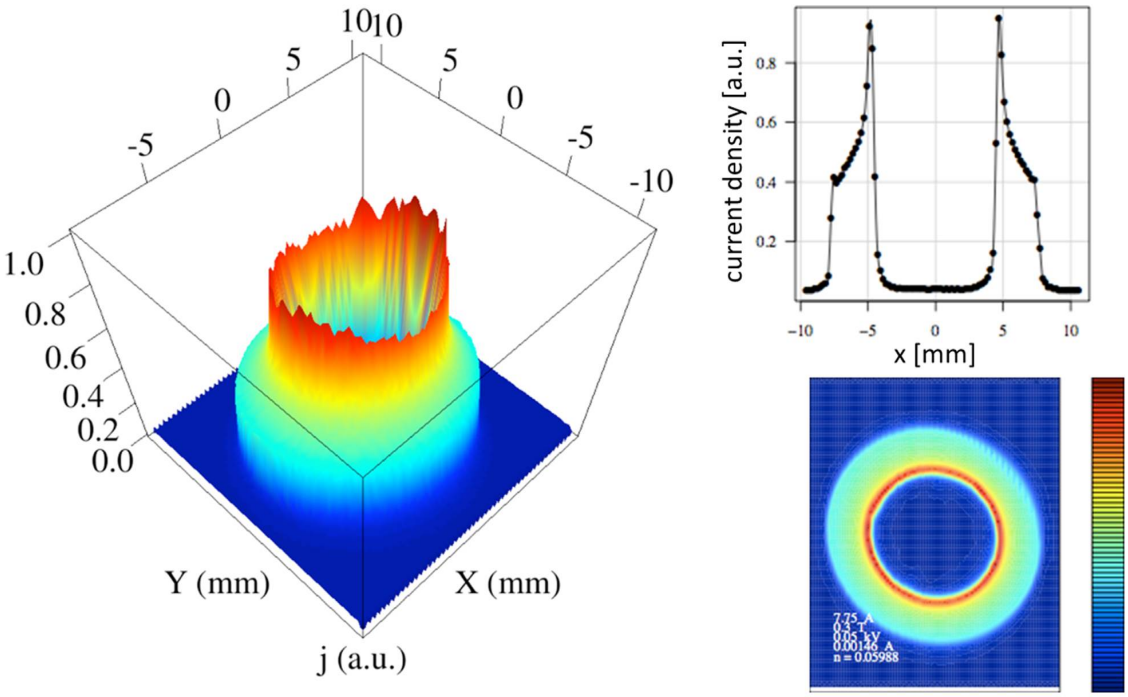


Figure 7.14.: Measured current density profile of the hollow electron beam at Tevatron (courtesy of G. Stancari [167]).

The discussed tail depletion would allow corresponding fast trajectory perturbations while limiting the beam losses to the design values[23]. In particular, this does not confine the longitudinal beam distribution for crab cavity operation and would ensure a protection against crab cavity voltage and phase changes.

A complementary strategy is to reduce the sensitivity to beam losses by increasing the damage level of the collimation system for example by the installation of "disposable" collimators for protection against high accidental beam losses which can occur in rare cases.

## 7.5. Conclusions and Outlook

Several crab cavity failure scenarios with ultra fast and very fast time constants were identified and classified. Corresponding MAD-X simulations show that such failures can lead to global betatron oscillations with machine critical amplitudes, which are significantly above $1\,\sigma_{\mathrm{nom}}$. Particularly critical are phase changes, since then the densely populated bunch center is displaced. A simple scaling law (see Eq. 7.10) shows that the maximal transverse displacement amplitude is inversely proportional to the crab cavity frequency, $\beta^*$ and the number of independent crab cavities on either side of the IP. Related strategies for a failure detection, interlock-processing and mitigation are proposed.

In particular ultra fast common-cause failures of multiple crab cavities have to be avoided by design. This includes independent power supplies and cryostats for each cavity. The crab cavity failures are especially critical due to the highly overpopulated tails in the transverse beam distribution. This may in case of a fast beam trajectory perturbation lead to beam losses at the collimation system, which are significantly beyond design. In order to ensure a passive protection against ultra fast and very fast crab cavity failures, dependable diagnostics, interlock mechanisms and control techniques (e.g. a hollow electron-lens) for the transverse tail population are required.

A better understanding of the transient field behavior in particular for ultra fast internal crab cavity failures is still needed. Corresponding cavity simulations and experimental studies (e.g. as part of the cavity tests at SM18, CERN) are strongly encouraged. As presented in Sec. 2.5, a crab cavity test program in the Super Proton Synchrotron (SPS) for 2016/17 is in preparation. This allows to test and demonstrate the dependability of an active failure compensation by the proposed coupled low-level RF architecture with two crab cavities. In the same context,

[23] This does not exclude magnet quenches; corresponding SIXTRACK simulations are ongoing [158].

further machine protection tests, including interlock tests and dedicated quench tests, are to be performed. This includes high intensity beam tests to address related beam-loading effects. A complementary extension of the simulation framework by beam-loading effects is recommended.

# 8. Summary and Conclusion

The first years of LHC operation demonstrated a remarkable reliability of the major machine protection systems, foremost of the beam interlock system, the beam dump system and the beam loss monitoring (BLM) system, which protect the LHC well against any failures on fast or slow timescales. However, it was also seen that the LHC is vulnerable to beam losses on timescales which are faster than the reaction time of the LHC machine protection systems. Moreover, unexpected beam loss mechanisms on these timescales were observed after the LHC start-up, which have even been limiting the LHC performance (e.g. UFOs).
The focus of this thesis lies on the investigation and mitigation of such ultra/very fast beam losses of the circulating LHC beams for LHC operation during run 1 as well as in the mid-term and long-term future.

The most critical equipment failures which can lead to very fast beam losses were reviewed with the operational experience gained during run 1.
Whereas the fast magnet current change monitors (FMCMs) which are installed on critical warm magnet circuits showed a remarkable sensitivity and dependability during run 1, they triggered many beam dumps due to small external electrical perturbations. This limited the LHC availability at times. In the context of this thesis, dedicated simulations were performed which demonstrated the possibility of partial increases of the FMCM thresholds to reduce the number of unnecessary beam dumps. These threshold increases were implemented in 2012. During the first long LHC shutdown (LS1), the corresponding power converters are modified to stabilize the circuits against external electrical perturbations. Failure simulations and the related machine protection for operation in the High-Luminosity LHC (HL-LHC) era are discussed in Sec. 4.1.
A failure of the transverse damper is another cause for potentially critical beam losses on very fast timescales. Therefore, experimental excitation measurements were performed and are compared to expectations in Sec. 4.2. Corresponding weaknesses of the machine protection systems are identified and improvements are proposed.

One of the most relevant surprises after the LHC start-up are (un)identified falling objects (UFOs), as discussed in Chap. 5. UFOs caused 58 premature protection beam dumps during run 1. Extensive studies were performed in the context of this

thesis, which include comprehensive improvements of the diagnostics, intensive data analysis and dedicated experiments in the LHC, including a magnet quench test. These were complemented by laboratory tests, FLUKA and MAD-X simulations and theoretical studies. As a result, fundamental correlations are found, the UFOs at the injection kicker magnets (MKIs) are identified as macro particles originating from the ceramic tube inside these magnets, the macro particle dynamics are characterized and the response of the BLM system is understood. This allows mid-term extrapolations which indicate that UFOs could become a major performance limitation for LHC operation after LS1. Particularly critical is the increased sensitivity of the superconducting elements to UFOs for operation at higher beam energy. The effectiveness of various mitigation measures against UFOs at the MKIs was demonstrated and they are applied to all MKIs during LS1. The impact of UFOs in the rest of the LHC can be partly mitigated by BLM threshold increases up to the quench limit of the superconducting magnets, which may be significantly higher than initially expected, as indicated by the preliminary analysis of a beam-based magnet quench test. Moreover, a large-scale relocation of the arc BLMs is ongoing which provides a more efficient detection and protection against arc UFOs.

Following the systematic diagnostics improvements as part of this thesis, an unconsidered single-turn beam loss mechanism was observed in July 2012, as discussed in Chap. 6. It was found that the sudden absence of the long-range beam-beam deflections after the dump of a single beam results in a bunch-by-bunch trajectory perturbation of the counter-rotating beam and related beam losses. Experimental studies were performed to characterize this effect. The results are in well agreement with complementary simulations. Extrapolations show that the effect increases for future LHC operation and may be critical for operation after LS1 and in particular for HL-LHC operation. Appropriate mitigation strategies are proposed.

In order to increase the luminosity beyond the nominal LHC specifications, crab cavities will be installed as part of the HL-LHC upgrade program. However, in a failure case, they can lead to significant betatron oscillations of the beam within the reaction time of the LHC machine protection systems. The relevant failure mechanisms are classified and dedicated failure simulations are presented in Chap. 7. Comprehensive failure detection and mitigation strategies to limit the impact of crab cavity failures to an acceptable level are proposed.

The studies described in Chap. 4, Chap. 6 and Chap. 7 identify ultra/very fast trajectory perturbations of the order of $1\,\sigma_{\mathrm{nom}}$ which may be machine critical when considering the present LHC beam distribution with typically highly overpopulated transverse tails. Trajectory perturbations on this level can result in beam losses in the betatron collimation system which exceed the specifications by more than

one order of magnitude. Therefore a reliable "online" diagnostics for the transverse tail population is believed to be essential to ensure an adequate protection for operation with even higher stored beam energies. The investigation of tail-depletion mechanisms (e.g. by a hollow electron-lens) is strongly advised.

This thesis covers one of the most critical challenges for LHC operation: beam losses of the circulating LHC beams on timescales that are faster than the reaction time of the machine protection systems. As a result, the relevant beam loss mechanisms are identified and understood. Specific optimizations of the diagnostics and the machine protection systems are implemented and mitigation strategies are developed. Throughout run 1, substantial contributions to improve the efficiency and safety of LHC operation were made in the context of this thesis. This document provides the baseline for the future protection against very fast losses of the circulating LHC beams. The results and achievements are of fundamental importance for improvements of the LHC performance while ensuring a safe LHC operation in the mid-term and long-term future.

# Glossary

| | |
|---|---|
| ADT | LHC transverse damper. |
| ALICE | **A** **L**arge **I**on **C**ollider **E**xperiment: main LHC experiment in IR2. |
| ATLAS | **A** **T**oroidal **L**HC **A**pparatu**s**: main LHC experiment in IR1. |
| BBQ | **B**ase-**b**and tune (**Q**) measurement system: the standard LHC tune measurement system. |
| BIC | **B**eam **i**nterlock **c**ontroller (see Sec. 2.3.4). |
| BIS | **B**eam **i**nterlock **s**ystem (see Sec. 2.3.4). |
| BLM | **B**eam **L**oss **M**onitor (see Sec. 2.3.3). |
| BPM | **B**eam **P**osition **M**onitor. |
| BSRT | LHC synchroton light monitor. |
| CMS | **C**ompact **M**uon **S**olenoid: main LHC experiment in IR5. |
| FLUKA | Multi-particle transport code for simulations [95, 96]. |
| FMCM | **F**ast **m**agnet **c**urrent change **m**onitor (see Sec. 2.3.1). |
| HL-LHC | **H**igh-**L**uminosity **LHC** upgrade program (see Sec. 2.5). |
| IP | **I**nteraction **P**oint: collision point of beam 1 and beam 2 in a main experiment or center of the long straight section for IRs without collision point. |
| IQC | **I**njection **q**uality **c**heck. |
| IR | **I**nsertion **R**egion, long straight section between two neighboring arcs. |
| LHC | **L**arge **H**adron **C**ollider (see Chap. 2). |
| LHCb | **L**arge **H**adron **C**ollider **b**eauty experiment: main LHC experiment in IR8. |
| LS1 | **L**ong **s**hutdown **1** in 2013/14 [37]. |
| MAD-X | Particle accelerator simulation code [88]. |
| MD | **M**achine **d**evelopment. |

| | |
|---|---|
| MKD | Beam dump kicker magnet (see Sec. 2.3.1). |
| MKI | Injection kicker magnet (see Sec. 2.3.1). |
| MKQ | Tune kicker magnet. |
| PACMAN | Bunches with reduces number of long-range beam-beam encounters (see Sec. 3.2). |
| QPS | **Q**uench **p**rotection **s**ystem (see Sec. 2.3.1). |
| RMS | **R**oot-**m**ean-**s**quare (see also Appendix A). |
| SIXTRACK | Particle accelerator tracking code [156, 157]. |
| SPS | **S**uper **P**roton **S**ynchrotron (see Sec. 2.2). |
| TCP | Primary LHC collimator (see Sec. 2.3.2). |
| TCT | Tertiary LHC collimator (see Sec. 2.3.2). |
| TI 2 | Beam 1 transfer line from SPS to LHC (see Sec. 2.2). |
| TI 8 | Beam 2 transfer line from SPS to LHC (see Sec. 2.2). |
| UFO | (**U**n)identified **f**alling **o**bject (see Chap. 5). |

# Bibliography


[1] The ATLAS Collaboration, "A Particle Consistent with the Higgs Boson Observed with the ATLAS Detector at the Large Hadron Collider", *Science*, vol. 338, no. 6114, pp. 1576–1582, Dec. 2012.

[2] The CMS Collaboration, "Observation of a New Boson with Mass Near 125 GeV in pp Collisions at $\sqrt{s} = 7$ and 8 TeV", *J. High Energ. Phys.*, vol. 2013, no. 6, pp. 1–127, Jun. 2013.

[3] Nobelprize.org, "The Nobel Prize in Physics 2013", Nobel Media AB, <http://www.nobelprize.org/nobel_prizes/physics/laureates/2013/>, Oct. 2013.

[4] R. Filippini and J. Uythoven, "Dependability Analysis of a Safety Critical System: the LHC Beam Dumping System at CERN", Ph.D. dissertation, Pisa University/CERN, Apr. 2006, CERN-THESIS-2006-054.

[5] T. Kramer and B. Goddard, "LHC Beam Dump System: Analysis of Beam Commissioning, Performance and the Consequences of Abnormal Operation", Ph.D. dissertation, Technical University Graz/CERN, Oct. 2011, CERN-THESIS-2011-135.

[6] R. Versaci *et al.*, "FLUKA Studies of the Asynchronous Beam Dump Effects on LHC Point 6", in *Proceedings of IPAC'11*, Sep. 2011, pp. 2397–2399, WEPC175.

[7] V. Kain and R. Schmidt, "Machine Protection and Beam Quality During the LHC Injection Process", Ph.D. dissertation, Technical University Vienna/CERN, Oct. 2005, CERN-THESIS-2005-047.

[8] N. Magnin, "LBDS Kickers", in *Proceedings of the 2013 MPP Workshop*, Mar. 2013.

[9] J. Uythoven *et al.*, "Beam Commissioning and Performance Characterization of the LHC Beam Dump Kicker Systems", in *Proceedings of IPAC'10*, May 2010, pp. 1659–1661, TUPEB062.

[10] Y. Baconnier *et al.*, "Large Hadron Collider in the LEP Tunnel", CERN, DIR-TECH Note 84-01, May 1984.

[11] O. S. Brüning *et al.*, *LHC Design Report - The LHC Main Ring.* CERN, 2004, vol. 1.

[12] S. Dittmaier *et al.*, "Handbook of LHC Higgs Cross Sections: 1. Inclusive Observables", CERN, Yellow Report 2011-002, Jan. 2011.

[13] A. Macpherson, "LHC Availability and Performance in 2012", in *Proceedings of the 2012 Evian Workshop on LHC Beam Operation*, Dec. 2012.

[14] M. Lamont, "Potential Performances: Putting it all together", in *Proceedings of the 2012 Evian Workshop on LHC Beam Operation*, Dec. 2012.

[15] O. S. Brüning and F. Zimmermann, "Parameter Space for the LHC Luminosity Upgrade", in *Proceedings of IPAC'12*, May 2012, pp. 127–129, MOPPC005.

[16] C. Lefèvre, "The CERN accelerator complex. Complexe des accélérateurs du CERN", <http://cds.cern.ch/record/1260465>, Dec. 2008.

[17] Maalpu.org, "LHC Layout Diagram", maalpu.org (CC) BY-NC-SA, <http://maalpu.org/lhc/LHC.layout.png>, 2011.

[18] M. Brice, "Cross Section of an LHC Dipole in the Tunnel.", <http://cds.cern.ch/record/1365795>, Jul. 2011.

[19] J. B. Jeanneret *et al.*, "Quench Levels and Transient Beam Losses in the LHC Magnets", CERN, LHC Project Report 44, May 1996.

[20] R. Denz, private communication, Jun. 2013.

[21] V. Kain, "Power Converter Failure of the Normal Conducting D1 Magnet at Experiment Insertions IR1 and IR5", CERN, LHC Project Note 322, Sep. 2003.

[22] M. Zerlauth, "FMCM Sensitivity to Mains Perturbations", presentation at 49$^{\text{th}}$ CERN Machine Protection Panel Meeting, Sep. 2011.

[23] M. Zerlauth *et al.*, "Detecting Failures in Electrical Circuits Leading to Very Fast Beam Losses in the LHC", in *Proceedings of EPAC'04*, Jul. 2004, pp. 1930–1932.

[24] M. Werner, "Einrichtung zur Bestimmung der Stärke des Magnetfeldes eines Elektromagneten", Patent DE102005045537B3 28.12.2006, Sep. 2005.

[25] M. Werner *et al.*, "Requirements for the Fast Magnet Current Change Monitors (FMCM) in the LHC and the SPS-LHC Transfer Lines", CERN, EDMS Doc. No. 678140, Nov. 2005.

[26] T. Baer and M. Zerlauth, "FMCM Thresholds", CERN, EDMS Doc. No. 1211450, Apr. 2012.

[27] R. Bruce *et al.*, "Collimator Hierarchy Limits: Assumptions and Impact on Machine Protection and Performance", in *Proceedings of the 2013 MPP Workshop*, Mar. 2013.

[28] S. Redaelli *et al.*, "2012 Aperture Measurements - Preliminary Results", presentation at 33rd LHC Beam Operation Committee Meeting, CERN, Mar. 2012.

[29] M. Hempel *et al.*, "Application of Diamond Based Beam Loss Monitors at LHC", Master thesis, Brandenburg University of Technology/CERN/ DESY Zeuthen, Nov. 2012, CERN-THESIS-2012-307.

[30] A. Saba, "The LHC Tunnel. Le Tunnel du LHC", <http://cds.cern.ch/ record/1436155>, Feb. 2012.

[31] B. Dehning *et al.*, "The LHC Beam Loss Measurement System", in *Proceedings of PAC'07*, Jun. 2007, pp. 4192–4194, FRPMN071.

[32] E.B. Holzer *et al.*, "Commissioning and Optimization of the LHC BLM System", in *Proceedings of HB2010*, Sep. 2010, pp. 487–491, WEO1C01.

[33] E. Nebot del Busto *et al.*, "Study of the Response of Low Pressure Ionisation Chambers", in *Proceedings of IPAC'12*, May 2012, pp. 888–890, MOPPR047.

[34] M. Zerlauth *et al.*, "First Operational Experience with the LHC Machine Protection System when Operating with Beam Energies Beyond the 100MJ Range", in *Proceedings of IPAC'12*, May 2012, pp. 4062–4064, THPPR040.

[35] B. Todd *et al.*, "A Look Back on 2012 LHC Availability", in *Proceedings of the 2012 Evian Workshop on LHC Beam Operation*, Dec. 2012.

[36] G. Spiezia *et al.*, "R2E - Experience and Outlook", in *Proceedings of the 2012 Evian Workshop on LHC Beam Operation*, Dec. 2012.

[37] F. Bordry *et al.*, "The First Long Shutdown (LS1) for the LHC", in *Proceedings of IPAC'13*, May 2013, MOZB202.

[38] P. Lebrun *et al.*, "Report of the Task Force on the Incident of 19th September 2008 at the LHC", CERN, LHC Project Report 1168, Mar. 2009.

[39] A.W. Chao *et al.*, *Handbook of Accelerator Physics and Engineering*, 2nd ed. World Scientific, 2013.

[40] E. Métral *et al.*, "Review of the Instabilities Observed During the 2012 Run and Actions Taken", in *Proceedings of the 2012 Evian Workshop on LHC Beam Operation*, Dec. 2012.

[41] N. Mounet *et al.*, "Beam Stability With Separated Beams at 6.5 TeV", in *Proceedings of the 2012 Evian Workshop on LHC Beam Operation*, Dec. 2012.

[42] G. Rumolo *et al.*, "Electron Cloud Effects in the LHC in 2011", in *Proceedings of the 2011 Evian Workshop on LHC Beam Operation*, Dec. 2011, pp. 165–175.

[43] G. Iadarola *et al.*, "Electron Cloud and Scrubbing in 2012 in the LHC", in *Proceedings of the 2012 Evian Workshop on LHC Beam Operation*, Dec. 2012.

[44] B. Salvant *et al.*, "Beam Induced RF Heating", in *Proceedings of the 2012 Evian Workshop on LHC Beam Operation*, Dec. 2012.

[45] R. Assmann *et al.*, "Collimation for the LHC High Intensity Beams", in *Proceedings of HB2010*, Sep. 2010, pp. 21–33, MOIB03.

[46] F. Burkart *et al.*, "Halo Scrapings with Collimators in the LHC", in *Proceedings of IPAC'11*, Sep. 2011, pp. 3756–3758, THPZ030.

[47] S. Redaelli *et al.*, "Experience with High-Intensity Beam Scraping and Tail Population at the Large Hadron Collider", in *Proceedings of IPAC'13*, May 2013, MOPWO039.

[48] A. Bertarelli *et al.*, "Updated Robustness Limits for Collimator Materials", in *Proceedings of the 2013 MPP Workshop*, Mar. 2013.

[49] L. Rossi *et al.*, "High Luminosity Large Hadron Collider", European Strategy Preparatory Group, Tech. Rep., Sep. 2012.

[50] S. Fartoukh and R. De Maria, "Optics and Layout Solutions for HL-LHC with Large Aperture $NB_3Sn$ and Nb-Ti Inner Triplets", in *Proceedings of IPAC'12*, May 2012, pp. 145–147, MOPPC011.

[51] L. Rossi, "LHC Upgrade Plans: Options and Strategy", in *Proceedings of IPAC'11*, Sep. 2011, pp. 908–912, TUYA02.

[52] Y. Yamamoto *et al.*, "Beam Commissioning Status of Superconducting Crab Cavities in KEKB", in *Proceedings of IPAC'10*, May 2010, pp. 42–44, MOOCMH03.

[53] S. U. De Silva, "Superconducting RF-Dipole Deflecting and Crabbing Cavities", presentation at SRF'13, Sep. 2013.

[54] S. U. De Silva and J. R. Delayen, "Design Evolution and Properties of Superconducting Parallel-Bar RF-Dipole Deflecting and Crabbing Cavities", *Phys. Rev. ST Accel. Beams*, vol. 16, p. 012004, Jan 2013.

[55] S. U. De Silva and J. R. Delayen, "Design and Development of Superconducting Parallel-Bar Deflecting/Crabbing Cavities", in *Proceedings of IPAC'12*, May 2012, WEPPC102.

[56] S. U. De Silva *et al.*, "Compact Superconducting RF-Dipole Cavity Designs for Deflecting and Crabbing Applications", in *Proceedings of IPAC'13*, May 2013, WEPWO080.

[57] Z. Li *et al.*, "HOM Damping Coupler Design for the 400-MHz RF Dipole Compact Crab Cavity for the LHC HiLumi Upgrade", in *Proceedings of IPAC'13*, May 2013, WEPWO072.

[58] B. Hall *et al.*, "Analysis of the Four Rod Crab Cavity for HL-LHC", in *Proceedings of IPAC'12*, May 2012, pp. 2275–2277, WEPPC032.

[59] G. Burt *et al.*, "Manufacture of a Compact Prototype 4R Crab Cavity for HL-LHC", in *Proceedings of IPAC'13*, May 2013, WEPWO051.

[60] P. Ambattu *et al.*, "First Test Results of the 4-Rod Crab Cavity", in *Proceedings of IPAC'13*, May 2013, WEPWO046.

[61] R. Calaga *et al.*, "A Double Quarter-Wave Deflecting Cavity for the LHC", in *Proceedings of IPAC'13*, May 2013, WEPWO047.

[62] Q. Wu *et al.*, "HOM Damping and Multipacting Analysis of the Quarter-Wave Crab Cavity", in *Proceedings of IPAC'12*, May 2012, pp. 2020–2022, TUPPR084.

[63] B. P. Xiao *et al.*, "Mechanical Study of 400 MHz Double Quarter Wave Crab Cavity for LHC Luminosity Upgrade", in *Proceedings of IPAC'13*, May 2013, WEPWO050.

[64] Q. Wu, "Developing Quarter Wave SRF Cavities for Hadron Colliders", presentation at SRF'13, Sep. 2013.

[65] P. Baudrenghien *et al.*, "Functional Specifications of the LHC Prototype Crab Cavity System", CERN, ACC Note 2013-003, Feb. 2013.

[66] E. Jensen, "Overall Planning & HiLumi Meeting Highlights", presentation at LHC Crab Cavity Engineering Meeting, FNAL, Dec. 2012.

[67] J. R. Delayen and S. U. De Silva, "Proof of Principle Cavity Preparation and Testing: ODU/SLAC RF-Dipole Design", presentation at HiLumi LHC/LARP Meeting, Napa Valley, Apr. 2013.

[68] Q. Wu *et al.*, "Double Quarter Wave Crab Cavity", presentation at 2$^{nd}$ HiLumi LHC/LARP Meeting, INFN Frascati, Nov. 2012.

[69] K. Fuchsberger *et al.*, "Novel Concepts for Optimization of the CERN Large Hadron Collider Injection Lines", Ph.D. dissertation, Technical University Vienna/CERN, Jun. 2011, CERN-THESIS-2011-075.

[70] H. Wiedemann, *Particle Accelerator Physics*, 1st ed. Springer-Verlag, 1993.

[71] F. Hinterberger, *Physik der Teilchenbeschleuniger und Ionenoptik*, 2nd ed. Springer-Verlag, 2008.

[72] K. Wille, *The Physics of Particle Accelerators*, 1st ed. Oxford University Press, 2000.

[73] G. W. Hill, "On the Part of the Motion of the Lunar Perigee which is a Function of the Mean Motions of the Sun and Moon", *Acta Mathematica*, vol. 8, no. 1, pp. 1–36, Dec. 1886.

[74] D. W. Kerst, "The Acceleration of Electrons by Magnetic Induction", *Phys. Rev.*, vol. 60, no. 1, pp. 47–53, Jul. 1941.

[75] M. Schaumann *et al.*, "Beam-Beam Interaction Studies at LHC", Master thesis, RWTH Aachen/CERN, Sep. 2011, CERN-THESIS-2011-138.

[76] W. Herr, "Beam-Beam Interactions", in *Proceedings of CAS'03*, Sep. 2003, pp. 379–406.

[77] W. Herr, "Concept of Luminosity", in *Proceedings of CAS'03*, Sep. 2003, pp. 361–377.

[78] R. Calaga *et al.*, "Crab Cavities", presentation at CARE-HHH Workshop, CERN, Nov. 2008.

[79] Y. P. Sun *et al.*, "Beam Dynamics Aspects of Crab Cavities in the CERN Large Hadron Collider", *Phys. Rev. ST Accel. Beams*, vol. 12, p. 101002, Oct 2009.

[80] R. Calaga *et al.*, "Beam Losses Due to Abrupt Crab Cavity Failures in the LHC", in *Proceedings of PAC'11*, Mar. 2011, pp. 76–78, MOODN4.

[81] H. Padamsee *et al.*, *RF Superconductivity for Accelerators*, 2nd ed. WILEY-VCH, 2008.

[82] J. Tückmantel, "Cavity-Beam-Transmitter Interaction Formula Collection with Derivation", CERN, ATS Note 2011-002 TECH, Jan. 2011.

[83] W. K. H. Panofsky and W. A. Wenzel, "Some Considerations Concerning the Transverse Deflection of Charged Particles in RadioFrequency Fields", *Rev. Sci. Instrum.*, vol. 27, pp. 967–968, jul 1956.

[84] R. Schmidt *et al.*, "Beam Loss Scenarios and Strategies for Machine Protection at the LHC", in *AIP Conference Proceedings of HALO'03*, vol. 693, Aug. 2003, pp. 184–187.

[85] M. Sapinski *et al.*, "Beam Induced Quenches of LHC Magnets", in *Proceedings of IPAC'13*, May 2013, THPEA045.

[86] W. Höfle, "Transverse Damper", in *Proceedings of the Chamonix 2012 Workshop on LHC Performance*, Feb. 2012, pp. 157–162.

[87] A. Gómez Alonso and R. Schmidt, "Redundancy of the LHC Machine Protection Systems in case of Magnet Failures", Ph.D. dissertation, Universitat Politècnica de Catalunya/CERN, Apr. 2009, CERN-THESIS-2009-023.

[88] H. Grote and F. Schmidt, "MAD-X - An Upgrade from MAD8", in *Proceedings of PAC'03*, May 2003, pp. 3497–3499.

[89] I. Romera Ramirez, "Change of Protection Threshold for Fast Magnet Current Change Monitors (FMCM) Installed on the ALICE Compensators and the Twin Aperture Warm Separation Circuits", CERN, EDMS Doc. No. 1213337, Apr. 2012.

[90] I. Romera Ramirez, "Changes in Powering Interlocks", in *Proceedings of the 2013 MPP Workshop*, Mar. 2013.

[91] A. Priebe *et al.*, "ADT Fast Losses MD", CERN, ATS Note 2013-017 MD, Apr. 2013.

[92] M. Sapinki *et al.*, "Generation of Controlled Losses in Millisecond Timescale with Transverse Damper in LHC", in *Proceedings of IPAC'13*, May 2013, WEPME044.

[93] W. Höfle and D. Valuch, "Transverse Feedback: High Intensity Operation, Abort Gap Cleaning, Injection Gap Cleaning and Lessons for 2012", in *Proceedings of the 2011 Evian Workshop on LHC Beam Operation*, Dec. 2011, pp. 97–100.

[94] W. Höfle, private communication, Jun. 2013.

[95] G. Battistoni *et al.*, "The FLUKA Code: Description and Benchmarking", in *AIP Conference Proceedings of HSS'06*, Sep. 2006, pp. 31–49.

[96] A. Ferrari *et al.*, "FLUKA: a Multi-Particle Transport Code", CERN, Report CERN-2005-010, Oct. 2005.

[97] E. Nebot del Busto *et al.*, "Analysis of Fast Losses in the LHC with the BLM System", in *Proceedings of IPAC'11*, Sep. 2011, pp. 1344–1346, TUPC136.

[98] T. Baer *et al.*, "UFOs in the LHC", in *Proceedings of IPAC'11*, Sep. 2011, pp. 1347–1349, TUPC137.

[99] T. Baer *et al.*, "UFOs in the LHC", presentation at 4$^{\text{th}}$ CERN Machine Advisory Committee Meeting, Aug. 2011.

[100] T. Baer *et al.*, "UFOs: Observations, Studies and Extrapolations", in *Proceedings of the 2011 Evian Workshop on LHC Beam Operation*, Dec. 2011, pp. 105–109.

[101] T. Baer *et al.*, "UFOs in the LHC after LS1", in *Proceedings of the Chamonix 2012 Workshop on LHC Performance*, Feb. 2012, pp. 294–298.

[102] N. Fuster Martinez *et al.*, "Simulation Studies of Macroparticles Falling into the LHC Proton Beam", in *Proceedings of IPAC'11*, Sep. 2011, pp. 634–636, MOPS017.

[103] E. Nebot del Busto *et al.*, "Detection of Unidentified Falling Objects at LHC", in *Proceedings of HB2012*, Sep. 2012, TUO1C04.

[104] T. Baer *et al.*, "UFO Statistics and Extrapolations", presentation at 6$^{\text{th}}$ CERN Machine Advisory Committee Meeting, Aug. 2012.

[105] Y. Tanimoto *et al.*, "Experimental Demonstration and Visual Observation of Dust Trapping in an Electron Storage Ring", *Phys. Rev. ST Accel. Beams*, vol. 12, p. 110702, Nov. 2009.

[106] A. Kling, "Dust Macroparticles in HERA and DORIS", in *Proceedings of EPAC'06*, May 2006, pp. 1486–1488, TUPLS002.

[107] S. Heifets *et al.*, "Life of the Dust Macroparticles in Storage Rings", *Phys. Rev. ST Accel. Beams*, vol. 8, p. 061002, Jun. 2005.

[108] D. Sagan, "Mass and Charge Measurement of Trapped Dust in the CESR Storage Ring", *Nucl. Instrum. Meth. A*, vol. 330, no. 3, pp. 371–379, 1993.

[109] H. Saeki *et al.*, "Observations of Dust Trapping Phenomena in the TRISTAN Accumulation Ring and a Study of Dust Removal in a Beam Chamber", *Rev. Sci. Instrum.*, vol. 62, no. 4, pp. 874–885, 1991.

[110] F. Zimmermann *et al.*, "Trapped Macroparticles in Electron Storage Rings", in *Proceedings of PAC'95*, May 1995, pp. 517–519.

[111] H. Frischholz and T. Wikberg, "ISR Running-in Run 95, 9th August 1971, Test with a Dust Shaker in Straight Section 349", CERN, Tech. Rep., Aug. 1971.

[112] V. Baglin, "Vacuum System - How to get Ready for Beam?", in *Proceedings of the Chamonix 2009 Workshop on LHC Performance*, Feb. 2009, pp. 90–94.

[113] A. Lechner *et al.*, "FLUKA Simulations of UFO-induced Losses in the LHC Arc", presentation at 2nd Quench Test Strategy Working Group Meeting, CERN, May 2012.

[114] A. Lechner *et al.*, "Analysis of 2012 UFO Events in 19R3", presentation at 5th LHC UFO Study Group Meeting, CERN, Aug. 2012.

[115] R. Versaci *et al.*, "Exploiting the Undesired: Beam-Gas Interactions in the LHC", in *Proceedings of IPAC'12*, May 2012, pp. 927–929, MOPPR063.

[116] R. Giachino *et al.*, "Diagnostics Needs for Beam-Beam Studies and Optimization", presentation at BB2013 workshop, CERN, Mar. 2013.

[117] B. Goddard *et al.*, "Transient Beam Losses in the LHC Injection Kickers from Micron Scale Dust Particles", in *Proceedings of IPAC'12*, May 2012, pp. 2044–2046, TUPPR092.

[118] T. Baer *et al.*, "Update on UFO Studies", presentation at 2nd LHC UFO Study Group Meeting, CERN, Aug. 2011.

[119] T. Baer *et al.*, "MKI UFOs at Injection", CERN, ATS Note 2011-065 MD, Aug. 2011.

[120] T. Baer *et al.*, "MD on UFOs at MKIs and MKQs", CERN, ATS Note 2012-018 MD, Feb. 2012.

[121] R. A. Barlow *et al.*, "Control of the MKQA Tuning and Aperture Kickers of the LHC", CERN, TE Note 2010-001, Jan. 2010.

[122] A. Gérardin, "EDS Analyses of Filters used for UFO Sampling", CERN, EDMS Doc. No. 1162034, Sep. 2011.

[123] G. Bregliozzi *et al.*, "Vacuum Pressure Observations during 2011 Proton Run", in *Proceedings of the 2011 Evian Workshop on LHC Beam Operation*, Dec. 2011, pp. 177–182.

[124] R. Morón Ballester and M. Guinchard, "Vibration Measurements on a LHC Kicker Prototype for UFOs Investigation", CERN, EDMS Doc. No. 1153686, Aug. 2011.

[125] F. Zimmermann, "Update on Dynamics Modeling - Effect of Kicker Field", presentation at 66th LHC Injection and Beam Dump Coordination Meeting, Nov. 2011.

[126] A. Lechner *et al.*, "FLUKA Simulations of UFO-induced Losses in IR2", presentation at 3rd LHC UFO Study Group Meeting, CERN, Sep. 2011.

[127] A. P. Verweij, "QP3: Users Manual", CERN, EDMS Doc. No. 1150045, 2011.

[128] L. Bottura *et al.*, "A General model for Thermal, Hydraulic and Electric Analysis of Superconducting Cables", CERN, LHC Project Report 456, Dec. 2000.

[129] T. Baer *et al.*, "UFOs: Observations, Statistics and Extrapolations", presentation at 7th CERN Machine Advisory Committee Meeting, Mar. 2013.

[130] Agostinelli, S. and others, "Geant4 - A Simulation Toolkit", *Nucl. Instrum. Meth. A*, vol. 506, no. 3, pp. 250–303, Jul. 2003.

[131] M. J. Barnes *et al.*, "Upgrade of the LHC Injection Kicker Magnets", in *Proceedings of IPAC'13*, May 2013, MOPWA030.

[132] A. Rossi, "SEY and Electron Cloud Build-up with NEG Materials", in *Proceedings of ECLOUD'04*, Apr. 2004.

[133] H. A. Day *et al.*, "Measurements and Simulations of Impedance Reduction Techniques in Particle Accelerators", Ph.D. dissertation, Manchester University/CERN, Jun. 2013, CERN-THESIS-2013-083.

[134] T. Baer *et al.*, "UFOs in the LHC: Observations, Studies and Extrapolations", in *Proceedings of IPAC'12*, May 2012, pp. 3936–3938, THPPP086.

[135] E. Nebot del Busto, "Beam Losses and Thresholds", in *Proceedings of the 2013 MPP Workshop*, Mar. 2013.

[136] T. Baer, "Fast Beam Losses during Beam Dump Process", presentation at 143rd LHC Machine Committee Meeting, CERN, Aug. 2012.

[137] E. Effinger *et al.*, "A Prototype Readout System for the Diamond Beam Loss Monitors at LHC", CERN, ACC Note 2013-0022, Jun. 2013.

[138] E. Griesmayer *et al.*, "A Prototype Readout System for the Diamond Beam Loss Monitors at LHC", in *Proceedings of IBIC'13*, Sep. 2013, MOPC45.

[139] R. J. Steinhagen *et al.*, "First Results from the LHC BBQ Tune and Chromaticity Systems", CERN, LHC Performance Note 007, Jan. 2009.

[140] P. Hopchev, "LHCb Beam-Gas Imaging Results", in *Proceedings of LHC Lumi Days'11*, Jan. 2011, pp. 64–68.

[141] G. Stancari *et al.*, "Collimation with Hollow Electron Beams", *Phys. Rev. Lett.*, vol. 107, p. 084802, Aug. 2011.

[142] S. Redaelli *et al.*, "Proceedings of Internal Review of Tevatron Hollow E-Lens Usage at CERN", Nov. 2012.

[143] P. Baudrenghien, "LLRF For Crab Cavities", presentation at 2nd HiLumi LHC/LARP Meeting, INFN Frascati, Nov. 2012.

[144] S. Myers *et al.*, "Workshop Summary of LHC-CC'11", CERN, ATS Note 2012-055, Apr. 2012.

[145] T. Pieloni *et al.*, "Leveling Scenarios: Present and Future Prospectives", presentation at 2nd HiLumi LHC/LARP Meeting, INFN Frascati, Nov. 2012.

[146] J.R. Delayen, "RF Dipole Deflecting/Crabbing Cavities", presentation at 2nd HiLumi LHC/LARP Meeting, INFN Frascati, Nov. 2012.

[147] T. Baer *et al.*, "Very Fast Crab Cavity Failures and their Mitigation", in *Proceedings of IPAC'12*, May 2012, pp. 121–123, MOPPC003.

[148] I.N. Bronstein *et al.*, *Taschenbuch der Mathematik*, 5th ed. Verlag Harri Deutsch, 2001.

[149] J. Tückmantel, "Failure Scenarios and Mitigation", presentation at 4th LHC Crab Cavity Workshop, CERN, Dec. 2010.

[150] K. Nakanishi *et al.*, "Beam Behavior Due to Crab Cavity Breakdown", in *Proceedings of IPAC'10*, May 2010, pp. 2938–2940, WEPEC022.

[151] T. Hays and H. Padamsee, "Response of Superconducting Cavities to High Peak Power", in *Proceedings of PAC'95*, May 1995, pp. 1617–1619, TPP02.

[152] A.C. Dexter and G. Burt, "Modelling LLRF Performance for Crab Cavities", presentation at 2nd HiLumi LHC/LARP Meeting, INFN Frascati, Nov. 2012.

[153] S.A. Pande and M. Jensen, "Multipactor Studies for Diamond Storage Ring Cavities", in *Proceedings of SRF'11*, Jul. 2011, pp. 718–723, THPO010.

[154] P. Gu *et al.*, "Reliability Improvements of the Diamond Superconducting Cavities", in *Proceedings of SRF'11*, Jul. 2011, pp. 267–270, MOPO068.

[155] T. Baer *et al.*, "LHC Machine Protection Against Very Fast Crab Cavity Failures", in *Proceedings of IPAC'11*, Sep. 2011, pp. 1816–1818, TUPZ009.

[156] G. Ripken and F. Schmidt, "A Symplectic Six-Dimensional Thin-Lens Formalism for Tracking", CERN, SL Note 95-12 AP, Apr. 1995.

[157] F. Schmidt, "SixTrack Version 4.2.16 Single Particle Tracking Code Treating Transverse Motion with Synchrotron Oscillations in a Symplectic Manner", CERN, SL Note 94-56 AP, Jan. 2012.

[158] B. Yee-Rendon *et al.*, "Machine Protection Studies for a Crab Cavity in the LHC", in *Proceedings of IPAC'13*, May 2013, MOPWO010.

[159] R. J. Steinhagen, "Planned & Possible Upgrades Related to: LHC Inter- and Intra-Bunch (Head-Tail) Diagnostics", presentation at Review on Functional Requirements on LHC Transverse Instability Diagnostics after LS1, CERN, Mar. 2013.

[160] M. Zerlauth *et al.*, "The LHC Post Mortem Analysis Framework", in *Proceedings of ICALEPCS'09*, Oct. 2009, pp. 131–133, TUP021.

[161] R. De Maria *et al.*, "HLLHCV1.0: HL-LHC Layout and Optics Models for 150mm Nb3Sn Triplets and Local Crab-Cavities", in *Proceedings of IPAC'13*, May 2013, TUPFI014.

[162] K. Wittenburg, "Beam Halo and Bunch Purity Monitoring", in *Proceedings of CAS'08*, May 2008, pp. 557–580.

[163] H. J. Kim *et al.*, "Studies of Wire Compensation and Beam-Beam Interaction in RHIC", in *Proceedings of EPAC'08*, Jun. 2008, pp. 3119–3121, THPC059.

[164] H. Schmickler, "Possible Alternatives for Halo Scraping at the LHC", presentation at Internal Review of Tevatron Hollow E-Lens Usage at CERN, Nov. 2012.

[165] A. Chao, "Halo Generation and Beam Cleaning by Resonance Trapping", in *Proceedings of HALO'03*, May 2003, pp. 291–292.

[166] O. S. Brüning, "An Analysis of the Long-Term Stability of the Particle Dynamics in Hadron Storage Rings", Ph.D. dissertation, Universität Hamburg/DESY, May 1994.

[167] G. Stancari, "Hollow Electron Beam Collimation: Tevatron Experiments", presentation at Internal Review of Tevatron Hollow E-Lens Usage at CERN, Nov. 2012.

[168] A. Rossi *et al.*, "Feasibility of Installation in the LHC and SPS", presentation at Internal Review of Tevatron Hollow E-Lens Usage at CERN, Nov. 2012.

[169] V. Moens *et al.*, "Experimental and Numerical Studies on the Proposed Application of Hollow Electron Beam Collimation for the LHC at CERN", Master thesis, École Polytechnique Fédérale de Lausanne/Fermilab/CERN, Aug. 2013, CERN-THESIS-2013-126.

[170] V. Previtali *et al.*, "Simulations of Hollow E-Lens in the LHC and SPS", presentation at Internal Review of Tevatron Hollow E-Lens Usage at CERN, Nov. 2012.

[171] B. Salvachua *et al.*, "Lifetime Analysis at High Intensity Colliders Applied to the LHC", in *Proceedings of IPAC'13*, May 2013, MOPWO049.

# Appendix

# Appendix A

# RMS Beam Position

When measuring the beam position, often the root mean square (RMS) of the measurements from all beam position monitors (BPMs) is used to quantify the difference to the reference orbit. The RMS over $N$ BPMs is defined as

$$RMS = \sqrt{\frac{1}{N}\sum_{i=0}^{N} \bar{x}_i^2},$$

where $\bar{x}_i = x_i - x_i^{\mathrm{ref}}$ is (usually) the position measurement $x_i$ of BPM $i$ w.r.t. the reference beam position $x_i^{\mathrm{ref}}$ at this BPM. Additionally, the dispersive part is often subtracted: $\bar{x}_i = x_i - x_i^{\mathrm{ref}} - D_i \frac{\Delta p}{p}$ ($D_i$ is the dispersion at BPM $i$).

While the RMS is easy to calculate, it is a measure of the beam position at discrete locations and its absolute value depends on the distribution of the BPMs and the optics. In the LHC arcs, the BPMs are regularly placed close to the quadrupole magnets with nominal $\beta$-functions of $\beta_{\mathrm{BPM,l}} = 171.0\,\mathrm{m}$ and $\beta_{\mathrm{BPM,s}} = 30.9\,\mathrm{m}$ (beam 1, horizontal) for BPMs with large and small $\beta$-function. Assuming a uniform phase space coverage by the BPMs, the RMS for a free betatron oscillation starting at phase $\varphi = 0$ and with amplitude $A = a \cdot \sqrt{\beta}$ is given by

$$\begin{aligned} RMS &= \sqrt{\frac{1}{2} \cdot \left( \frac{1}{2\pi} \int_0^{2\pi} \left( a \cdot \sin(\varphi) \sqrt{\beta_{\mathrm{BPM,l}}} \right)^2 + \left( a \cdot \sin(\varphi) \sqrt{\beta_{\mathrm{BPM,s}}} \right)^2 d\varphi \right)} \\ &= \frac{a}{2\sqrt{\pi}} \sqrt{(\beta_{\mathrm{BPM,l}} + \beta_{\mathrm{BPM,s}}) \cdot \int_0^{2\pi} \sin^2 \varphi d\varphi} \\ &= a \cdot \frac{\sqrt{\beta_{\mathrm{BPM,l}} + \beta_{\mathrm{BPM,s}}}}{2}. \end{aligned}$$

Thus, there is an optics dependent correlation between the amplitude $A_{\max}$ of the oscillation at locations with maximal $\beta$-function $\beta_{\max}$ and the RMS:

$$\frac{A_{\max}}{RMS} = \frac{2 \cdot \sqrt{\beta_{\max}}}{\sqrt{\beta_{\mathrm{BPM,l}} + \beta_{\mathrm{BPM,s}}}}.$$

For the LHC arcs, the nominal optics is rather constant and $\frac{A_{\max}}{RMS}$ is for all optics, beams and planes between 1.87 and 1.89.

It has to be noted that there are also other definitions of the RMS beam position which are frequently used. In MAD-X for example, the RMS position is not based on the beam position at the BPMs only but takes into account the beam position at all elements of the accelerator.

# Appendix B

# Protection Beam Dumps due to UFOs

| Number | Timestamp (local) | Location | Beam | Energy [GeV] | Intensity [# protons] |
|---|---|---|---|---|---|
| 1 | 07.07.2010 20:22:19 | MBB.8L7 | 2 | 3500 | 8.40E+11 |
| 2 | 30.07.2010 07:26:38 | MQ.4L5 | 2 | 3500 | 1.90E+12 |
| 3 | 07.08.2010 02:14:39 | 11L4 | 1 | 3500 | 2.05E+12 |
| 4 | 08.08.2010 01:10:47 | 15L5 | 1 | 3500 | 2.10E+12 |
| 5 | 14.08.2010 19:13:36 | RP.6R5 | 1 | 3500 | 2.30E+12 |
| 6 | 23.08.2010 13:50:38 | 22R3 | 2 | 3500 | 3.70E+12 |
| 7 | 26.08.2010 17:25:57 | 25R5 | 1 | 3500 | 4.50E+12 |
| 8 | 22.09.2010 12:48:05 | MBB.8L7 | 2 | 3024 | 2.60E+12 |
| 9 | 25.09.2010 11:06:15 | RP.6R5 | 1 | 3500 | 6.00E+12 |
| 10 | 28.09.2010 21:43:42 | MKIC.5L2 | 1 | 3500 | 1.70E+13 |
| 11 | 30.09.2010 05:29:03 | 25R8 | 1 | 3500 | 1.60E+13 |
| 12 | 02.10.2010 07:06:24 | 5R2 | 2 | 3500 | 1.50E+13 |
| 13 | 16.10.2010 03:23:47 | LHCb | 2 | 3500 | 3.70E+13 |
| 14 | 18.10.2010 05:03:09 | BSRT.5R4 | 1 | 3500 | 3.60E+13 |
| 15 | 26.10.2010 01:15:35 | 17L4 | 2 | 3500 | 4.71E+13 |
| 16 | 26.10.2010 07:49:33 | MBB.8L5 | 2 | 3500 | 4.35E+13 |
| 17 | 28.10.2010 20:04:19 | ALICE | 1 | 3500 | 4.40E+13 |
| 18 | 29.10.2010 01:26:40 | MKID.5L2 | 1 | 3500 | 4.40E+13 |
| 19 | 14.04.2011 16:13:23 | ALICE | 1 | 3154 | 2.91E+13 |
| 20 | 01.05.2011 14:58:23 | MKID.5L2 | 1 | 2974 | 9.00E+13 |
| 21 | 29.05.2011 04:46:13 | 28L8 | 1 | 3500 | 1.11E+14 |
| 22 | 31.05.2011 06:22:03 | MKID.5L2 | 1 | 3500 | 1.33E+14 |
| 23 | 31.05.2011 22:20:38 | MKID.5L2 | 1 | 3500 | 1.24E+14 |
| 24 | 02.06.2011 21:50:17 | LHCb | 1 | 3500 | 1.24E+14 |
| 25 | 03.06.2011 18:24:50 | MKID.5R8 | 2 | 3500 | 1.34E+14 |

| **Number** | **Timestamp (local)** | **Location** | **Beam** | **Energy** [GeV] | **Intensity** [# protons] |
|---|---|---|---|---|---|
| 26 | 04.06.2011 20:20:38 | MKID.5L2 | 1 | 3500 | 1.29E+14 |
| 27 | 05.06.2011 06:56:37 | MKID.5L2 | 1 | 3500 | 1.29E+14 |
| 28 | 06.06.2011 13:15:24 | MKID.5L2 | 1 | 450 | 1.31E+14 |
| 29 | 08.06.2011 19:04:29 | MKID.5L2 | 1 | 3500 | 1.30E+14 |
| 30 | 16.06.2011 03:28:33 | LHCb | 2 | 2275 | 1.27E+14 |
| 31 | 16.07.2011 01:00:06 | MKID.5L2 | 1 | 3500 | 9.81E+13 |
| 32 | 16.07.2011 05:52:33 | MKID.5L2 | 1 | 3500 | 1.01E+14 |
| 33 | 16.07.2011 14:09:18 | MKID.5L2 | 1 | 3500 | 1.02E+14 |
| 34 | 30.07.2011 23:53:11 | 31L8 | 1 | 3500 | 1.65E+14 |
| 35 | 31.07.2011 06:47:01 | ATLAS | 2 | 3500 | 1.67E+14 |
| 36 | 17.08.2011 09:48:19 | ATLAS | 1 | 3500 | 1.62E+14 |
| 37 | 10.05.2012 18:05:26 | MKID.5L2 | 1 | 4000 | 1.55E+14 |
| 38 | 14.05.2012 00:03:38 | 6R8 | 2 | 4000 | 1.56E+14 |
| 39 | 30.05.2012 18:02:52 | ALICE | 1 | 4000 | 1.94E+14 |
| 40 | 06.06.2012 03:25:29 | MKIB.5L2 | 1 | 450 | 2.56E+13 |
| 41 | 02.07.2012 20:01:33 | MKID.5L2 | 1 | 4000 | 1.24E+14 |
| 42 | 03.08.2012 04:37:50 | MKID.5L2 | 1 | 4000 | 1.98E+14 |
| 43 | 03.08.2012 06:28:58 | MKID.5L2 | 1 | 4000 | 2.14E+14 |
| 44 | 06.08.2012 16:21:34 | ALICE | 1 | 4000 | 2.08E+14 |
| 45 | 07.08.2012 06:20:44 | ALICE | 1 | 4000 | 1.96E+14 |
| 46 | 16.08.2012 20:24:39 | TCSG.4L6.B2 | 2 | 1038 | 2.23E+14 |
| 47 | 19.08.2012 11:54:13 | MKIB.5L2 | 1 | 450 | 2.44E+13 |
| 48 | 27.08.2012 23:17:12 | BSRT.5L4 | 2 | 4000 | 2.20E+14 |
| 49 | 04.09.2012 10:58:16 | MKID.5L2 | 1 | 4000 | 2.21E+14 |
| 50 | 05.10.2012 06:19:41 | 31L3 | 1 | 4000 | 1.96E+14 |
| 51 | 21.10.2012 23:27:43 | MKID.5L2 | 1 | 2361 | 2.34E+14 |
| 52 | 26.10.2012 06:39:04 | BSRT.5L4 | 2 | 4000 | 2.22E+14 |
| 53 | 14.11.2012 13:52:03 | RP.6R5 | 1 | 4000 | 1.67E+14 |
| 54 | 16.11.2012 02:58:57 | TCL.5L5 | 2 | 4000 | 2.20E+14 |
| 55 | 02.12.2012 18:52:05 | TCL.5L5 | 2 | 4000 | 2.23E+14 |
| 56 | 02.12.2012 20:34:16 | TCSG.4L6.B2 | 2 | 491 | 2.32E+14 |
| 57 | 07.12.2012 17:53:26 | ALICE | 1 | 450 | 2.14E+14 |
| 58 | 27.01.2013 10:58:51 | ALICE | 1 | 4000 | 5.87E+12 |

Table B.1.: Protection beam dumps due to UFOs.

# Appendix C

# Calibration of BLMs in IR7

The LHC ionization chambers BLMEI.06L7.B1E10_TCHSH.6L7.B1 and BLMEI.06R7.B2I10_TCHSH.6R7.B2 are installed 5 m - 10 m downstream of the primary betatron collimators in IR7 for beam 1 and beam 2, respectively. Thus, their BLM signal is closely related to the beam loss rate at the primary collimators. In order to calibrate the BLM signal (in Gy/s) against the beam loss rate at the primary collimators (in protons/s), the beam losses for fills between March and November 2012 were analyzed [171]. The calibration is based on a comparison of the BLM reading in the 1.3 s running-sum with the beam intensity changes, measured with the DC beam current transformer. The analysis is based on the beam mode squeeze (see Sec. 2.4.1) only, because the beam losses are dominated by betatron losses at the primary collimators in IR7 in this operational phase. A detailed description of the analysis procedure is given in [171].

Figure C.1 illustrates the calibration factors obtained for each fill. For beam 1 (BLMEI.06L7.B1E10_TCHSH.6L7.B1) the average calibration factor is

$$(2.1 \pm 0.3) \cdot 10^{11}\,\text{protons/Gy}.$$

The average calibration factor for beam 2 (BLMEI.06R7.B2I10_TCHSH.6R7.B2) is

$$(1.6 \pm 0.2) \cdot 10^{11}\,\text{protons/Gy}$$

(courtesy of B. Salvachua).

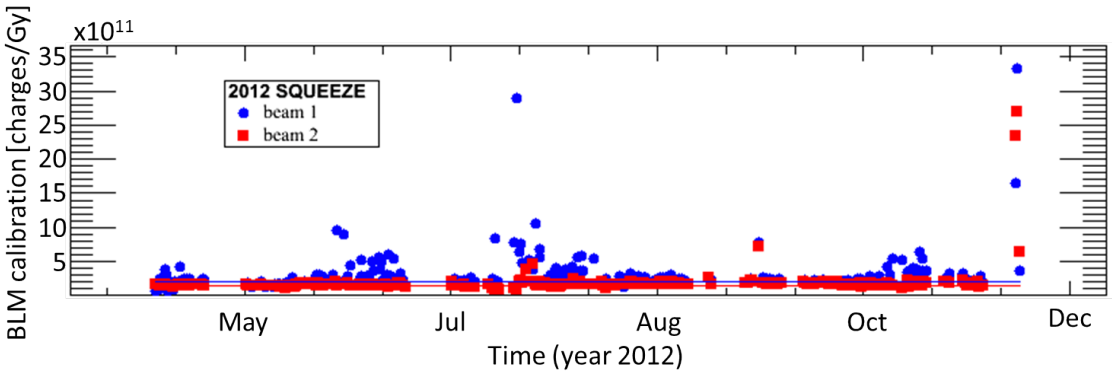


(a) BLM calibration as function of time.

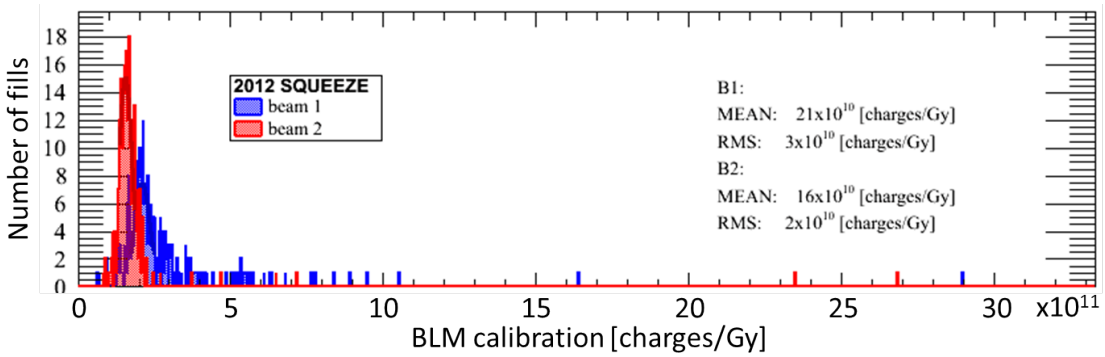


(b) Histogram of calibration factors from 2012 fills.

Figure C.1.: BLM calibration factors based on beam losses during the squeeze for LHC proton fills in 2012 (courtesy of B. Salvachua).